# ABSTRACT

Title of dissertation: NUMERICAL INVESTIGATIONS OF GASEOUS SPHERICAL DIFFUSION FLAMES

Vivien R. Lecoustre, Doctor of Philosophy, 2009

Dissertation directed by: Professor Peter B. Sunderland
Department of Mechanical Engineering

Spherical diffusion flames have several unique characteristics that make them attractive from experimental and theoretical perspectives. They can be modeled with one spatial dimension, which frees computational resources for detailed chemistry, transport, and radiative loss models. This dissertation is a numerical study of two classes of spherical diffusion flames: hydrogen micro-diffusion flames, emphasizing kinetic extinction, and ethylene diffusion flames, emphasizing sooting limits. The flames were modeled using a one-dimensional, time-accurate diffusion flame code with detailed chemistry and transport. Radiative losses from products were modeled using a detailed absorption/emission statistical narrow band model and the discrete ordinates method. During this work the code has been enhanced by the implementation of a soot formation/oxidation model using the method of moments.

Hydrogen micro-diffusion flames were studied experimentally and numerically. The experiments involved gas jets of hydrogen. At their quenching limits, these flames had heat release rates of 0.46 and 0.25 W in air and in oxygen, respectively.

These are the weakest flames ever observed. The modeling results confirmed the quenching limits and revealed high rates of reactant leakage near the limits. The effects of the burner size and mass flow rate were predicted to have a significant impact on the flame chemistry and species distribution profiles, favoring kinetic extinction.

Spherical ethylene diffusion flames at their sooting limits were also examined. Seventeen normal and inverse spherical flames were considered. Initially sooty, these flames were experimentally observed to reach their sooting limits 2 s after ignition. Structure of the flames at 2 s was considered, with an emphasis on the relationships among local temperature, carbon to oxygen atom ratio (C/O), and scalar dissipation rate. A critical C/O ratio was identified, along with two different sooting limit regimes. Diffusion flames with local scalar dissipation rates below 2 $s^{-1}$ were found to have temperatures near 1410 K at the location of the critical C/O ratio, whereas flames with greater local scalar dissipation rate exhibited increased temperatures.

The present work sheds light on important combustion phenomenon related to flame extinction and soot formation. Applications to energy efficiency, pollutant reduction, and fire safety are expected.

# NUMERICAL INVESTIGATIONS OF GASEOUS SPHERICAL DIFFUSION FLAMES

by

Vivien R. Lecoustre

Dissertation submitted to the Faculty of the Graduate School of the
University of Maryland, College Park in partial fulfillment
of the requirements for the degree of
Doctor of Philosophy
2009

Advisory Committee:
Professor Peter B. Sunderland, Advisor
Professor André W. Marshall
Professor Arnaud Trouvé
Professor Gregory J. Jackson
Professor James G. Quintiere, Dean's representative

# Foreword

*"So spake Zeus in anger, whose wisdom is everlasting; and from that time he was always mindful of the trick, and would not give the power of unwearying fire to the Melian, race of mortal men who live on the earth. But the noble son of Iapetus outwitted him and stole the far-seen gleam of unwearying fire in a hollow fennel stalk. And Zeus who thunders on high was stung in spirit, and his dear heart was angered when he saw amongst men the far-seen ray of fire."*

Hesiod - Theogony, 561 - 584

# Dedication

To my parents, Michel and Nathalie. To my brother and sister, Guillaume and Aurore.

# Acknowledgments

This work was supported by the National Aeronautics and Space Administration, under the direction of David Urban, and by the National Institute of Standards and Technology, under the direction of Jiann Yang. Research and Teaching Assistantship support was provided by the Department of Fire Protection Engineering and the Department of Mechanical Engineering.

I owe my gratitude to all the people who have made this thesis possible and who have made my life as a graduate student at University of Maryland in College Park one that I will cherish forever.

First and foremost I'd like to thank my advisor, Professor Peter Sunderland, for giving me the invaluable opportunity to work on challenging and extremely interesting projects over the past three years and half. He has always made himself available for help and advice. It has been a pleasure to work with him and to learn from such an extraordinary and talented individual.

I would also like to thank my committee members, Professor Arnaud Trouvé, Professor André Marshall, Professor James Quintiere, and Professor Gregory Jackson for their precious help, comments and advice. I would like to thank them also for their wonderful teaching and the knowledge they brought me over the course of my study.

I would to thank the whole Fire Protection Engineering Department Faculty and staff members for their generous support, help and cordial environment which contribute to the excellent work ambiance, propitious to high-level research and

learning.

I would also like to acknowledge the invaluable help of Professors Richard Axelbaum and Beei-Huan Chao. I have a profound admiration and respect for their knowledge. I am very honored to have the opportunity to collaborate with them and to learn from them. My gratitude goes also to David Urban and Dennis Stocker for their support. I would like to thank Hai Wang for its help with the soot model.

I would like to thank my fellow colleagues and graduate students K.B. Lim "the Singaporean Meister", Nick Morton, and Chris Moran, who performed the measurements in Chapter 4, for their precious help and contributions on hydrogen flames. Special thanks to my colleagues Praveen Narayanan, Justin Williamson, and Victor Scott Sam Hu for their stimulating discussions on physics phenomena and mathematics. I am not forgetting my fellow graduate students for the joy they brought me working with them and for the friendships we developed. I would like to thank Amarildo DaMata, Robin Berthier, Nicolas Rentz, Danielle Chrun, Vasilis and Karya Sotiris, Anand Veeraragavan, Roland Probst, and Angelo Gomez. Your friendships have enriched my graduate life in many ways!

My sincere thanks to Chrisy Button who taught me that perseverance and determination leads to success, to Francine Espinoza for dragging me into the life of a graduate student, and to Danielle Merta for her help in writing this manuscript.

# Table of Contents

# List of Tables

# List of Figures

# Nomenclature

**Physical Constants**

| | |
|---|---|
| $c$ | Speed of light in vacuum ($c = 299792458$ m/s) |
| $g$ | Acceleration of gravity ($g = 9.80665$ m/s$^2$) |
| $h_p$ | Planck constant ($h_p = 6.626075 \times 10^{-34}$ J.s) |
| $k_B$ | Boltzmann constant ($k_B = 1.380658 \times 10^{-23}$ J/K ) |
| $N_{av}$ | Avogadro number ($N_{av} = 6.0221367 \times 10^{23}$ molecules/mol) |
| $R$ | Ideal gas constant ($R = 8.314510$ J/mol.K) |

**Dimensionless Numbers**

| | |
|---|---|
| $Da$ | Damköhler number |
| $Fr$ | Froude number |
| $Kn$ | Knudsen number |
| $Le$ | Lewis number |
| $Pe$ | Peclet number |
| $Re$ | Reynolds number |
| $Sc$ | Schmidt number |

**Greek Symbols**

| | |
|---|---|
| $\alpha$ | Thermal diffusivity coefficient |
| $\bar{\eta}$ | Average radiative heat loss from the flame per unit volume |
| $\beta_i$ | $i^{th}$ conserved scalar |
| $\beta_{i,j}$ | Collision frequency particles of $i^{th}$ and $j^{th}$ class |
| $\chi$ | Scalar dissipation rate |
| $\chi_S$ | Number density of surface sites |
| $\Delta H_c$ | Heat of combustion per unit mass |
| $\Delta h_c$ | Heat of combustion |
| $\Delta t$ | Time step |
| $\delta$ | Infinitesimal quantity |
| $\delta(x)$ | Dirac function |
| $\delta_a$ | Reduced Damköhler number |
| $\dot{\omega}_k$ | $k^{th}$ species molar production |
| $\epsilon$ | Contribution of the Van der Waals forces |
| $\eta$ | Mixture dynamic viscosity |
| $\kappa$ | Bulk viscosity |
| $\kappa_\lambda$ | Spectral absorption coefficient for a wavelength $\lambda$ |
| $\lambda$ | Mixture thermal conductivity |
| $\lambda$ | Wavelength |
| $\mu_i$ | Abscissa of the ordinates $i$ |
| $\mu_k$ | Reduced moments of order $k$ |
| $\nu$ | Mixture kinetic viscosity |
| $\nu$ | Stoichiometric coefficient |
| $\omega_i$ | Quadrature weight associated with the $i^{th}$ direction |
| $\phi$ | Zenith angle (spherical coordinates) |

$\Psi$ Stream function
$\rho$ Mixture density
$\rho_l$ Density of the fuel in liquid phase
$\sigma_\lambda$ Spectral scattering coefficient for a wavelength $\lambda$
$\theta$ Azimuth angle (spherical coordinates)
$\Theta_k$ Thermal diffusion ratio of the $k^{th}$ species
$\xi$ $i^{th}$ root of a Legendre polynomial

**Roman Symbols**

$[X_k]$ Molar concentration of the $k^{th}$ species
$\bar{W}$ Mean molecular weight of the mixture
$\Delta G_i^o$ Standard-state Gibbs free energy for the $i^{th}$ reaction
$\dot{m}$ Mass flow rate
$\dot{q}_i$ Rate of progress for the $i^{th}$ reaction
$\mathbb{C}$ Set of all complex numbers
$\mathbb{D}_{kj}$ Binary diffusion coefficient of $i^{th}$ and $k^{th}$ species
$\mathbb{N}$ Set of all natural numbers
$\mathbb{P}$ Pressure tensor
$\mathbb{R}$ Set of all real numbers
$\mathbb{U}$ Unit tensor
$\mathscr{X}$ Computational domain
$\vec{f}_k$ Body forces acting on the $k^{th}$ species
$\vec{q_r}$ Radiative heat losses vector
$\vec{U}$ Velocity vector
$\vec{U}_T$ Thermophoretic velocity
$\vec{U}_{d,k}$ $k^{th}$ species diffusion velocity
$B$ Pre-exponential factor
$C/O$ Carbon to oxygen atom ratio
$c_p$ Mixture heat capacity at constant pressure
$C_s$ Soot mass loading
$c_{p,k}$ $k^{th}$ species heat capacity at constant pressure
$C_v$ Molar heat capacity at constant volume
$D$ Diffusion coefficient
$D_{km}$ $k^{th}$ species mixture-averaged diffusion coefficient
$E_a$ Activation energy
$h^s$ Sensible enthalpy
$h_k^o$ $k^{th}$ species formation enthalpy per mass unit
$h_{fg}$ Fuel latent heat of vaporization
$II$ Number of elementary reactions involved in a reacting flow
$J_F$ Jacobian of operator $F$
$JJ$ Number of mesh points
$K_{ci}$ Equilibrium constant of the $i^{th}$ reaction
$k_{fi}$ Forward rate of the $i^{th}$ reaction
$k_{ri}$ Reverse rate of the $i^{th}$ reaction
$KK$ Number of species present in a reacting flow

| | |
|---|---|
| $L$ | Radiance |
| $M_r$ | $r^{th}$ moment of a particle distribution |
| $p$ | Pressure |
| $Q$ | Heat exchanged |
| $r$ | Radius |
| $R$ | Rate of nucleation |
| $S$ | Entropy |
| $T$ | Temperature |
| $t$ | Time |
| $T_f$ | Flame temperature |
| $U$ | Internal Energy of a closed system |
| $V_k$ | Ordinary diffusion velocity of the $k^{th}$ species |
| $W$ | Work exchanged |
| $W_K$ | Thermal diffusion velocity of the $k^{th}$ species |
| $W_k$ | Molecular weight of the $k^{th}$ species |
| $X_k$ | $k^{th}$ species mole fraction |
| $Y_k$ | $k^{th}$ species mass fraction |
| $Z$ | Mixture fraction |
| $Z_{rot}$ | Rotational relaxation collision number |
| $Z_{st}$ | Stoichiometric mixture fraction |

**Subscripts and Superscripts**

| | |
|---|---|
| 0 | Condition inside the burner |
| $\infty$ | Condition at infinity |
| $\tilde{}$ | Dimensionless quantity |
| $ad$ | Adiabatic condition |
| $b$ | Burner property |
| $f$ | Fuel property |
| $ox$ | Oxidizer property |
| $s$ | Surface property |

# Chapter 1

# Introduction

## 1.1 Fire and Humans

### 1.1.1 Genesis

One of the greatest accomplishments of the human species is the domestication of fire. The ability to handle fire is a universal and exclusively human attainment. Although it is not formally established, evidence of the use of fire by *Homo erectus* some 400,000 years ago has been observed in various parts of Asia and Europe, long before the arrival of *Homo sapiens* [1].

The transition from living without fire to living with fire has made life easier and safer for humans. Man can appreciate the advantage of fire for warmth, light, cooking, and hunting. The domestication of fire brought tremendous change and sophistication to human society; however it also created new constraints and risks such as uncontrolled fires and fire use in warfare.

In early agrarian societies, the use of fire helped the development and growth of agriculture. Patches of forests were burned to provide enough land for cultivation, which in turn allowed settlement of a larger population.

As growing societies organized, specialized classes of people with different functions appeared. Smiths started to use fire in furnaces for manufacturing proposes such as forging of tools, weapons and jewelry. Through the ages, efforts toward understanding and controlling fire were realized. As cities became more populated, fires became more devastating, forcing the development of fire codes. In ancient Rome, there is a report of city regulations regarding fire as early as 450 B.C.

Attempts to understand the underlying nature of fire have been realized. Through the ancient world and middle-age, fire was perceived as one of the four Greek classical elements, along with water, air, and earth. During the Renaissance, Johann Joachim Becher developed what would become the phlogiston theory, which states that combustion is due to the liberation and the change of form of phlogiston, a substance with no mass but present in all flammable materials.

### 1.1.2 The Industrial Revolution

The process of understanding fire really started in the late eighteenth century. In 1777, Lavoisier demonstrated that combustion is a chemical process that consists of combining fuel with oxygen, overthrowing the theory of phlogiston [2]. What was perceived before as one of the four elements by smiths, alchemists, and philosophers, has became a rigorous science to the eyes of engineers, chemists, and physicists.

The advent of the steam machine, and therein the use of fire at an industrial scale, is coincident with the development of thermodynamics to treat fire as heat and energy. This epoch saw the radical switch in fuels, with the increased exploita-

tion of fossil fuels. Being marginal during the classical epoch and middle-age, the exploitation of first coal and later oil supplanted the use of wood as the principal fuel. Coal was first regarded as an inferior fuel because of its combustion, which generated more soot and smoke than wood did. Before the industrial revolution, coal was used principally during periods of wood shortage for heating. Its use cloaked cities in smog.

However, coal, with its high flame temperature, soon became an attractive fuel for industrial purposes, particularly metal working. The invention of the steam engine in the early $18^{th}$ century had a profound impact on society and contributed to the development and progress in understanding fire and establishing the foundation of a now rigorous science.

The establishment of thermodynamics, thanks to the work of Sadi Carnot [3], Rodulf Clausius, William Rankine, Lord Kelvin, and James Joules, contributed greatly to the understanding of fire from a macroscopic point of view. Among the most important contributions of this discipline are the first and second principles.

The first principle expresses the conservation of energy. It states the relation between the internal energy $U$ of a closed system, defined as having a fixed mass, with the heat $Q$ exchanged with the exterior and the work received $W$ by this system. Mathematically and for an infinitesimal process, this is expressed by:

$$dU = \delta Q + \delta W. \tag{1.1}$$

The second law of thermodynamics states that there exists an extensive quantity $S$, named entropy, which obeys, for a closed system, and for an infinitesimal

process, the following relationship:

$$TdS - \delta Q \geq 0, \tag{1.2}$$

with $T$ the temperature of the system and $\delta Q$ the infinitesimal amount of heat exchanged by the system with the exterior. The inequality is valid for all real processes, but the equality holds only for reversible processes.

Those two principles have enormous consequences in physics. Understanding of fire has greatly benefit from thermodynamics but also from the development of chemistry, mathematics, and engineering.

The development of the internal combustion engine by Samuel Brown in 1823 and its further improvements in the first modern car by Karl Benz in 1879, added to the increasing use of combustion in society. At this time petroleum started to be used intensively as a source of energy, benefiting from its high energy density its ease of use and transport due to its liquid phase.

### 1.1.3 Combustion in Today's Societies

Today, energy is an integral part of our society and its role is as important as food and water. Shown in Fig. 1.1, the overall consumption of energy in 2007 for the U.S.

In 2007, about 107 Exajoules (which corresponds to $1.07 \times 10^{20}$ Joules) was consumed in the U.S. [4]. More than 80% of this energy is originated from combustion, which corresponds to more than 85 Exajoules. This phenomenal conversion of energy is problematic due to the large amount of $CO_2$ and pollutants released.

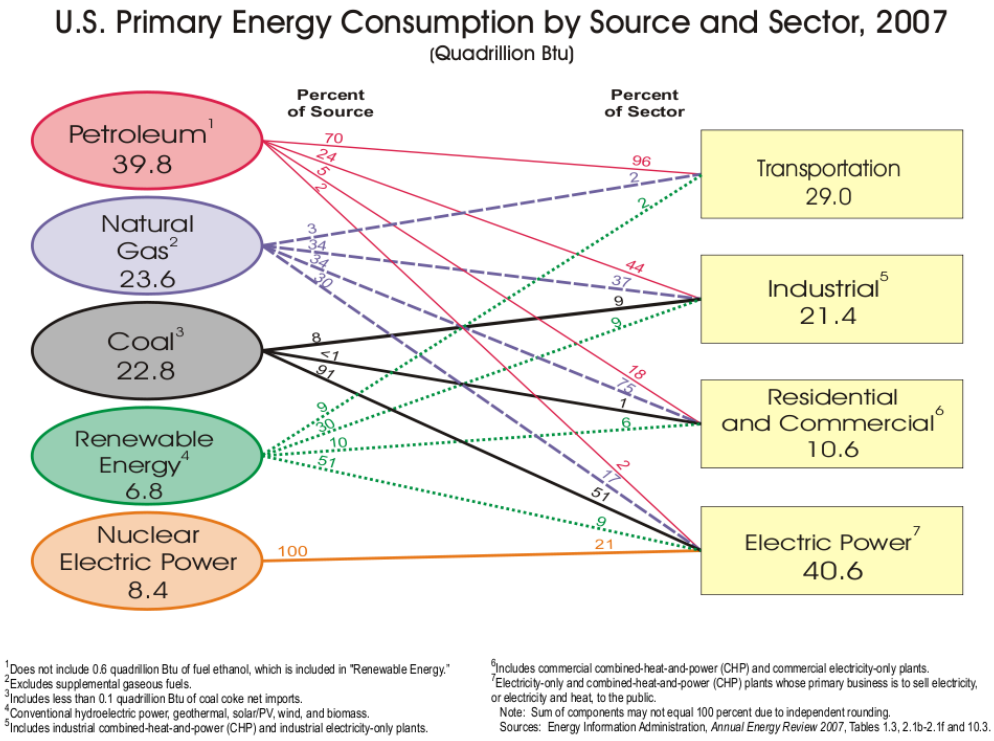


Figure 1.1: U.S. primary energy consumption by source and sector, 2007. From [4]. Note: 1 Btu = 1.06 kJ.

While $CO_2$ is the final product with water of a combustion of a hydrocarbon with oxygen, following the general chemical reaction:

$$C_nH_m + \left(n + \frac{m}{4}\right)\left(O_2 + 3.76N_2\right) \rightarrow nCO_2 + \frac{m}{2}H_2O + 3.76\left(n + \frac{m}{4}\right)N_2, \quad (1.3)$$

other pollutants such as soot, carbon monoxide (CO), sulfur dioxide ($SO_2$), nitrogen oxides (NOx), and volatile organic compounds (VOCs) can arise from incomplete combustion, operating in specific ranges, or contaminated fuels.

Air pollution, caused largely by combustion, increases the risk of cancer and

can cause premature death. Worldwide, about 2 million infant deaths are attributed to air pollution annualy [5]. Advances in understanding the causes of global warming show that $CO_2$ (along with soot and methane) is most likely to be the leading contributor to the observed climatic modifications [6]. Just for the year 2006, it is estimated that about 29,000 million tons of carbon were released worldwide into the atmosphere [7].

Progress has been realized to understand the formation of, and to reduce, some of the combustion by-products in industrial furnaces, gas-jet turbines, and internal combustion engines. Efforts promoting the use of alternative and less polluting fuels have been achieved by various governments to reduce the environmental impact of combustion. It is interesting to note that combustion of any hydrocarbon fuel, produces $CO_2$. In this regard, hydrogen is the only 'clean' fuel generating heat and water. Its reaction with air gives:

$$H_2 + \frac{1}{2}O_2 + 1.88N_2 \rightarrow H_2O + 1.88N_2. \tag{1.4}$$

Hydrogen is now considered as a possible energy carrier for the next generation of transport vehicles.

Progress has also been realized in the field of preventing, detecting, and suppressing unwanted and uncontrolled fires. Building codes have been developed and applied. Suppression devices have been improved and can be found in many buildings. However fire still kills. In the U.S. and for the year 2006, more than 3,245 fire related deaths were reported [8].

With the constant presence of man in space, fire in the unusual condition

of microgravity can cause a serious threat. This demands different means of fire detection and suppression.

## 1.2 Diffusion Flame Governing Equations

Diffusion flames, or nonpremixed flames, are the combustion phenomena in which a fuel and an oxidizer, separated before the flame, are brought together by diffuso-convective transport. This is different from premixed flames, where the mixing occurs prior to combustion. Unlike premixed flames, diffusion flames are widely present in nature. A good example is a candle flame.

Despite having different behaviors and characteristics, premixed and nonpremixed flames share the same governing equations. Those are expressed below, under the low Mach number assumption [9]:

(a) Conservation of mass:

$$\frac{\partial \rho}{\partial t} + \nabla \cdot \left(\rho \vec{U}\right) = 0. \tag{1.5}$$

(b) Conservation of species:

$$\frac{\partial \rho Y_k}{\partial t} + \nabla \cdot \left[\rho Y_k \left(\vec{U} + \vec{U}_{d,k}\right)\right] = \dot{\omega}_k, \quad k = 1, \ldots, KK. \tag{1.6}$$

(c) Conservation of momentum:

$$\rho \frac{\partial \vec{U}}{\partial t} + (\rho \vec{U} \cdot \nabla)\vec{U} = -\nabla \cdot \mathbb{P} + \rho \sum_{k=1}^{KK} Y_k \vec{f}_k. \tag{1.7}$$

(d) Conservation of energy:

$$\frac{\partial \rho c_p T}{\partial t} + \nabla \cdot \left( \rho c_p T \vec{U} \right) = -\nabla \cdot \left( \vec{q_r} + \rho \sum_{k=1}^{KK} Y_k c_{p,k} T \vec{U}_{d,k} - \lambda \nabla T \right) + \frac{dp}{dt} - \sum_{k=1}^{KK} h_k^o \dot{\omega}_k. \tag{1.8}$$

The body forces acting on a species $k$, $\vec{f_k}$ are usually due to gravity. Therefore $\vec{f_k} = \vec{g}$.

The pressure tensor $\mathbb{P}$ can be expressed, for a Newtonian fluid, by :

$$\mathbb{P} = \left[ p + \left( \frac{2}{3}\eta - \kappa \right) \left( \nabla \cdot \vec{U} \right) \right] \mathbb{U} - \eta \left[ \left( \nabla \vec{U} \right) + \left( \nabla \vec{U} \right)^T \right], \tag{1.9}$$

where $\mathbb{U}$ represents the unit tensor and the superscript $T$ denotes the transpose of a tensor or vector. Note that the bulk viscosity $\kappa$ present here is often neglected, achieving the hypothesis of Stokes. This is a fair assumption for incompressible flows.

Species reaction rate is expressed by the law of mass action, which can be stated as:

$$\dot{\omega}_k = W_k \sum_{l=1}^{II} \left( \nu''_{k,l} - \nu'_{k,l} \right) B_l T^{\alpha l} \exp\left( -\frac{E_{a,l}}{RT} \right) \prod_{j=1}^{KK} c_j^{\nu'_{j,l}}. \tag{1.10}$$

This expression is formulated for a general reacting system involving $KK$ species, most of them being intermediate species created by the cracking of reactants into more or less stable radicals, and whose evolutions are assessed through $II$ elementary reactions. These reactions are formally represented by:

$$\sum_{k=1}^{KK} \nu'_{k,l} M_k \rightleftharpoons \sum_{k=1}^{KK} \nu''_{k,l} M_k, \; l = 1, 2, \ldots, II. \tag{1.11}$$

The set of governing equations can closed by an equation of state, linking state

variables together. Under the assumption of ideal gas, it can be written:

$$p = \rho \frac{R}{\bar{W}} T, \tag{1.12}$$

where $\bar{W}$ represents the mean molecular weight of the mixture.

This set of coupled nonlinear partial differential equations has been solved analyticaly only under restrictive assumptions. The solutions presented by Burke and Schumann [10] are one example. Laminar spherical flames are another.

## 1.3 Modeling Physical Phenomena

The equations of combustion presented in the previous section are very complex for three dimensional unsteady flames. Moreover, the presence of turbulent structures, caused by flow instability at high Reynolds numbers, will have a profound impact on the flame behavior. This greatly complicates the task of solving numerically the conservation equations. Reynolds-Averaged Navier-Stokes simulations (RANS), Large Eddy Simulation (LES), and Direct Numerical Simulation (DNS) are approaches that have been developed to solve the turbulent flames governing equations.

The first two are attractive by providing a fast execution time and allowing the resolution of large scale problems. However they suffer from a lack of resolution due to their approximate nature and require additional closure models to resolve correlations of scalar fluctuations. DNS methods offer the most accuracy in modeling the physics of combustion phenomena, but they are extremely demanding in computational time, which limits their use for engineering purposes to very small

scales. Advances in turbulence combustion modeling [11, 12] presage their future use as high-fidelity tools to understand the inherent physics of turbulent reacting flows.

Investigation of fundamental phenomena and the development of accurate models require simplified configurations. This allows one to draw conclusions that are independent from the initial problem configuration, and broadens the applicability of developed models to different configurations. A typical example is the widely used flamelet concept for 3-D turbulent flames, where a local part of a turbulent flame is modeled as a laminar flame whose structure is determined by using the mixture fraction $Z$ as the only dimension [13–20]. This methodology eases the use of concepts and formulations to extremely complicated problems, providing a cheap and efficient way to numerically predict them.

One dimensional flames are attractive from experimental and theoretical points of view. They are inherently not affected by multidimensional effects that can significantly affect the flame structure [21, 22]. Remaining laminar is another important simplification.

## 1.4 Unbounded One Dimensional Flames

One dimensional flames can be planar, cylindrical, or spherical. It can be proven mathematically that there is no steady plane or cylindrical flame with fuel and/or oxidizer supplied at infinite distance [23, 24]. The only possible steady one-dimensional flame with infinite boundaries is the spherical flame. A simplified math-

ematical formulation of this problem is provided in the following sections, loosely based on Law [9].

### 1.4.1 Unlimited Plane Flame

Consider a planar and unlimited non-premixed flame with a reaction fast enough to be considered as infinitely fast. The reaction area is confined to a reaction sheet, whose location $x_f$ is the origin of the $x$ axis, which is normal to the flame surface. The flame is assumed to have a fixed and uniform temperature, $T_f$. For simplicity, it is assumed that the mass flow is null, hence $\vec{U} = 0$. The pressure is assumed to be uniform over the whole domain. Also assume equidiffusion of species and temperature. Hence the Lewis number, $Le = \dfrac{\lambda}{\rho c_p D}$, is equal to 1. In addition, assume $\rho D_i$ and $\dfrac{\lambda}{c_p}$ are constant. Finally heat losses by radiation, $\vec{q_r}$, are neglected. With the above assumptions, the energy Eq. (1.8) becomes:

$$\frac{\lambda}{c_p}\nabla^2\left(c_p T\right) = \Delta h_c \dot{\omega}_k \delta(x), \tag{1.13}$$

where $\delta(x)$ is the Dirac function, defined by:

$$\forall\, x\ \in \mathbb{R}, \delta(x) = \begin{cases} 1 & \text{for } x = 0 \\ 0 & \text{for } x \neq 0 \end{cases} \tag{1.14}$$

Considering the geometry of the problem, and assuming $c_p$ constant, Eq. (1.13) can be expressed by:

$$\lambda \frac{\partial^2 T}{\partial x^2} = \Delta h_c \dot{\omega}_k \delta(x). \tag{1.15}$$

The oxidizer supply is located far upstream, at an infinite distance from the flame location $x_f$. The fuel side is located far downstream, at an infinite distance

from the flame location. Both are assumed to have a constant temperature, $T_{ox}$ and $T_{fuel}$, respectively. Those temperatures are assumed to be different from the flame temperature.

The solution $T(x)$ of Eq. (1.15) in the non-reactive areas, which are defined by $x \neq 0$, is a linear function. It can be expressed by:

$$\forall\, x < 0,\ T(x) = C_1 x + C_2;\ \forall\, x > 0,\ T(x) = C_3 x + C_4. \tag{1.16}$$

The integration constants $C_1$,$C_2$,$C_3$, and $C_4$ are determined by applying the boundary conditions. On the oxidizer side, this gives $\lim_{x \to -\infty} T(x) = T_{ox}$. Hence, $C_1 = 0$ and $C_2 = T_{ox}$ to match the boundary condition. In the vicinity of the flame, due to the continuity of temperature $\lim_{x \to 0^-} T(x) = T_f$. Therefore $C_2 = T_f$. However, applying the boundary condition at the oxidizer side gives $C_2 = T_{ox}$, with $T_{ox} \neq T_f$. Therefore there cannot exist a solution on the oxidizer side. This is also true for the fuel side.

However, a steady solution can be obtained when the fuel and the oxidizer are supplied at a finite location, e.g., in the case of a counterflow diffusion flame.

### 1.4.2 Unlimited Cylindrical Flame

In cylindrical coordinates, assuming that the flame is located at $r_f$, Eq. (1.13) becomes:

$$\lambda \frac{1}{r} \frac{\partial}{\partial r} \left( r \frac{\partial T}{\partial r} \right) = \Delta h_c \dot{\omega}_k \delta(r - r_f). \tag{1.17}$$

Similarly to the above problem, assume that the fuel supply is located at $r_{fuel}$ such that $0 < r_{fuel} < r_f$, with a constant temperature $T_{fuel}$. The oxidizer side is

located at an infinite radius and has a constant temperature $T_{ox}$. Solving Eq. (1.19) on the oxidizer side yields:

$$\frac{\partial}{\partial r}\left(r\frac{\partial T}{\partial r}\right) = 0 \quad \Leftrightarrow \quad \frac{\partial T}{\partial r} = \frac{C_1}{r},$$
$$\Leftrightarrow \quad T(r) = C_1 \ln(r) + C_2. \tag{1.18}$$

The temperature must be bounded at infinity, therefore $C_1 = 0$ and $C_2 = T_{ox}$. Near the flame surface, we must have $T(r = r_b) = T_f$. Hence, considering the above, it is obtained $C_2 = T_f$. This is impossible because $T_{ox} \neq T_f$. Therefore there cannot exist a solution of the energy equation on the oxidizer side.

### 1.4.3 Unlimited Spherical Flame

In spherical coordinates, the energy conservation Eq. (1.13) becomes:

$$\frac{1}{r^2}\frac{\partial}{\partial r}\left(r^2\frac{\partial T}{\partial r}\right) = \Delta h_c \dot{\omega}_k \delta(r - r_f), \tag{1.19}$$

where $r_f$ is the radius of the flame. Similar to the cylindrical problem, we assume that the fuel side is located between the burner, of radius $r_b$ and of constant temperature $T_{fuel} < T_f$, and the flame location $r_f$. The oxidizer side is located at an infinite distance from the flame, with a constant temperature $T_{ox} < T_f$.

Integrating Eq. (1.19) on the non-reactive oxidizer side gives:

$$\frac{1}{r^2}\frac{\partial}{\partial r}\left(r^2\frac{\partial T}{\partial r}\right) = 0 \quad \Leftrightarrow \quad \frac{\partial T}{\partial r} = \frac{C_1}{r^2}, \tag{1.20}$$
$$\Leftrightarrow \quad T(r) = C_2 - \frac{C_1}{r}. \tag{1.21}$$

Matching the boundary condition on the oxidizer side gives $\lim_{r\to+\infty} T(r) = T_{ox} \Leftrightarrow C_2 = T_{ox}$ and near the flame $\lim_{r\to r_f+} T(r) = T_f \Leftrightarrow C_1 = (T_{ox} - T_f)\, r_f$. The solution

exists and it is expressed, on the oxidizer side by:

$$T(r) = T_{ox} + \frac{(T_f - T_{ox})\, r_f}{r}. \tag{1.22}$$

Thus the spherical configuration is the only fully one-dimensional system for which steady state flames are possible when one or more boundary conditions is applied at infinity.

This configuration can be achieved experimentally by the combustion of fuel droplets or by the use of a spherical burner, issuing the reactants from a porous sphere into a stagnant and unbounded oxidizing environment. In spherically configuration the convective, diffusive, and radiative transports are all in the radial direction. The downside of this configuration is that most of the experiments must be performed in microgravity conditions to avoid distortions brought by buoyancy forces.

### 1.4.4 Counterflow Diffusion Flame

The widely used counterflow flame, opposing jets of fuel and oxidant, is a one dimensional planar flame for which the fuel and oxidizer are supplied at a finite distance from the flame.

Figure 1.2 is a conceptual representation of such flame. Extensive research [25–30] has been carried using this configuration, which is easily set up experimentally. However, by its inherent construction, the flow pattern in a counterflow flame presents some two dimensional features. This induces a flame stretch due to the flow strain, which may have some significant effects on the flame structure [9]. Moreover,

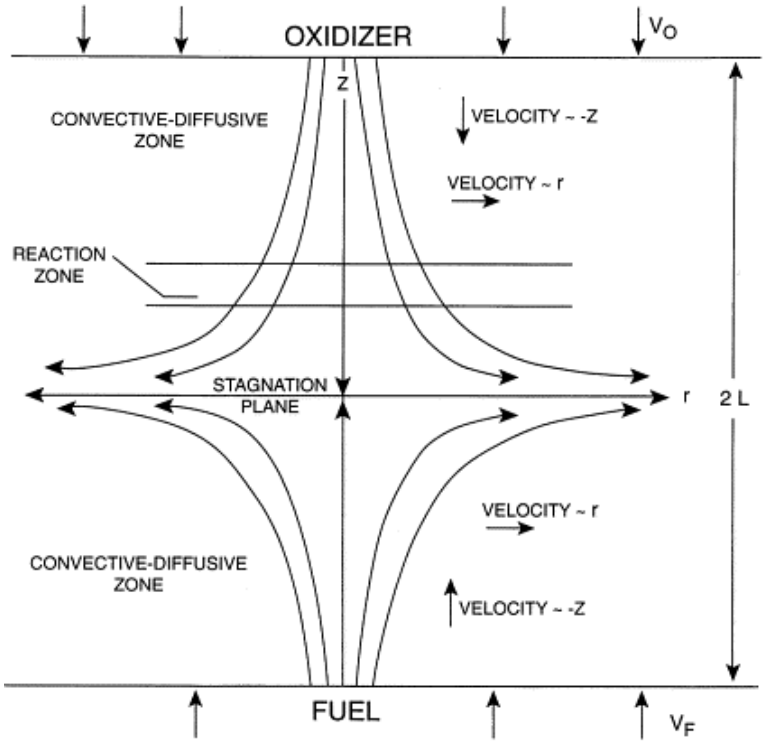


Figure 1.2: Counterflow diffusion flame. From [18].

the convective direction and flame structure cannot be fully decoupled.

## 1.5 Fuel Drop

The combustion of a fuel droplet in microgravity is an example of a spherical diffusion flame burning in an unbounded environment. In this configuration, the liquid fuel is vaporized at its surface by heat conducted from the flame.

Its characteristics have been extensively studied, under the quasi-steady approximation [31–33]. Whereas the quasi-steady assumption gives good predictions for droplet burning, its combustion is an inherently unsteady phenomenon [34, 35].

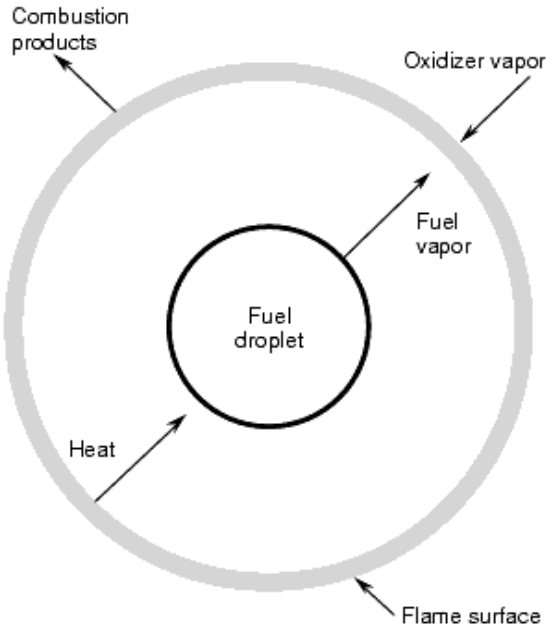


Figure 1.3: Schematic of a burning fuel droplet.

The fuel mass flow rate $\dot{m}_f$ issued from the liquid droplet by evaporation is not a parameter that can be controlled independently, but it is a function of the droplet and fuel characteristics, and it decays with time, as stated by the following relation [9, 36]:

$$\dot{m}_f(t) = \frac{\pi \rho_l}{4} K_c \sqrt{d_0^2 - K_c t}, \tag{1.23}$$

with

$$K_c = \frac{8\lambda}{\rho_l c_{p,g}} \ln\left(1 + B_{o,q},\right), \tag{1.24}$$

and

$$B_{o,q} = \frac{\frac{Y_{ox,\infty}}{\nu_{st}} \Delta h_c + c_{p,g}\left(T_\infty - T_s\right)}{h_{fg}}, \tag{1.25}$$

with $\rho_l$ the density of the fuel in liquid phase, $h_{fg}$ the fuel latent heat of vaporization, $d_0$ the initial fuel droplet diameter prior ignition, $Y_{ox,\infty}$ the downstream oxidizer mass

fraction, $\Delta h_c$ the heat of combustion, $\nu_{st}$ the stoichiometric mass ratio of oxidizer to fuel, $T_\infty$ the temperature at infinity, and $T_s$ the temperature at the fuel droplet surface.

## 1.6 Outline of the Thesis

The purpose of this thesis is the investigation of two classes of spherical diffusion flames: hydrogen micro-diffusion flames, emphasizing kinetic extinction, and ethylene diffusion flames, emphasizing sooting limits. Numerical tools are used to predict the physics of the flames and to identify critical parameters.

In Chapter 2, a short review of spherical diffusion flame characteristics is presented. Conservation equations for spherical diffusion flames are established, with a short review of previous work.

In Chapter 3, the numerical code used to predict the structure and the dynamics of spherical diffusion flames is presented in detail. Presentations of the discretized equations, the detailed chemistry, and transport model can be found along with a description of the model used to solve the radiative transport equation.

In Chapter 4, the numerical code is used to predict weak hydrogen diffusion flames at their kinetic extinction limits. Structures of those flames are predicted and the combined effects of the mass flow rate and burner size are investigated.

Chapter 5 discusses the phenomenology of soot formation in flames. Then the description and prediction of spherical sooting limit flames are presented. Coupled effects of local temperature, local C/O ratio, and characteristic transport times on

limit flames are investigated.

In Chapter 6, the numerical model is coupled with a model of soot formation based on the method of moments. A comprehensive description is provided along with the prediction of soot formation in a spherical diffusion flame.

In Chapter 7, conclusion and recommendations for future work are given.

# Chapter 2

# Burner-Supported Spherical Diffusion Flames

Spherical diffusion flames are a particular case of one dimensional flames. As demonstrated in the previous chapter, they are the only 1-D configuration possible with a steady state solution when fuel and/or oxidizer are supplied at infinity. Burner-generated spherical diffusion flames are established by issuing fuel from a porous spherical burner into a quiescent oxidizer environment. This configuration can be inverted, realizing an inverse flame. Microgravity conditions are necessary to achieve sphericity of the flame.

## 2.1 Background

A fair number of studies have considered spherical diffusion flames. Matalon *et al.* [24, 37] developed an extensive analytical model of steady state spherical diffusion flames. They have also identified kinetic and radiative extinctions. These phenomena have also been predicted for fuel droplets by Chao *et al.* [38]. An an-

alytical study of spherical diffusion flames considering ignition and extinction was published by Buckmaster [23].

Sung *et al.* [39] observed experimentally and numerically $H_2$-$CH_4$ inverse spherical flames presenting two distinct luminous zones. Reduction of buoyancy effects was accomplished with the use of reduced pressure ($< 0.2$ bar) and large burner diameter (1.27 cm). Numerical simulations were performed using a modified Sandia PREMIX code [40].

Tse *et al.* [41] performed experiments on burner-generated spherical diffusion flames with $H_2/CH_4$/inert mixtures issuing into atmospheric air. The use of a 2.2 s drop tower provided microgravity conditions. Using the same numerical model as Sung *et al.* [39], updated with a statistical narrow band model, they were able to predict with good accuracy the transient evolution of spherical flames. They also reported important radiative absorption-emission within those flames.

Santa *et al.* [42] observed experimentally and investigated numerically extinction of spherical diffusion flames in microgravity. They considered $C_2H_4$ and $C_3H_8$ issued from a 0.3175 cm radius burner, and reacting with a mixture of $N_2$ and $O_2$. The computational model used was similar to the model used by Tse *et al.* [41]. One of the significant findings was that flame extinction occurs when the ratio of the radiation heat loss to heat release rate reaches a critical value of 0.7 and that radiative heat loss scales with the surface area of the flame.

Important studies, mostly experimental, were published by Atreya and coworkers [43–46]. Using a 2.2 s drop tower, they reported observations of $CH_4$ and $C_2H_4$ transient flames with measurements of temperature inside a $C_2H_4$ flame, along with

the radiative heat losses. They also studied the effects of diluents, $N_2$, and $CO_2$, on the flame structure. They observed that the addition of $CO_2$ inhibits soot formation and can strengthen the flame due to increased re-absorption when present in the oxidizer side.

Christiansen and coworkers [47,48] studied the transient extinction behavior of $H_2/N_2/CO_2$/He flames with diluted oxidizer of various Lewis numbers issuing from a 1.27 cm burner radius. Microbouyancy conditions were created using pressures below than 0.1 bar. Oscillatory behavior of the flames near radiative extinction and with frequencies around 2 Hz was reported. Their numerical predictions for $CH_4/O_2$/He and $H_2$/He/$O_2$ show that oscillations, triggered by the introduction of small perturbations in the steady state solution, are the result of thermal expansion in the flame. They predicted oscillation frequencies ranging from 0.25 - 60 Hz.

Matalon *et al.* [49] found that oscillatory regimes in spherical diffusion flames can be triggered by either sufficiently large Lewis numbers (even without heat loss) or by appreciable heat losses (even for unity Lewis numbers). This oscillatory behavior was first observed for a candle in microgravity [50].

The inception of soot inside a spherical diffusion flame has been an important subject of studies. Liu *et al.* [51] analytically studied soot inception in spherical diffusion $C_2H_4$ flames for various flame structures. Fuel oxidation and soot precursor inception/oxidation were modeled by a simplified three-step model with high activation energy. Their results show a critical soot formation reaction rate exists at which the net soot production is the highest. They also conclude that the flame has a strong impact on the soot inception and argue that the flow rate alone cannot

suppress the soot precursor formation.

Ezekoye *et al.* [52] used a numerical code to model the transient evolution of sooty spherical diffusion flames. They used a two-step global reaction mechanism for $C_2H_2$/air reaction with an optically thin radiation model for radiating gas species and soot. They considered a semi-empirical soot model with nucleation, coagulation, surface growth due to $C_2H_2$, and oxidation due to $O_2$ taken from the Fairweather model [53] with a different model for soot oxidation by OH. They also assume incipient carbon particles of 9000 carbon atoms. Their results show that OH oxidation reaction rate is larger than $O_2$ oxidation reaction rate and has a significant impact on the overall soot formation.

Sooting spherical diffusion flames have been observed experimentally by Sunderland *et al.* [54, 55]. Microgravity conditions were obtained in 2.2 and 5 s drop facilities. A 0.3175 cm radius spherical burner was used to issue $C_2H_4/N_2$ or $O_2/N_2$ mixtures. Effects of stoichiometric mixture fraction and convection direction (defining normal or inverse flames) on flame sooting behavior were studied. They suggest that sooting tendency of flames are more affected by flame structure than by convection direction.

Sooting limits of spherical diffusion flames have been characterized experimentally [55] for $C_2H_4/O_2/N_2$ for a wide range of flame structures and convection conditions. In this work, 17 different flames have been identified to reach their sooting limits after 2.0 s. Results show that the sooting limits follow a linear relationship between the adiabatic flame temperature and the stoichiometric mixture fraction. Based on a Burke-Schumann analysis, Ref. [55] identified a critical value for the

local carbon to oxygen atom ratio and a threshold temperature for soot inception.

Some of those flames [54] have been numerically modeled by Santa *et al.* [56]. Only gas phase species were considered, with the use of a detailed chemistry model for the reaction of $C_2H_4$ with air. Close agreement with experimental data based on flame location is obtained when heat and diffusivity coefficients are increased by 30%. Results show that the effect of Lewis number for transient radiating flames is small.

## 2.2 Governing Equations

This section states the general governing equations for a one dimensional, spherical diffusion flame, after giving the expression of the operator gradient $\nabla$ and divergence $\nabla\cdot$ in spherical coordinates.

In spherical coordinates, any point $M$ of space is assigned a set of coordinates $(r, \theta, \phi)$, with r the radial, $\theta$ the azimuth, and $\phi$ the zenith angle coordinates, and a local orthogonal base $(\vec{e}_r, \vec{e}_\theta, \vec{e}_\phi)$. For any scalar $f = f(r, \theta, \phi)$, its gradient, $\nabla f$, is expressed by:

$$\nabla f = \frac{\partial f}{\partial r}\vec{e}_r + \frac{1}{r\sin\phi}\frac{\partial f}{\partial \theta}\vec{e}_\theta + \frac{1}{r}\frac{\partial f}{\partial \phi}\vec{e}_\phi. \tag{2.1}$$

The divergence of a vector $\vec{\Phi} = (\Phi_r, \Phi_\theta, \Phi_\phi)$ is given by:

$$\nabla\cdot\vec{\Phi} = \frac{1}{r^2}\frac{\partial}{\partial r}\left(r^2\Phi_r\right) + \frac{1}{r\sin\phi}\frac{\partial \Phi_\theta}{\partial \theta} + \frac{1}{r\sin\phi}\frac{\partial}{\partial \phi}\left(\Phi_\phi \sin\phi\right). \tag{2.2}$$

Because of the spherical symmetry of the problem, $f(r, \theta, \phi) = f(r)$ and

$\vec{\Phi}(r,\theta,\phi) = \Phi_r(r)\vec{e}_r$. Hence, Eqs. (2.1) and (2.2) become:

$$\nabla f = \frac{\partial f}{\partial r}\vec{e}_r, \tag{2.3}$$

$$\nabla \cdot \vec{\Phi} = \frac{1}{r^2}\frac{\partial}{\partial r}\left(r^2\Phi_r\right). \tag{2.4}$$

With these simplifications, under the assumption of constant and uniform pressure, and with the hypothesis of Stokes, i.e. $\kappa = 0$:, the general governing equations, Eqs. (1.5)-(1.8) become:

(a) Conservation of mass:

$$\frac{\partial \rho}{\partial t} + \frac{1}{r^2}\frac{\partial}{\partial r}\left(\rho r^2 U_r\right) = 0. \tag{2.5}$$

(b) Conservation of species:

$$\frac{\partial \rho Y_k}{\partial t} + \frac{1}{r^2}\frac{\partial}{\partial r}\left[\rho r^2 Y_k\left(U_r + U_{dr,k}\right)\right] = \dot{\omega}_k,\ k = 1,\ldots,KK. \tag{2.6}$$

(c) Conservation of momentum:

$$\rho\frac{\partial U_r}{\partial t}\vec{e}_r + \rho U_r\frac{1}{r^2}\frac{\partial}{\partial r}\left(r^2 U_r\right)\vec{e}_r = \eta\left[\frac{\partial^2 U_r}{\partial r^2} + \frac{2}{r}\frac{\partial U_r}{\partial r} - \frac{2U_r}{r^2}\right]\vec{e}_r. \tag{2.7}$$

(d) Conservation of energy:

$$\begin{aligned}\frac{\partial}{\partial t}\left(\rho c_p T\right) + \frac{1}{r^2}\frac{\partial}{\partial r}\left(\rho r^2 c_p T U_r\right) = -\nabla\cdot\left(\vec{q}_r\right) - \frac{1}{r^2}\frac{\partial}{\partial r}\left(r^2\rho\sum_{k=1}^{KK} c_{p,k}TY_kU_{rd,k}\right)\\ + \frac{1}{r^2}\frac{\partial}{\partial r}\left(r^2\lambda\frac{\partial T}{\partial r}\right) - \sum_{k=1}^{KK} h_k^o\dot{\omega}_k.\end{aligned} \tag{2.8}$$

Neglecting the effects of viscosity on the fluid, the equation of conservation of momentum, Eq. (2.7), can be further simplified to:

$$\rho\frac{\partial U_r}{\partial t} + \rho U_r\frac{1}{r^2}\frac{\partial}{\partial r}\left(r^2 U_r\right) = 0. \tag{2.9}$$

Assuming that the radiation term $\vec{q}_r$, the species production term $\dot{\omega}_k$, the species specific heat, and the species diffusion velocity $U_{rd,k}$ are functions of the state variables $(T, Y_1, \ldots, Y_{KK})$, then the system of $KK + 3$ unknowns is closed by an equal number of equations. Another possibility for the resolution of this system is to replace the conservation of momentum, Eq. (2.9), by an equation of state such as the ideal gas law:

$$p = \rho \frac{R}{\bar{W}} T. \tag{2.10}$$

## 2.3 Characteristics of Steady State Spherical Diffusion Flames

The approach of Mills and Matalon [24] is valuable to understand and predict the characteristics of steady state spherical diffusion flames. Consider a steady state spherical diffusion flame, generated by a burner of radius $r_b$ with no radiative heat loss, and assuming a single step reaction defined by:

$$\nu_f \mathrm{F} + \nu_{ox} O \rightarrow (\nu_f + \nu_{ox}) P, \tag{2.11}$$

where $\nu_f$ and $\nu_{ox}$ are the stoichiometric coefficients for the fuel and the oxidizer, respectively. The reaction rate is assumed to be of Arrhenius type with an activation energy $E_a$ and a pre-exponential factor $B$. The product $\rho D_k$ is assumed constant. The governing equations, Eqs. (2.5),(2.6), and (2.8), in dimensionless form, are then expressed by:

$$\tilde{r}^2 \tilde{\rho} \tilde{U}_r = M, \tag{2.12}$$

$$\frac{M}{\tilde{r}^2}\frac{d\tilde{T}}{d\tilde{r}} - \frac{1}{\tilde{r}^2}\frac{d}{d\tilde{r}}\left(\tilde{r}^2\frac{d\tilde{T}}{d\tilde{r}}\right) = \tilde{q}\dot{\tilde{\omega}}, \tag{2.13}$$

$$\frac{M}{\tilde{r}^2}\frac{d\tilde{Y}_f}{d\tilde{r}} - \frac{1}{Le_f}\frac{1}{\tilde{r}^2}\frac{d}{d\tilde{r}}\left(\tilde{r}^2\frac{d\tilde{Y}_f}{d\tilde{r}}\right) = -\dot{\tilde{\omega}}, \tag{2.14}$$

$$\frac{M}{\tilde{r}^2}\frac{d\tilde{Y}_{ox}}{d\tilde{r}} - \frac{1}{Le_{ox}}\frac{1}{\tilde{r}^2}\frac{d}{d\tilde{r}}\left(\tilde{r}^2\frac{d\tilde{Y}_{ox}}{d\tilde{r}}\right) = \nu\dot{\tilde{\omega}}, \tag{2.15}$$

with the dimensionless rate of production $\dot{\tilde{\omega}}$ expressed by:

$$\dot{\tilde{\omega}} = \rho^2 D_a Y_{ox} Y_f \exp\left(-\frac{\theta}{T}\right). \tag{2.16}$$

The equation of state becomes:

$$\tilde{\rho}\tilde{T} = 1, \tag{2.17}$$

where $Y_{ox}$ and $Y_f$ are the mass fraction of oxidizer and fuel, respectively, $\tilde{\rho} = \dfrac{\rho}{\rho_\infty}$ and $\tilde{T} = \dfrac{T}{T_\infty}$, the subscript $\infty$ denotes the value at the ambient. The radius of the burner $r_b$ is used as a unit of length such that we have $\tilde{r} = \dfrac{r}{r_b}$. The diffusion velocity $\dfrac{\lambda}{\rho_\infty c_p r_b}$ is used as a unit of velocity such that $\tilde{U}_r = \dfrac{U_r}{\lambda/\rho_\infty c_p r_b}$. The ratio of the mass weighted stoichiometric coefficient is $\nu = \dfrac{\nu_{ox} W_{ox}}{\nu_f W_f}$.

The other dimensionless parameters are the dimensionless activation energy $\theta = \dfrac{E_a}{RT_\infty}$ and the heat release per unit mass of fuel $\tilde{q} = \dfrac{\Delta h_c}{c_p T_\infty \nu_f W_f}$ with $\Delta h_c$ the total heat of combustion.

The Lewis numbers of the fuel and the oxidant are defined by $Le_f = \dfrac{\lambda}{\rho c_p D_f}$ and $Le_{ox} = \dfrac{\lambda}{\rho c_p D_{ox}}$, corresponding to the ratio of the thermal diffusivity of the mixture to the molecular diffusivity of the reactant considered (fuel or oxidant).

Two other dimensionless parameters are defined as follow. The dimensionless mass flow rate $M = \dfrac{\dot{m} c_p}{4\pi\lambda r_b}$ , is the ratio of the mass flow rate issued from the spherical burner, $\dot{m}$, to the reference mass flow rate defined by the diffusivity velocity and

the ambient density. The Damköhler number $D_a$, defined as the ratio of a characteristic residence or diffusion time to the chemical reaction time, can be expressed by $D_a = \frac{r_b^2 \rho_\infty c_p}{\lambda} \nu_f \rho_\infty B W_f$, where the characteristic time is given by the ratio of the burner radius $r_b$ divided by the characteristic diffusion speed. The chemistry time is defined by the characteristics of the fuel and its combustion with the oxidant.

By expanding the solution for the variables sought (temperature, fuel, and oxidant mass fraction) in the convective diffusive region of the flame and considering the first order terms, Mills and Matalon have shown [24] that the flame radius of a steady state spherical diffusion flame, without radiative heat losses, is given by:

$$r_f = \frac{c_p}{4\pi\lambda \ln\left(1 + \frac{Y_{ox,\infty}}{\nu}\right)^{\frac{1}{Le_{ox}}}} \dot{m}. \tag{2.18}$$

Equation (2.18) shows that the mass flow rate issued from the burner has a linear effect on the radius of the flame at steady state. Also, only the Lewis number of the oxidizer has an effect on the flame location.

## 2.4 Kinetic and Radiative Extinction of Spherical Diffusion Flames

When solving for the inner structure of a flame, a reduced Damköhler number $\delta_a$ can be introduced. When a flame exchanges heat with the surroundings solely by conduction at the burner surface, the reduced Damköhler number is proportional to the square of the mass flow rate, $\dot{m}$:

$$\delta_a \sim D_a \dot{m}^2. \tag{2.19}$$

There is a minimum value $\delta_{a,min}$ such no solution is possible for lower $\delta_a$. The flame is then extinguished. This is achieved when the mass flow rate is low enough. Since there is no radiative loss, this represents purely kinetic extinction.

In the presence of radiative heat loss, theoretical analyses by Chao *et al.* [38] and Mills and Matalon [37] have shown that there is a maximum mass flow above which the flame extinguishes due to excessive radiative heat losses. The reduced Damköhler number, with the effects of the radiative heat losses, is now expressed as:

$$\delta_a \sim D_a \dot{m}^2 \exp\left(-A\dot{m}^2\right), \tag{2.20}$$

where A includes the effects of oxidizer and fuel Lewis number.

The graph of the function given by Eq. (2.20) shows that the minimum value permissible for the reduced Damköhler $\delta_{a,min}$ can be reached by both small and high mass flow rates. Extinction at high mass flow rates represents radiative extinction.

Figure 2.1 represents the predicted flame temperature of a steady-state spherical methane diffusion flame versus the mass flow rate for a case with an adiabatic flame configuration and for another with radiative heat losses.

Radiative extinction was experimentally and numerically investigated by Santa *et al.* [42]. They noticed at high mass flow rates, extinction occurs when the heat lost by radiation is nearly 70% of the overall heat of combustion generated by the flame. Other findings are that the extinction diameter scales with the square root of the flow rate, the rate of radiative loss scales with the flame area, and that the peak temperature before flame extinction is independent of the mass flow rate and

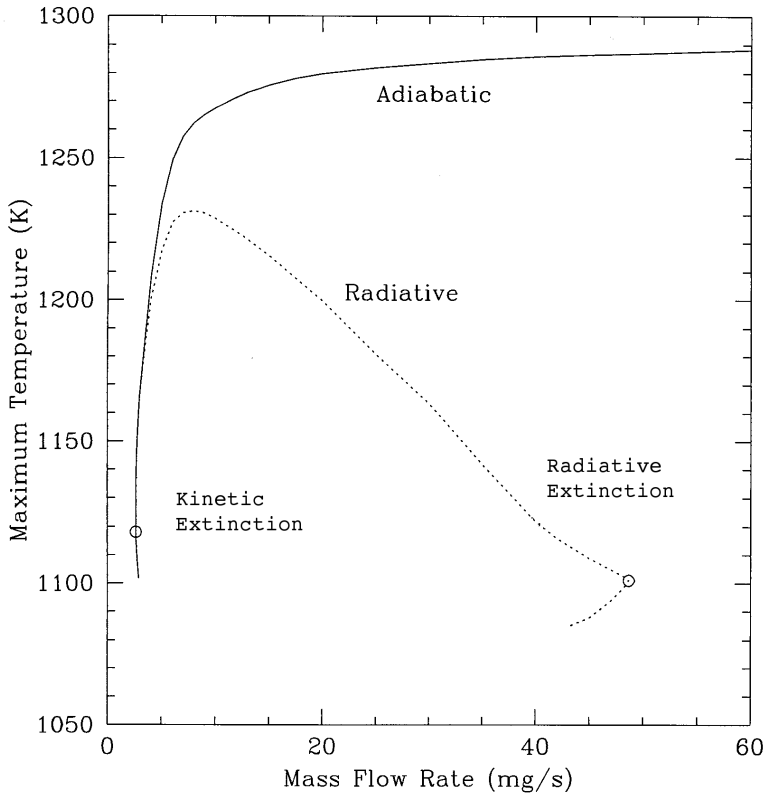


Figure 2.1: Maximum temperature for a steady-state spherical diffusion flame of 50% $CH_4$/50% He into 29% $O_2$/79% He for various mass flow rate, with both adiabatic and radiative heat loss cases. Adapted from [57].

ranges around 1100 K.

## 2.5 Transient Approach

Section 2.3 states some of the characteristics of spherical diffusion flames at steady state and neglecting heat losses by radiation. However, as mentioned in Section 2.4, radiation can have a profound impact on the flame behavior. Moreover, transient behavior is observed before reaching steady state. Therefore it is of interest

to model analytically the transient behavior of a radiating spherical flame from its ignition to its steady state. This has been achieved by Atreya *et al.* [43, 44]. Some of their main results are provided below.

### 2.5.1 Formulation

Consider an expanding spherical diffusion flame of initial radius $r_{init} = r_f(0)$ generated by a constant mass flow rate $\dot{m}$ of fuel issued from a spherical burner of radius $r_b$. Equidiffusivity is assumed, hence $D_k = D$, and unity species Lewis number is assumed. In addition, an infinitely fast, one step reaction is considered:

$$\mathrm{F} + \nu_{ox} O \rightarrow (1 + \nu_{ox}) P. \tag{2.21}$$

The conditions inside the burner are $Y_f = Y_{f,0}$, $Y_{ox} = O$, $Y_p = 0$, and the sensible enthalpy is $h^s = h_0^s$. At the burner surface, the following boundary conditions are observed:

$$\frac{\dot{m}}{4\pi r_b^2} = \rho U_r(r_b), \tag{2.22}$$

$$\frac{\dot{m}}{4\pi r_b^2} \left(Y_{f,0} - Y_f(r_b)\right) = -\rho D \left.\frac{\partial Y_f}{\partial t}\right|_{r_b}, \tag{2.23}$$

$$\frac{\dot{m}}{4\pi r_b^2} \left(h_0^s - h^s(r_b)\right) = -\rho D \left.\frac{\partial h^s}{\partial t}\right|_{r_b}. \tag{2.24}$$

The amount of soot present in the flame is assumed to be small enough such that a conserved scalar $Z_f$ can be defined by:

$$Z_f = \frac{Y_C + Y_H}{Y_{f,0}}, \tag{2.25}$$

where $Y_C$ and $Y_H$ are the atomic mass fractions. Being a conserved scalar, $Z_f$ verifies the homogeneous equation:

$$\rho\frac{\partial Z_f}{\partial t} + \rho U_r\frac{\partial Z_f}{\partial r} - \frac{1}{r^2}\frac{\partial}{\partial r}\left(\rho r^2 D\frac{\partial Z_f}{\partial r}\right) = 0. \tag{2.26}$$

A conserved scalar $Z_O$ can also be formed for the oxidizer and can replace $Z_f$ in Eq. (2.26). The energy equation is made homogeneous by considering the total enthalpy $h_T$ and by approximating the heat loss by radiation as a fraction of the heat of combustion. Hence the conservation equation of total enthalpy is similar in form to Eq. (2.26).

### 2.5.2 Approach to Solution

The equations of mass conservation, Eq. (2.5) and scalar conservation, Eq. (2.26) are sufficient to describe the transient problem:

$$\frac{\partial \rho}{\partial t} + \frac{1}{r^2}\frac{\partial}{\partial r}\left(\rho r^2 U_r\right) = 0, \tag{2.5}$$

$$\rho\frac{\partial Z}{\partial t} + \rho U_r\frac{\partial Z}{\partial r} - \frac{1}{r^2}\frac{\partial}{\partial r}\left(\rho r^2 D\frac{\partial Z}{\partial r}\right) = 0. \tag{2.26}$$

The mass conservation equation is solved by defining a stream function $\Psi(r,t)$ that satisfies Eq. (2.5). Quantity $\Psi$ is defined by:

$$\frac{\partial \Psi}{\partial t} = -r^2\rho U_r \; ; \; \frac{\partial \Psi}{\partial r} = r^2\rho. \tag{2.27}$$

Applying the initial and boundary conditions gives:

$$\begin{aligned}\Psi(r,t) &= \int_{r_b}^{r} r^2\rho(r,t)dr - \frac{\dot{m}t}{4\pi} \\ &= \int_0^t r^2\rho(r,t)U_r(r,t)dt + \rho_f\left(\frac{r^3 - r_b^3}{3}\right).\end{aligned} \tag{2.28}$$

Rewriting Eq. (2.26) in terms of $\Psi$ and assuming constant $\rho^2 D$ yields:

$$\frac{\partial Z}{\partial t} = \rho_f^2 D \frac{\partial}{\partial \Psi}\left(r^4 \frac{\partial Z}{\partial \Psi}\right). \tag{2.29}$$

Solving Eq. (2.29) with $r = r_f$, Atreya [44] found that the scalar $Z$ solution of Eq. (2.29), can be expressed as:

$$Z = \frac{1 - \text{erf}\left(\frac{\Psi}{2\sqrt{\tau}}\right)}{1 + \text{erf}\left(\frac{\dot{m}t}{8\pi\sqrt{\tau}}\right)}, \tag{2.30}$$

where $\tau$ is defined such that at the flame location, given by $\Psi = 0$, $Z = Z_{st}$, with $Z_{st}$ defined by:

$$Z_{st} = \left(1 + \frac{Y_{f,0}\nu_{ox}M_{ox}}{Y_{ox,\infty}M_f}\right)^{-1}. \tag{2.31}$$

Atreya gives an expression for the flame location:

$$r_f(t) = \left[r_{init}^3 + \left(\frac{3\dot{m}\left(\rho_{ox}h_0^s + \Delta H_c \rho_{ox} Y_{f,0} Z_{st}\right)}{4\pi\rho_f\left(\rho_{ox}h_0^s + \bar{\eta}t\right)}\right)t\right]^{\frac{1}{3}}, \tag{2.32}$$

where $\Delta H_c$ is the heat released per unit mass $\Delta H_c = \dfrac{\Delta h_c}{M_f}$ and $\bar{\eta}$ is the average radiative heat loss from the flame per unit volume. Equation (2.32) has been used to normalize measured transient flame radii [44] with significant successes, data falling along a constant value of 1.3 for different flames.

# Chapter 3

# Numerical Methods

In Chapter 2, governing equations and general characteristics of spherical diffusion flames were stated.

The particular geometry of the problems investigated allows great simplications of the general combustion equations. Indeed, the spherical symmetry reduces the number of spatial coordinates to only one, as established in Eqs. (2.5)-(2.8). This decreases considerably the number of mesh points required. A general 3-D problem requiring $N$ mesh points or cells, requires only $\sqrt[3]{N}$ cells when spherical symmetry is observed with the same grid spacing. Computational workload can be diverted such as for the use of more detailed chemistry models.

The code used here is a modified version of the Sandia's PREMIX code [40]. It was originally developed for the study of one-dimensional freely propagating and burner-stabilized premixed laminar flames. This code is part of the Sandia's CHEMKIN package [58] and therefore provides the user with a vast choice of libraries developed to model detailed chemistry kinetics with complex and customizable reaction mechanisms. It also models detailed transport properties using Sandia's TRANSPORT package [59]. Transient and steady-state problems are solved using

a modified Newton algorithm from the Sandia's TWOPNT package [60]. General descriptions of those functions are presented in this chapter, along with a description of the radiative model used to solve the radiative transfer equation.

## 3.1 Modeling Approach

Steady state and transient problems are solved by the code. In this section, the solved governing equations for a spherical transient problem are recalled. Boundary conditions associated with the different configurations investigated in this work are also discussed.

### 3.1.1 Governing Equations

The set of equations that are solved numerically is similar to the set of Eqs. (2.5)-(2.8), described in spherical coordinates $(r, \theta, \phi)$. The main assumptions considered here are: isobaricity of the flow, negligible flow viscosity forces, and no body forces. Integrating Eqs. (2.5)-(2.8) over $-\pi < \theta \leq \pi$ and $-\frac{\pi}{2} \leq \phi \leq \frac{\pi}{2}$ gives:

(a) Continuity (mass conservation):

$$A(r)\frac{\partial \rho}{\partial t} + \frac{\partial}{\partial r}\left(\dot{m}\right) = 0. \tag{3.1}$$

(b) Energy conservation:

$$\rho A(r)\frac{\partial T}{\partial t} + \dot{m}\frac{\partial T}{\partial r} + \frac{A(r)}{c_p}\sum_{k=1}^{KK}\left(\rho c_{p,k} Y_k U_{dr,k}\frac{\partial T}{\partial r} + h_k^o \dot{\omega}_k\right) - \frac{1}{c_p}\frac{\partial}{\partial r}\left(A(r)\lambda\frac{\partial T}{\partial r}\right) - \frac{\partial}{\partial r}\left(A(r)q_r\right) = 0. \tag{3.2}$$

(c) Species conservation:

$$\rho A(r)\frac{\partial Y_k}{\partial t}+\dot{m}\frac{\partial Y_k}{\partial r}+\frac{\partial}{\partial r}\left(\rho A(r)Y_k U_{dr,k}\right)-A(r)W_k\dot{\omega}_k=0, k=1,\ldots,KK \quad (3.3)$$

(d) Equation of state:

$$\rho=\frac{p\bar{W}}{RT}, \quad (3.4)$$

with $A(r)=4\pi r^2$ the area of the radius $r$ and $\dot{m}=\rho A(r)U_r$ the mass flow rate at the location of radius $r$. Note that the mass flow rate is constant in steady state, hence Eq. (3.1) becomes:

$$\dot{m}=\rho U_r A(r)=\dot{m}_b, \quad (3.5)$$

with $\dot{m}_b$ the mass flow rate prescribed at the burner surface. The above set of $KK+2$ equations has $KK+2$ unknowns, which are: $\dot{m}, T, Y_1, \ldots, Y_{KK}$. The density is computed using the equation of state Eq. (3.4), where the pressure $p$ is a constant. The other terms present in the equations, $U_{dr,k}, \dot{\omega}_k$, $W_k$, $\bar{W}$, $h_k^o$, and $q_r$ are computed knowing the thermodynamic state of the system. The following sections present briefly the models used to assess these parameters.

### 3.1.2 Boundary Conditions

Good problem statements are important for accurate predictions. Different problem configurations were considered in this study. This section describes the observed boundary conditions for the different cases treated.

(a) Inlet boundary (burner surface), $r=r_b$.

* For continuity equation: $\dot{m}=\dot{m}_b$, where $\dot{m}_b$ is prescribed by the user.

* For species conservation: the species mass flux is conserved, i.e. $\dot{m}_b Y_{k,0} = \dot{m}_b Y_{k,b} + \rho Y_{k,b} V_k A(r_b)$, where $Y_{k,0}$ is the mass fraction of the $k^{th}$ species inside the burner. This value is prescribed by the user. This equation states the preservation of the species mass flux balance.

* For energy conservation (non-adiabatic case): $T = T_b$ for the fixed burner temperature case, with $T_b$ prescribed by the used. The user can choose to include or not gas-phase radiative heat losses.

* For energy conservation (adiabatic case): $\dot{m}_b \left(h_b^s - h_0^s\right) - \lambda A(r_b) \left.\dfrac{\partial T}{\partial r}\right|_{r=r_b}$, with $h_b^s$ the sensible enthalpy of the mixture at the burner surface and $h_0^s$ the sensible enthalpy of the mixture inside the burner. Note that the radiative heat losses are neglected across the whole domain for the adiabatic case.

(b) Outflow boundary (outer domain boundary), $r = r_\infty$.

* For continuity equation: $\left.\dfrac{\partial \dot{m}}{\partial r}\right|_{r \to r_\infty} = 0$

* For species conservation: $Y_k = Y_{k,\infty}$. $Y_{k,\infty}$ is prescribed by the user.

* For energy conservation: $T = T_\infty$, with $T_\infty$ prescribed by the user.

Note that radiative heat losses from the burner surface are neglected.

## 3.2 Discretization

### 3.2.1 Spatial Discretization

The governing equations are discretized on a nonuniform mesh that spans the computational domain, from $x_1$ representing the burner surface, to $x_{JJ}$, representing the mesh point at the outer (cold) boundary. The spatial discretization can either be prescribed by the user or generated automatically by the code, using a mesh refinement procedure. The maximum number of mesh points allowed by the code is 300. Usually, about 200 points are used to model problems that span from $x_1 =$ 0.317 cm to $x_{JJ} = 100$ cm. Using nonuniform a mesh allows the construction of a grid with the finer part in the area of interest near the flame peak temperature, and with a coarser mesh point distribution close to the outer boundary. Since the generation of a smooth nonuniform mesh can be a difficult task, a generating mesh function $\Phi$ was used to create a distribution of 200 points.

The domain is divided in three areas: $\mathscr{X}_1$, $\mathscr{X}_2$, and $\mathscr{X}_3$. The first area $\mathscr{X}_1$ corresponds to the zone between the burner, $x_1$, and the flame area, $x_{end,1}$. Usually 100 points are used here. The second area $\mathscr{X}_2$ corresponds to the area of 20 points uniformly spaced with an increment of $\Delta x$. Those points are centered around a user estimate $x_{flame}$. The third area $\mathscr{X}_3$ corresponds to the remaining zone extending from the end of the second zone, $x_{end,2}$ to the outer boundary $x_{JJ}$. This area contains 80 points. For the first and third area, function $\Phi$ was used. The function $\Phi$, defined over $\mathscr{X}$ of first element $x_{begin}$ and of last element $x_{end}$ and of cardinality$|\mathscr{X}|$ , is

expressed by:

$$1 \leq i \leq |\mathscr{X}|\,,\ \Phi(i) = x_{begin} + \frac{\sum_{k=2}^{i} A \exp\left[-\alpha\left(\tilde{x}_k - x_{mid}\right)^2\right]}{\sum_{k=2}^{|\mathscr{X}|} A \exp\left[-\alpha\left(\tilde{x}_k - x_{mid}\right)^2\right]} \left(x_{end} - x_{begin}\right), \quad (3.6)$$

where $\alpha$ and $A$ are user defined constants that can be varied to change the shape of the generated mesh. The variable $x_{mid}$ corresponds to the location of an inflection point. It is usually taken as the middle of the range, but it can be varied manually. The intermediate mesh $\tilde{x}_i$ is expressed by:

$$\tilde{x}_i = \frac{i-1}{|\mathscr{X}|-1}\left(x_{end} - x_{begin}\right) + x_{begin}. \quad (3.7)$$

This generating function is called to create the mesh of $\mathscr{X}_1$ and $\mathscr{X}_3$.

The governing equations are discretized over the domain using first and second order finite-difference approximations. Hence a continuous function $y(x)$ is approximate by $y_i = y(x_i)$, where $i \in [1; |\mathscr{X}|]$.

Due to its hyperbolic structure, the advection term in the continuity equation, Eq. (3.1) is calculated using a first order backward difference operator [61, 62].

$$\left.\frac{\partial \dot{m}}{\partial x}\right|_{x_i} = \frac{\dot{m}_i - \dot{m}_{i-1}}{x_i - x_{i-1}} + O(\Delta x_i), \quad (3.8)$$

with $\Delta x_i = (x_i - x_{i-1})$. The advection terms in the energy conservation and species conservation equations are calculated using either a first order backward difference operator or a second order central difference operator. Those two methods are illustrated below using the convective term in the energy equation, Eq. (3.2). The first order backward operator is:

$$\left.\dot{m}\frac{\partial T}{\partial x}\right|_{x_i} = \dot{m}_i \frac{T_i - T_{i-1}}{x_i - x_{i-1}} + O(\Delta x_i). \quad (3.9)$$

The central difference formula is:

$$\dot{m}\frac{\partial T}{\partial x}\bigg|_{x_i} = \dot{m}_i \frac{\Delta^2 x_i T_{i+1} + \left(\Delta^2 x_{i+1} - \Delta^2 x_i\right) T_i - \Delta^2 x_{i+1} T_{i-1}}{\Delta x_i \Delta x_{i+1} \left(\Delta x_{i+1} + \Delta x_i\right)} + O(\Delta^2 x_i). \tag{3.10}$$

The choice of the operator is left to the user. Note that the backward formulation introduces artificial diffusion on a coarse mesh and is less accurate than the central difference formula.

In the energy equation, Eq. (3.2), discretization, the term accounting for the transport of heat by species diffusion is expressed using the central difference formula. The coefficient value $\rho c_{p,k} Y_k U_{dr,k}$ is averaged at $i - \frac{1}{2}$ based on its value at $i - 1$ and $i$. The diffusive terms in the energy equation, Eq. (3.2), and species equation, Eq. (3.3), are expressed using the following second order central difference:

$$\frac{\partial}{\partial x}\left(\lambda A(x)\frac{\partial T}{\partial x}\right)\bigg|_{x_i} = \tag{3.11}$$
$$\left(\frac{2}{x_{i+1} - x_{i-1}}\right)\left[\lambda_{i+\frac{1}{2}} A(x_{i+\frac{1}{2}})\left(\frac{T_{i+1} - T_i}{\Delta x_{i+1}}\right) - \lambda_{i-\frac{1}{2}} A(x_{i-\frac{1}{2}})\left(\frac{T_i - T_{i-1}}{\Delta x_i}\right)\right].$$

The thermal conductivity $\lambda$ is evaluated using the average of its dependent variables between mesh points.

$$\lambda_{j+\frac{1}{2}} = \lambda\left(\frac{T_{j+1} + T_j}{2}, \frac{Y_{1,j+1} + Y_{1,j}}{2}, \ldots, \frac{Y_{KK,j+1} + Y_{KK,j}}{2}\right). \tag{3.12}$$

The diffusivity term in species conservation equation, Eq. (3.3), is approximated in a similar way. The diffusion velocities are approximated at the location $j + \frac{1}{2}$, with:

$$\left(Y_k U_{dr,k}\right)_{i+\frac{1}{2}} = -\alpha_{i+\frac{1}{2}}\left(\frac{X_{k,i+1} - X_{k,i}}{x_{i+1} - x_i}\right), \tag{3.13}$$

where $\alpha_{i+\frac{1}{2}}$ is evaluated by the detailed transport subroutines presented below. The

diffusive term in the species conservation equation is then given by:

$$\frac{\partial}{\partial x}\left(\rho A(r) Y_k U_{dr,k}\right)\Big|_{x_i} = \frac{\left(\rho A(r) Y_k U_{dr,k}\right)_{i+\frac{1}{2}} - \left(\rho A(r) Y_k U_{dr,k}\right)_{i-\frac{1}{2}}}{x_{i+\frac{1}{2}} - x_{i-\frac{1}{2}}}. \tag{3.14}$$

Production terms are evaluated at the location $x_i$ with its associated conditions. The definition of the operators used at each mesh point $x_i$ involves the variables $(T_i, \dot{m}_i, Y_{1,i}, \ldots, Y_{KK,i})$ at this location and at the adjacent cell in $i-1$, and at $i+1$ for some of the terms in the equations.

### 3.2.2 Temporal Discretization

The transient terms in the governing equations are expressed using an implicit Euler method, which is stated as:

$$\frac{y_{n+1} - y_n}{\Delta t} = F(t_{n+1}, y_{n+1}). \tag{3.15}$$

The right hand side is evaluated at the time $t_{n+1}$. If the function $F(t, y)$ is nonlinear, then Eq. (3.15) has to be evaluated iteratively. Implicit methods are less straightforward to implement than explicit methods and the cost per time step of an implicit method is larger than of an explicit method. However, they are unconditionally stable for linear problems [61, 62]. Ergo, the time step can be chosen primarily to maintain accuracy. In slowly varying regions of stiff problems, the time steps can be very large compared to those required to maintain stability for explicit time marching algorithms. The implicit Euler time marching method is a first order method.

The transient continuity equation is then written, at a location $x_i$ and at a

time $t_{n+1}$, as:

$$A(x_i)\frac{\rho_i^{n+1}-\rho_i^n}{\Delta t}+\frac{\dot{m}_i^{n+1}-\dot{m}_{i-1}^{n+1}}{x_i-x_{i-1}}=0. \tag{3.16}$$

### 3.2.3 Discretized Equations

This section recalls the expression of the equations in their full discretized form, considering a central difference scheme for the convective terms in the species and energy equation.

(a) Continuity (mass conservation):

$$A(x_i)\frac{\rho_i^{n+1}-\rho_i^n}{\Delta t}+\frac{\dot{m}_i^{n+1}-\dot{m}_{i-1}^{n+1}}{x_i-x_{i-1}}=0. \tag{3.17}$$

(b) Energy conservation:

$$\begin{aligned}
&\rho_i^{n+1}A(x_i)\frac{T_i^{n+1}-T_i^n}{\Delta t}+\\
&\dot{m}_i^{n+1}\frac{\Delta^2 x_i T_{i+1}^{n+1}+\left(\Delta^2 x_{i+1}-\Delta^2 x_i\right)T_i^{n+1}-\Delta^2 x_{i+1}T_{i-1}^{n+1}}{\Delta x_i\Delta x_{i+1}\left(\Delta x_{i+1}+\Delta x_i\right)}+\\
&\frac{A(x_i)}{c_{p,i}^{n+1}}\sum_{k=1}^{KK}\Bigg(\left(\rho_{i+1}^{n+1}c_{p,k}Y_{k,i+\frac{1}{2}}^{n+1}U_{dr,i+\frac{1}{2}}^{n+1}\right)\times\\
&\frac{\Delta^2 x_i T_{i+1}^{n+1}+\left(\Delta^2 x_{i+1}-\Delta^2 x_i\right)T_i^{n+1}-\Delta^2 x_{i+1}T_{i-1}^{n+1}}{\Delta x_i\Delta x_{i+1}\left(\Delta x_{i+1}+\Delta x_i\right)}\Bigg)-\\
&\frac{1}{c_{p,i}^{n+1}}\left(\frac{2}{x_{i+1}-x_{i-1}}\right)\times\\
&\left[\lambda_{i+\frac{1}{2}}^{n+1}A(x_{i+\frac{1}{2}})\left(\frac{T_{i+1}^{n+1}-T_i^{n+1}}{\Delta x_{i+1}}\right)-\lambda_{i-\frac{1}{2}}^{n+1}A(x_{i-\frac{1}{2}})\left(\frac{T_i^{n+1}-T_{i-1}^{n+1}}{\Delta x_i}\right)\right]-\\
&\frac{A(x_i)q_{r,i}^{n+1}-A(x_{i-1})q_{r,i-1}^{n+1}}{\Delta x_i}+\frac{A(x_i)}{c_{p,i}^{n+1}}\sum_{k=1}^{KK}h_k^o\dot{\omega}_{k,i}^{n+1}=0.
\end{aligned} \tag{3.18}$$

(c) Species conservation:

$$\rho_i^{n+1} A(x_i) \frac{Y_{k,i}^{n+1} - Y_{k,i}^{n}}{\Delta t} +$$
$$\dot{m}_i^{n+1} \frac{\Delta^2 x_i Y_{k,i+1}^{n+1} + \left(\Delta^2 x_{i+1} - \Delta^2 x_i\right) Y_{k,i}^{n+1} - \Delta^2 x_{i+1} Y_{k,i-1}^{n+1}}{\Delta x_i \Delta x_{i+1} \left(\Delta x_{i+1} + \Delta x_i\right)} +$$
$$+ \frac{\left(\rho_{i+\frac{1}{2}}^{n+1} A(x_{i+\frac{1}{2}}) Y_{k,i+\frac{1}{2}}^{n+1} U_{dr,k,i+\frac{1}{2}}^{n+1}\right) - \left(\rho_{i-\frac{1}{2}}^{n+1} A(x_{i-\frac{1}{2}}) Y_{k,i-\frac{1}{2}}^{n+1} U_{dr,k,i-\frac{1}{2}}^{n+1}\right)}{x_{i+\frac{1}{2}} - x_{i-\frac{1}{2}}} -$$

$$A(x_i) W_k \dot{\omega}_k^{n+1} = 0. \tag{3.19}$$

## 3.3 Solver

In the previous section, the discretized governing equations were presented, along with their observed boundary conditions. These equations, either under their steady state or transient form, are solved using a modified Newton method through the program TWOPNT [60]. A brief overview is presented below. Detailed descriptions can be found in Refs. [60–63].

### 3.3.1 Newton Method: Generalities

This subsection recalls some generalities about the Newton-Kantorovich method (or Newton method) in Banach spaces. First, some important definitions are stated [63].

**Definition 1.** *Given a normed vector space* $(V, ||.||)$*, a sequence* $(x_k)$ *in* $V$ *forms a Cauchy sequence in* $V$ *if* $\forall\, \varepsilon \in \mathbb{R}$ *with* $\varepsilon > 0, \exists N \in \mathbb{N}\, \forall (n,m) \in \mathbb{N}$ *with* $(n,m) > N$, $||x_m - x_n|| < \epsilon$.

**Definition 2.** *A Banach space is a vector space V over* $\mathbb{R}$ *(set of real numbers) or* $\mathbb{C}$ *(set of complex numbers) with a norm* $||.||$ *such that every Cauchy sequence in V has a limit in V.*

**Definition 3.** *An operator F mapping a Banach space X into a Banach space Y is said to be Fréchet-differentiable at* $x_0$ *if there exists a bounded linear operator L from X into Y such that*

$$\lim_{||\Delta x|| \to 0} \frac{||F(x_0 + \Delta x) - F(x_0) - L(\Delta x)||}{||\Delta x||} = 0.$$

*In such case we have* $L = F'(x_0)$.

In the case where X and Y are vector spaces of finite dimension, $F'(x_0)$ is given by its Jacobian evaluated at this location:

$$F'(x_0) = J_F(x_0). \tag{3.20}$$

Given F, a Fréchet-differentiable operator mapping a Banach space X into a Banach space Y, consider the equation

$$F(x) = 0. \tag{3.21}$$

A succession of approximations $x_n$ to a solution $x^*$, if the solution exists, is given by the linear function:

$$L_n(x) = F(x_n) + F'(x_n)\,(x - x_n)\,, \tag{3.22}$$

if $F'(x_n)^{-1}$ is a bounded linear operator from Y into X, then the approximation $x_{n+1}$, which is the root of $L_n(x_{n+1}) = 0$, is given by:

$$x_{n+1} = x_n - F'(x_n)^{-1} F(x_n). \tag{3.23}$$

The iterative procedure generated by Eq. (3.23) is the base of the Newton-Kantorovitch method. Modified methods can be defined by changing the linear function $L_n$, Eq. (3.22), with another approximation. An example is given by:

$$L_s(x) = F(x_n) + F'(x_s)(x - x_n), \tag{3.24}$$

where the derivative of F is evaluated only at certain iterations $s$, with $s \leq n$.

If we assume that F is Fréchet-differentiable on a subset $D$ of $X$ and that $F'(x)$ satisfies the condition of Lipschitz:

$$\exists l\ 0,\ \forall x, y \in D,\ ||F'(x) - F'(y)|| \leq l||x - y||, \tag{3.25}$$

and assuming that $F'(x_0)^{-1}$ exists, we can state the Newton-Kantorovitch theorem for approximating solutions of Eq. (3.23), where $x_0$ is an initial approximation for the method [63]:

**Theorem 1.** *Assume that*

$$F'(x_0)^{-1} \leq b_0,$$

$$||F'(x_0)^{-1}F(x_0)|| \leq \eta_0,$$

$$h_0 = lb_0\eta_0 \leq \frac{1}{2},$$

$$r_0 = \frac{1 - \sqrt{1 - 2h_0}}{h_0}\eta_0,$$

$$\textit{and } \{x \in X |\ ||x - x_0|| \leq r_0\} \subseteq D,$$

*then the Newton-Kantorovitch method, Eq.* (3.23)*, converges to a solution* $x^*$ *of Eq.* (3.21) *in the ball* $\{x \in X |\ ||x - x_0|| \leq r_0\}$.

The proof is by induction. It can be found in Ref. [63]. It can be shown that the scalar sequence $\{s_n\}$ defined by

$$s_0 = 0,\ s_1 = \eta_0,\ s_{n+2} = s_{n+1} + \frac{l\,(s_{n+1} - s_n)^2}{2 - l s_n}, \tag{3.26}$$

is a majorizing sequence for $\{x_n\}$ such that $0 \leq s_0 \leq s_1 \leq \ldots \leq s_n \leq \ldots \leq s^*$, where $\lim_{n\to\infty} s_n = s^*$, and verifying :

$$\forall n \in \mathbb{N},\ ||x_{n+1} - x_n|| \leq s_{n+1} - s_n. \tag{3.27}$$

The convergence of the sequence is dependent on the initial approximation $x_0$. A good approximation $x_0$ can lead to a faster rate of convergence, whereas a bad approximation may lead to a failure in finding the root of Eq. (3.21). From Eqs. (3.26)-(3.27) it can be seen that the Newton-Kantorovitch sequences converge quadratically, assuming that the initial estimate lies in the range of convergence.

General characteristics of the Newton method were presented in this section. Section 3.3.2 presents how this method is used to solve the governing equations.

### 3.3.2 Implementations

The discretized governing equations, Eqs. (3.17)-(3.19), form a set of $N_{eq} \times N_p$ equations with $N_{eq} \times N_p$ unknowns, with $N_{eq} = 2 + KK$, and $N_p$ being the number of mesh points. For a steady state problem, it can be stated:

$$F(\phi) = 0, \tag{3.28}$$

with vector $\phi$ of $N_{eq} \times N_p$ elements defined as:

$$\phi = (T_1, Y_{1,1}, \ldots, Y_{KK,1}, \dot{m}_1, \ldots, T_{JJ}, Y_{1,JJ}, \ldots, Y_{KK,JJ}, \dot{m}_{JJ})^T. \tag{3.29}$$

A modified damped Newton method is used to solve this general problem, using the sequence:

$$\phi^{n+1} = \phi^n - \lambda^n J_F \left(\phi^s\right)^{-1} F(\phi^n), \tag{3.30}$$

where $s \leq n$ and $\lambda^n$ is the $n^{th}$ damping parameter ($0 < \lambda \leq 1$). The damping parameter is chosen to be as large as possible but needs to satisfy two criteria. The first is that each component of $\phi$ remains within bounds that are given by the physic of the problem, e.g. positive temperature. The second requires the norm of a successful step to decrease in magnitude:

$$\|J_F(\phi^n)^{-1} F(\phi^{n+1})\| < \|J_F(\phi^n)^{-1} F(\phi^n)\|. \tag{3.31}$$

The search of a suitable damping coefficient starts by considering $\lambda^0 = 1$. If the criteria are not met, the value is decreased until criteria are met or until its value becomes vanishingly small. In the latter case, a new Jacobian is re-evaluated. If the new Jacobian did not resolved the criteria, then pseudo-time marching is considered.

Convergence is achieved when the solution correction vector $\Delta\phi^n = \phi^{n+1} - \phi^n$ satisfies:

$$\|\Delta\phi^n\| \leq max\left(A_t, R_t \|\phi^n\|\right), \tag{3.32}$$

where $A_t$ is the user prescribed absolute tolerance and $R_t$ is the relative tolerance.

The Jacobian $J_F\left(\phi^s\right) = \left.\dfrac{\partial F}{\partial \phi}\right|_{\phi=\phi^s}$ is not re-evaluated at each iteration but is conserved for a given number of iterations before being re-evaluated again. This reduces the cost of its evaluation. The criterion determining the iteration number, $s$, requiring the re-evaluation of $J_F$ can be expressed as:

$$\Delta t_{si} \leq \alpha \tau_J, \tag{3.33}$$

where $\Delta t_{si}$ is the computational time difference between the current moment $t_s$ (corresponding to the beginning of the $r^{th}$ iteration) and the moment $t_i$, which is the time of the previous Jacobian evaluation. The variable $\tau_J$ is the computational time required to compute and factor the Jacobian $J_F$ and $\alpha$ is an optimization parameter on the order of unity.

The Jacobian is a tridiagonal block matrix with $(N_{eq} \times N_p)^2$ elements. From Eqs. (3.17)-(3.19), the residual vector $F$ is expressed as:

$$F(\phi)_{i,j} = f_i(\phi^{(j-1)}, \phi^{(j)}, \phi^{(j+1)}),\ 1 \leq i \leq N_{eq}\ \&\ 1 < j < N_p, \tag{3.34}$$

$$F(\phi)_{i,1} = f_i(\phi^{(1)}, \phi^{(2)}),\ 1 \leq i \leq N_{eq}, \tag{3.35}$$

$$F(\phi)_{i,N_p} = f_i(\phi^{(N_p-1)}, \phi^{(N_p)}),\ 1 \leq i \leq N_{eq}, \tag{3.36}$$

where $f_i$ is the $i^{th}$ conservation equation and $\phi^{(j)} = (T_j, Y_{1,j}, \ldots, Y_{KK,j}, \dot{m}_j)^T$.

Therefore, for the internal mesh points $1 < n < N_p$ the elements of the Jacobian depend on the index $k$ representing the $n^{th}$ node and also the node $k = n-1$ and $k = n+1$,

$$J_{Fi,j}^{(n,k)} = \frac{\partial f_i^n}{\partial \phi_j^k}, \tag{3.37}$$

with $n = 1, \ldots, N_p,\ k = n-1, n, n+1,\ i, j = 1, \ldots, N_p \times N_{eq}$. Because of the definition of $k$, it is convenient to view the $J^{(n,k)}$ Jacobian blocks as structures composed of 3 $N_{eq} \times N_{eq}$ sub-matrices $A_{i,j}^{(n)}$, $B_{i,j}^{(n)}$ and $C_{i,j}^{(n)}$ defined as:

$$A_{i,j}^{(n)} = J_{Fi,j}^{(n,n-1)},$$

$$B_{i,j}^{(n)} = J_{Fi,j}^{(n,n)},$$

$$C_{i,j}^{(n)} = J_{Fi,j}^{(n,n+1)}.$$

Hence, the Jacobian can be expressed by:

$$J_F(\phi) = \begin{bmatrix} \left[B_{i,j}^{(1)}\right] & \left[C_{i,j}^{(1)}\right] & & & & \\ \left[A_{i,j}^{(2)}\right] & \left[B_{i,j}^{(2)}\right] & \left[C_{i,j}^{(2)}\right] & & & \\ & \cdots & \cdots & \cdots & & \\ & & \cdots & \cdots & \cdots & \\ & & & \left[A_{i,j}^{(N_p-1)}\right] & \left[B_{i,j}^{(N_p-1)}\right] & \left[C_{i,j}^{(N_p-1)}\right] \\ & & & & \left[A_{i,j}^{(N_p)}\right] & \left[B_{i,j}^{(N_p)}\right] \end{bmatrix}$$

Due to the tri-diagonal nature of the Jacobian, Eq. (3.30) can be solved using a Gaussian elimination algorithm. The Jacobian evaluation matrix is computed by finite difference perturbations:

$$J_{Fi,j} = \frac{f_i\left(\phi^{(j)} + \delta\right) - f_i\left(\phi^{(j)}\right)}{\delta}, \tag{3.38}$$

where

$$\delta = r\phi^{(j)} + a, \tag{3.39}$$

the relative and absolute perturbations, $r$ and $a$, are taken as the square root of the computer unit roundoff.

As stated earlier, when the Newton method fails to converge for a steady state problem, transient equations are solved for a given number of time steps before another attempt is performed. If $F$ is the steady state residual function, then the transient formulation of the problem, Eq. (3.28) is expressed by:

$$\left[I - \Delta t J_F(\phi^n)\right]\left(\phi^{n+1} - \phi^n\right) = \Delta t F(\phi^n). \tag{3.40}$$

Transient problems are easier to solve than steady state ones. One can see from Eq. (3.40) that the iteration for a small time step is very stable, the iteration matrix

approaching the identity matrix. Thus, even for a poorly conditioned Jacobian, the Newton iteration for a single time step can be highly stable.

## 3.4 Modeling Chemistry

Complex and detailed chemistry kinetic models are used here. As mentioned in Chapter 1, the combustion reactions are not as straightforward as a single step reaction, but involve a number of intermediate species in a number of elementary reactions. As an example, the reaction of $H_2$ with $O_2$ is modeled in GRI-Mech 3.0 by a set of 28 elementary reaction involving 7 species. Detailed reactions mechanisms have been developed for a large variety of fuels, combining experimental results and quantum mechanics modeling.

In this study, CHEMKIN [58] is used to provide the description of the gas phase reactions based on detailed models describing the kinetics of the elementary reactions involved. An example of such model is presented in Appendix A, where the GRI-Mech 3.0, written using the CHEMKIN format, is presented. Furthermore, CHEMKIN provides gas-phase species properties using their associated thermodynamic data.

A set of $II$ elementary reactions involving $KK$ chemical species $M_k$ can be represented by:

$$\sum_{k=1}^{KK} \nu'_{k,i} M_k \rightleftharpoons \sum_{k=1}^{KK} \nu''_{k,i} M_k,\ i = 1, 2, \ldots, II. \tag{1.11}$$

The stoichiometric coefficients $\nu_{k,i}$ are integers and superscript $'$ indicates a forward stoichiometric coefficient, while superscript " indicates reverse stoichiometric

coefficient. Typical elementary reactions $i$ involve only three or four species. Each forward and reverse reaction is assigned a constant rate of reaction, $k_{fi}$ for the forward rate, and $k_{ri}$ for the reverse rate. CHEMKIN generally expresses the forward constant rate in a modified Arrhenius form:

$$k_{fi} = B_i T^{\alpha i} \exp\left(-\frac{E_{a,i}}{RT}\right), \tag{3.41}$$

where the pre-exponential factor $B_i$, the temperature exponent $\alpha i$ and the activation energy $E_{a,i}$ are specified by the chemistry model. The reverse rate $k_{ri}$ relates to the forward constant rate through the equilibrium constant $K_{ci}$ by:

$$k_{ri} = \frac{k_{fi}}{K_{ci}}. \tag{3.42}$$

For the $i^{th}$ reaction, the equilibrium constant $K_{ci}$ is expressed by:

$$K_{ci} = \left(\frac{P_{atm}}{RT}\right)^{\sum_{k=1}^{KK} \nu_{k,i}} \exp\left(\frac{\Delta S_i^o}{R} - \frac{\Delta H_i^o}{RT}\right), \tag{3.43}$$

where $\nu_{k,i} = \nu''_{k,i} - \nu'_{k,i}$, and the change in standard-state Gibbs free energy $\Delta G_i^o$ for the reaction $i$ is given by:

$$\Delta G_i^o = \sum_{k=1}^{KK} \nu_{k,i} \left(H_k^o - T S_k^o\right). \tag{3.44}$$

CHEMKIN assumes that standard-state thermodynamics properties of a given species are only function of temperature. The thermodynamics data are expressed in a form of temperature polynomial ($a_{ik}$) fit. The standard-state enthalpy and entropy of the $k^{th}$ species are given by:

$$\frac{H_k^o}{RT} = a_{1k} + \frac{a_{2k}}{2}T + \frac{a_{3k}}{3}T^2 + \frac{a_{4k}}{4}T^3 + \frac{a_{5k}}{5}T^4 + \frac{a_{6k}}{T}, \tag{3.45}$$

$$\frac{S_k^o}{R} = a_{1k}\ln T + a_{2k}T + \frac{a_{3k}}{2}T^2 + \frac{a_{4k}}{3}T^3 + \frac{a_{5k}}{4}T^4 + a_{7k}. \tag{3.46}$$

Other species thermodynamics properties can be computed using those polynomials and the thermodynamics formula.

The forward and reverse rates for a given reaction $i$ allows one to express the rate of progress $\dot{q}_i$ for the $i^{th}$ reaction, which is the difference of the forward and reverse reaction rates:

$$\dot{q}_i = k_{fi} \prod_{k=1}^{KK} [X_k]^{\nu'_{k,i}} - k_{ri} \prod_{k=1}^{KK} [X_k]^{\nu''_{k,i}}, \tag{3.47}$$

where $[X_k]$ is the molar concentration of the $k^{th}$ species.

Finally, the knowledge of the rate of progress of every elementary reaction involved in the mechanism allows the computation of the rate of production of the $k^{th}$ species:

$$\dot{\omega}_k = \sum_{i=1}^{II} \nu_{k,i} \dot{q}_i. \tag{3.48}$$

For third body reactions, such as $\mathrm{H} + \mathrm{O}_2 + \mathrm{M} \rightarrow \mathrm{HO}_2 + \mathrm{M}$, the rate of progress expression is modified to account for the concentration of the effective third body and for the effective contribution ($a_{ki}$) of species as third body. The rate of progress for such reactions is expressed by:

$$q_i = \left( \sum_{k=1}^{KK} a_{ki} [X_k] \right) \left( k_{fi} \prod_{k=1}^{KK} [X_k]^{\nu'_{k,i}} - k_{ri} \prod_{k=1}^{KK} [X_k]^{\nu''_{k,i}} \right). \tag{3.49}$$

In the present work, two detailed chemistry models are used. The first is GRI-Mech 3.0, which is an optimized mechanism designed to model natural gas combustion, including NO formation and reburn chemistry. It contains 53 species (including Ar) and 325 reactions [64]. Its chemical mechanism gives results in good agreement with experiments [65]. Initially developed to model methane combustion,

this model has been demonstrated to be valid for the combustion of ethylene ($C_2H_4$) and ethane ($C_2H_6$). This combustion model considers hydrocarbon species up to $C_3$. However the mechanism is not designed for $C_3$-chain reaction calculation and therefore modeled $C_3$ species concentration should be taken with precaution.

The second chemistry model considered, the Appel, Bockhorn, Frenklach (ABF) model, is a modified version of the Wang and Frenklach model [66]. The detailed kinetic mechanism consists of 101 species, 544 reactions, and was initially proposed by Wang and Frenklach [66], and later modified by Appel *et al.* [67]. It includes pyrolysis and oxidation of $C_1$ and $C_2$ species, formation of higher, linear hydrocarbons up to $C_6$, formation of benzene $C_6H_6$ ($A_1$), and further reactions leading to pyrene $C_{12}H_{10}$ ($A_4$), as well as the oxidation pathways of aromatic species.

## 3.5 Transport Property Modeling

The transport coefficients present in the governing equations, namely the mixture thermal conductivity $\lambda$ and the species diffusion velocity $U_{dr,k}$, are evaluated using TRANSPORT subroutines [59]. Similar to CHEMKIN, TRANSPORT uses an input file containing the species transport properties to compute their diffusion coefficients and the mixture properties such as viscosity, thermal conductivity, and thermal diffusion coefficient.

The user has the option to evaluate the transport properties using mixture-average formulas or the more expensive multicomponent model. For the scope of this work, mixture-averaged formulas were used for the evaluation of the transport

coefficients. We provide here some details.

In the mixture-averaged formulation, the diffusion velocity of the $k^{rh}$ species, $U_{dr,k}$, is the result of the contribution of three parts:

$$U_{dr,k} = V_k + W_k + V_c, \tag{3.50}$$

where $V_k$ is the ordinary diffusion velocity and is expressed by:

$$V_k = -D_{km}\frac{1}{X_k}\frac{\partial X_k}{\partial r}, \tag{3.51}$$

$X_k$ represents the mole fraction of the $k^{th}$ species, and $D_{km}$ represents the $k^{rh}$ species mixture-averaged diffusion coefficient. This coefficient is a function of the binary diffusion coefficients $\mathbb{D}_{kj}$, as expressed by:

$$D_{km} = \frac{1 - Y_k}{\sum_{j \neq k}^{KK} \frac{X_j}{\mathbb{D}_{kj}}}. \tag{3.52}$$

The binary diffusion coefficients are functions of the temperature $T$ and pressure $p$. They are expressed by:

$$\mathbb{D}_{kj} = \frac{3}{16}\frac{\sqrt{2\pi k_B^3 T^3 m_{jk}^{-1}}}{p\pi\sigma_{jk}^2\Omega^{(1,1)*}}, \tag{3.53}$$

where $m_{jk}$ is the reduced molecular mass for the $(j,k)$ species pair:

$$m_{jk} = \frac{m_j m_k}{m_j + m_k}, \tag{3.54}$$

and $\sigma_{jk}$ is the reduced diameter. $\Omega^{(1,1)*}$ represents the collision integral based on Stockmayer potentials. More details can be found in [59].

The term $W_K$ represents the thermal diffusion velocity. This velocity is only computed for the low molecular weight species H, $H_2$, and He. It is expressed by:

$$W_k = \frac{D_{km}\Theta_k}{X_k}\frac{1}{T}\frac{\partial T}{\partial r}, \tag{3.55}$$

where $\Theta_k$ is the thermal diffusion ratio of the $k^{th}$ species. Its expression can be found in [59].

The third term in Eq. (3.50), $V_c$, is the correction velocity, which is independent of species but is a function of the location $r$. This term is included to ensure that $\sum_{k=1}^{KK} Y_k U_{dr,k} = 0$. Its formulation can be found in [68].

The mixture viscosity $\eta$ is determined using the semi-empirical Wilke formula [69]:

$$\eta = \sum_{k=1}^{KK} \frac{X_k \eta_k}{\sum_{j=1}^{KK} X_j \Phi_{kj}}, \tag{3.56}$$

where

$$\Phi_{kj} = \frac{\left[1 + \left(\frac{\eta_k}{\eta_j}\right)^{\frac{1}{2}} \left(\frac{m_j}{m_k}\right)^{\frac{1}{4}}\right]^2}{\left[8\left(1 + \frac{m_k}{m_j}\right)\right]^{\frac{1}{2}}}. \tag{3.57}$$

Species viscosities are determined from the standard kinetic theory:

$$\eta_k = \frac{5}{16} \frac{\sqrt{\pi m_k k_B T}}{\pi \sigma_k^2 \Omega^{(2,2)*}}, \tag{3.58}$$

where $\sigma_k$ is the Lennard-Jones collision diameter, $m_k$ is the molecular mass of the $k^{th}$ species, and $\Omega^{(2,2)*}$ is the collision integral.

The mixture-averaged thermal conductivity is expressed by the average formula [62]:

$$\lambda = \frac{1}{2}\left(\sum_{k=1}^{KK} X_k \lambda_k + \frac{1}{\sum_{k=1}^{KK} \frac{X_k}{\lambda_k}}\right). \tag{3.59}$$

The pure species thermal conductivity is computed assuming it results from trans-

lational, rotational, and vibrational contributions, using the viscosity $\eta_k$:

$$\lambda_k = \frac{\eta_k}{W_k}\left(f_{trans}C_{v,trans} + f_{rot}C_{v,rot} + f_{vib}C_{v,vib}\right), \tag{3.60}$$

with $W_k$ the molecular weight of the $k^{th}$ species and:

$$f_{trans} = \frac{5}{2}\left(1 - \frac{2}{\pi}\frac{C_{v,rot}}{C_{v,trans}}\frac{A}{B}\right), \tag{3.61}$$

$$f_{rot} = \frac{\rho\mathbb{D}_{kk}}{\eta_k}\left(1 + \frac{2}{\pi}\frac{A}{B}\right), \tag{3.62}$$

$$f_{vib} = \frac{\rho\mathbb{D}_{kk}}{\eta_k}, \tag{3.63}$$

$$A = \frac{5}{2} - \frac{\rho\mathbb{D}_{kk}}{\eta_k}, \tag{3.64}$$

$$B = Z_{rot} + \frac{2}{\pi}\left(\frac{5}{3}\frac{C_{v,rot}}{R} + \frac{\rho\mathbb{D}_{kk}}{\mu_k}\right) \tag{3.65}$$

The translational contribution to the molar heat capacity $C_{v,trans}$ is given by:

$$C_{v,trans} = \frac{3}{2}R. \tag{3.66}$$

The rotational contribution to the molar heat capacity $C_{v,rot}$ is given by:

$$C_{v,rot} = R, \text{(for a linear molecule)}, \tag{3.67}$$

$$C_{v,rot} = \frac{3}{2}R, \text{(for a nonlinear, polyatomic molecule)}. \tag{3.68}$$

The vibration contribution to the molar heat capacity $C_{v,vib}$ is computed using the relation:

$$C_v = C_{v,trans} + C_{v,rot} + C_{v,vib}, \tag{3.69}$$

where $C_v$ is obtained using polynomial fits for a given species, as mentioned above.

The self-diffusion coefficient $\mathbb{D}_k$ expression is obtained from the kinetic gas theory:

$$\mathbb{D}_{kk} = 38\frac{\sqrt{\pi k_B^3 T^3 m_k^{-1}}}{p\pi\sigma_{jk}^2\Omega^{(1,1)*}}. \tag{3.70}$$

The rotational relaxation collision number $Z_{rot}$ represents the number of collisions needed to deactivate a rotationally excited molecule. Usually a small number, around unity, it can be important for molecules with small moments of inertia such as $H_2$. The rotational relaxation collision number is expressed using a Parker-Brau-Jonkman expression:

$$Z_{rot}\left(T\right) = Z_{rot}\left(298\right)\frac{F(298)}{F(T)}, \tag{3.71}$$

where the function $F(T)$ is a function of the temperature and of the Lennard-Jones potential well depth $\frac{\epsilon}{k_B}$ for a given species:

$$F(T) = 1 + \frac{\pi^{\frac{3}{2}}}{2}\left(\frac{\epsilon}{k_B T}\right)^{\frac{1}{2}} + \left(\frac{\pi^2}{4} + 2\right)\left(\frac{\epsilon}{k_B T}\right) + \pi^{\frac{3}{2}}\left(\frac{\epsilon}{k_B T}\right)^{\frac{3}{2}}. \tag{3.72}$$

To expedite the evaluation of the transport properties, some of the pure species properties are computed using polynomial temperature fits. In the code, the default is the use of third order polynomials, which reduces fitting errors below 1%. The computation of fitting polynomial coefficients is performed prior to computation, using a TRANSPORT interpreter. The interpreter reads an input file containing species characteristics and computes the fitting coefficients, which are then stored in a linking file that is accessed by the main driver code during the computations when transport properties evaluation are needed.

Following the work of Santa *et al.*, [42] who used the same code to model radiative extinction of spherical diffusion flames, the diffusion velocities, and the thermal conductivity are enhanced by 30%. Santa *et al.* [42] have shown that this increase provides better agreement between numerical and experimental results. This strategy is adopted for all the simulations.

## 3.6 Radiation Model

The radiation model involves two submodels: a radiation property model, which deals with the calculation of gas radiation properties of radiative species, namely $CO_2$, $H_2O$, and CO, and a radiative transfer model, which solves the radiative transfer equation (RTE). For a quasi-steady system, with typical time scales greater than the radiative time scale, the general formulation of the radiative transfer equation of the radiance $L(s, \vec{\Omega}, t)$, for an absorbing, emitting, and anisotropic scattering medium, at a position $s$, along a direction $\vec{\Omega}$, and for a wavelength $\lambda$, neglecting coherence, polarization, non-linearity, and assuming Kirchhoff's law, is expressed by:

$$\vec{\Omega} \cdot \nabla L_\lambda(s, \vec{\Omega}, t) = \kappa_\lambda(s) L^o_\lambda(T) - \kappa_\lambda(s) L_\lambda(s, \vec{\Omega}, t) - \sigma_\lambda L_\lambda(s, \vec{\Omega}, t) + \frac{1}{4\pi}\sigma_\lambda \int_{4\pi} P_\lambda(\vec{\Omega}' \rightarrow \vec{\Omega}) L_\lambda(s, \vec{\Omega}', t) d\Omega', \tag{3.73}$$

with $L^o_\lambda(T)$ the radiance emitted following Planck's law:

$$L^o_\lambda(T) = \frac{2h_p c}{\lambda^5} \frac{1}{\exp\left(\frac{h_p c}{\lambda k_B T} - 1\right)}. \tag{3.74}$$

The variable $\kappa_\lambda$ and $\sigma_\lambda$ represent the absorption and scattering coefficient for a wavelength $\lambda$. The term $P_\lambda(\vec{\Omega}' \rightarrow \vec{\Omega})$ is the phase function, representing the probability of a light beam propagating in a direction $\vec{\Omega}'$ to be scattered into the direction $\vec{\Omega}$. The divergence of the radiation term in the energy equation, Eq. (3.2), is the integral of the spectral divergence of radiative heat flux vector:

$$\nabla \cdot \vec{q_r} = \int_0^{+\infty} \nabla \cdot \vec{q_\lambda} d\lambda. \tag{3.75}$$

Remarking that:

$$\vec{\Omega} \cdot \nabla L_\lambda(s, \vec{\Omega}, t) = \nabla \cdot \left( \vec{\Omega} L_\lambda(s, \vec{\Omega}, t) \right), \tag{3.76}$$

and:

$$\vec{q_\lambda} = \int_{4\pi} \vec{\Omega}.L_\lambda(s, \vec{\Omega}, t) d\vec{\Omega}, \tag{3.77}$$

the RTE, Eq. (3.73), can be written as:

$$\nabla \cdot \vec{q_\lambda} = 4\pi\kappa_\lambda(s) L^o_\lambda(T) - \int_{4\pi} \kappa_\lambda(s) L_\lambda(s, \vec{\Omega}, t) d\Omega - \int_{4\pi} \sigma_\lambda L_\lambda(s, \vec{\Omega}, t) d\Omega + \int_{4\pi} \frac{1}{4\pi} \sigma_\lambda \int_{4\pi} P_\lambda(\vec{\Omega}' \rightarrow \vec{\Omega}) L_\lambda(s, \vec{\Omega}', t) d\Omega' d\Omega. \tag{3.78}$$

Considering the anisotropic scattering medium assumption, we have the following simplified equation:

$$\int_{4\pi} \frac{1}{4\pi} \sigma_\lambda \int_{4\pi} P_\lambda(\vec{\Omega}' \rightarrow \vec{\Omega}) L_\lambda(s, \vec{\Omega}', t) d\Omega' d\Omega = \int_{4\pi} \sigma_\lambda L_\lambda(s, \vec{\Omega}, t) d\Omega. \tag{3.79}$$

With this simplification, the RTE is written:

$$\nabla \cdot \vec{q_\lambda} = 4\pi\kappa_\lambda(s) L^o_\lambda(T) - \int_{4\pi} \kappa_\lambda(s) L_\lambda(s, \vec{\Omega}, t) d\Omega, \tag{3.80}$$

finally, Eq. (3.75) is written as:

$$\nabla \cdot \vec{q_r} = \int_0^\infty \kappa_\lambda(s) \left( 4\pi L^o_\lambda(T) - \int_{4\pi} L_\lambda(s, \vec{\Omega}, t) d\Omega \right) d\lambda. \tag{3.81}$$

The spectral absorption coefficient $\kappa_\lambda$ is the resultant of the contribution of radiating species, namely $CO_2$, $H_2O$, and CO absorptions. The contribution of soot can also be included, see Chapter 6. This equation is solved using a method of discrete ordinates over 20 discrete paths.

### 3.6.1 Absorption Coefficient

The species spectral absorption coefficient $\kappa_{\lambda,CO_2}$, $\kappa_{\lambda,H_2O}$, and $\kappa_{\lambda,CO}$, are computed following the same approach than Tse *et al.* [41] and Santa *et al.* [42]. The absorption coefficients are computed using a statistical narrow band model with exponential-tailed inverse line strength distributions for wavenumber varying between 150 - 9300 $cm^{-1}$. In the narrow band model, the entire spectral domain (practically a sufficiently wide spectral range) is divided into many narrow spectral bands, and radiation properties (absorption coefficients) are appropriately averaged over each narrow spectral band.

As mentioned above, wavenumbers between 150 - 9300 $cm^{-1}$ are considered. This domain is divided into 366 bands, which represents a resolution of 25 $cm^{-1}$. It has been shown [70] that this width is sufficiently narrow to assume a constant Planck function inside each band for a given temperature in the range of 300 - 2500 K. Radiative properties of $CO_2$, $H_2O$, and CO are taken from the HITRAN database [71]. Those properties are averaged over a spectral band considering a Lorentz spectral line shape of random spacing and strength. The probability distribution of line strength is modeled by an exponential-tailed inverse distribution [72].

Radiative molecular absorption coefficients for $CO_2$, $H_2O$, and CO are prepared for 10 different temperatures ranging from 300 - 2500 K. Figure 3.1 presents the radiative molecular absorption coefficient profile for $H_2O$ at 300 K used by the code.

Those values are then stored in a file that can be accessed anytime to assess

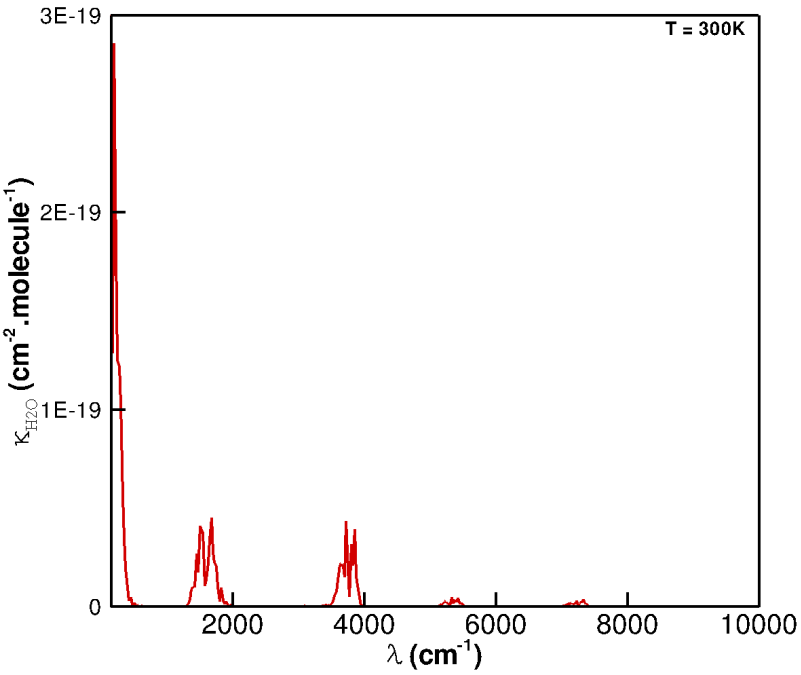


Figure 3.1: Spectral radiative absorption for molecular $H_2O$ at 300 K.

$\kappa_\lambda$. Linear interpolation is performed to obtain $\kappa_\lambda$ at a desired temperature.

### 3.6.2 Discrete Ordinates Method

The discrete ordinates method (or $S_N$ method) converts the RTE into a group of simultaneous partial differential equations. It was initially developed for the modeling of stellar and atmospheric radiation, and is applied in neutron transport [73] as well as in thermal radiation.

In discrete ordinate method, the RTE is solved for a set of N different directions $\vec{\Omega}_i$ with $i = 1, \ldots, N$, and the integrals over those directions are replaced by a

numerical quadrature:

$$\int_{4\pi} f(s,\vec{\Omega},t) = \sum_{i=1}^{N} \omega_i f(s,\vec{\Omega}_i,t), \tag{3.82}$$

where $\omega_i$ is the quadrature weight associated with the direction $\vec{\Omega}_i$. Figure 3.2 represents a diagram of discrete ordinates for $N = 4$.

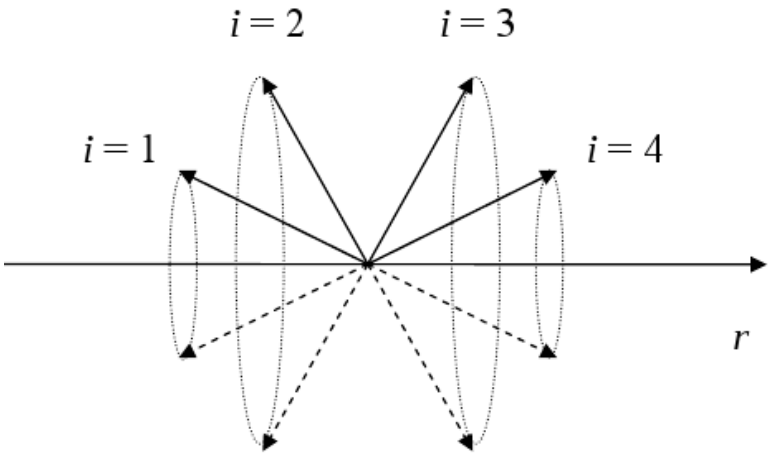


Figure 3.2: Example of diagram of discrete ordinates for 4 ordinates.

A Legendre-Gauss quadrature is used in the model. For any function $f$, its approximated integral value over the segment $[a, b]$, using a n-point quadrature, is given by:

$$\int_a^b f(x)dx \approx \frac{b-a}{2} \sum_{i=1}^{n} \omega_i f\left(\frac{b-a}{2}\xi_i + \frac{b+a}{2}\right), \tag{3.83}$$

with $\xi_i$ being the $i^{th}$ root of the $n^{th}$ degree Legendre polynomial $P_n(\xi)$. The quadrature weight $\omega_i$ is given by

$$\omega_i = \frac{2}{(1-\xi_i^2)\left(P_n'(\xi_i)\right)^2}. \tag{3.84}$$

Since the problem of interest was of spherical symmetry, the radiation intensity $q_r$ is a function of the radius only. Neglecting scattering ($\sigma_\lambda = 0$) and stating $\vec{r} \cdot \vec{\Omega} = \mu = \cos(\theta)$, the RTE can be rewritten in $(r, \mu)$ coordinates [73]:

$$\mu \frac{\partial L_\lambda(r,\mu)}{\partial r} + \frac{1-\mu^2}{r} \frac{\partial L_\lambda(r,\mu)}{\partial \mu} + \kappa_\lambda \left( L_\lambda(r,\mu) - L^o_\lambda(T) \right) = 0, \tag{3.85}$$

or alternatively,

$$\frac{\mu}{r^2} \frac{\partial}{\partial r} \left( r^2 L_\lambda(r,\mu) \right) + \frac{1}{r} \frac{\partial}{\partial \mu} \left[ \left( 1-\mu^2 \right) L_\lambda(r,\mu) \right] + \kappa_\lambda \left( L_\lambda(r,\mu) - L^o_\lambda(T) \right) = 0. \tag{3.86}$$

Following Tsai's method [74], Eq. (3.86) is discretized using a central difference stencil on the derivative term of $\mu$ [75]. The discretized equation is written with $L = L_\lambda(r,\mu)$ for $m = 1, \ldots, N$:

$$\frac{\mu_m}{r^2} \frac{\partial}{\partial r} \left( r^2 L_m \right) + \frac{1}{r} \frac{\alpha_{m+\frac{1}{2}} L_{m+\frac{1}{2}} - \alpha_{m-\frac{1}{2}} L_{m-\frac{1}{2}}}{\omega_m} + \kappa_\lambda \left( L_m - L^o(T) \right) = 0, \tag{3.87}$$

with the geometrical coefficients $\alpha$ determined by:

$$\alpha_{m+\frac{1}{2}} = \alpha_{m-\frac{1}{2}} - 2\mu_m \omega_m, \tag{3.88}$$

and

$$\alpha_{\frac{1}{2}} = \alpha_{N+\frac{1}{2}} = 0. \tag{3.89}$$

Multiplying Eq. (3.87) by $4\pi r^2 dr$ and integrating over the domain between $r = r_i$ and $r = r_{i+1}$ gives:

$$\mu_m \left( A_{i+1} L_{m,i+1} - A_i L_{m,i} \right) + \left( A_{i+1} - A_i \right) \frac{\alpha_{m+\frac{1}{2}} \tilde{L}_{m+\frac{1}{2}} - \alpha_{m-\frac{1}{2}} \tilde{L}_{m-\frac{1}{2}}}{2\omega_m} + \kappa_{\lambda,i} \tilde{V}_i \left( \tilde{L}_m - \tilde{L}^o(T_i) \right) = 0, \tag{3.90}$$

with

$$A_i = 4\pi r_j^2, \tag{3.91}$$

$$\tilde{V}_i = \frac{4}{3}\pi \left(r_{i+1}^3 - r_i^3\right). \tag{3.92}$$

The quantities with a overscript ˜ denote values at the node center, $i + \frac{1}{2}$. The radiance $\tilde{L}_m$ is related to the radiances $L_{m,i}$ and $L_{m,i+1}$ by:

$$\tilde{L}_m = \frac{L_{m,i} + L_{m,i+1}}{2}. \tag{3.93}$$

The radiance $\tilde{L}_m$ is also related to the radiances $\tilde{L}_{m-\frac{1}{2}}$ and $\tilde{L}_{m+\frac{1}{2}}$ by:

$$\tilde{L}_m = \frac{\tilde{L}_{m-\frac{1}{2}} + \tilde{L}_{m+\frac{1}{2}}}{2}. \tag{3.94}$$

The computation of Eq. (3.87) is performed from $r_{j+1}$ to $r_j$ (inward) for negative $\mu_m$ and from $r_j$ to $r_{j+1}$ (outward) for positive $\mu_m$ as follows.

For $\mu_m < 0$, inward calculations are performed. Eliminating $L_{m,i}$ and $\tilde{L}_{m-\frac{1}{2}}$ from Eq. (3.90) using Eqs. (3.93)-(3.94) gives:

$$\tilde{L}_m = \frac{-\mu_m A L_{m,i+1} + \gamma_m \tilde{L}_{m-\frac{1}{2}} + \kappa_{\lambda,i}\tilde{V}_i \tilde{L}^o(T_i)}{-\mu_m A + \gamma_m + \kappa_{\lambda,i}\tilde{V}_i}, \tag{3.95}$$

where

$$A = A_i + A_{i+1}, \tag{3.96}$$

$$\gamma_m = \frac{\left(\alpha_{m-\frac{1}{2}} + \alpha_{m+\frac{1}{2}}\right)(A_{i+1} - A_i)}{2\omega_m}. \tag{3.97}$$

For positive $\mu_m$, computations are performed outwardly. Similarly, $L_{m,i+1}$ and $\tilde{L}_{m+\frac{1}{2}}$ are eliminating from Eq. (3.90) using Eqs. (3.93)-(3.94):

$$\tilde{L}_m = \frac{\mu_m A L_{m,i} + \gamma_m \tilde{L}_{m-\frac{1}{2}} + \kappa_{\lambda,i}\tilde{V}_i \tilde{L}^o(T_i)}{\mu_m A + \gamma_m + \kappa_{\lambda,i}\tilde{V}_i}, \tag{3.98}$$

with $A$ and $\gamma_m$ defined above.

Combining Eqs. (3.93), (3.95), and (3.98) along with the corresponding boundary conditions allows the computation of the radiance on all the grids and for all the ordinates. This method eliminates the need for iterations. The boundary conditions observed are $L_{m,1} = 0.6L^o(T_1)$ and $L_{m,JJ} = 0.6L^o(T_{JJ})$.

The spectral irradiance at a given mesh point is then obtained by integrating the radiance over all the ordinates. Using the Gauss-Legendre quadrature described above, it can be written:

$$q_{\lambda,i} = \sum_{m=1}^{N} \mu_m \omega_m \tilde{L}_{m,i}, \tag{3.99}$$

the value of the heat flux loss by radiation is then obtained by integrating the spectral irradiance over the whole spectra:

$$q_{r,i} = \int_0^\infty q_{\lambda,i} d\lambda. \tag{3.100}$$

As mentioned above, 20 ordinates are used. Their abscissa and weight are given in Table 3.1.

Table 3.1: Ordinates abscissa and weight.

| $m$ | $\mu_m$ | $\omega_m$ | $m$ | $\mu_m$ | $\omega_m$ |
|---|---|---|---|---|---|
| 1 | -0.99313 | 0.9598 | 11 | 0.07653 | 0.1106 |
| 2 | -0.96397 | 0.9373 | 12 | 0.22779 | 0.2551 |
| 3 | -0.91223 | 0.8928 | 13 | 0.37371 | 0.3938 |
| 4 | -0.83912 | 0.8274 | 14 | 0.51087 | 0.5233 |
| 5 | -0.74633 | 0.7426 | 15 | 0.63605 | 0.6404 |
| 6 | -0.63605 | 0.6404 | 16 | 0.74633 | 0.7426 |
| 7 | -0.51087 | 0.5233 | 17 | 0.83912 | 0.8274 |
| 8 | -0.37371 | 0.3938 | 18 | 0.91223 | 0.8928 |
| 9 | -0.22779 | 0.2551 | 19 | 0.96397 | 0.9373 |
| 10 | -0.07653 | 0.1106 | 20 | 0.99313 | 0.9598 |

Note: $\sum_m \omega_m = 4\pi$. This model has been used and validated in a number of studies [41, 42, 56, 76].

## 3.7 Code Structure and Time of Execution

This section provides a description of the main structure of the program. The interactions between the core code, based on PREMIX, the chemistry model

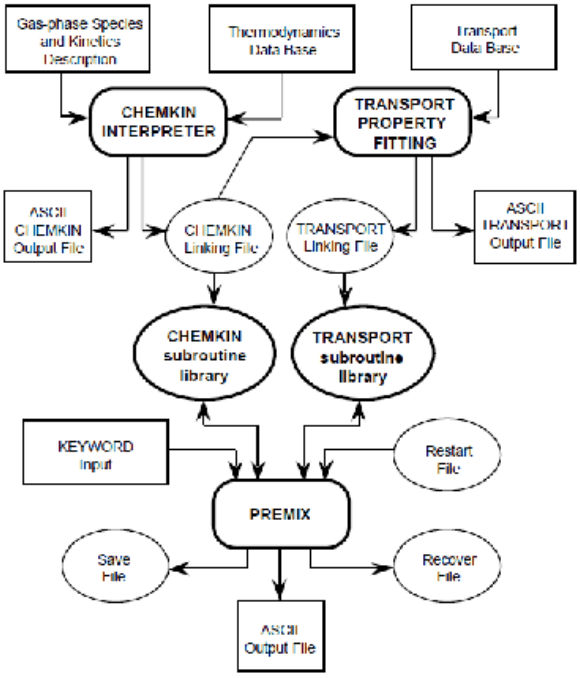


Figure 3.3: Interactions between PREMIX, CHEMKIN, and TRANSPORT processors. Adapted from [40].

CHEMKIN, and the transport evaluation model TRANSPORT are represented by Fig. 3.3.

As mentioned earlier, the chemistry model and species properties are first pre-processed by CHEMKIN and TRANSPORT routines, creating polynomial fits

to compute some thermodynamic properties. The chemistry model is evaluated and stored in an array form. The pre-processors create two linking files containing the chemistry and transport properties. The evaluation of the chemistry model is usually done every time the chemistry model is changed.

When executed, PREMIX does the following:

(1) First, the subroutines from CHEMKIN and TRANSPORT are initialized. Species properties are loaded into a consequent matrix in memory.

(2) Then, an input file describing the problem and containing some of code controls such as the number of iterations, steady-state or transient evaluation, etc., is read.

(3) A first guess is then either created from the description provided in the input file or, if available, a previous solution is read from a restart file. When a restart solution is not available, linear temperature and main species profiles are assumed as a first guess, with Gaussian profiles for the intermediate species and with an estimate of the flame location.

(4) The program evaluates the residuals for each equation and creates a Jacobian to solve the governing equations at a given time step (transient) or to solve the steady state problem. Then TWOPNT is called. CHEMKIN and TRANSPORT subroutines are called during the evaluation of the residuals.

(5) When a solution cannot be found, time stepping is used (steady-state) or a smaller time-step is used (transient and pseudo-transient).

Table 3.2: Relative CPU time for main functions.

| **Function** | **CPU time %** |
|---|---|
| Main | 100 |
| Gauss Elimination | 26 |
| Residuals | 73 |
| Chemistry | 38 |
| Soot | 3 |
| Transport | 21 |

(6) When a solution is found, it is stored in a save file and in an output file.

In systems containing a large number of species, evaluating species transport properties can be expensive. Moreover, due to the nature of the solver, the function calculating the residuals is called many times. To reduce the computational time, species transport properties are saved and their evaluation is performed only at certain iterations. This is also performed for the radiation model.

Using the compilation command -pg, the relative CPU time used per function can be obtained. Relatively times have been measured for a relative trivial case using the ABF model and the soot model described in Chapter 6. The relevant information is reported in Table 3.2.

More than a quarter of the time is dedicated to the Gaussian elimination routine. Almost all the remaining time is used to compute the function residuals. This also includes computation of the Jacobian matrix, computation of the chemical terms, computation of the transport coefficients, and the soot function. About 38% of the CPU time is dedicated to the computation of chemical production terms.

Those terms are evaluated every time the residuals are computed. The transport terms evaluation consumes 21% of the CPU time. This function is by far the most demanding in CPU-time after the Gauss-elimination function. Note that unlike the chemical production terms evaluation function, the transport coefficients are not evaluated at each iteration but they are saved and reused for a couple of iterations until the code decides reevaluates them. Even with this optimization, this process still uses 21% of the CPU time. The soot model does not increase significantly the time of execution, its overall contribution being 3%.

## 3.8 Some Post-Processed Quantities

This section presents some quantities that are computed after a solution is established. Those quantities are important for the evaluation of the solutions obtained. The two most important computed post-processed quantities are the mixture fraction $Z$ and the scalar dissipation rate $\chi$.

### 3.8.1 Mixture fraction

Under the steady-state and species equidiffusivity assumption, coupling functions or conserved scalars can be formed. Any conserved scalar, noted $\beta_i$, follows the relation:

$$L\left(\beta_i\right) = 0, \tag{3.101}$$

with

$$L\left(.\beta_i\right) = \left[\frac{\partial \rho}{\partial t} + \nabla \cdot \left(\rho \vec{U} - \rho D \nabla\right)\right]\left(\beta_i\right). \tag{3.102}$$

Since atomic elements are conserved in chemical reactions, an element mass fraction $Z_l$, defined for a mixture of $KK$ species of $Y_k$ made up of $L$ elements and defined by $Z_l = \sum_{k=1}^{KK} \mu_{l,k} Y_k$, $l = 1, \ldots, L$, is an example of conserved scalar. In the above formulation, $\mu_{l,k}$ is the mass fraction of the $l^{th}$ atomic element in the $k^{th}$ species.

The well known mixture fraction is another coupling function. It has been found to be suitable for modeling turbulent non-premixed flames [15, 77].

To define the mixture fraction, consider the global reaction: $\mathrm{F} + \nu \mathrm{O}_2 \rightarrow (\nu + 1)\,\mathrm{P}$. A coupling function can be defined as

$$\beta_{F,O} = Y_F - \frac{1}{r_S} Y_{\mathrm{O}_2}, \tag{3.103}$$

with

$$r_S = \frac{\nu W_{\mathrm{O}_2}}{W_F}. \tag{3.104}$$

Defining the mixture fraction $Z$ as a conserved scalar bounded between 0 and 1, with $Z_{ox} \rightarrow 0$ on the oxidizer side and $Z_f \rightarrow 1$ on the fuel side, gives the following formulation for $Z$:

$$Z = \frac{Y_F - \frac{1}{r_S} Y_{\mathrm{O}_2} - Y_{F,ox} + \frac{1}{r_S} Y_{\mathrm{O}_2,ox}}{Y_{F,f} - \frac{1}{r_S} Y_{\mathrm{O}_2,f} - Y_{F,ox} + \frac{1}{r_S} Y_{\mathrm{O}_2,ox}}. \tag{3.105}$$

This mixture fraction is a useful parameter to characterize the relative amount of fuel and oxidizer present at a given location. This quantity is also helpful to understand the strength of the mixing by convection-diffusion process. Moreover, describing the flame structure using the mixture fraction is equivalent to describing the flame structure using the radius. This is due to the nature of the mixture fraction distribution across the flame, which is a one-to-one mapping function between the

spatial domain and the mixture fraction space. Therefore, it allows the comparison between flames of different geometries.

In the code, computation of mixture fraction is performed as a post-process, using the computed species distribution function across the flame. For sooting limits flames, a detailed definition of mixture fraction using atomic elements has been developed and used. Its definition can be found in Chapter 5.

### 3.8.2 Scalar Dissipation Rate

In this section, the scalar dissipation rate $\chi$ is defined.

The energy equation, Eq. (1.8), written for the sensible enthalpy $h^s$, and considering a unity Lewis number gives:

$$\rho\frac{\partial h^s}{\partial t} + \rho\vec{U}\cdot\nabla h^s - \nabla\cdot(\rho D\nabla h^s) = -\dot{\omega}. \tag{3.106}$$

Consider an orthogonal coordinate system where $Z$ is a coordinate and coordinates $X$ and $Y$ defines a surface of constant $Z$. Since the problem is of spherical symmetry, the mixture fraction $Z$ is a function of the radius alone and the surfaces of constant mixture fraction are the surfaces of constant radius. Equation (3.106) in spherical symmetry is written by:

$$\rho\frac{\partial h^s}{\partial t} + \rho U_r\frac{\partial h^s}{\partial r} - \frac{1}{r^2}\frac{\partial}{\partial r}\left(r^2\rho D\frac{\partial h^s}{\partial r}\right) = -\dot{\omega}. \tag{3.107}$$

Then, a change of coordinates is performed, from $(t, r)$ to the new one $(\tau, Z)$,

with $t = \tau$, which gives:

$$\frac{\partial}{\partial t} = \frac{\partial}{\partial \tau} + \frac{\partial Z}{\partial t}\frac{\partial}{\partial Z}, \tag{3.108}$$

$$\frac{\partial}{\partial r} = \frac{\partial Z}{\partial r}\frac{\partial}{\partial Z} \tag{3.109}$$

the temporal, convective and diffusion terms of Eq. (3.107) become:

$$\rho\frac{\partial h^s}{\partial t} = \rho\frac{\partial h^s}{\partial \tau} + \rho\frac{\partial Z}{\partial t}\frac{\partial h^s}{\partial Z}, \tag{3.110}$$

$$\rho U_r\frac{\partial h^s}{\partial r} = \rho U_r\frac{\partial Z}{\partial r}\frac{\partial h^s}{\partial Z}, \tag{3.111}$$

$$\begin{aligned}\frac{1}{r^2}\frac{\partial}{\partial r}\left(\rho D r^2\frac{\partial h^s}{\partial r}\right) &= \frac{1}{r^2}\frac{\partial Z}{\partial r}\frac{\partial}{\partial Z}\left(\rho D r^2\frac{\partial Z}{\partial r}\frac{\partial h^s}{\partial Z}\right), \\ &= \frac{1}{r^2}\frac{\partial Z}{\partial r}\left(\rho D r^2\frac{\partial Z}{\partial r}\frac{\partial^2 h^s}{\partial Z^2} + \frac{\partial h^s}{\partial Z}\frac{\partial}{\partial Z}\left(\rho D r^2\frac{\partial Z}{\partial r}\right)\right), \\ &= \rho D\left(\frac{\partial Z}{\partial r}\right)^2\frac{\partial^2 h^s}{\partial Z^2} + \frac{1}{r^2}\frac{\partial h^s}{\partial Z}\frac{\partial}{\partial r}\left(\rho D r^2\frac{\partial Z}{\partial r}\right),\end{aligned} \tag{3.112}$$

the energy equation. Eq. (3.107), is then rewritten:

$$\rho\frac{\partial h^s}{\partial \tau} - \rho D\left(\frac{\partial Z}{\partial r}\right)^2\frac{\partial^2 h^s}{\partial Z^2} + \frac{\partial h^s}{\partial Z}\left(\rho\frac{\partial Z}{\partial t} + \rho U_r\frac{\partial Z}{\partial r} - \frac{1}{r^2}\frac{\partial}{\partial r}\left(\rho D r^2\frac{\partial Z}{\partial r}\right)\right) = -\dot{\omega}, \tag{3.113}$$

recognizing that $L(Z) = 0$ gives:

$$\rho\frac{\partial h^s}{\partial \tau} - \rho\frac{\chi}{2}\frac{\partial^2 h^s}{\partial Z^2} = -\dot{\omega}, \tag{3.114}$$

where

$$\chi = 2D\left(\frac{\partial Z}{\partial r}\right)^2, \tag{3.115}$$

defines the scalar dissipation rate. The scalar dissipation rate is an indication of the rate of reactant mixing by convection-diffusion processes. It has units of $s^{-1}$.

Numerically, the scalar dissipation rate is computed as a post-process application. It uses the distribution of the mixture fraction across the domain. The

diffusivity coefficient used to compute the scalar dissipation rate is the local thermal diffusivity coefficient.

# Chapter 4

# Weak Hydrogen Diffusion Flames

General characteristics of spherical diffusion flames have been presented in the previous chapters along with the numerical model used in this present study. In this chapter, kinetic extinction limits of $H_2$ spherical diffusion flames are investigated to understand the underlying fundamental physics of weak $H_2$ flames.

As mentioned previously, kinetic extinctions of spherical diffusion flames are realized by reducing the mass flow rate of reactant. Moreover, those flames present different inner structures, depending on the regime of combustion.

A general overview on weak or micro-diffusion flames is followed by a description of the experimental assessment of hydrogen flames near their quenching limits. Then numerical predictions of spherical flames at their quenching limits are presented, with a complete description of their structure and chemistry. Finally, an evaluation of the effects of the burner size on the flame is reported. An identified estimate of the lowest $H_2$ mass flow rate sustaining an adiabatic flame is provided.

## 4.1 Background

The use of micro-combustion processes for electric power generation has potential advantages over conventional electrochemical batteries, in terms of power generation per unit volume and energy storage per unit mass [78]. The increasing needs and demand for smaller scale and higher density power sources motivates the development of micro-power devices.

Recent developments in silicon technologies and development of new materials have led to opportunities of creating highly effective small thermoelectric power generators [79]. Their use opens new prospects in creation of micro scale energy supply devices. Recent developments of Micro-Electro-Mechanical Systems (MEMS) [80] have enabled new micro-combustor designs. Micro-combustors can be defined as reactors with characteristic length scales on the order of millimeters or less.

Laminar diffusion flames can be classified in three categories. The first corresponds to diffusion controlled flames, which can be accurately modeled using Burke-Schumann theory [10]. The second category comprises flames that are controlled by momentum or buoyancy, such as the Roper flame [81]. The third category corresponds to micro-diffusion flames, where momentum and diffusion effects are comparable.

Recent attention has been dedicated to micro-flames. Ban *et al.* [82] observed flame shapes of small hydrocarbon laminar diffusion flames issuing from small fuel jets and compared them to the shapes predicted analytically. They found that buoyancy effects are negligible for small flames and their shapes tend to be spherical.

At this size, the effects of diffusion are comparable to the effects of convection. Matta *et al.* [83] reached the same conclusion considering a preheated weak propane flame with a heat release rate of 0.49 W issued from a 101 $\mu$m tube.

Cheng *et al.* [84] characterized micro-jet methane diffusion flames issued from burners with inner diameters ranging from 186 - 778 $\mu$m. They compared the measured flame shapes with those predicted using a 2-D code with detailed chemistry model based on GRI-Mech 3.0. They observed that near extinction, the flame burns in a diffusion mode. Hydrogen micro-scale flames were also studied both experimentally and numerically [85]. Those flames were produced from small tubes (0.2 and 0.48 mm) and were spherical, with a radius of 1 mm. They observed that the increased diffusivity of $H_2$ leads to increased oxidizer leakage across the flame.

Nakamura *et al.* [86] numerically studied methane micro diffusion flames on circular burners of diameter less than 1 mm. They found that small flames have the same, nearly spherical, structure as those in microgravity, with similar species and temperature distributions. The spherical shape occurs when the Peclet number, $Pe$, of the flame is lower than 5 [82] . The Peclet number is defined as the ratio of the mean exit velocity $U$ to the diffusion velocity $U_d$ and assesses the dominance of diffusion over momentum as the main transport process. This number is defined as:

$$Pe = \frac{U l_D}{D_f}, \tag{4.1}$$

where $l_D$ is a characteristic diffusion length and $D_f$ is the fuel mass diffusivity coefficient.

Nakurama *et al.* [86] predicted a near quenching methane-air micro-flame re-

leasing 0.5 W. The existence of a minimum flame size below which no flame exists was predicted, the minimum flame height being comparable to the reaction layer thickness. This is confirmed by Matta *et al.* [83], who concluded that a micro-flame must be longer than its quenching distance to exist.

More recently, Kazunori *et al.* [87] developed a model based on the Burke-Schumann theory to predict extinction of micro-diffusion jet flames. Considering a one-step chemistry with finite rates, they show analytically that the average velocity at extinction is proportional to the the square of the burner diameter, $d_b^2$.

Ronney *et al.* [88] observed the burning of spherical flame balls in microgravity during the STS-83/MSL-1 Space Shuttle mission. Heat released by those flames was as low as 1 W. Subsequently they achieved flames as weak as 0.5 W.

Experimentally, Butler *et al.* [89, 90] examined quenching limits associated with various fuels and burner configurations. Their weakest flames involved hydrogen issuing downward into air from a hypodermic tube with an inside diameter of 0.15 mm. These flames, and a related flame burning in oxygen, are the subject of this chapter. Before presenting the predicted flames at their quenching limits, the experiments that are the base of this work are presented.

## 4.2 Experiments

The experiments involved hydrogen non-premixed jet flames burning in quiescent air and weakly counter-flowing pure oxygen. Experimental details can be found in Butler *et al.* [90]. The burners used were made of stainless steel with inside

and outside diameters of 0.15 and 0.30 mm, and with downward orientation. Hydrogen flow rates were measured with a soap bubble meter. The hydrogen flames were not visible but were detected with a thermocouple 1 cm above the burner tip. Quenching limits were reached by slowly reducing the $H_2$ flow rate until the flame extinguished.

Images of the two hydrogen flames at their quenching limits are shown in Fig. 4.1. The test conditions associated with these flames are given in Table 4.1. The images were recorded with a Nikon D100 camera at ISO 200, f/1.4, and with an exposure time of 30 s.

Table 4.1: Summary of the hydrogen flames at their quenching limits.

| Oxidizer | Flow rate $\mu$g/s | $U_b$ m/s | $Re$ | $Fr$ | $Pe$ | Power W |
|---|---|---|---|---|---|---|
| air | 3.9 | 2.5 | 3.96 | 65 | 5.3 | 0.46 |
| $O_2$ | 2.1 | 1.4 | 2.13 | 36 | 3.0 | 0.25 |

The word WE is included at flame scale to show that the flames are smaller than the smallest letters on a U.S. dime. The flames are hazy, suggesting distributed reaction zones rather than thin flame sheets.

The heat release rates associated with the mass flow rates are provided in Table 4.1, assuming complete combustion and a heat of combustion of 120 kJ/g. Also presented in this table are the Reynolds numbers, $Re$, at the burner exit based on hydrogen properties at laboratory conditions. At these low Reynolds numbers, the hydrogen flow in the hypodermic tube has similar conditions to those experienced in a Stokes flow, where viscosity is important. The velocities of the issued hydrogen


Figure 4.1: Color image of hydrogen flames at their quenching limits burning in air (left) and oxygen (right).

are 2.5 m/s, and 1.4 m/s for $H_2$/air, and $H_2/O_2$, respectively.

The Froude number is defined here as:

$$Fr = \frac{U_b}{(gd_b)^{\frac{1}{2}}}, \tag{4.2}$$

with $U_b$ the mean exit velocity and $d_b$ the burner diameter.

The relatively high Froude numbers in Table 4.1 reveal that the flames are minimally affected by gravity. The Peclet number $Pe$ defined by Eq. (4.1) can be expressed as function of the Reynolds and Schmidt numbers, $Sc$ :

$$Pe = ScRe_b\frac{l_D}{d_b}, \tag{4.3}$$

with $Re_b$ the Reynolds number associated with the conditions at the burner outlet, $l_D$ the characteristic diffusion length, and $Sc$ the Schmidt number of the fuel, taken here as 0.204 for $H_2$/air and 0.22 for $H_2/O_2$ [91]. If the characteristic diffusion length is taken as the same order of magnitude as the flame size, 1 mm, the Peclet numbers are 5.3 and 3 for the $H_2$/air and $H_2/O_2$ flames, respectively. According to Han *et al.* [82], flames with Peclet numbers lower or equal to 5 are spherical.

## 4.3 Numerical Method

Numerical predictions of steady state hydrogen flame were performed considering four different burner sizes, 1 $\mu$m, 75 $\mu$m, 300 $\mu$m, and 3.175 mm, and two different oxidizers, quiescent air and quiescent oxygen. Predictions of flames were realized using the 1-D spherical code previously mentioned and described in Chapter 3. The use of spherical coordinates is motivated by the low values of the Peclet

number for the experimental flames, see Table 4.1.

The detailed hydrogen chemistry mechanism was extracted from GRI-Mech. 3.0. Reactions considered are reported in Table 4.2. Those flames were modeled considering adiabatic condition at the burner surface. Cheng [25] estimated burner temperatures of about 1010 K based on the burner glowing. Moreover, in a computational study [92], he showed that for small flames with low Reynolds numbers, variable wall temperature conditions yielded better agreement between computed and measured data.

Cheng *et al.* [92] also showed that the effects of radiation on flame structure are small for low Reynolds number flames. In this study, radiation was neglected. This condition frees the study from effects of heat losses to the burner and emphasizes the effects due to the burner. The mass flux allowed backward species diffusion into the burner, condition similar to those adopted by Chang *et al.* [85]. This corresponds to the condition mentioned in Section 3.1.2. The pressure was held constant over the domain at 0.98 bar.

At the outer boundary, temperature was kept constant. Species mass fractions at this boundary were set to either air or oxygen. For all the simulations, attention was dedicated to the position of the outer boundary such that it did not interfere with the flame, simulating an infinite boundary. The gradients at the outer boundary were negligible. Typically, the computational domains for the predictions of diffusion hydrogen micro-flames ranged from the burner exit to 150 cm.

Adaptive mesh point addition was used to reduce the gradients and curvature, improving accuracy. New grid points were automatically added until values of gra-

Table 4.2: $H_2$-$O_2$ reactions mechanisms considered for the simulations. From GRI-Mech. 3.0. [64]

| No. | Reaction | A ($cm^3 mol^{-1} s^{-1}$) | n | $E_a$ ($kcal/mol$) |
|---|---|---|---|---|
| R1 | $2\,O + M \longrightarrow O_2 + M$ | 1.20 x $10^{17}$ | -1.0 | 0.0 |
| R2 | $O + H + M \longrightarrow OH + M$ | 5.0 x $10^{17}$ | -1.0 | 1.0 |
| R3 | $O + H_2 \longrightarrow H + OH$ | 3.87 x $10^{4}$ | 2.7 | 6.26 |
| R4 | $O + HO_2 \longrightarrow OH + O_2$ | 2.0 x $10^{13}$ | 0.0 | 0.0 |
| R5 | $O + H_2O_2 \longrightarrow OH + HO_2$ | 9.63 x $10^{6}$ | 2.0 | 4.0 |
| R33 | $H + O_2 + M \longrightarrow HO_2 + M$ | 2.80 x $10^{18}$ | -0.86 | 0.0 |
| R34 | $H + 2\,O_2 \longrightarrow HO_2 + O_2$ | 2.08 x $10^{19}$ | -1.24 | 0.0 |
| R35 | $H + O_2 + H_2O \longrightarrow HO_2 + H_2O$ | 1.13 x $10^{19}$ | -0.76 | 0.0 |
| R36 | $H + O_2 + N_2 \longrightarrow HO_2 + N_2$ | 2.60 x $10^{19}$ | -1.24 | 0.0 |
| R37 | $H + O_2 + Ar \longrightarrow HO_2 + Ar$ | 7.00 x $10^{17}$ | -0.8 | 0.0 |
| R38 | $H + O_2 \longrightarrow O + OH$ | 2.65 x $10^{16}$ | -0.67 | 17.041 |
| R39 | $2\,H + M \longrightarrow H_2 + M$ | 1.0 x $10^{18}$ | -1.0 | 0.0 |
| R40 | $2\,H + H_2 \longrightarrow 2\,H_2$ | 9.0 x $10^{16}$ | -0.6 | 0.0 |
| R41 | $2\,H + H_2O \longrightarrow H_2 + H_2O$ | 6.0 x $10^{19}$ | -1.25 | 0.0 |
| R43 | $H + OH + M \longrightarrow H_2O + M$ | 2.2 x $10^{22}$ | -2.0 | 0.0 |
| R44 | $H + HO_2 \longrightarrow O + H_2O$ | 3.97 x $10^{12}$ | 0.0 | 0.671 |
| R45 | $H + HO_2 \longrightarrow O_2 + H_2$ | 4.48 x $10^{13}$ | 0.0 | 1.068 |
| R46 | $H + HO_2 \longrightarrow 2\,OH$ | 8.40 x $10^{13}$ | 0.0 | 0.635 |
| R47 | $H + H_2O_2 \longrightarrow HO_2 + H_2$ | 1.21 x $10^{07}$ | 2.0 | 5.2 |
| R48 | $H + H_2O_2 \longrightarrow OH + H_2O$ | 1.0 x $10^{13}$ | 0.0 | 3.6 |
| R84 | $OH + H_2 \longrightarrow H + H_2O$ | 2.16 x $10^{08}$ | 1.51 | 3.430 |
| R85 | $2\,OH + M \longrightarrow H_2O_2 + M$ | 7.4 x $10^{13}$ | -0.37 | 0.0 |
| R86 | $2\,OH \longrightarrow O + H_2O$ | 3.57 x $10^{4}$ | 2.4 | -2.11 |
| R87 | $OH + HO_2 \longrightarrow O_2 + H_2O$ | 1.45 x $10^{13}$ | 0.0 | -0.5 |
| R88 | $OH + H_2O_2 \longrightarrow HO_2 + H_2O$ | 2.0 x $10^{12}$ | 0.0 | 0.427 |
| R89 | $OH + H_2O_2 \longrightarrow HO_2 + H_2O$ | 1.7 x $10^{18}$ | 0.0 | 29.410 |
| R115 | $2\,HO_2 \longrightarrow O_2 + H_2O_2$ | 1.3 x $10^{11}$ | 0.0 | -1.630 |
| R116 | $2\,HO_2 \longrightarrow O_2 + H_2O_2$ | 4.2 x $10^{14}$ | 0.0 | 12.000 |

$$k_{f,i} = AT^n \exp(-E_a/RT)$$

dients and curvature fell below user specified limits. Typically the computational domain consisted of 300 points.

Steady state solutions of $H_2$/air and $H_2/O_2$ were considered. For the study of quenching limits, the following process was observed. A first solution based on the characteristic of the flame studied was generated by the code with a moderate mass flow rate. Then this solution was used as the starting condition for a new simulation using the same parameters but with a lower mass flow rate. The process was reiterated until extinction was reached. Extinction was defined when a solution with no reaction was obtained, i.e. where there was no significant raise of temperature.

Solutions of the flames at steady state were investigated with special consideration for $H_2$, $O_2$, H, O, OH, $H_2O$, and $HO_2$. Among the other characteristics considered in this study are the local temperature, species mass fraction distribution, local heat release rate, elementary reaction heat release rates, and rates of progress of the most important reactions.

## 4.4 Numerical Results

Numerical esults are presented in the following subsections. First, estimates of the lowest mass flow rate sustaining a hudrogen flame in air and pure oxygen are sought. This represents the numerical counterpart of the experiments presented in Section 4.2. Then the effects of the burner size and the mass flow rate on the flame structure are presented.

### 4.4.1 Modeling Weak $H_2$/air Flame

Numerical investigations were performed to characterize the lowest mass flow rate sustaining a flame in an ideal condition. For cases where the burner size is small enough such that it has a negligible effect on the reaction zone, the lowest mass flow rate sustaining a flame represents a physical limit below which a flame cannot be sustained. This correspond to seeking a fundamental limit in an ideal case.

As mentioned above, the quenching mass flow rate was reached by decreasing the mass flow rate and reusing a former steady state solution with a higher mass flow rate. For the $H_2$/air flame, two burner radii were considered, 75 $\mu$m and 1 $\mu$m. The 75 $\mu$m burner radius was chosen to match the experimental burner radius. The 1 $\mu$m burner was chosen because this provides solutions that are not affected by the burner size, as shown below.

For the burner of 75 $\mu$m radius, the lowest mass flow rate sustaining a flame is predicted to be 3.65 $\mu$g/s for the $H_2$/air flame. This corresponds to a flame with a heat release rate of 0.41 W. These values are in reasonable agreement with the measured mass flow rates and heat released rates observed experimentally, and reported in Table 4.1. Experimentally, a mass flow rate of 3.9 $\mu$g/s was obtained near extinction. This corresponds to an overall heat release rate of 0.46 W. These results are remarkably close, despite the configuration difference between the experiment (jet) and numerical simulation (sphere).

A lower mass flow rate is achieved for the 1 $\mu$m radius burner. For this burner, a mass flow rate of 3.49 $\mu$g/s sustains a 0.4 W flame. Experimental and predicted

mass flow rate values are reported in Table 4.3.

Table 4.3: Predicted and experimental mass flow rates near extinction for a $H_2$/air flame.

| Radius $r_b$ $\mu$m | Flow rate $\mu$g/s | Power W |
|---|---|---|
| 75 (exp) | 3.9 | 0.46 |
| 75 (num) | 3.65 | 0.41 |
| 1 (num) | 3.49 | 0.4 |

In Figs. 4.2-4.5, predicted $H_2$/air flame structure prior to extinction and from a 75 $\mu$m radius is plotted and compared with the structure of a $H_2$/air flame issued from a 1 $\mu$m radius burner and with a mass flow rate of 3.49 $\mu$g/s.

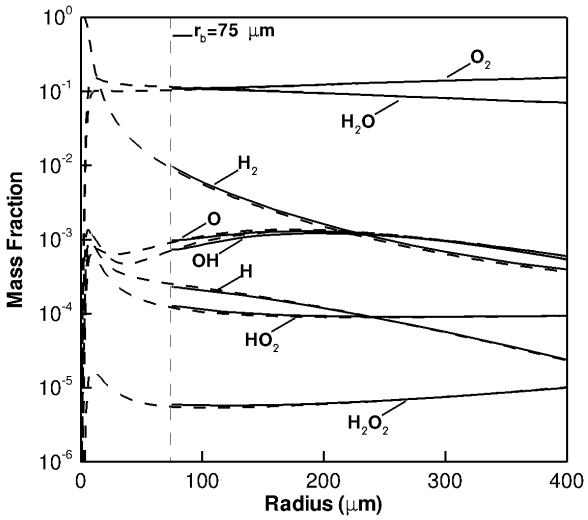


Figure 4.2: Predicted species mass fraction at the onset of kinetics extinction. Burner radii are 75 $\mu$m plain line (1 $\mu$m dashed) and supplied mass flow rate is set at 3.65 $\mu$g/s (3.49 $\mu$g/s).

Superimposing the two data sets shows similarities shared by the two flames. A common region is located beyond 75 $\mu$m, corresponding to the radius of the burner.

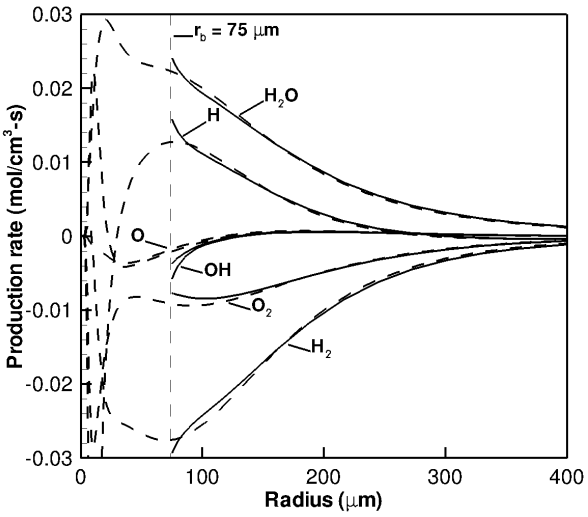


Figure 4.3: Predicted species production rate at the onset of kinetics extinction. Burner radii are 75 $\mu$m plain line (1 $\mu$m dashed) and supplied mass flow rate is set at 3.65 $\mu$g/s (3.49 $\mu$g/s).

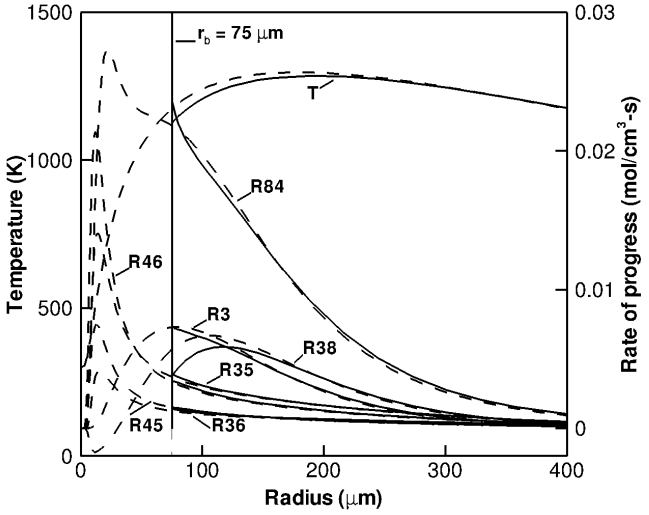


Figure 4.4: Predicted elementary reactions rate of progress at the onset of kinetics extinction. Burner radii are 75 $\mu$m plain line (1 $\mu$m dashed) and supplied mass flow rate is set at 3.65 $\mu$g/s (3.49 $\mu$g/s).

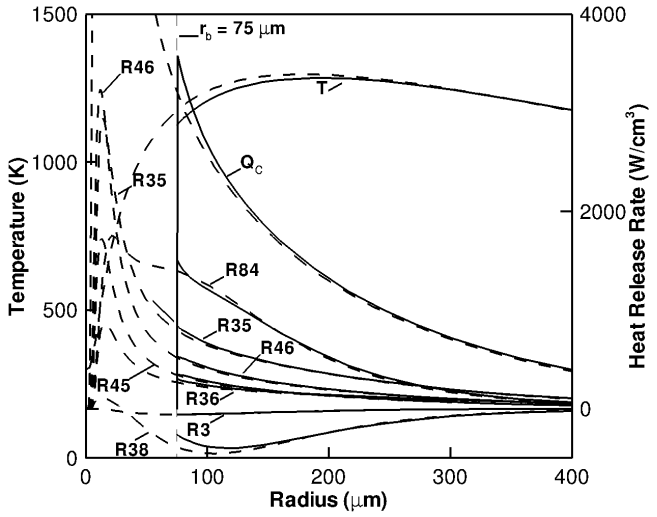


Figure 4.5: Predicted elementary reactions heat release rate at the onset of kinetics extinction. Burner radii are 75 $\mu$m plain line (1 $\mu$m dashed) and supplied mass flow rate is set at 3.65 $\mu$g/s (3.49 $\mu$g/s).

Figures 4.2-4.5 show the flame truncation induced by the presence of the burner. Both flames present the same peak temperature of 1290 K. Scalar dissipation rates at the flame location $\chi_{st}$ are 0.98 $s^{-1}$ for the 75 $\mu$m burner, and 1.18 $s^{-1}$ for the 1 $\mu$m burner. Due to the small flame radii, about 200 $\mu$m for both, the heat release rate density is very high, peaking at 3800 and 8000 W/$cm^3$, respectively.

The smallest burner considered presents the highest scalar dissipation rate prior to extinction. Its predicted surface temperature is 300 K, which implies that the burner does not remove any heat from the system. Moreover, at the burner surface, the mass fraction of $H_2$ is close to unity, which is not the case for the 75 $\mu$m burner. The oxidizer leakage is important near the burner for the 75 $\mu$m burner case. The oxygen and intermediate species mass fractions at the burner surface are

high.

The mass fraction of $H_2$ drops considerably outside the burner. For the 75 $\mu$m burner, $H_2$ mass fraction at the burner surface is lower than 1%. The reaction zone exists under lean conditions. This was also observed by Chang *et al.* [85].

The main reactions contributing to the heat release rate for the 75 $\mu$m burner are:

$$\text{(R84) } OH + H_2 \longrightarrow H_2O + H,$$

$$\text{(R35) } H + O_2 + H_2O \longrightarrow HO_2 + H_2O,$$

$$\text{(R46) } H + HO_2 \longrightarrow 2\,OH,$$

$$\text{(R45) } H + HO_2 \longrightarrow O_2 + H_2,$$

and

$$\text{(R36) } H + O_2 + N_2 \longrightarrow HO_2 + N_2.$$

There is a significant endothermic reaction, the chain branching reaction

$$\text{(R38) } H + O_2 \longrightarrow OH + O,$$

which consumes part of the energy released to generate radicals.

The major contributors to the heat release rate are not necessarily the reactions with the highest rates of progress. Indeed, although reaction

$$\text{(R84) } OH + H_2 \longrightarrow H_2O + H$$

shows the highest rate of progress and heat release rate, reaction

$$\text{(R3) } O + H_2 \longrightarrow H + OH,$$

which does not contribute to the heat release rate, has the second highest rate of progress. The third highest belongs to the radical-producing, chain-branching reaction

$$\text{(R38) } H + O_2 \longrightarrow OH + O,$$

followed by chain termination reaction:

$$\text{(R35) } H + O_2 + H_2O \longrightarrow HO_2 + H_2O,$$

$$\text{chain branching (R46) } H + HO_2 \longrightarrow 2\,OH,$$

and to a lesser measure:

$$\text{(R45) } H + HO_2 \longrightarrow H_2 + O_2,$$

$$\text{and (R36) } H + O_2 + N_2 \longrightarrow HO_2 + N_2.$$

The main reactions predicted for the 1 $\mu$m radius burner flame are the same, except their order of importance is different. The main reaction, in terms of heat release rate is

$$\text{(R46) } H + HO_2 \longrightarrow 2\,OH,$$

followed by:

$$\text{(R45) } H + HO_2 \longrightarrow H_2 + O_2,$$

$$\text{(R35) } H + O_2 + H_2O \longrightarrow HO_2 + H_2O,$$

$$\text{and (R84) } OH + H_2 \longrightarrow H_2O + H.$$

All are reactions involving the consumption of H radical except for reaction (R84).

In terms of rate of progress, the important reactions are:

$$\text{(R84) } OH + H_2 \longrightarrow H_2O + H,$$

$$\text{(R46) } H + HO_2 \longrightarrow 2\,OH,$$

$$\text{(R35) } H + O_2 + H_2O \longrightarrow HO_2 + H_2O,$$

$$\text{(R45) } H + HO_2 \longrightarrow H_2 + O_2,$$

$$\text{and (R36) } H + O_2 + N_2 \longrightarrow HO_2 + N_2.$$

Note that reactions:

$$\text{(R3) } O + H_2 \longrightarrow H + OH,$$

$$\text{and (R38) } H + O_2 \longrightarrow OH + O,$$

have negative rates of progress close to the burner.

### 4.4.2 Modeling Weak $H_2/O_2$ Flames

The quenching limits of $H_2/O_2$ diffusion flames has been found experimentally using a 75 $\mu$m radius hypodermic tube. As reported in Table 4.1, the lowest mass flow rate sustaining a flame is found to be $\dot{m} = 2.1$ $\mu$g/s, which is almost half that of $H_2$/air flames issued from the same burner. This section presents here the predicted results for $H_2/O_2$ flames at the onset of kinetic extinction, and generated by a 75 $\mu$m burner.

Following the same procedure as the $H_2$/air flame, the predicted lowest mass flow rate sustaining a flame was found by considering steady-state solutions with decreased mass flow rates until kinetic extinction.

The predicted mass flow rate at the onset of extinction is found at $\dot{m} = 2.67$ $\mu$g/s. This is 27% higher than the experimental result of $\dot{m} = 2.1$ $\mu$g/s. This

represents a heat release rate of 0.31 W, which is by far the smallest heat release rate observed or predicted for a micro-flame. The peak temperature of the $H_2/O_2$ flame near extinction is than the $O_2$/air flame, the former peaked at 1400 K and the latter at 1290 K. The predicted scalar dissipation rate at the peak temperature is $\chi_{st} = 2.43\ s^{-1}$. This value is twice the scalar dissipation rate of the extinction limit of the $H_2$/air flame generated by the 1 $\mu$m radius burner.

The flame structure is presented in Figs. 4.6-4.9.

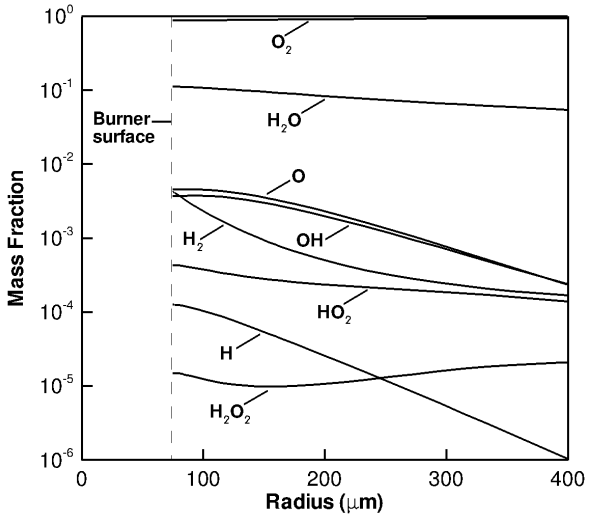


Figure 4.6: Predicted species mass fraction at the onset of kinetics extinction for the $H_2/O_2$ flame. Burner radius is 75 $\mu$m and supplied mass flow rate is set at 2.67 $\mu$g/s.

For the same burner size, higher O and OH radical leakage at the flame location is observed for the system $H_2/O_2$ than for the $H_2$/air system. However $H_2/O_2$ flames present faster chemistry, with peak values of species production rate about 5 times those predicted for the $H_2$/air flame. This is a consequence of increased reaction

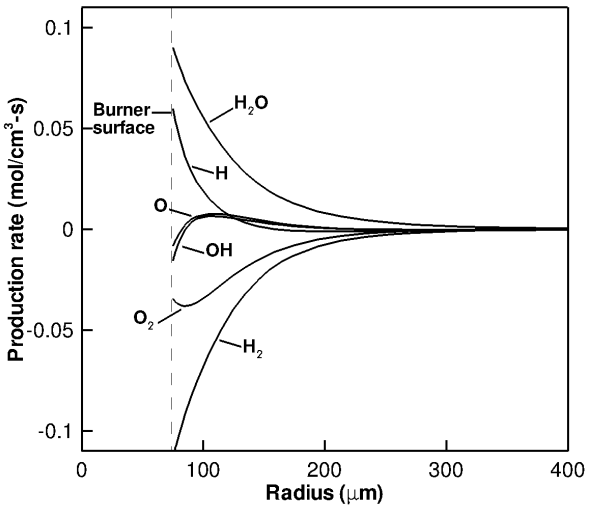


Figure 4.7: Predicted species production rate at the onset of kinetics extinction for the $H_2/O_2$ flame. Burner radius is 75 $\mu$m and supplied mass flow rate is set at 2.67 $\mu$g/s.

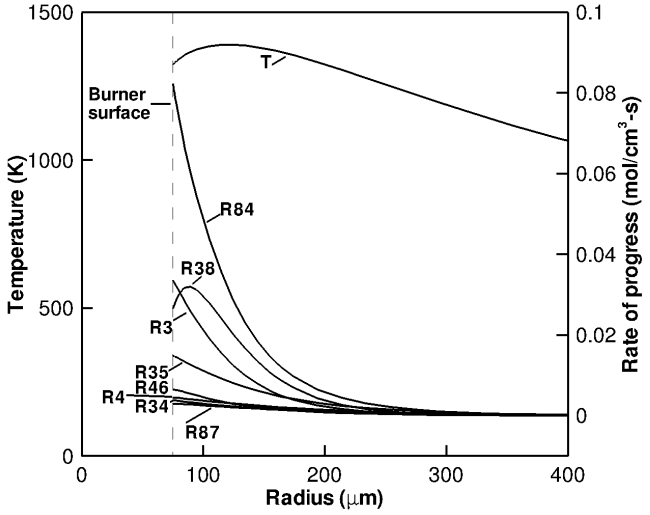


Figure 4.8: Predicted elementary reactions rate of progress at the onset of kinetics extinction for the $H_2/O_2$ flame. Burner radius is 75 $\mu$m and supplied mass flow rate is set at 2.67 $\mu$g/s.

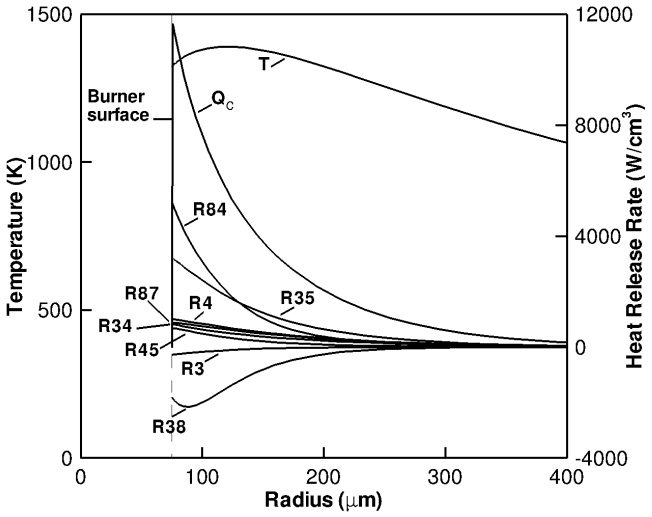


Figure 4.9: Predicted elementary reactions heat release rate at the onset of kinetics extinction for the $H_2/O_2$ flame. Burner radius is 75 $\mu$m and supplied mass flow rate is set at 2.67 $\mu$g/s.

rates of progress in the $H_2/O_2$ flames. Note that the mass fraction of H radical is lower for $H_2/O_2$ than it is for $H_2$/air, with a decrease more pronounced at the outer side of the flame. The mass fraction of other radicals, ($HO_2$, $H_2O_2$, O, and OH) are higher for this flame. However, the mass fraction of the product of reaction, $H_2O$ remains similar to the $H_2$/air flame.

The main chemical reactions contributing to the heat release rate for $H_2/O_2$ flames at the onset of extinction are:

$$\text{(R84) } OH + H_2 \longrightarrow H_2O + H,$$

$$\text{(R35) } H + O_2 + H_2O \longrightarrow HO_2 + H_2O,$$

$$\text{(R4) } O + HO_2 \longrightarrow OH + O_2,$$

$$\text{(R87) } OH + HO_2 \longrightarrow O_2 + H_2O,$$

$$\text{(R34) } H + 2\,O_2 \longrightarrow HO_2 + O_2,$$

$$\text{and (R45) } H + HO_2 \longrightarrow O_2 + H_2$$

for the exothermic reactions. The endothermic reactions are:

$$\text{(R3) } O + H_2 \longrightarrow H + OH,$$

$$\text{and (R38) } H + O_2 \longrightarrow O + OH.$$

The important reactions by decreasing rate of progress, are similar to the main contributors to the heat release rate:

$$\text{(R84) } OH + H_2 \longrightarrow H_2O + H,$$

$$\text{(R38) } H + O_2 \longrightarrow O + OH,$$

$$\text{(R3) } O + H_2 \longrightarrow H + OH,$$

$$\text{(R35) } H + O_2 + H_2O \longrightarrow HO_2 + H_2O,$$

$$\text{(R46) } H + HO_2 \longrightarrow 2\,OH,$$

$$\text{(R4) } O + HO_2 \longrightarrow OH + O_2,$$

$$\text{and (R34) } H + 2\,O_2 \longrightarrow HO_2 + O_2.$$

The $H_2/O_2$ flame has a slightly higher temperature at the onset of extinction (1400 K versus 1290 K) than the $H_2$/air flame. However, its flame extent is smaller than that of the $H_2$/air flame. The location of the peak temperature is located at a radius of 130 $\mu$m for the $H_2/O_2$ flame and at almost 200 $\mu$m for the $H_2$/air flame.

### 4.4.3 Combined Effects of the Burner Size and Mass Flow Rate

The impact of the mass flow rate and of the burner size was studied for the $H_2$/air flame. Their effects on flame temperature, flame position, and scalar dissipation rate were investigated, and are plotted in Fig. 4.10. Four different burner radii were considered: 3.175 mm, 300 $\mu$m, 75 $\mu$m, and 1 $\mu$m.

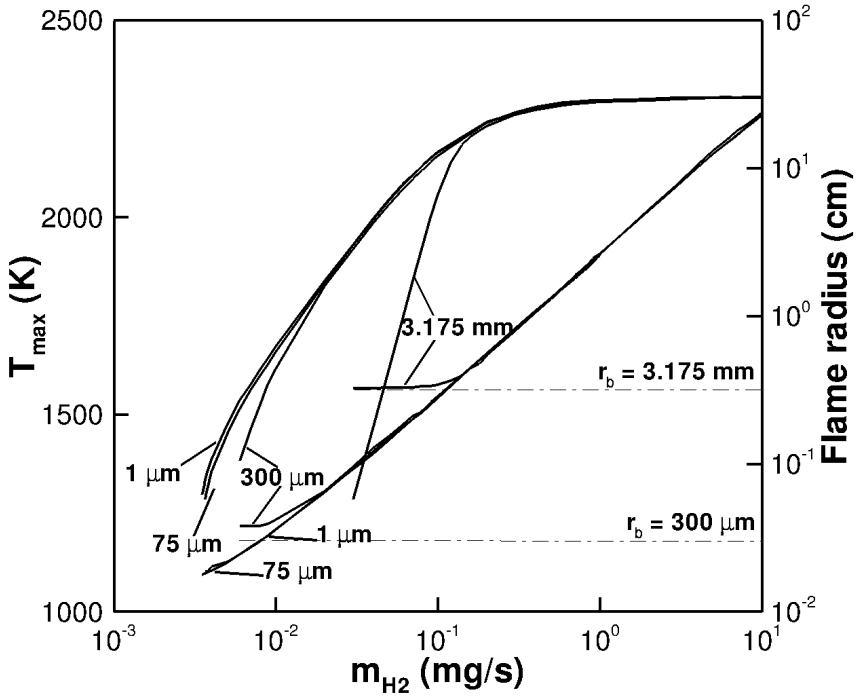


Figure 4.10: Evolution of predicted $H_2$/air flame temperature and flame radius with supplied mass flow rate issued from 3.175 mm, 300 $\mu$m, 75 $\mu$m, and 1 $\mu$m burners.

At high mass flow rates, flame temperature and radius are independent of the burner radius. The flame temperature plateaus at about 2300 K for mass flow rates

higher than 0.3 mg/s. Decreasing the mass flow rate reduces the flame radius, the flame moving closer to the burner. As the flow rate diminishes, the flame moves closer to the burner until any further decrease in mass flow rate does not change the flame position, the burner preventing the flame from moving inward. This has a truncating effect on the flame and accelerates flame extinction.

Extinction is observed for a peak temperature of about 1300 K. This value is common for the four burner radii considered. Reducing the mass flow rate below 0.1 mg/s leads to a similar drop in peak temperature for burner radii of 300 $\mu$m, 75 $\mu$m, and 1 $\mu$m. The 1 $\mu$m radius burner does not affect the flame, as observed in Fig. 4.2, and thus it can be taken as reference. Therefore, the mass flow rate of 3.49 $\mu$g/s is the lowest predicted mass flow rate sustaining a $H_2$/air flame regardless of burner size. The flame produced generates a heat release rate of 0.4 W, which is the weakest flame predicted numerically.

In the following subsections, differences in flame structure are investigated as the regime of combustion changes from a well developed flame with a mass flow rate high enough to be free from the burner effects to a flame at the onset of extinction, as illustrated in Sections 4.4.1 and 4.4.2.

Two burning regimes are presented for a $H_2$/air flame issued from a spherical burner of 3.175 mm. The first burning regime, following Law's denomination [9], is called the near-equilibrium regime. It corresponds to the combustion regime of an established diffusion flame with a large mass flow rate. The second regime is named partial burning regime and corresponds to the combustion regime of a truncated flame.

### 4.4.4 Modeling Near-Equilibrium Regime of $H_2$/Air Diffusion Flame

The characteristics of an $H_2$/air flame burning in near-equilibrium regime are presented in this subsection. This regime is achieved considering a spherical diffusion flame of hydrogen issuing from a 3.175 mm burner at a rate of 10 mg/s into quiescent air. Figure 4.11 plots the species mass fraction profiles, Fig. 4.12 plots the species production rate, Fig. 4.13 plots the main elementary reaction rates of progress, and Fig. 4.14 plots the temperature and the local heat release rate with the contribution of main elementary reactions.

This flame is typical of a strong diffusion flame. The flow rate produces a relatively large diffusion flame, with a peak temperature of 2303 K located 22 cm from the burner center. The predicted heat release rate is 1275 W. The mass flow rate is larger than the mass flow rates presented in the former sections. Therefore, according to Eq. (2.19), this flame has an important Damköhler number. The transport time controls the flame structure. The scalar dissipation rate at the peak temperature is $\chi_{st} = 5.2 \times 10^{-6}$ s$^{-1}$, indicating a low mixing rate. Note that the velocities involved at the burner surface are sufficiently hight to prevent a rise in the surface temperature.

The $H_2$ and $O_2$ mass fractions near the reaction zone are low, indicating negligible leakage of fuel or oxidizer.

For this flame, two peaks are present in the total heat release profile. This is a noticeable difference from flames near their kinetic extinction, presented in Figs. 4.5

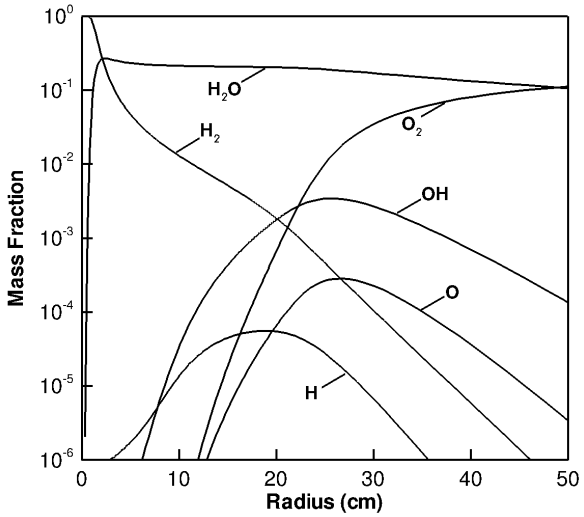


Figure 4.11: Predicted species mass fraction for a $H_2$/air flame. Burner radius is 3.175 mm and supplied mass flow rate is set at 10 mg/s.

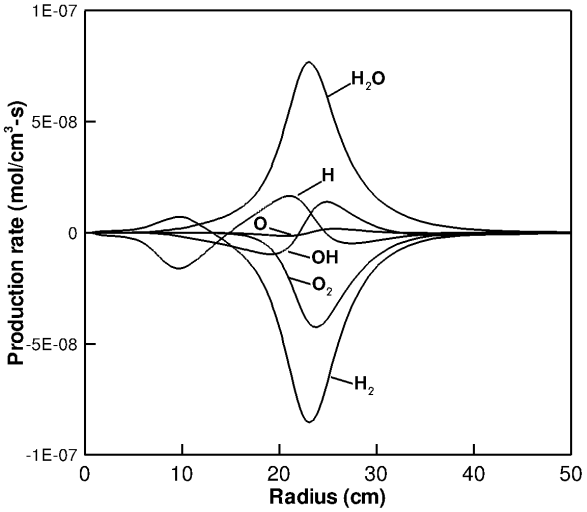


Figure 4.12: Predicted species production rate for a $H_2$/air flame. Burner radius is 3.175 mm and supplied mass flow rate is set at 10 mg/s.

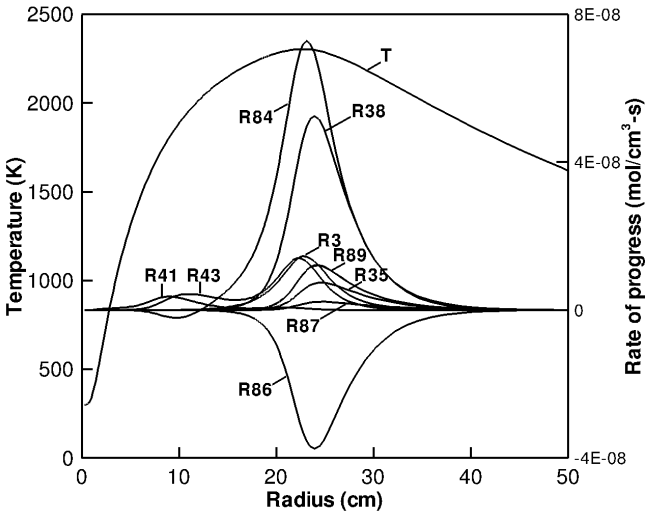


Figure 4.13: Predicted elementary reactions rate of progress for a $H_2$/air flame. Burner radius is 3.175 mm and supplied mass flow rate is set at 10 mg/s.

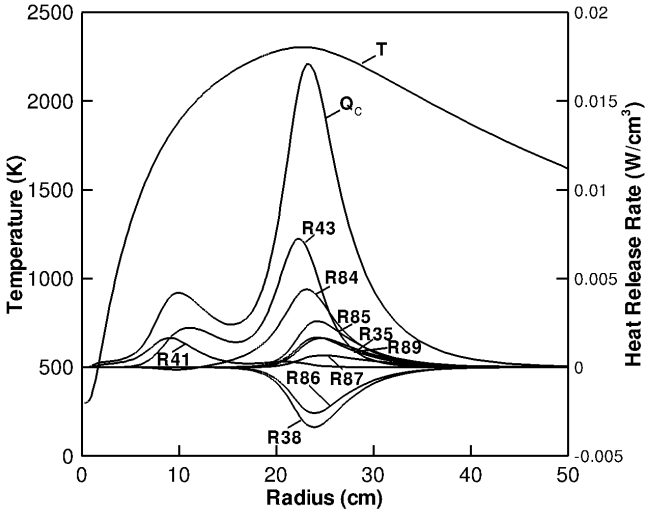


Figure 4.14: Predicted elementary reactions heat release rate for a $H_2$/air flame. Burner radius is 3.175 mm and supplied mass flow rate is set at 10 mg/s.

and 4.9. The greatest peak is located near peak temperature, while the smallest peak is located closer to the burner, at a lower temperature.

The first peak corresponds to the main location of water formation, and $H_2$ and $O_2$ depletion. The reaction

$$\text{(R43) } H + OH + M \longrightarrow H_2O + M$$

is the major contributor to the heat release rate at this location. Other less important reactions at this location are the exothermic reactions, in decreasing order of contribution:

$$\text{(R84) } OH + H_2 \longrightarrow H_2O + H,$$

$$\text{(R85) } 2\,OH + M \longrightarrow H_2O_2 + M,$$

$$\text{(R35) } H + O_2 + H_2O \longrightarrow HO_2 + H_2O,$$

$$\text{(R89) } OH + H_2O_2 \longrightarrow HO_2 + H_2O,$$

$$\text{and (R87) } OH + HO_2 \longrightarrow O_2 + H_2O.$$

The main endothermic reactions are:

$$\text{(R86) } 2\,OH \longrightarrow O + H_2O,$$

$$\text{and the chain branching reaction (R38) } H + O_2 \longrightarrow O + OH.$$

In terms of rate of progress, the importance of the reactions varies. The exothermic reaction:

$$\text{(R84) } OH + H_2 \longrightarrow H_2O + H$$

is the reaction having the highest rate of progress, followed by the endothermic chain branching reaction:

$$\text{(R38) } H + O_2 \longrightarrow O^+OH.$$

The rate of progress of these two reactions is 4 times higher than the rate of progress of the other reactions, namely:

$$\text{(R3) } O + H_2 \longrightarrow H + OH,$$

$$\text{(R35) } H + O_2 + H_2O \longrightarrow HO_2 + H_2O,$$

$$\text{(R89) } OH + H_2O_2 \longrightarrow HO_2 + H_2O,$$

$$\text{and (R43) } H + OH + M \longrightarrow H_2O + M.$$

It is interesting to note that reaction (R86) has a negative rate of progress, particularly in the high temperature region near the flame. This reaction does not play an important role in the chemistry of near extinction flames. The highly exothermic reaction

$$\text{(R43) } H + OH + M \longrightarrow H_2O + M$$

has no significant role in the chemistry of near extinction flame.

Molecular oxygen O is consumed by reactions (R35) and (R38). Molecular hydrogen H is consumed by reaction (R84). The hydroxyl radical OH is consumed within the inner part of the flame and is produced in the outer part of the flame, mostly by (R38) and by (R86).

The second and smallest peak of heat release rate corresponds to the contributions of different reactions, namely:

$$\text{(R43) } H + OH + M \longrightarrow H_2O + M,$$

$$\text{(R41) } 2\,H + H_2O \longrightarrow H_2 + H_2O,$$

and (R40) $2\,H + H_2 \longrightarrow 2\,H_2$.

Those three reactions take place at lower temperatures than the main peak. They are modeled with a zero activation energy and a weak temperature dependency. Note that at this location, reaction (R84) has a negative rate of progress, contributing to the formation of molecular hydrogen $H_2$. Also, at this location, H radicals recombine into $H_2$. Hydrogen atom radical H is mostly produced in the zone of high temperatures, with its production rate peaking near the flame location, located at a reasonable distance from its consumption location, implying that H radicals diffuse upstream before being recombined into $H_2$.

### 4.4.5 Partial Burning Regimes of $H_2$/Air Diffusion Flames

In this subsection, the characteristics of an $H_2$/air flame burning in partial burning regime are presented. This regime is characterized by an important leakage of both fuel and oxidizer across the flame. The partial burning regime is achieved considering a spherical $H_2$/air diffusion flame sustained by a 3.175 mm burner at a mass flow rate of 0.1 mg/s into quiescent air. This represents a two order of magnitude decrease in mass flow rate from the near equilibrium regime presented above.

Figures 4.15-4.18 plot the species distributions, species production rates, key reaction rates of progress, temperature, and local heat release rates of the predicted flame. This flame is at the turning point of the burning regime and corresponds to the dramatic change of slope evident in Fig. 4.10.

This flame shows a different structure than the near equilibrium diffusion flame. In this regime, a peak temperature of 2059 K is predicted. This value is higher than the temperature observed and predicted at kinetic extinction, 1300 K. The predicted heat release rate is 12.52 W, which is larger than the weak $H_2$/air flames presented above. The scalar dissipation rate at the peak temperature is $\chi_{st} = 1.6.10^{-2}$ $s^{-1}$, which is about four orders of magnitude larger than the scalar dissipation rate observed for the near-equilibrium regime flame. This regime corresponds to a lower Damköhler number. Transport time scales are diminished and start to be comparable with chemical time scales.

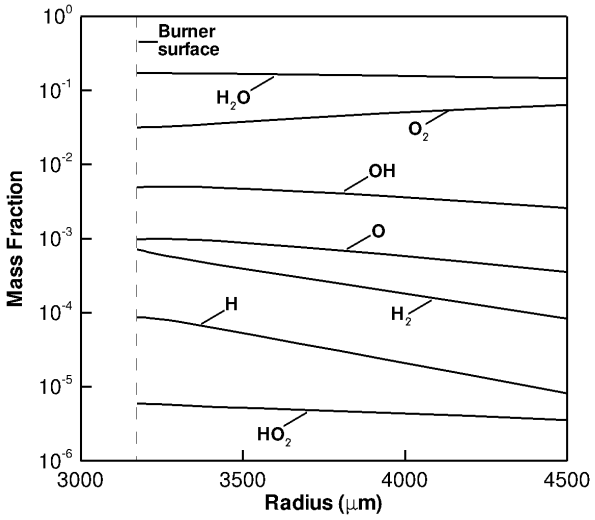


Figure 4.15: Predicted species mass fraction for a $H_2$/air flame. Burner radius is 3.175 mm and supplied mass flow rate is set at 0.1 mg/s.

The low Damköhler number of this flame brings profound changes on the flame structure. Due to the low mass flow rate, the flame is close to the burner. The peak temperature is located about 400 $\mu$m from the burner surface. The flame radius,

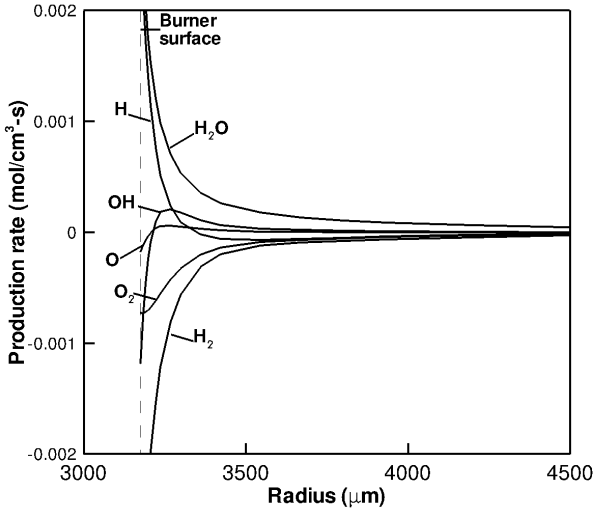


Figure 4.16: Predicted species production rate for a $H_2$/air flame. Burner radius is 3.175 mm and supplied mass flow rate is set at 0.1 mg/s.

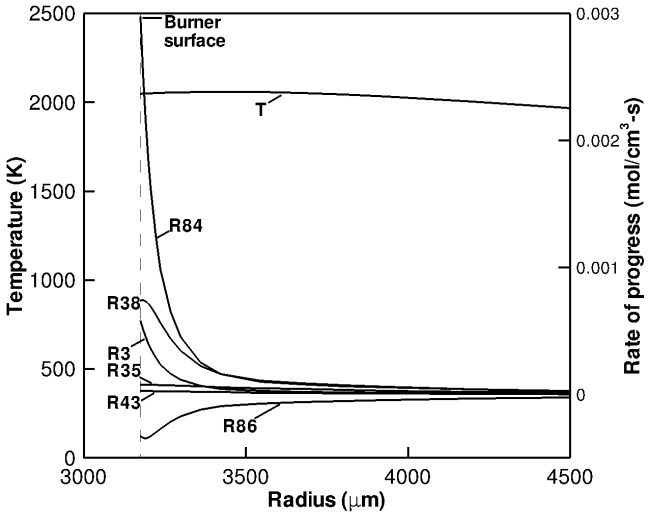


Figure 4.17: Predicted elementary reactions rate for a $H_2$/air flame. Burner radius is 3.175 mm and supplied mass flow rate is set at 0.1 mg/s.

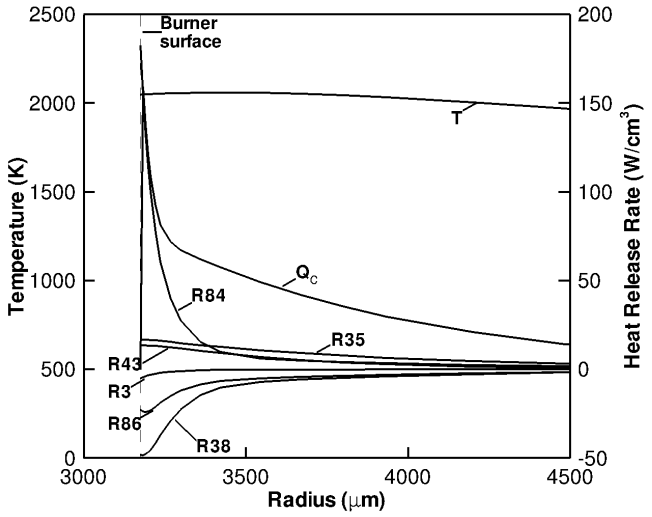


Figure 4.18: Predicted elementary reactions heat release rate for a $H_2$/air flame. Burner radius is 3.175 mm and supplied mass flow rate is set at 0.1 mg/s.

defined at the peak temperature, is then $r_f = 3.48$ mm. In fact, the theoretical flame radius should be smaller than this value. Considering Eq. (2.18), one can see that the flame radius is proportional to the mass flow rate. For a mass flow rate of 10 mg/s, the flame radius is predicted to be 22 cm. Therefore the predicted flame radius for a mass flow rate 1% as large should be about 2.2 mm, which is impossible because of the presence of the burner. Hence the truncation of the flame.

The temperature profile of the flame is relatively flat, compared to the profiles exhibited by flames at the onset of kinetic extinction. Burner surface temperature is close to 2000 K.

Significant oxygen leakage is observed for this flame. The mass fraction of $H_2$ near the burner surface is very low, less than 0.1%. This is less than the $H_2$ mass

fraction observed for hydrogen flames near kinetic extinction, about 0.01. However, a higher mass fraction of hydroxyl radical OH is observed across the flame. Its value is about 10 times higher than the value found in $H_2$/air flame at the onset of kinetic extinction, see Fig. 4.2. An important feature is the significant presence of hydroperoxy radical $HO_2$. This radical is not observed in significant proportion in the near-equilibrium regime (less than $10^{-6}$ in mass), but it is present in flames near kinetic extinction.

The heat release rate curve presents only one peak, which is located close to the burner. This corresponds to the production of $H_2O$ and H radicals. The exothermic contributors to total heat release rate are reactions:

$$\text{(R84) } OH + H_2 \longrightarrow H_2O + H,$$

$$\text{(R35) } H + O_2 + H_2O \longrightarrow HO_2 + H_2O,$$

$$\text{and (R43) } H + OH + M \longrightarrow H_2O + M.$$

This pattern tends to be similar to the pattern observed in premixed $H_2$-$O_2$ flames, with (R84) and (R35) as the key reactions [9].

The main endothermic reactions are:

$$\text{(R38) } H + O_2 \longrightarrow O + OH,$$

$$\text{(R86) } 2\,OH \longrightarrow O + H_2O,$$

$$\text{and (R3) } O + H_2 \longrightarrow H + OH.$$

Note that similarly to the near-equilibrium regime, (R86) has a negative rate of progress. However its importance is less than in near-equilibrium regime. This is due to the lower temperatures predicted across the flame.

Reaction (R84) has the highest rate of progress. This reaction is stronger than the reaction (R43), which has a higher contribution at near-equilibrium regime. The other key reactions in terms of reaction rate progress and in decreasing order of importance, are:

$$\text{(R38) } H + O_2 \longrightarrow O + OH,$$

$$\text{(R3) } O + H_2 \longrightarrow H + OH,$$

$$\text{(R35) } H + O_2 + H_2O \longrightarrow HO_2 + H_2O,$$

$$\text{and (R43) } H + OH + M \longrightarrow H_2O + M.$$

### 4.4.6 Scalar Dissipation Rate

Kinetic extinction is achieved as the mass flow rate is gradually decreased. This diminishes the flame temperature and the flame radius, as seen in Fig. 4.10. Decreasing the mass flow rate also increases the scalar dissipation rate at the flame location, $\chi_{st}$.

The evolution of scalar dissipation rate with the mass flow rate can be observed in Fig. 4.19. The scalar dissipation rate is increased by 6 orders of magnitude as the flow is decreased by 3 orders of magnitude. In Chapter 2 is provided an expression, from Mills and Matalon [24], of the reduced Damköhler number for an adiabatic spherical diffusion flame:

$$\delta_a \sim D_a \dot{m}^2. \tag{4.4}$$

From Eq. (4.4), a decrease in mass flow rate leads to a decrease in the Damköhler number. The characteristic time of transport is reduced to eventually be of the

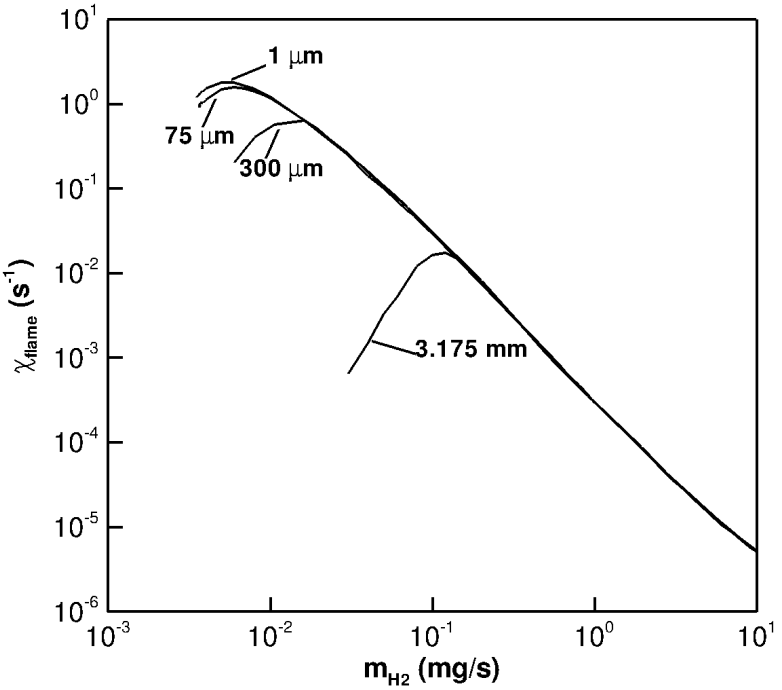


Figure 4.19: Evolution of predicted scalar dissipation rate of $H_2$/air flame with supplied mass flow rate issued for 3.175 mm, 300 $\mu$m, 75 $\mu$m, and 1 $\mu$m burners.

same order of magnitude as the chemistry time scale, and this can lead to kinetic extinction.

Scalar dissipation rate scales as the inverse of a characteristic transport time. Modeling the reaction rate with the Arrhenius law, the reduced Damköhler number can be expressed by:

$$\delta_a \sim \chi_{st}^{-1} \exp\left(-\frac{E_a}{RT_{ad}}\right), \tag{4.5}$$

with $T_{ad}$ the adiabatic flame temperature.

Because reducing the mass flow affects only the scalar dissipation rate, it can

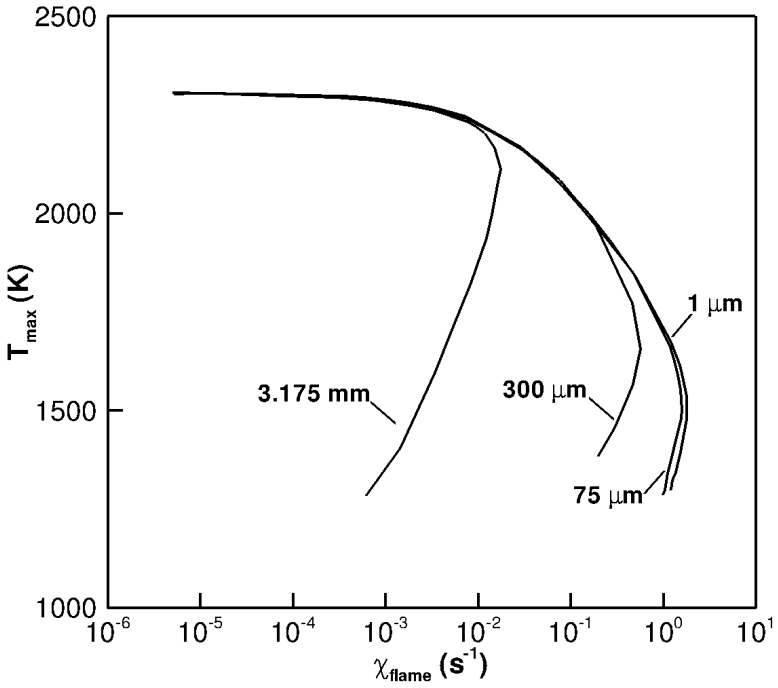


Figure 4.20: Evolution of predicted peak temperature of $H_2$/air flame with scalar dissipation rate at flame location for 3.175 mm, 300 $\mu$m, 75 $\mu$m, and 1 $\mu$m burners.

be written:

$$\chi_{st} \sim m^{-2}. \tag{4.6}$$

Plotting the peak temperature, $T_f$, against the scalar dissipation rate at its location, $\chi_{st}$, yields a S-curve as illustrated in Fig. 4.20. At low scalar dissipation rates, the peak temperature remains constant and nearly equal to the adiabatic $H_2$/air flame temperature. At this point, there is no reactant leakage across the flame. This corresponds to the near-equilibrium regime.

Reducing the mass flow rate leads to an increase of scalar dissipation rate and hence to a decrease of the Damköhler number. When $\chi_{st} > 10^{-3}$ $s^{-1}$, the flame

peak temperature starts to diminish. Increasing the scalar dissipation rate leads to flame size reductions proportional to the decrease of mass flow rate.

At some point, the flame cannot move closer to the burner even when the mass flow decreases. When this occurs, the flame position is not affected by a reduction of mass flow rate. However this decreases the velocity at the flame location, decreasing the strength of the mixing, and thus the scalar dissipation rate. This creates this backward branch, which can be taken as the middle branch of the S-curve, corresponding to partial burning conditions. This part of the curve corresponds to a flame structure with an important oxidizer leakage, as seen in Figs. 4.15-4.18.

Smaller burners present less oxidizer leakage. For the smallest burner considered, quenching occurs at the turning point of the S-curve, presenting the highest scalar dissipation rate, characteristic of kinetic extinction.

## 4.5 Summary

In this chapter, $H_2$ micro-flames were studied numerically using a spherical model. The weakest flames observed experimentally have mass flow rates as low as 3.9 $\mu$g/s for the $H_2$/air flames, and 2.1 $\mu$g/s for the $H_2/O_2$ flames, corresponding to heat release rates of 0.46 W and 0.25 W, respectively.

The weakest flames observed numerically, with a burner radius matching the experimental dimensions, have mass flow rates of 3.65 $\mu$g/s for the $H_2$/air flame and 2.67 $\mu$g/s for the $H_2/O_2$ flame, corresponding to heat release rates of 0.4 W and 0.31 W, respectively. Those value are in reasonable agreement with the experimen-

tally measured quenching limits.

Kinetic extinction, arising from hydrogen mass flow rate reduction, was numerically observed for adiabatic flames. For the larger burners, the presence of the burner prevents the flames from moving inward when the flow rate is reduced, resulting in truncated flames. This forces extinction at higher flow rates even under adiabatic conditions, and high level of oxidizer leakage across the flame are observed.

The flames are predicted to extinguish at high scalar dissipation rate. At the onset of extinction, it is predicted $\chi_{st}$ =1 $s^{-1}$ for $H_2$/air flames, and $\chi_{st}$ =2 $s^{-1}$ for $H_2/O_2$ flames. This represents an increase by 6 orders of magnitude from the predicted value of the near-equilibrium $H_2$/air diffusion flame at $\dot{m}$ = 10 mg/s. Because heat losses are neglected in this study, the flames predicted are at the onset of pure kinetic extinction.

The main reactions contributing to the flame heat release rate differ with the Damköhler number. Flames with high Damköhler number present a double peaked heat release rate profile. The main exothermic reactions are, in order of contribution to the heat release rate:
the chain terminating reaction:

$$H + OH + M \longrightarrow H_2O + M$$

and the chain propagating reaction:

$$OH + H_2 \longrightarrow H_2O + H$$

for the main peak, and the chain-terminating reaction:

$$2\,H + H_2O \longrightarrow H_2 + H_2O$$

and the chain propagating reaction:

$$OH + H_2 \longrightarrow H_2O + H$$

the for the second and smallest peak.

Flames with low Damköhler number do not present a double peaked heat release rate profile but a single peak profile, with the maximum heat release rate close to the burner. The main exothermic reactions are, in order of contribution to the heat release rate:

the chain propagating reactions:

$$H + O_2 + H_2O \longrightarrow HO_2 + H_2O,$$

$$OH + H_2 \longrightarrow H_2O + H,$$

and the chain-branching reaction

$$H + HO_2 \longrightarrow 2\,OH.$$

The hydroperoxy radical $HO_2$ plays an important role in those flames.

The main endothermic reaction, which absorbs a part of the heat released by exothermic reactions, is the chain-branching reaction:

$$H + O_2 \longrightarrow O + OH.$$

Its contribution remains the same regardless of the Damköhler number.

# Chapter 5

# Spherical Diffusion Flames at their Sooting Limits

In this chapter, the numerical model is used to investigate the fundamental problem of sooting limits of ethylene spherical diffusion flames. This chapter first provides a general discussion on the phenomenology of soot formation and destruction in flames. Secondly, a description of the experimental characterization of 17 sooting limit spherical diffusion flames follows. Those 17 flames were investigated numerically. The results of this investigation are presented in this chapter.

## 5.1 Background

### 5.1.1 Introduction

Soot is a major pollutant produced by combustion. It can be formed in the combustion of virtually all fuels, except hydrogen. Soot formation in flames is a very active research area and some extensive review articles can be found [93–100].

Soot is formed in flames of many industrial combustors and open fires. Being

a major pollutant and a health hazard, the emission of soot is aimed to be reduced, if not completely eliminated, in engines and industrial combustors. In terms of efficiency, soot is responsible for large fractions of the radiative heat loss in luminous flames, decreasing the efficiency of a combustor and damaging it. In large-scale fires, radiation due to the presence of soot is responsible for the growth and spread of secondary fires.

The structure of soot particles in both premixed and nonpremixed flame is similar. Soot particles consist of nearly spherical primary particles that form aggregates. These primary particles are relatively small, with sizes ranging between 5 to 80 nm. The properties of soot are similar to the properties of carbon blacks. Their density is between 1820 - 2050 kg/m$^3$ [100]. They consist almost exclusively of carbon, except for young soot particles. Indeed, for an aged particle, the atomic carbon to hydrogen ratio, C/H, ranges from C/H = 8.3 - 18.3, the atomic carbon to oxygen ratio, C/O ranges from 58 - 109, and the atomic carbon to nitrogen ratio ranges from 292 - 976 [101].

### 5.1.2 General Aspects of Soot Formation and Oxidation

Soot particles are produced on the fuel rich side of flame. Fuel pyrolysis produces smaller hydrocarbons, in particular acetylene ($C_2H_2$), which is a major contributor to the formation of aromatic species like benzene ($C_6H_6$), and larger polycyclic aromatic hydrocarbons (PAH) species. Even though soot inception is still a domain of controversy, it is generally accepted that acetylene and PAHs are

major precursors of soot particles [98].

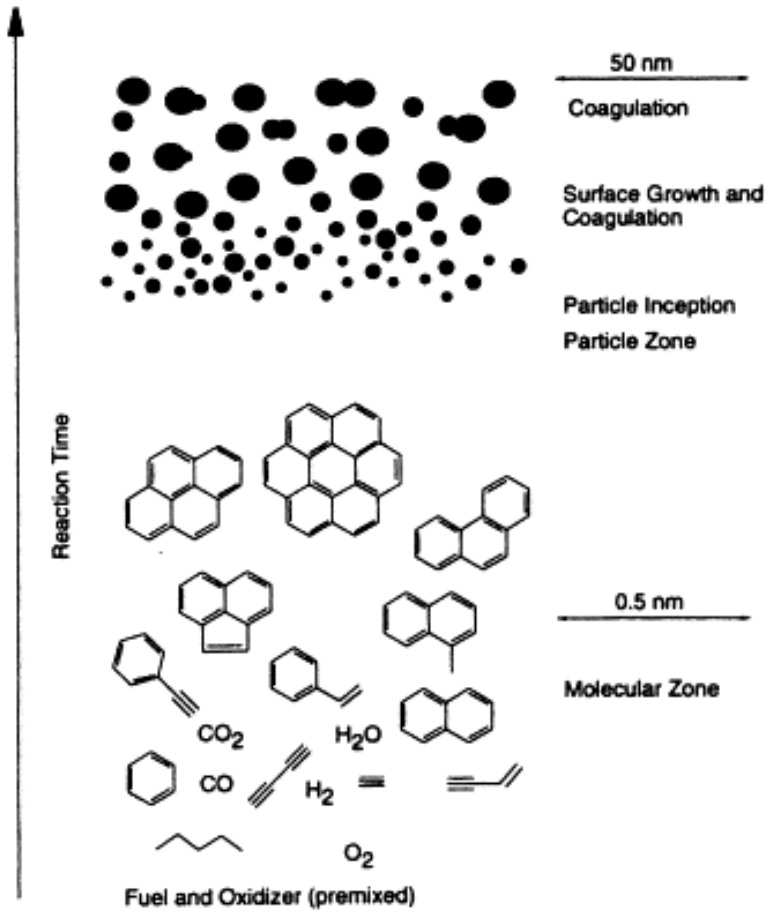


Figure 5.1: Soot formation in homogeneous mixture. From [93].

The initial transformation from gaseous molecules to solid particles *via* PAH precursors is called particle inception or nucleation. Once soot particles are formed, they can grow through two mechanisms: surface growth and coagulation. A schematic of soot formation processes is shown in Fig. 5.1. The commonly accepted concurrent processes in soot formation/oxidation are [102]:

(a) formation of soot precursors,

(b) particle nucleation,

(c) particle coagulation and aggregation,

(d) surface growth,

(e) particle oxidation.

Each of these processes is explained in the following sections.

## 5.2 Description of Soot Formation and Oxidation

This section provides details of soot formation and oxidation. Since soot formation results from the creation of soot precursors, which are large polycyclic aromatic hydrocarbon molecules, a description of the mechanisms involved in PAH creation is also provided.

### 5.2.1 Ethylene Pyrolysis

In the combustion of ethylene ($C_2H_4$) with air, the carbon found in soot particles originates from ethylene. The first reaction step is triggered by abstraction of a hydrogen atom from the fuel molecule [9, 62]. In a fuel-lean environment and at high temperatures, $C_2H_4$ is more likely to be attacked by O radical through:

$$C_2H_4 + O \longrightarrow CH_3 + HCO. \tag{5.1}$$

In fuel-rich environment, $C_2H_4$ is consumed by H and OH, producing vinyl $C_2H_3$ radical:

$$C_2H_4 + H \longleftrightarrow C_2H_3 + H_2, \tag{5.2}$$

$$C_2H_4 + OH \longleftrightarrow C_2H_3 + H_2O. \tag{5.3}$$

In fuel-rich conditions, the highly reactive vinyl reacts to form acetylene through the reactions:

$$C_2H_3 + (H, O_2) \longrightarrow C_2H_2 + (H_2, HO_2), \tag{5.4}$$

$$C_2H_3 + M \longleftrightarrow C_2H_2 + H + M. \tag{5.5}$$

Equation (5.5) is an endothermic reaction. Acetylene is a major intermediate species in hydrocarbon fuels burning in fuel-rich conditions. Its formation is favored by the significant amount of entropy it creates, 128.9 J/mol-K at 1600 K [9]. This results in a negative Gibb's function value, favoring equilibrium toward the product side, with the corresponding equilibrium constant, $K_p$ greater than unity ($\sim 200$).

Acetylene plays a dominant role in soot growth by surface addition. It is also the starting species for the formation of the first aromatic ring [95]. A basic description of benzene formation in ethylene flames is provided below.

### 5.2.2 Formation of the First Aromatic Ring

The formation of the first ring, at least in ethylene flames, is perceived as the rate-limiting reaction to further development of larger molecules. The first aromatic ring is formed by the decomposition of $C_2H_4$ into lighter elements as shown

above. Starting from $C_2H_2$ and vinyl radical ($C_2H_3$), different pathways lead to the formation of the first ring, being either benzene ($C_6H_6$) or phenyl ($C_6H_5$).

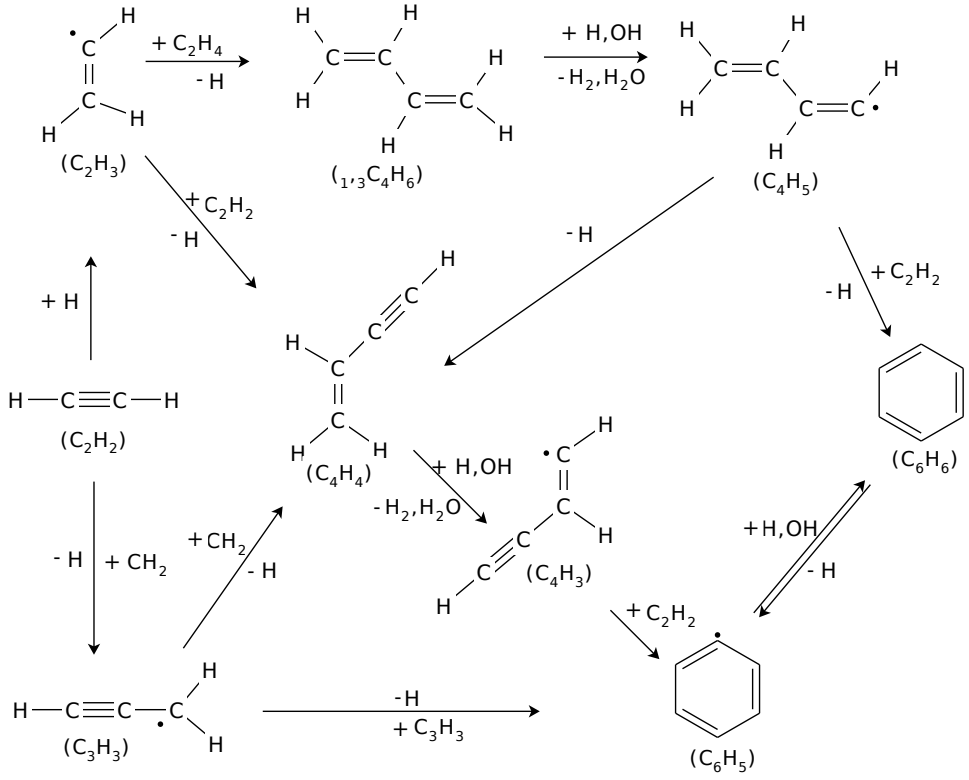


Figure 5.2: Selected pathways of benzene formation in ethylene combustion. Adapted from [9, 103].

Figure 5.2 displays some of these pathways. Note the important role played

by acetylene and H radical. Namely, the pathways suggested are:

$$C_4H_3 + C_2H_2 \longrightarrow C_6H_5, \tag{5.6}$$

$$C_4H_5 + C_2H_2 \longrightarrow C_6H_6 + H, \tag{5.7}$$

$$C_3H_3 + C_3H_3 \longrightarrow C_6H_5 + H, \tag{5.8}$$

$$C_5H_5 + CH_3 \longrightarrow C_6H_6 + H + H, \tag{5.9}$$

$$C_3H_3 + C_2H_2 \longrightarrow C_5H_5. \tag{5.10}$$

It is not completely understood which of the above pathways is the leading reaction producing the first ring. Frenklach [98] suggests, based on results from shock tube acetylene pyrolysis, that Eqs. (5.6) and (5.7) are the dominant pathways whereas Miller and others [98] suggest that combination of propargyl radical ($C_3H_3$) *via* Eq. (5.8) is more likely to be the main pathway, thanks to the stability of $C_3H_3$ radicals. However, in ethylene diffusion flames, the relative importance of those two pathways are similar, as shown in the work of Sun *et al.* [104].

Finally the reaction of formation of cyclopentadienyl ($C_5H_5$), Eq. (5.10), can be a major contributor to benzene formation for temperatures above 1700 K. It can be 2000 times faster than Eq. (5.8) [98]. Cyclopentadienyl recombines with methyl radical ($CH_3$) to form benzene. The other pathway proposed by Marinov and Castaldi is the combination, and rearrangement of cyclopentadienyl radicals to form naphthalene:

$$C_5H_5 + C_5H_5 \longrightarrow C_{10}H_8 + 2\,H. \tag{5.11}$$

### 5.2.3 Growth of PAH

The further growth of PAH is thought to proceed mainly through two mechanisms: the H-abstraction-$C_2H_2$-addition (HACA) mechanism and by direct ring-ring condensation. The competition between the two is largely determined by the nature of the fuel.

The HACA mechanism consists of two distinct steps. The first step is the activation of a ring site by abstraction of a hydrogen atom by a hydrogen radical (H). The second step is the addition of an acetylene molecule to the radical site, forming then either a new ethynyl ($C_2H$) group with the aromatic ring or a new aromatic ring when an ethynyl group is already present.

The HACA mechanism can be described by [9]:

$$\mathrm{Ai} + \mathrm{H} \rightleftharpoons \mathrm{Ai}^- + \mathrm{H}_2, \tag{5.12}$$

$$\mathrm{Ai}^- + \mathrm{C}_2\mathrm{H}_2 \rightleftharpoons \mathrm{AiC}_2\mathrm{H}_2, \tag{5.13}$$

$$\mathrm{AiC}_2\mathrm{H}_2 + \mathrm{C}_2\mathrm{H}_2 \rightarrow \mathrm{Ai}_1^+ + \mathrm{H}. \tag{5.14}$$

Figure 5.4 is an illustration of this mechanism in the formation of pyrene from benzene. The first step in the HACA mechanism, hydrogen abstraction, is reversible. The second step, however, may not be reversible. This seems to be the case in the formation of stable aromatics, i.e. stabilomers. Stabilomers play an important role in the growth of PAH due to their relative stability. An example of stabilomer is pyrene ($C_{16}H_{10}$). Stabilomers are also thought to be responsible for the nucleation of soot particles.

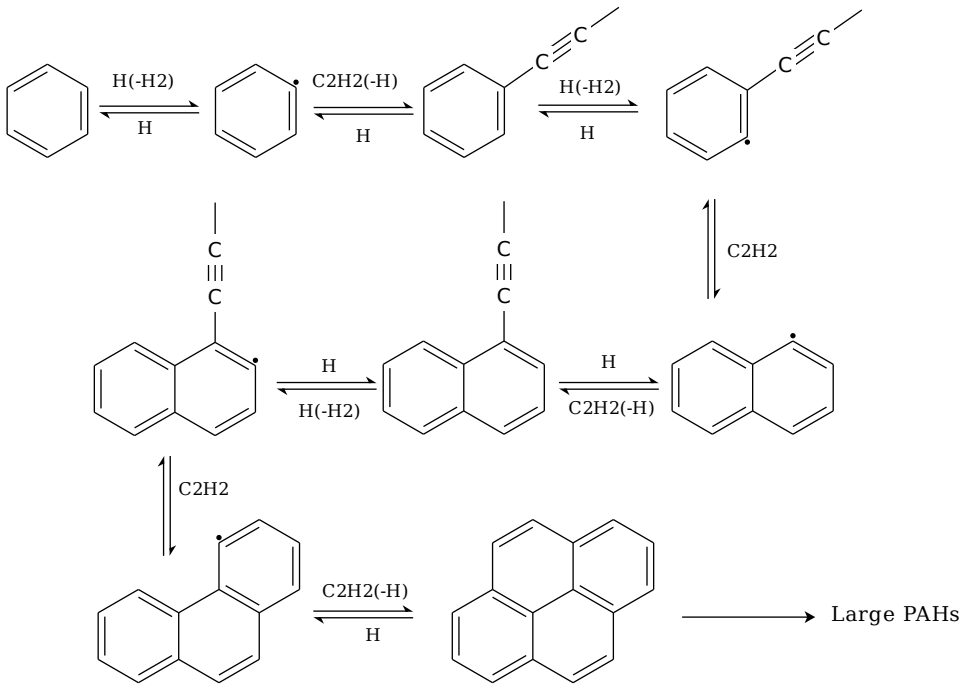


Figure 5.3: The H-abstraction-$C_2H_2$-addition (HACA) mechanism of PAH formation. Adapted from [9].

In addition to the two growth mechanisms mentioned above, other mechanisms are suggested for the formation of cyclic molecules up to at least 3 rings. It has been suggested that the cyclopentadienyl ($C_5H_5$) pathway to naphthalene ($C_{10}H_8$) and phenanthrene ($C_{10}H_{14}$) can be significant in ethylene flames [102]. The contribution of phenyl-substituted propargyl molecules to the formation of larger PAH has been shown to be significant [102]. However, comparing the pyrolysis of different fuels, Frenklach *et al.* [105] concluded that the pathways leading to the creation of larger molecules in the pyrolysis of every fuel always relax to the HACA mechanism, the fuel structure having an influence only at the early stages of the PAH formation.

### 5.2.4 Particle Nucleation

Particle nucleation, which describes the transition from gas-phase species to solid particles, is still not well understood. When a PAH molecule reaches a certain size, it may stick to another PAH molecule, forming a PAH dimer. PAH dimers collide with PAH molecules forming PAH trimers or with other dimers forming PAH tetramers, and so on [98]. As a practical measure, the formation of dimers is assumed to mark emergence of the soot particles. Nascent soot particles are assumed to have spherical shapes. Many detailed soot formation models consider the dimerization of pyrene ($C_{16}H_{10}$) as the initial nucleation step for particles. It has been demonstrated that this is a realistic approach [106].

The particle nucleation rate $R_0$, modeled here considering only the contribution of pyrene through coalescent collision, can be expressed by the following:

$$R_0 = \frac{1}{2}\beta_{C_{16}H_{10}} N^2_{C_{16}H_{10}}, \tag{5.15}$$

with $N_{C_{16}H_{10}}$ the number of pyrene particles per volume, and $\beta_{C_{16}H_{10}}$ the frequency factor given by:

$$\beta_{C_{16}H_{10}} = 2.2\sqrt{\frac{8\pi k_B T}{\frac{1}{2}m_{C_{16}H_{10}}}} d^2_{C_{16}H_{10}}, \tag{5.16}$$

where the factor before the square root sign is the Van der Waals enhancement factor.

The rate of nucleation is important since it is responsible for the increase of soot particle concentration.

### 5.2.5 Particle Growth

Larger soot particles are formed by coagulation with other soot particles and by mass addition through surface reaction and PAH condensation.

Nascent soot particles are spherical, and later acquire a fractal shape [95]. In coalescent coagulation, two particles collide due to their Brownian motion and coalesce completely, resulting in a new spherical particle of higher mass. This process does not change the total mass of soot present but decreases the number of soot particles.

The mathematical treatment of an ensemble of soot particles undergoing this process is described by the Smoluchowski master equations [107]. The rate of evolution of particles of size $k$ is described by the equation:

$$\frac{dN_k}{dt} = \frac{1}{2}\sum_{i=1}^{k-1} \beta_{i,k-i} N_i N_{k-i} - N_k \sum_{i=1}^{\infty} \beta_{i,k} N_i. \tag{5.17}$$

The collision frequency function depends on the size of the colliding particles, the local temperature, and pressure. The Knudsen number of a particle, $K_n$, is the ratio of the mixture mean free path, $l$, divided by particle radius, $r$, and thus depends on the thermodynamic state of the medium. It is expressed by: $K_n = \dfrac{l}{r}$.

If the Knudsen number is much greater than unity, then the free-molecular regime prevails. The expression of the collision frequency function $\beta_{i,j}$ is expressed by [108]:

$$\beta_{i,j} = \epsilon \left(\frac{3}{4\pi}\right)^{\frac{1}{6}} \sqrt{\frac{6k_B T}{\rho_s}\left(\frac{1}{V_i} + \frac{1}{V_j}\right)} \left(V_i^{\frac{1}{3}} + V_j^{\frac{1}{3}}\right)^2, \tag{5.18}$$

where $\epsilon$ represents the contribution of the Van der Waals forces, $V_i$ represents the volume of particles of size $i$, and $\rho_s$ is the density of the soot particles.

When the Knudsen number is smaller than unity, the continuum regime prevails. The collision frequency function $\beta_{i,j}$ becomes:

$$\beta_{i,j} = \frac{2k_B T}{3\eta}\left(\frac{C_i}{V_i^{\frac{1}{3}}} + \frac{C_j}{V_j^{\frac{1}{3}}}\right)\left(V_i^{\frac{1}{3}} + V_j^{\frac{1}{3}}\right), \tag{5.19}$$

with $\eta$ the viscosity of the mixture and $C$ the Cunningham slip correction factor, which is given by [109]:

$$C = 1 + 1.257K_n. \tag{5.20}$$

At some location in the flame, agglomeration of soot particle with chain-like structure begins. It is suggested that this process does not occur before a certain 'maturity' of the particle. Those chain like structures can be analyzed in terms of fractal geometry [98]. This change of geometry modifies the dynamics of the particles and their transport properties.

Addition of soot mass through PAH condensation, and acetylene addition through the HACA mechanism, strongly affects the carbon mass accumulated in soot [95, 110]. It is postulated that the surface growth by acetylene addition occurs through the same process involed in PAH growth, *via* chemical similarity. The surface of a soot particle is then assumed to resemble the edge of a large PAH molecule, covered with C-H bonds. This allows the description of surface reaction as elementary reaction and provides a generic rate of reaction for surface growth and oxidation. Similar to the gas-phase HACA mechanism, activation of radicals through H abstraction is needed. It has been shown that, while the concentration of H radical does not have an effect on soot surface growth when in high concentration, at low concentration it can hinder significantly the growth rate of soot particles [111].

Surface reactivity of soot particles is not constant but declines with the extent of surface growth [95, 98], a phenomenon named soot surface aging. This is attributed to the decrease of hydrogen radicals, as mentioned above, and to a decrease in the number of active sites capable of sustaining growth. The latter is attributed to the formation of surface defects. Attempts to model soot surface aging have lead to the introduction of a steric factor, $\alpha$, in the expression of surface reaction rates [67]. The steric factor can be expressed as a function of temperature and particle size [67], and it models the diminution of active surface sites.

The expression of the rate of surface reaction of a soot particle of size $k$ with acetylene becomes:

$$\dot{\omega}_{soot} = k_s[C_2H_2]\alpha\dot{\chi}_S S_k N_k, \tag{5.21}$$

where $\dot{\chi}_S$ represents the number density of activated surface sites, $S_k$, and $N_k$ the surface area and the number density of the $k^{th}$ particle, respectively. The per-site rate coefficient $k_s$ can be modeled through an Arrhenius equation. In their numerical model, Appel *et al.* [67] gives the following value for the per-site rate coefficient: $A = 8.0 \times 10^{13}$ cm$^3$/mol-s, $n = 1.56$, $E_a = 3.8$ kcal/mol, with $k_s = AT^n \exp\left(-\frac{E_a}{RT}\right)$.

### 5.2.6 Particle Oxidation

Oxidation of soot particles competes with surface growth. It is the only process that reduces the total amount of soot. Oxidation of soot particles occurs predominantly by $O_2$ molecules and OH radicals.

Neoh *et al.* [112] found that OH was the principle surface oxidant of soot.

The surface oxidation with OH was found to be weakly temperature dependent and based on a collision efficiency, with a value of 0.13 - 0.28.

Soot production can be limited by oxidizing soot precursors, e.g., aromatics. Numerical simulations in diffusion flames have shown that $O_2$ plays a major role, whereas OH plays only a minor role in oxidizing aromatics [98]. Also, the oxidation of $C_2H_3$ is one the key points of branching between carbon growth and carbon oxidation.

## 5.3 Elements Influencing Soot Presence in Flames

### 5.3.1 Local C/O Model, a Premixed Flame Concept Applied to Diffusion Flames

As mentioned above, net soot formation in flames arises from the competition between soot formation involving carbon containing species and soot oxidation, along with PAH oxidation, which involves oxygen containing species. Among the factors involved in such processes, the dominance of either species greatly influences soot formation. A simple and common way to assess this dominance is the use of local Carbon to Oxygen atom ratio or C/O ratio, defined as:

$$\frac{C}{O} = \frac{\sum N_{C,i}[X_i]}{\sum N_{O,i}[X_i]} \tag{5.22}$$

In the past, most data on fundamental sooting limits came from studies of laminar premixed flames [94–96, 113–115]. One reason for this is that both temperature and C/O are nearly constant in the soot-forming regions of premixed flames.

It was found that soot inception in premixed flames cannot occur when C/O is below a critical value, about 0.6 for ethylene [94–96, 113, 115] with an adiabatic flame temperature of 2200 K. In premixed flames, increasing the temperature enhances soot suppression. The critical value of C/O ratio, denoted $C/O_{cr}$ depends on the fuel structure, and especially on its carbon to hydrogen atom ratio. Fuels with lower C/H ratios tend to form less soot.

A similar competition between formation and oxidation, can occur on the fuel side of a diffusion flames due to the presence of oxygen in species such as $CO_2$ and $H_2O$ [55, 116]. Du *et al.* [116] shown that the addition of $CO_2$ to the fuel side of diffusion flames can suppress soot formation.

Despite the differences between soot inception in premixed and nonpremixed flames, the local C/O atom ratio has been shown to be relevant to describe sooting limits in diffusion flames [55, 117]. Past experimental work on spherical diffusion flames in microgravity identified a critical local C/O value of 0.59 for ethylene [55].

### 5.3.2 Effects of Temperature on Soot Formation

Temperature plays a different role in premixed and nonpremixed flames. It has been shown experimentally [96,115] that increasing temperature suppresses soot formation in premixed flames, favoring soot precursor oxidation reactions. In nonpremixed flames, an increase of temperature enhances the formation of soot in some regions of the flame. Previous studies on diffusion flames have identified an onset temperature at which soot particles are first observed to be in the range of 1250 -

1650 K [42, 96, 118–120].

### 5.3.3 Effects of Mixing Time

In addition to C/O ratio and temperature, residence time (or mixing rate) is also critical to soot inception limits. Soot induction times of 0.8 - 15 ms were reported by Tesner and Shurupov [121] for acetylene/nitrogen mixtures at 1473 K. Strain rates of 30 - 200 $s^{-1}$ were observed to prevent soot formation in counterflow diffusion flames [27,122]. Figure 5.4 plots the evolution of the maximum soot volume

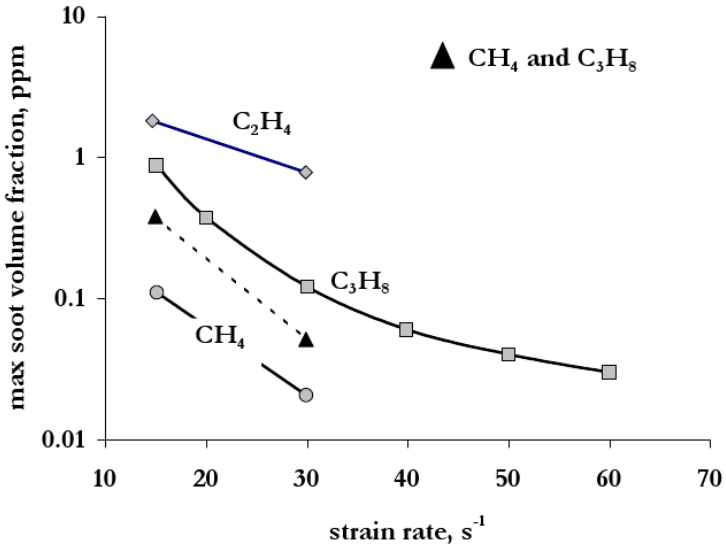


Figure 5.4: Experimental strain rate-dependences of soot volume fraction. From [123].

fraction produced in counterflow diffusion flames of acetylene, propane, and methane [123]. This is a good illustration of the effects of strain rate on soot fomation in diffusion flame. An increase of strain rate, and thus a decrease in the local characteristic time of mixing, leads to a decrease of the soot quantity present inside

the flame because soot kinetics are slower than gas-phase reactions in flames.

## 5.4 Experimental Observation of Sooting Limit Spherical Diffusion Flames

Transient spherical diffusion ethylene flames at their sooting limits have been characterized by Sunderland *et al.* [55]. This reference [55], presents 17 different flames of ethylene burning in microgravity. Microgravity was obtained in the NASA Glenn 2.2 s drop tower. These transient flames reached their sooting limits 2 s after the beginning of the drop.

The experimental apparatus was the same as in references [42,54,55]. A 6.4 mm diameter porous spherical burner was used to inject fuel or oxidizer at various level of nitrogen dilution, into a quiescent environment of either fuel or oxidizer at 295 K. The burner was positioned at the center of a cylindrical chamber whose diameter, length, volume were 25 cm, 53 cm, and 26 liters, respectively. The pressure was assumed constant across the vessel, taken as 0.98 bar. Ignition was performed immediately after release into microgravity using a Nichrome wire of 12 mm length and 0.36 mm diameter. The tests employed three gases: ethylene, nitrogen, and oxygen. A color video camera was used to image the flames.

The characteristics of the 17 sooting limit flames are presented in Table 5.1. Burner flow rates were selected such that all flames involved a steady-state ethylene consumption rate of 1.51 mg/s, which generates 71 W, assuming complete combus-

tion.

Table 5.1: General characteristics of the 17 experimentally identified sooting limit flames, from [55].

| Flame | Configuration | $X_{C_2H_4,1}$ | $X_{O_2,0}$ | $Z_{st}$ | $t_{res}$,s | $T_{ad}$,K | $T_f$,K |
|---|---|---|---|---|---|---|---|
| 1 | Normal | 1.0 | 0.22 | 0.065 | 2.72 | 2390 | 1545 |
| 2 | Normal | 0.6 | 0.21 | 0.102 | 1.63 | 2326 | 1492 |
| 3 | Normal | 0.31 | 0.21 | 0.18 | 0.91 | 2226 | 1479 |
| 4 | Normal | 0.25 | 0.23 | 0.225 | 0.665 | 2238 | 1498 |
| 5 | Normal | 0.18 | 0.28 | 0.333 | 0.351 | 2306 | 1592 |
| 6 | Normal | 0.17 | 0.29 | 0.353 | 0.33 | 2308 | 1593 |
| 7 | Normal | 0.11 | 0.5 | 0.586 | 0.11 | 2381 | 1795 |
| 8 | Normal | 0.11 | 0.8 | 0.685 | 0.044 | 2528 | 2057 |
| 9 | Normal | 0.15 | 1 | 0.661 | 0.024 | 2740 | 2262 |
| 10 | Inverse | 1 | 0.13 | 0.041 | 0.059 | 1847 | 1581 |
| 11 | Inverse | 0.8 | 0.13 | 0.051 | 0.072 | 1835 | 1549 |
| 12 | Inverse | 0.6 | 0.13 | 0.066 | 0.086 | 1814 | 1515 |
| 13 | Inverse | 0.21 | 0.25 | 0.277 | 0.119 | 2274 | 1689 |
| 14 | Inverse | 0.19 | 0.3 | 0.336 | 0.122 | 2370 | 1736 |
| 15 | Inverse | 0.15 | 0.5 | 0.509 | 0.148 | 2539 | 1802 |
| 16 | Inverse | 0.12 | 0.8 | 0.666 | 0.279 | 2578 | 1729 |
| 17 | Inverse | 0.13 | 1 | 0.692 | 0.249 | 2670 | 1814 |

Normal and inverse conditions are associated with environments of oxidizer and fuel, respectively. The fuel and oxygen mole fractions in the supply gases, $X_{C_2H_4,0}$ and $X_{O_2,0}$, vary widely. This yields a wide range of stoichiometric mixture fraction, $Z_{st}$, as shown in Table 5.1. The mixture fraction $Z_{st}$ is defined for $C_2H_4$ flames, by the following relation:

$$Z_{st} = \frac{Y_{O_2,0}}{Y_{O_2,0} + \frac{24}{7} Y_{C_2H_4,1}}, \tag{5.23}$$

where $Y_{O_2,0}$ denotes the mass fraction of oxygen supplied on the oxidizer side and $Y_{C_2H_4,1}$ the mass fraction of the ethylene supplied on the fuel side.

Adiabatic flame temperatures reported in Table 5.1 were calculated using

Chemical Equilibrium with Applications, CEA [124]. Flame temperatures shown are the code predictions at 2 s, the ignition being taken as the starting point of the simulation. Further descriptions of the *modus operandi* of the numerical simulations are provided below.

The 17 sooting limit flames have soot from the ignition point until 2 s. At 2 s, these flames reached their sooting limits. The assessment of soot presence was made by video observations of the yellow luminous region. This method has been proven to be a relatively good indicator of the presence or absence of soot particles [27] in flames.

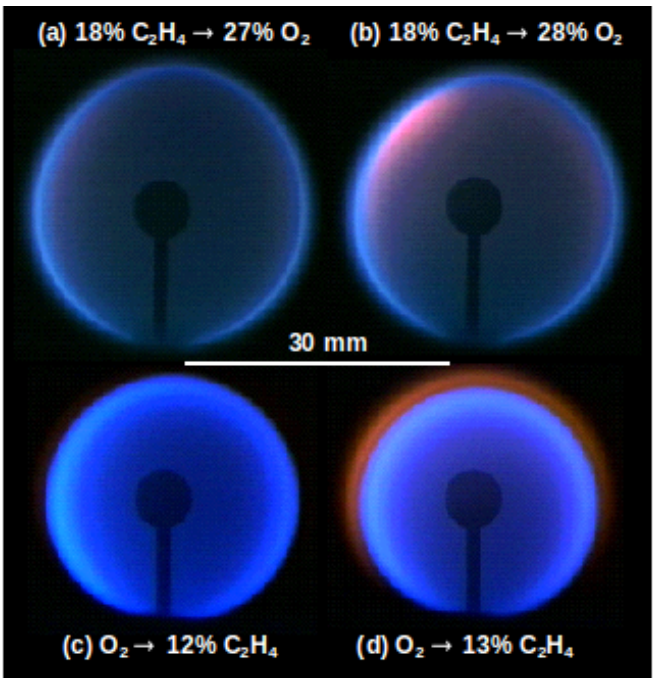


Figure 5.5: Color images of representatives flames below the sooting limits (a and c) and at sooting limits (b and d) for convection toward oxidizer (a and b) and convection toward fuel (c and d). Flames (b) and (d) correspond to Flames 5 and 17 in Table 5.1. Images were taken just before drop termination.

Four representative flames at or near their sooting limits are shown in Fig. 5.5. These flames represent both convection toward oxidizer (normal flames) and convection toward fuel (inverse flames). The flames (b) and (d) of Fig. 5.5 are considered here to be at their experimental sooting limits because a small reduction in reactant concentration yields blue conditions at 2 s. Note that soot, when present, appears inside the flame sheet for normal flames and outside the flame sheet for inverse flames. Those images were taken 2 s after the beginning of the drop.

## 5.5 Numerical Simulations of Sooting Limit Spherical Diffusion Flames

This study seeks to further investigate the effects of local C/O atom ratio, local temperature, and residence time on sooting limits of spherical diffusion flames. The 17 spherical diffusion flames summarized in Table 5.1 were simulated using the code described in Chapter 3. Since the object of this work is to investigate these flames at their sooting limits, only gas phase chemistry is modeled. Details of the numerical simulations are presented below.

### 5.5.1 Strategy

The 17 flames considered in this work reached their stooting limits 2 s after the beginning of the drop. Their behavior is inherently transient. Therefore, a transient approach should be considered to investigate the 17 flames and their conditions

associated at their sooting limits. The computation requires a set of initial conditions that resemble the experimental ignition process. Following the approach mentioned in Chapter 3, the initial (ignition) conditions were prescribed as the steady-state solution of the same flame obtained in a compressed domain. Flames were assumed to be adiabatic, and a constant temperature at the outer boundary was assumed. The compressed domain was chosen to extend 1.2 cm from the burner center.

The steady-state computations began with a set of prescribed initial distributions of grid points, temperature, species concentrations, and an estimate of the location and thickness of the reaction region. The chemistry models used for the simulations were GRI-Mech 3.0 and the ABF model [67]. Most of the results presented below use the ABF model. Note both models give similar results for the main flame characteristics.

Once the steady-state solution was obtained, the grid was adapted to reduce the gradients and curvature to improve accuracy. New grid points were added until all the values of the gradients and curvature were below the user specified limits, and further addition of grid points did not affect the solution. Typically, about 70 - 80 mesh points were used.

The steady state solution on the compressed domain was then used as the initial condition for the transient computations. The computational domain was extended to 15 cm from the center of the burner by adding grid points to fill the gap between the compressed and extended domains. All the transient computations used a grid of about 200 - 300 mesh points, finer in the area of high gradients (flame location), and coarser near the outer boundary. Test cases were run to ensure

grid independence. Typically, about 120 extra mesh points were added from the compressed to the extended domain. The initial conditions at those extra mesh points were user specified values for the outer boundary. The radiation model was turned on to simulate the transient solution and the burner temperature was kept constant at 300 K.

Predictions 2 s after ignition were emphasized to better understand the conditions associated with the observed sooting limits. The flames modeled covered both normal and inverse configurations for a wide range of residence time, stoichiometric mixture fraction, and adiabatic flame temperature.

### 5.5.2 Temporal Evolution

The temporal evolution of spherical diffusion flames temperature and flame radius can be found in Appendix B for all the flames investigated, in Figs. B.1-B.17. The temporal evolution of Flame 17 is shown in Fig. 5.6. The flame radius is defined as the radius where temperature peaks. The chemistry model used for this prediction is the ABF model [67].

The proximity of the cold outer boundary in the compressed (ignition) domain promotes conductive heat losses, reducing the peak temperature below its adiabatic value. Immediately after ignition, the absence of conductive heat losses at the outer boundary increases the flame temperature. The radius decreases before increasing again. The measurements and computations indicate that neither flame size nor peak temperature reaches steady state within 2 s for any of the present flames.

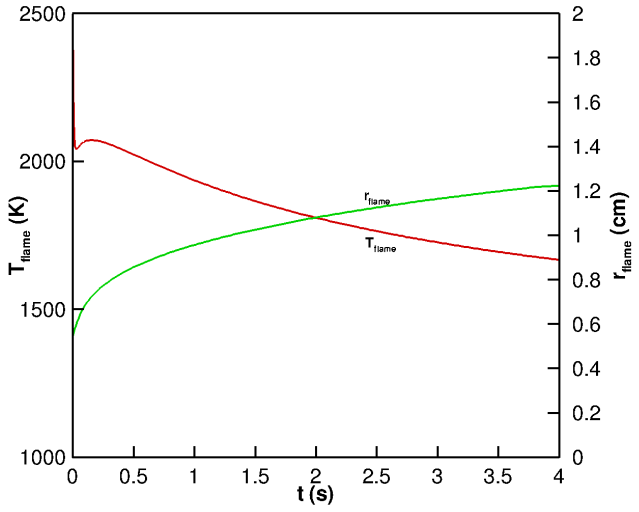


Figure 5.6: Predicted flame radius and peak temperature of Flame 17, from ignition (t = 0 s) to 4 s.

Flame expansion causes temperatures to drop owing to increased radiative losses, which are proportional to flame surface area [42].

At 2 s, the radiative heat loss fractions are around 0.42 for all flames except Flames 10, 11, and 12, whose heat loss fractions are about 0.28. Flame expansion is a critical aspect of all these flames. A similar evolution occurs for flame temperature. For the flames of Table 5.1, peak flame temperatures at 2 s span a broad range of 1479 - 2262 K. These temperatures are too high to cause radiative extinction at 2 s [42].

### 5.5.3 Effects of Residence Time

The 17 flames presented in Table 5.1 reach their sooting limits 2 s after ignition. Therefore their structures at this time is of particular interest. The present

study aims to identify the combined relationship between the local C/O ratio, the temperature, and mixing effects at sooting limits. A critical C/O ratio of 0.6 has been identified for ethylene premixed flame [94–96, 113, 115]. Therefore this value is a logic starting point to identify a possible relationship between temperature and mixing time. As a preliminary study, the flame residence time is taken as the characteristic mixing time.

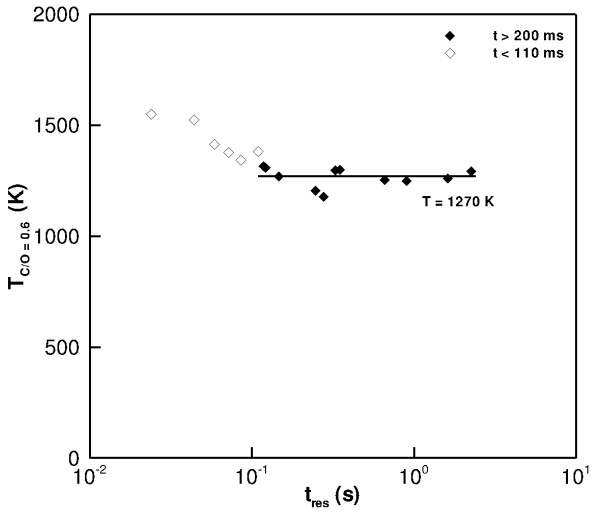


Figure 5.7: Predicted temperature at location of C/O = 0.6 as a function of residence time at 2 s for the 17 sooting limits flames.

Local temperature where the local C/O ratio is found equal to 0.6, predicted with GRI-Mech 3.0 for the 17 flames, is reported in Fig. 5.7 and plotted against the flame residence time.

Figure 5.7 reveals that for long residence times the critical temperatures are similar, while for short residence times increased temperatures are required to reach sooting limits. The data suggests, for the present flames, that short and long res-

idence times vis-à-vis soot inception are those less than 110 ms, and longer than 200 ms, respectively. Note that these flames vary by over two orders of magnitude of residence time. For long residence time flames, the average $T_{C/O=0.6} = 1270$ K. This is in reasonable agreement with the previously measured soot inception temperature in diffusion flames [42, 96, 118–120]. Figure 5.7 also shows a trend between temperature and mixing time.

It is of interest to study the impact of $Z_{st}$ on these flames. Previous studies have shown that an increase of $Z_{st}$ inhibits soot formation when the adiabatic flame temperature is kept constant [54, 55, 117, 125].

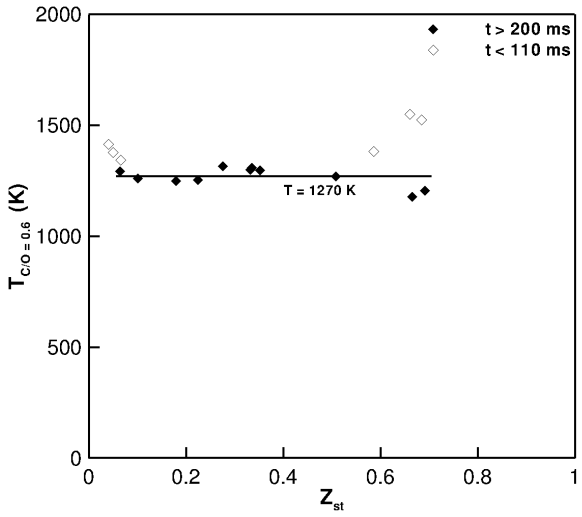


Figure 5.8: Predicted critical sooting limit temperatures against $Z_{st}$.

Figure 5.8 plots the predicted temperature of Fig. 5.7 versus the flame $Z_{st}$. For flames with long residence times (represented with solid symblos), Fig. 5.8 shows that the temperature at the expected location of soot inception is not strongly dependent

on $Z_{st}$. Note that this finding does not contradict the previous findings of Axelbaum and coworkers [54, 55, 117, 125]. Indeed, $Z_{st}$ determines the relative location of the soot inception area with respect to the flame location and changes the temperature profile in the vicinity of the soot inception area. Keeping the flame temperature constant but increasing $Z_{st}$ decreases the temperature at the critical location, defined by the local value of C/O. This is predicted by the equation proposed by Sunderland *et al.* [55] linking the flame temperature, $Z_{st}$, the inception temperature $T_c$, and the critical local C/O ratio using a Burke-Schumann approximation on the fuel side, as formulated by Eq. (5.24):

$$\frac{T_{flame} - T_f}{1 + Z_{st}\left[3\left(C/O_{cr}\right) - 1\right]} = T_c - T_f. \tag{5.24}$$

The paradigm considered here is that soot inception is only affected by the species (chemistry), temperature, and residence time at a given location. Therefore it is expected that $Z_{st}$ will not have an influence on the fundamental characteristics of soot inception for the 17 sooting limits flames. Observations from the preliminary work go in this direction.

Several points need further investigations. In particular the value of the critical C/O ratio needs to be assessed for this flame configuration. Moreover, the use of residence time as a characteristic time scale needs to be redefined. This is the main focus of the next subsection.

### 5.5.4 A Suitable Mixture Fraction Model

The previous section used residence time as a characteristic time scale. Residence time describes the average time for a fluid particle issued from the burner to reach the flame location, which is defined by the peak temperature. While this concept is representative of the time allowed for soot inception in normal flames, this is not the case in inverse flames. In inverse flames, residence time defined this way represents the time for a particle of oxidizer to travel from the burner to the flame location, and therefore it is not representative of the time provided for soot inception reactions, since these reactions are found in the outside layers surrounding the flame.

A local time scale independent of the flow direction and with a common meaning for normal and inverse flames is needed. Although spherical diffusion flames are strain-free, their scalar dissipation rates are not zero. As with strain, high scalar dissipation rate can impede soot inception. The expression of scalar dissipation rate, denoted $\chi$, in a spherical diffusion flame is derived in Chapter 3. Its expression is recalled here:

$$\chi = 2\alpha \left( \frac{\partial Z}{\partial r} \right)^2 . \tag{5.25}$$

Since unity Lewis number is assumed in the derivation of its expression, the local thermal diffusivity coefficient can be used to compute the local scalar dissipation rate. The mixture fraction profile, $Z(r)$, needs to be known in order to assess accurately the local value of $\chi$.

Recall that mixture fraction $Z$ is defined by:

$$Z = \frac{Y_F - \frac{1}{r_S}Y_{\mathrm{O}_2} - Y_{F,ox} + \frac{1}{r_S}Y_{\mathrm{O}_2,ox}}{Y_{F,f} - \frac{1}{r_S}Y_{\mathrm{O}_2,f} - Y_{F,ox} + \frac{1}{r_S}Y_{\mathrm{O}_2,ox}}, \tag{5.26}$$

with

$$r_S = \frac{\nu W_{\mathrm{O}_2}}{W_F}. \tag{5.27}$$

For the combustion of a general hydrocarbon $\mathrm{C}_n\mathrm{H}_m$ with air, the combustion reaction is expressed by:

$$\mathrm{C}_n\mathrm{H}_m + (n + \frac{m}{4})\mathrm{O}_2 \rightarrow n\mathrm{CO}_2 + \frac{1}{2}\mathrm{H}_2\mathrm{O}, \tag{5.28}$$

therefore $r_S$ becomes:

$$r_S = \frac{n + \frac{m}{4}W_{\mathrm{O}_2}}{W_{\mathrm{C}_n\mathrm{H}_m}}. \tag{5.29}$$

Equation 5.26 can be rearranged to account for detailed chemistry. Indeed, it is preferable to write $Z$ as a function of the atomic mass fractions of carbon, oxygen, and hydrogen, which are also conserved scalars. To conserve the stoichiometric value of $Z$ at the flame location, the variable $Y_{\mathrm{C}_n\mathrm{H}_m}$ is expressed as a function of $Y_{\mathrm{C}}$ and $Y_{\mathrm{H}}$, and $Y_{\mathrm{O}_2}$ is expressed as a function of $Y_{\mathrm{O}}$.

Because all the carbon atoms originate from the fuel $\mathrm{C}_n\mathrm{H}_m$, at the burner surface:

$$Y_{\mathrm{C}} = \frac{nW_{\mathrm{C}}}{W_{\mathrm{C}_n\mathrm{H}_m}}Y_{\mathrm{C}_n\mathrm{H}_m}, \tag{5.30}$$

and:

$$Y_{\mathrm{H}} = \frac{mW_{\mathrm{H}}}{W_{\mathrm{C}_n\mathrm{H}_m}}Y_{\mathrm{C}_n\mathrm{H}_m}. \tag{5.31}$$

Combining Eqs. (5.30) and (5.31) gives:

$$Y_{\mathrm{C}_n\mathrm{H}_m} = 0.5W_{\mathrm{C}_n\mathrm{H}_m}\left(\frac{Y_{\mathrm{H}}}{mW_{\mathrm{H}}} + \frac{Y_{\mathrm{C}}}{nW_{\mathrm{C}}}\right), \tag{5.32}$$

while $Y_{O_2}$:

$$Y_{O_2} = \frac{W_{O_2}}{2W_O} Y_O. \tag{5.33}$$

Inserting Eqs. (5.32) and (5.33) into Eq. (5.26) gives:

$$Z_{CHO} = \frac{\dfrac{Y_H - Y_{H,ox}}{mW_H} + \dfrac{Y_C - Y_{C,ox}}{nW_C} + \dfrac{Y_{O,ox} - Y_O}{\left(n + \frac{m}{4}\right) W_O}}{\dfrac{Y_{H,f} - Y_{H,ox}}{mW_H} + \dfrac{Y_{C,f} - Y_{C,ox}}{nW_C} + \dfrac{Y_{O,ox} - Y_{O,f}}{\left(n + \frac{m}{4}\right) W_O}}. \tag{5.34}$$

For ethylene, Eq. (5.34) becomes:

$$Z_{CHO} = \frac{\dfrac{Y_H - Y_{H,ox}}{4W_H} + \dfrac{Y_C - Y_{C,ox}}{2W_C} + \dfrac{Y_{O,ox} - Y_O}{3W_O}}{\dfrac{Y_{H,f} - Y_{H,ox}}{4W_H} + \dfrac{Y_{C,f} - Y_{C,ox}}{2W_C} + \dfrac{Y_{O,ox} - Y_{O,f}}{3W_O}}. \tag{5.35}$$

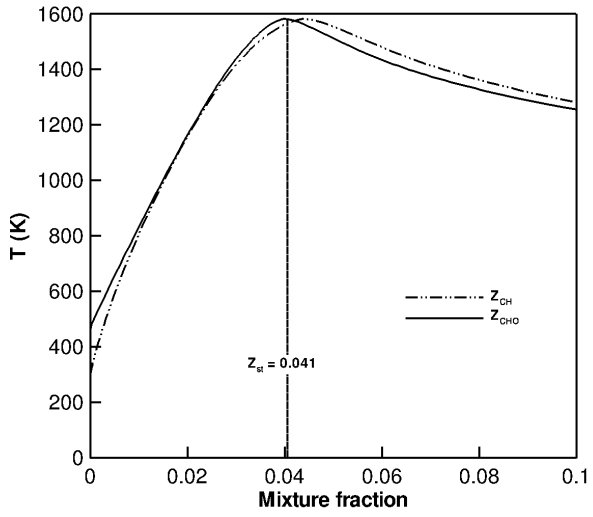


Figure 5.9: Predicted temperatures of Flame 10 plotted with respect to mixture fraction. Two definitions of mixture fraction are shown: $Z_{CH}$ and $Z_{CHO}$. Results are at 2 s after ignition.

Zhou and Mahalingam [126] evaluated various definitions of mixture fraction by plotting predicted temperature profiles with respect to mixture fraction. This approach was followed for Flame 10 in Fig. 5.9. Two definitions of mixture fraction

are considered, each yielding peak temperatures at different values of $Z$. The $Z_{CH}$ definition:

$$Z_{CH} = Y_{\mathrm{C}} + Y_{\mathrm{H}}, \tag{5.36}$$

results in peak temperature on the rich side of the flame with a $Z_{st}$ with a value of 0.041. In agreement with [126], the $Z_{CHO}$ definition of Eq. (5.35) does not have this problem, therefore it is adopted for the computation of the scalar dissipation rate for the rest of the study.

### 5.5.5 Structure at Sooting Limits

Profiles of local C/O ratio, temperature, and local scalar dissipation rate at 2 s were obtained for the 17 sooting limit flames. Figure 5.10 plots such profiles for Flame 10. Profiles for all 17 flames can be found in Appendix C. The chemistry model used was the ABF model [67]. However, due to the conserved scalar nature of $\mathrm{Y_C}$, $\mathrm{Y_H}$, and $\mathrm{Y_O}$, similar profiles were obtained when using GRI-Mech 3.0.

On the rich side, temperature increases as C/O ratio decreases and approaches 0.33, which corresponds to the location of the peak temperature. At low C/O ratio, oxygen containing species are abundant, and therefore oxidation reactions are favored over soot inception. Moreover higher temperatures are found for lower C/O ratio, on the fuel side. This contributes to the promotion of oxidation and to the decrease of PAH growth by reverse HACA reactions.

On the contrary, as the C/O ratio increases, the concentration of carbon containing species increases, and therefore soot inception is more likely to occur. How-

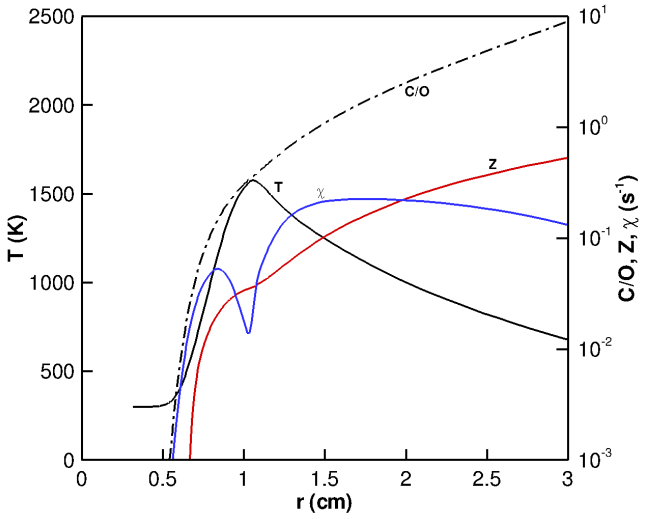


Figure 5.10: Predicted $T$, C/O, $Z$, and $\chi$ profiles from Flame 10 at its sooting limit, 2 s after ignition.

ever, for all the flames, high values of C/O ratio are found at lower temperatures, which hinders soot inception.

### 5.5.6 Critical C/O Ratio

The above study of residence time effects has shown there is a trend between the temperature at a critical location, $T_c$, and the characteristic time. It is assumed that for time scales long enough, sooting limits can be characterized by a critical temperature $T_c$, associated with the critical C/O ratio, and independent from the flame structure. Therefore at sooting limits, and at the location of critical C/O ratio, similar temperatures should be observed.

To identify the critical C/O ratio, various C/O ratios between 0.4 - 0.8 were studied. For each of the 17 flames, the associated local $T$ and $\chi$ were considered.

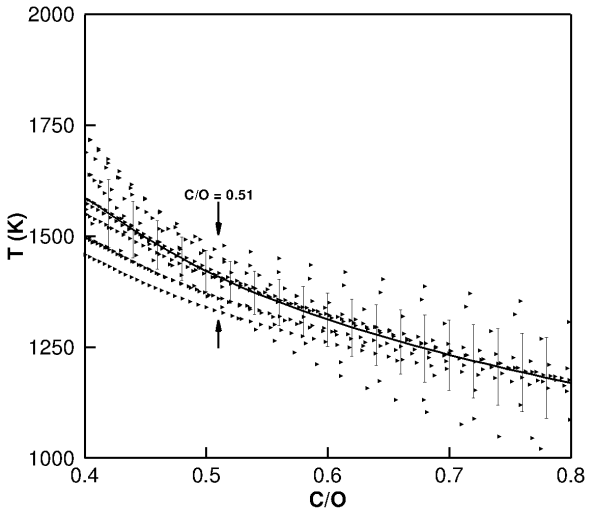


Figure 5.11: Local temperatures versus local C/O for Flames 1 - 6, and Flames 10 - 17. The vertical bars represent the associated temperature standard deviation.

For each value of C/O, the standard deviation of these temperatures was obtained, except for Flames 7, 8, and 9, since they had the highest $T$ and $\chi$ at the location of the C/O ratio considered. Figure 5.11 shows, for each of the other 14 flames, the local temperatures as a function of C/O ratio. These results were obtained using the ABF model.

An appreciable diminishing scatter can be observed in Fig. 5.11 for C/O ratio near 0.5. For improved clarity, the standard deviation of temperature is plotted against the C/O ratio in Fig. 5.12. This shows the relationship between the $T$ standard deviation and the local C/O for the flames considered in Fig. 5.11.

The temperature standard deviation has a minimum at C/O = 0.51. This is in reasonable agreement with previous reports of $\mathrm{C/O}_{crit} = 0.6$ in ethylene premixed

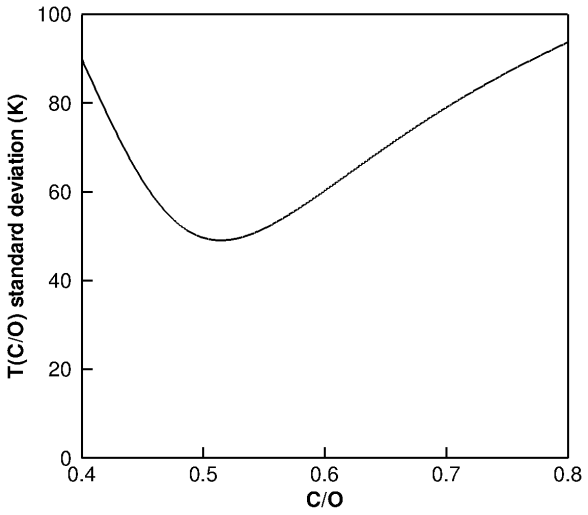


Figure 5.12: Evolution of standard deviation of $T(C/O)$ against C/O for sooting limit flames with low scalar dissipation rate.

flames [94–96,113,115]. A value of 0.59 was obtained using a simpler analysis of these spherical flames [55], and a value of 0.6 was identified for gas-jet diffusion flames [127] which was later revised to 0.53 [125]. Note that the standard deviation is not strongly dependent on the local C/O in the range of 0.45 - 0.6. The temperatures found at this location for flames with low scalar dissipation rates are similar, they correspond to the minimum temperatures needed for soot inception, and are identified here as the critical temperatures for soot inception.

### 5.5.7 Identification of Sooting Limit Conditions

The predicted temperatures associated with the local critical C/O ratio are plotted in Fig. 5.13 with respect to the inverse scalar dissipation rate found at this location. The inverse scalar dissipation rate gives a characteristic time associated

with transport processes. At the critical C/O location, this time covers a broad range, from 0.13 s (Flame 9) to 15.6 s (Flame 1).

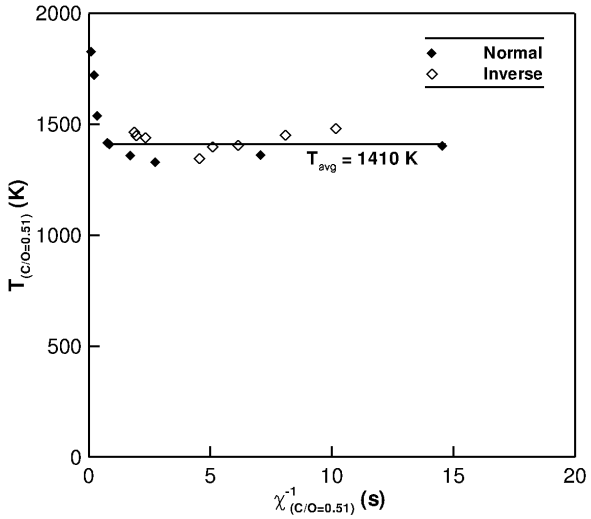


Figure 5.13: Predicted local temperatures where C/O = 0.51 versus corresponding local inverse scalar dissipation rate for normal (plain symbols) and inverse (open symbols) sooting limit flames.

The $T_c$ values are similar for most of the present flames. Excluding Flames 7 - 9, the average $T_c$ is 1410 K. The exceptions, Flames 7, 8, and 9, possess the highest local scalar dissipation rates, i.e., $1/\chi_{C/O_{crit}} < 0.5$ s, and thus reach their sooting limits at higher local temperatures. Their local temperatures increase with the local scalar dissipation rate at the location where C/O = 0.51.

Figure 5.13 reveals no statistically significant effect of the convection direction. The critical parameters are independent of flame structure, which was suggested by Fig. 5.8 and confirmed by Fig. 5.14. This figure shows the critical temperatures plotted with respect to $Z_{st}$. The critical temperature for soot inception is seen to

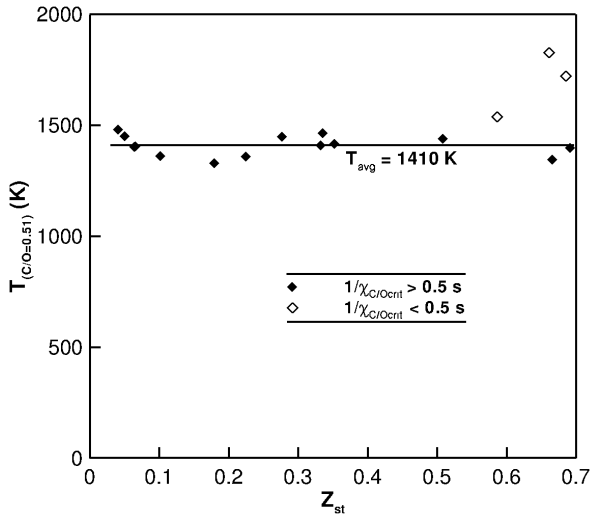


Figure 5.14: Predicted local temperature at C/O = 0.51 for the 17 sooting limits flames versus $Z_{st}$.

be independent of the flame structure (represented by $Z_{st}$) when Flames 7 - 9 are excluded.

The present 17 sooting limit flames represent a broad range of conditions in terms of fuel and oxidizer supply concentrations, $Z_{st}$, peak temperature, adiabatic flame temperature, convection direction, residence time, and scalar dissipation rate. Nevertheless, when the three flames with the highest local scalar dissipation rate are excluded, sooting limits for flames with a local scalar dissipation rate lower than 2 $s^{-1}$ occur when the local temperature at the critical C/O ratio of 0.51 is at a critical value of 1410 K.

The same conclusions hold when a different chemistry model is used. Figure 5.15 uses GRI-Mech 3.0 to plot the predicted critical temperature versus local inverse scalar dissipation rate. A similar trend with the predictions using the ABF

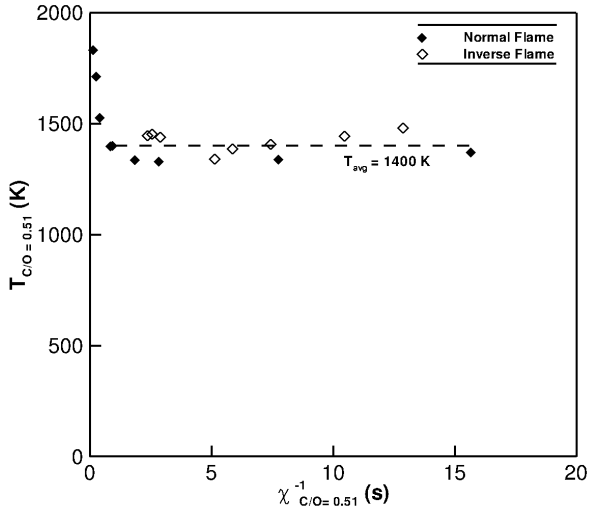


Figure 5.15: Predicted local temperatures against corresponding local inverse scalar dissipation rate for normal (plain symbols) and inverse (open symbols) sooting limit flames. Results are obtained with GRI-Mech 3.0.

model, Fig. 5.13 is found. The only noticeable difference is a slightly lower (10 K) average temperature.

Interesting insights can be gained by plotting temperatures and C/O profiles versus mixture fraction for sooting limits flames. This is shown in Fig. 5.16, where those profiles for Flames 1 and 17 are considered. Flame 1 is a normal flame whereas Flame 17 is an inverse flame.

Those two sooting limit flames have relatively low local scalar dissipation rates where C/O is 0.51. The upper limit of the second y-axis of Fig. 5.16 has been adjusted such that the horizontal line of ordinates C/O = 0.51 matches the horizontal line of T = 1410 K. For each flame, the intersection of the C/O curve with the temperature curve is located close to the line corresponding to the conditions C/O = 0.51

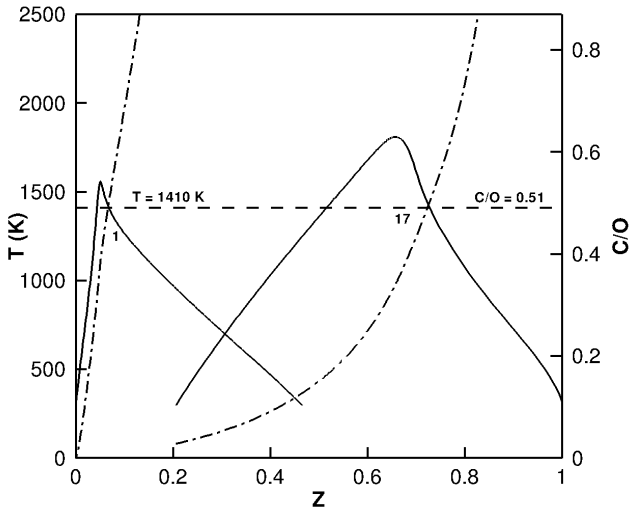


Figure 5.16: Temperature and C/O profiles in Z space for Flames 1 and 17.

and T = 1410 K. This was also observed for Flames 1 - 6 and 10 - 17.

The curves in Fig. 5.16 stop at Z = 0.5 for Flame 1 and start at Z = 0.2 for Flame 17. This is an effect of the backward species diffusion at the burner surface. This diffusion phenomenon modifies the species concentration and lowers the mass fraction of incoming reactants at the burner surface. The reference conditions for the mixture fraction calculations are obtained from user input and can be found in Table 5.1. Therefore, the mixture fraction at the burner surface is lower than 1 for normal flames, and greater than 0 for inverse flames.

In Fig. 5.17, the temperature and C/O profiles in mixture fraction space for Flame 5 at various times are considered. Flame 5 is a normal flame with $Z_{st} = 0.333$ and $T_{ad} = 2306$ K. Conditions at 0.1 and 1.0 s are sooty. This is seen experimentally, and by considering the regions where $T > T_{crit}$ and C/O > C/O$_{crit}$. At 0.1 and 1 s,

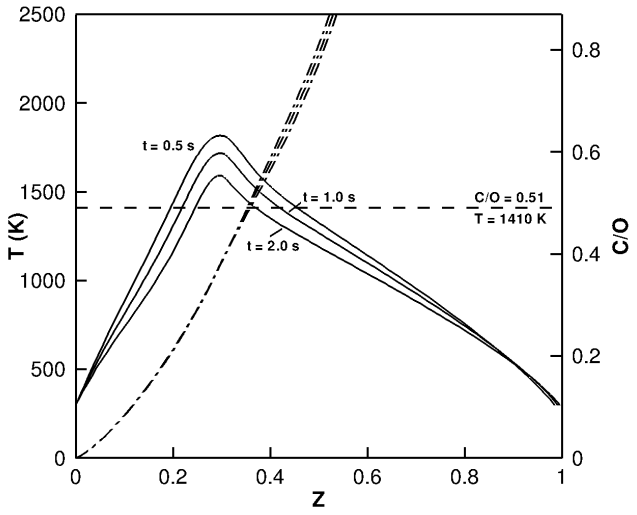


Figure 5.17: Temporal evolution of $T$ and C/O profiles in $Z$ space for Flame 5.

the area below the C/O and $T$ curves, and above the critical conditions (represented by the horizontal dashed line) is not finite. This implies the existence of a region in the flame where the C/O ratio is greater than 0.51 and the temperature is greater than the critical temperature. Consequently, those conditions allow soot formation. These conditions differ from those at 2 s, where this area is null, testifying to the flame sooting limits.

### 5.5.8 Total Production of $C_2H_2$ and $A_4$-assimilates

This section considers the temporal evolution of the total production of acetylene, pyrene, and pyrene-assimilates. Pyrene-assimilates include pyrene ($C_{16}H_{10}$) and denoted $A_4$, along with its site activated counterpart of chemical structure $A_4^-$ ($C_{16}H_9$), $A_3C_2H_2$ ($C_{16}H_{10}$), and $A_3C_2H$ ($C_{16}H_9$). As stated in the section relative to

soot inception and growth, these are key species in soot inception and growth. In particular, $A_4$-assimilates constitute the starting point for further PAH growth and soot nucleation.

Total production of these species are considered by integrating the species production rate over the whole domain. $A_4$-assimilates are identified here as $A_4$. The total production of species $k$, for a given time $t$, is given by:

$$\omega_k = \iiint_{\mathscr{X}} \dot{\omega}_k dV. \tag{5.37}$$

For each of the 17 flames, temporal evolution profiles of total production of $C_2H_2$ and $A_4$ were obtained. Those profiles are found in Appendix D, Figs. D.1-D.17.

Only gas-phase chemistry is modeled here, using the ABF and GRI-Mech 3.0 models to predict those quantities. The values of $A_4$-assimilates are overestimated since their consumption due to soot nucleation and surface growth is not considered. However, the total production can give a qualitative understanding of the mechanisms of soot inception and suppression. Positive production of PAH suggests conditions favorable for soot formation. On the other hand, a negative production suggests conditions where soot consumption is favored. Similar reasoning is valid for $C_2H_2$.

In the ABF model $A_4$-assimilates are formed through the HACA mechanism. These $A_4$-assimilates are depleted due to either favored reverse HACA reactions (mostly at high temperature) or by oxidation. The main oxidation pathways are given in Table 5.2, with their characteristics extracted from the ABF model [67].

Note: $k_f = AT^n exp(-E_a/RT)$.

Table 5.2: Selected $A_4$-assimilates oxidation reactions.

| Reaction | A ($cm^3 mol^{-1} s^{-1}$) | n | $E_a$ ($kcal/mol$) |
|---|---|---|---|
| $A_4^- + O_2 \longrightarrow A_3^- + 2\,CO$ | 2.1 x $10^{12}$ | 0.0 | 7.47 |
| $A_4 + O \longrightarrow A_3^- + HCCO$ | 2.2 x $10^{13}$ | 0.0 | 4.53 |
| $A_4 + OH \longrightarrow A_3^- + CH_2CO$ | 1.3 x $10^{13}$ | 0.0 | 10.6 |

From Figs. D.1-D.17 several observations can be made. Regardless of the flame structure, a common trend is observed. First, the production of $C_2H_2$ and $A_4$-assimilates increases until 0.5 s for all the flames. Then a decline is observed. The $C_2H_2$ profile always peaks before that of $A_4$-assimilates. The peak of production of $A_4$-assimilates decreases as $Z_{st}$ increases. A similar but less pronounced trend is observed in the production of $C_2H_2$.

Flames 1 - 6 share similar $C_2H_2$ and $A_4$ production behaviors. After 0.5 s, the total production declines in time, and eventually becomes negative. Negative production occurs between 1.8 s (flame 3) and 2.9 s (flame 6). The total production of $A_4$-assimilates always becomes negative first. Those flames present longer characteristic transport time scales.

Flames 7 and 8 do not present a negative total production of $A_4$-assimilates during the time considered. After a first peak, the total production declines steadily while remaining positive. However, the peak production for those flames is less than than the peak production value of Flame 1, by 2 orders of magnitude.

Flame 9 presents a different behavior than Flames 7 or 8, despite sharing similar scalar dissipation rates. Production of $A_4$ becomes negative about 1 s after ignition. Note that the production of $C_2H_2$ falls even more quickly. Furthermore,

the production of $A_4$ is not very high, about $2 \times 10^{-9}$ mol/s.

Inverse Flames 10 - 17 present different features than normal flames. In inverse flames, the fuel is located outside the flame, and therefore oxidation is less important because convection pushes the particles toward areas of high fuel concentration. This is depicted by the total production of $A_4$-assimilates, which peaks at a higher value (about $10^{-5}$) than in normal flames. Moreover, inverse flames do not present a negative total production of $A_4$ and $C_2H_2$. However, they do exhibit a peak of production followed by a decline. The positive production of $A_4$ is mostly attributed to the large region of high C/O ratio and low temperatures outside the flame. In fact PAH formation can be achieved at lower temperatures than soot inception. This confirms the limitation of soot formation due to low temperatures in inverse flames.

## 5.6 Summary

Computations with detailed chemistry and transport properties of spherical diffusion flames at their sooting limits were performed. Seventeen flames that have been previously observed to reach their sooting limits at 2 s in microgravity were considered. The predicted temperatures and species profiles have been investigated to advance a model of sooting limits based on local C/O, local temperature, and scalar dissipation rate.

For these flames, a critical C/O ratio has been identified to be 0.51. At this location, flames with local scalar dissipation rate lower than 2 $s^{-1}$ present similar temperatures, which average 1410 K. This finding is valid regardless of $Z_{st}$

or convection direction. This temperature represents the critical value above which soot starts to form, providing there is enough time at local C/O greater than 0.51.

Flames with a local scalar dissipation rate higher than 2 $s^{-1}$ reveal that higher temperatures at C/O = 0.51 can be achieved at sooting limits, with the temperature increasing with the local scalar dissipation rate. For those flames, higher temperatures are needed at the sooting limit to overcome the limitations imposed by short time scales.

# Chapter 6

# Detailed Numerical Modeling of Soot Kinetics in Steady Spherical Diffusion Flames

In this chapter, detailed modeling of soot formation in ethylene spherical diffusion flames is presented. The focus of this work is to first present the implementation of a detailed soot model, and second to present its application in steady state soot modeling in spherical diffusion flames.

Phenomenology of soot formation and oxidation was presented in Chapter 5. After a brief overview on the different numerical models of soot formation in Section 6.1, the soot model used in this study, based on the method of moments is presented in Section 6.2. Section 6.3 reports the implementation of this model in the code and the different validation tests performed. Section 6.4 presents the numerical results of soot formation in steady state spherical diffusion flames.

## 6.1 Numerical Models

Many models have been developed to described the formation of soot in various combustion configurations. Kennedy [128] classified the existing models into three groups:

(a) empirical models or correlations based completely on experimental data,

(b) semi-empirical models combining a mathematical description and data from experimental results, and

(c) detailed models combining a detailed description of gas-phase chemistry with an aerosol description of soot population.

### 6.1.1 Empirical and Semi-empirical Models

Empirical models were the first ones developed. They represent a computationally inexpensive but crude attempt to model soot formation for well established configurations. To model the sooting tendencies of fuels in diffusion flames, Calcote and Manos [129] proposed the use of a threshold sooting index (TSI). This index is defined, for a given fuel, by:

$$TSI = a\left(\frac{W_f}{SP}\right) + b, \tag{6.1}$$

where $a$ and $b$ are empirical constants, $W_f$ is the fuel molecular weight, and $SP$ the fuel smoke point. This model is still used and gives reasonable predictions of fuel sooting tendency [130].

Another empirical model was proposed by Khan *et al.* [131] to model soot emissions from diesel engines. Assuming constant soot primary diameter, and defining soot inception as the controlling factor of soot formation, they developped a general soot equation:

$$\frac{dC_s}{dt} = c\frac{V_u}{V_{NTP}} P_u \phi_{unburn}^n \exp\left(-\frac{E_a}{RT_u}\right), \tag{6.2}$$

where $C_s$ is the soot mass loading, $c$ and $n$ are modeling parameters, $V_u$ is the soot formation zone volume, $V_{NTP}$ the volume of the cylinder contents at normal temperature and pressure, $P_u$ the partial pressure of unburned fuel, $\phi_{unburn}$ the local unburned equivalence ratio, $E_a$ the activation energy, and $T_u$ the local temperature. Modeling parameters $c$, $n$, and $E_a$ are empirical. This method obtained good agreement [128] for different configurations.

Despite good agreement for applications for which they were developed, empirical models do not fully capture the complex physics of soot formation, and they generally cannot predict detailed soot characteristics such as soot volume fraction and soot density number.

Semi-empirical models represent an attempt to remedy these limitations by incorporating more aspects of physics and chemistry. They usually include simple kinetics models for soot precursors and soot formation without solving for the entire aerosol soot population. Most are based on a two-step mechanism to describe the evolution of soot.

This is illustrated by the pioneering work of Tesner *et al.* [132], who presented a soot model based on measurements of soot particle formation in diffusion flames

for an acetylene-hydrogen mixture. They proposed a two-step model describing the density of soot nuclei, $n$, and soot particle number density, $N$:

$$\frac{dn}{dt} = n_o + (f - g)n - g_o N n, \tag{6.3}$$

$$\frac{dN}{dt} = (a - bN)n, \tag{6.4}$$

where $n_o$ is a temperature dependent rate of spontaneous formation of soot nuclei, $f$ and $g$ are branching and termination coefficients, $g_o$ is the coagulation factor, and $a$ and $b$ are empirical constants.

Another semi-empirical model is that of Moss *et al.* [133]. Similarly to Tesner, soot formation is modeled *via* a two-step model for the soot volume fraction $f_v$ and the soot number density $N$. Thoses equations are coupled assuming mono-sized spherical particles. Using a flamelet approach, the model is written as a function of mixture fraction $Z$:

$$\frac{d}{dt}\left(\frac{n}{N_{av}}\right) = \alpha(Z) - \beta(Z)\left(\frac{n}{N_{av}}\right)^2, \tag{6.5}$$

$$\rho_s \frac{df_v}{dt} = \gamma(Z)n + \delta Z, \tag{6.6}$$

with the soot density $\rho_s$ taken to be 1800 kg/m$^3$. The particle source terms for nucleation $\alpha(z)$, coagulation $\beta(Z)$, surface growth $\gamma(Z)$, and nucleation $\delta(Z)$ are

given below:

$$\alpha = C_\alpha \rho^2 T^{\frac{1}{2}} X_f \exp\left(-\frac{T_\alpha}{T}\right), \tag{6.7}$$

$$\delta = 144\alpha, \tag{6.8}$$

$$\beta = C_\beta T^{\frac{1}{2}}, \tag{6.9}$$

$$\gamma = C_\gamma T^{\frac{1}{2}} X_f \exp\left(-\frac{T_\gamma}{T}\right), \tag{6.10}$$

with $X_f$ the fuel mole fraction. The constants $C_\alpha$, $C_\beta$, and $C_\gamma$ need to be experimentally determined in laminar flames, along with the activation temperatures $T_\alpha$ and $T_\beta$. This model was later improved to include the effects of soot oxidation by OH [134].

A similar model was developed by Lindstedt [53,135] for laminar and turbulent diffusion flames. In this model acetylene is assumed to be primarily responsible for the nucleation and the growth of particles. In particular the nucleation step is treated by a one-step reaction:

$$\mathrm{C_2H_2} \longrightarrow 2\,\mathrm{C_{soot}} + \mathrm{H_2}.$$

Kaplan *et al.* [136] modeled soot formation in a flickering methane/air diffusion flame. They used the model of Moss [133] for soot formation. This model was coupled with an optically thin radiation model. Ezekoye *et al.* [52] modeled soot formation in spherical diffusion flames using a semi-empirical model based on Fairweather *et al.* [53] for soot nucleation and growth based on $C_2H_2$ addition, and oxidation by $O_2$. They also included soot oxidation by OH using Moss model [133].

Other semi-empirical soot models have been developed to model soot formation

in various applications such as fires [137] and diesel engines [138]. Lautenberger and de Ris [137] developed a semi-empirical model relating the peak soot formation rate with fuel laminar smoke point to predict soot formation in fires.

### 6.1.2 Detailed Soot Models

Empirical and semi-empirical models of soot formation are generally limited to a particular class of flames. Detailed soot models overcome this by providing a more fundamental description of the physics and chemistry of soot formation. The downside of detailed models is the increased computational time. Detailed soot models comprise two distinct parts. The first part consists of a gas-phase reaction mechanism and includes soot precursor kinetics. The second part is an aerosol model describing the dynamics of soot particles, including soot nucleation, coagulation, surface growth, and oxidation. The role of the aerosol model is to predict the dynamic evolution of the particle population, characterized by its particle size density function (PSDF), typically without assuming *a priori* its shape.

#### 6.1.2.1 Aerosol Modeling

Soot particles in flames constitute a polydisperse aerosol. Because soot particles are made mostly of carbon, models generally characterize soot particles by the number of carbon atoms they contain. For a given location $r$ of space and at a given time $t$, the soot population is described by a discrete PSDF function ($N_k(r,t)$), with $N_k(r,t)$ describing the number of particles with $k$ carbon atoms at the location $r$

anf for the time $t$. The number $N_\infty(r,t)$ of soot particles per unit volume is then given by:

$$N_\infty(r,t) = \sum_{k=1}^{\infty} N_k(r,t). \tag{6.11}$$

The rate of change in the discrete PSDF with time, due to nucleation, coagulation, growth, oxidation, and transport is given by the General Dynamic Equation (GDE) for each class $k$, $N_k$:

$$\frac{\partial N_k}{\partial t} + \nabla.N_k\vec{U} - \nabla.D_k\nabla N_k + \nabla.\vec{U}_T N_k = \left[\frac{\partial N_k}{\partial t}\right]_{nucleation} \left[\frac{\partial N_k}{\partial t}\right]_{coagulation} + \left[\frac{\partial N_k}{\partial t}\right]_{growth} + \left[\frac{\partial N_k}{\partial t}\right]_{oxidation}, \tag{6.12}$$

with $\vec{U}_T$ the thermophoretic velocity. This velocity is induced by the presence of temperature gradients. As a result, the particles are driven toward lower temperature regions. For particles with a large Knudsen number, $K_n \gg 1$ (free molecular regime), the thermophoretic velocity is given by [108]:

$$\vec{U}_T = -\frac{3\nu}{4\left(1+\frac{\pi\alpha}{8}\right)T}\nabla T, \tag{6.13}$$

with $\alpha$ the accommodation coefficient, usually taken to be about 0.9. Thermophoretic velocity is independent of the particle size. This is not the case for the diffusion coefficient $D_k$, whose expression depends on the Knudsen number of the particles.

The diffusion coefficient $D_k$ in Eq. 6.12 is given by the Stokes-Einstein expression for the coefficient of diffusion [108]:

$$D_k = \frac{k_B T}{f}, \tag{6.14}$$

where $f$ is the friction coefficient. For a large Knudsen number, $f$ is expressed by:

$$f = \frac{2}{3}d_k^2\rho\left(\frac{2\pi k_B T}{m}\right)^{\frac{1}{2}}\left[1+\frac{\pi\alpha}{8}\right], \tag{6.15}$$

where $\rho$ is the gas density and $m$ is the molecular mass of the gas molecules.

In the continuum regime, $K_n \ll 1$, the friction coefficient is that of Stokes flow:

$$f = 3\pi\mu d_k. \tag{6.16}$$

Therefore, for small soot particles, the diffusion coefficient is proportional to $d_k^{-2}$. For larger particles, the diffusion coefficient is proportional to $d_k^{-1}$.

Recall from Eqs. 5.18-5.19 that the coagulation coefficient is:

$$\beta_{i,j} = \epsilon \left(\frac{3}{4\pi}\right)^{\frac{1}{6}} \sqrt{\frac{6k_B T}{\rho_s}\left(\frac{1}{V_i} + \frac{1}{V_j}\right)} \left(V_i^{\frac{1}{3}} + V_j^{\frac{1}{3}}\right)^2, \tag{6.17}$$

in the free-molecular regime and:

$$\beta_{i,j} = \frac{2k_B T}{3\eta}\left(\frac{C}{V_i^{\frac{1}{3}}} + \frac{C}{V_j^{\frac{1}{3}}}\right)\left(V_i^{\frac{1}{3}} + V_j^{\frac{1}{3}}\right), \tag{6.18}$$

in the continuum regime. The Cunningham slip correction factor, $C$, is given by [109]:

$$C = 1 + 1.257K_n. \tag{6.19}$$

The temporal evolution of the PSDF is obtained by solving Eq. (6.12) for each $N_k$. Direct solution of this large and coupled system of equations is generally prohibitive. However indirect methods have been developed to solve this problem: e.g., Monte-Carlo (stochastic) models, method of moments models, and sectional models. The stochastic and sectional models are briefly presented subsequently below. The method of moments is presented next.

#### 6.1.2.2 Stochastic Modeling

Recently, stochastic approaches have been developed [139–141] to solve the GDE. Those methods are based on a stochastic description of the particle ensemble. Mathematically, proofs exist that the stochastic particle system converges to the exact solution of the GDE. In these models, the processes of soot formation and oxidation are treated in a probabilistic manner, using Monte-Carlo techniques.

The Monte Carlo technique represents a population of gas particles as a collection of particles that can be tracked in time. In the model developed by Balthasar *et al.* [139], the stochastic particle method is coupled with a detailed kinetic soot model considering particle nucleation based on the dimerization of pyrene, coagulation, surface growth by $C_2H_2$ through HACA mechanism and pyrene addition, and surface oxidation by $O_2$ and OH.

The evolution of the PSDF is expressed as [140]:

$$\begin{aligned}\frac{\partial N(k,t)}{\partial t} =& R(t)\delta^*_{in} + \frac{1}{2}\sum_{j=1}^{k-1}\beta_{k-j,j}N(k-j,t)N(j,t) \\ &- \sum_{j=1}^{\infty}\beta_{k,j}N(k,t)N(j,t) \\ &+ \sum_{l=1}^{4}\left[k^l_{k-\delta(l)}N(k-\delta(l),t) - k^l_k N(k,t)\right], \end{aligned} \tag{6.20}$$

where $k^l_i$ represents the rate of the $l^{th}$ surface reaction for particles of size $i$, $\delta^*_{in}$ represents the size of the incepted particles from pyrene dimerization, and $\delta(l)$ represents the mass added or subtracted by surface reaction, with $\delta(l) = 2$ for $C_2H_2$ addition, $\delta(l) = 16$ for $C_{16}H_{10}$ addition, $\delta(l) = -2$ for $O_2$ oxidation and $\delta(l) = -1$ for OH oxidation. The rates used for these reactions are taken from Frenklach *et*

*al.* [66, 67].

Equation (6.20) is solved using a stochastic algorithm, whose flow chart is presented in Fig. 6.1.

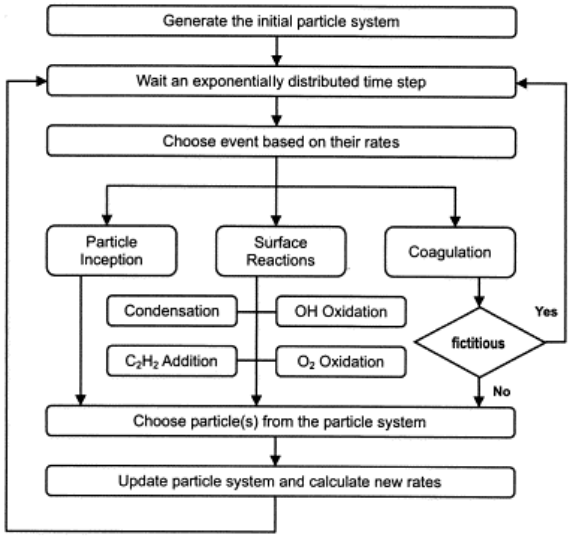


Figure 6.1: Flow chart of the stochastic particle algorithm. From [139].

The Monte-Carlo algorithm operates by first calculating the rates of inception, coagulation, condensation, surface growth, oxidation by $O_2$, and oxidation by OH. Then, using these rates, the size of the individual time step or the waiting time is determined according to an exponentially distributed random variable. Next, one of the events is chosen based on its rate.

The appropriate number of particles needed to perform this event is chosen according to the individual particle rates. Once a step is performed, the state of the particle system is updated, and a new time step is determined. This cycle is repeated until the final simulation time is reached.

The use of majorant kernels for particle event enables faster execution time.

More details about this method can be found in reference [142].

This method allows the determination of the PSDF with limited assumptions and individual particles can be tracked. However those algorithms have been used only as post-processing algorithms and their fully coupled applications with the transport equations have not been demonstrated.

#### 6.1.2.3 Sectional Method

The discrete sectional method was first developed by Gelbart *et al.* [143]. The aerosol size range is divided into a discrete number of sections $M$. Because the size range can be large ( mass variation can represent 6 orders of magnitude), a log normal distribution is generally used to defined the boundary of the different sections. For example:

$$m_l = m_0 \left( \frac{m_\infty}{m_0} \right)^{\frac{l}{M}}, \tag{6.21}$$

divides the PSDF into $M$ sections where each section $l$ is defined by its boundary masses $[m_{l-1}; m_l]$. The symbol $m_0$ is the mass of the smallest soot particle and $m_\infty$ is the mass of the largest soot particle considered.

Within each section, the soot number density function or the mass density function are assumed constant. The soot density number distribution $N(m, r, t)$ is then approximated by a set of section density numbers $(N_l)_{l=1;M}$:

$$N_l(r, t) = \frac{1}{m_l - m_{l-1}} \int_{m_{l-1}}^{m_l} N(m, r, t) dm, \tag{6.22}$$

for a continuous PSDF.

The sectional coefficients of coagulation, surface growth, and oxidation are

also calculated by integrating them over the section of interest. The advantage of this method is that for a fixed sectionalization of the PSDF, the coefficients are calculated only once. The set of GDE is then reduced to a smaller set of $M$ ordinary differential equations describing the evolution of the soot aerosol within the flame.

This method has been used by Smooke and coworkers [94, 144, 145] to model soot formation in a coflow laminar diffusion flame for which 20 sections were used. Recently, the formation of fractal-like soot aggregates with sectional models has been modeled [146].

## 6.2 Method of Moments with Interpolative Closure

In this section, details of method of moments used in this work are presented. This method has been developed principally by Frenklach and coworkers [93, 147–149]. It provides an efficient way to solve the dynamics of an aerosol population by solving the first six moments of the unknown PSDF.

This method was first used to predict the dynamic evolution of an aerosol undergoing only coagulation, but was quickly extended to soot nucleation, coagulation, surface growth, and aggregation in premixed flames [67,109,150]. Convincing results have been obtained in laminar diffusion flames [151], in diesel engine [152], and even in large eddy simulations of turbulent premixed and non-premixed flames [153,154].

### 6.2.1 Moments of a Distribution

This section provides the mathematical basis of the method of moments. Let $P$ be a probability distribution with a bounded density function $f$ over a segment $S$ of $\mathbb{R}$, associated with a random variable $X \in \mathbb{R}$. The $k^{th}$ moment $\mu_k$ of the distribution P is given by [155]:

$$\mu_k = \int_S x^k f(x)dx. \tag{6.23}$$

**Definition 4.** *The characteristic function $\varphi_X$ of the random variable $X$ is defined by:*

$$\forall t \in \mathbb{R}\,, \varphi_X(t) = \int_S e^{ix} f(x)dx. \tag{6.24}$$

**Theorem 2.** *If all the moments $\mu_k$ of $P$ exist, then each of the following conditions are sufficient for [155]:*

$$\varphi_X(t) = \sum_{k=0}^{\infty} \frac{(it)^k}{k!}\mu_k, \tag{6.25}$$

*(a)* $\forall\, t \in \mathbb{R}\ \lim_{n\to\infty} \frac{|t|^n}{n!}\mu_n = 0,$

*(b)* $\forall\, t \in \mathbb{R}\ \sum_{k=o}^{\infty} \frac{|t|^k}{k!}\mu_k < \infty,$

*(c)* $\forall\, t \in \mathbb{R}\ \int_S e^{|tx|} f(x)dx,$

*(d)* $\forall\, t \in \mathbb{R}\ \int_S e^{tx} f(x)dx.$

Since the density function $f$ is bounded over $S$, condition $(d)$ is verified. The characteristic function $\varphi_X$ is fully defined by the knowledge of all the moments. The inversion theorem, given below, relates the characteristic function of a random variable $X$ to its density function:

**Theorem 3.** *If* $\int |\varphi_X(t)|dt < \infty$ *then* $X$ *is continuous with a bounded and continuous density function* $f$ *defined by:*

$$f = \frac{1}{2\pi} \int e^{-itx} \varphi_X(t) dt. \tag{6.26}$$

Theorem 3 corresponds to the Fourier inversion theorem. It also shows that there is unicity between the characteristic function of the random variable and its density function. Moreover, the characteristic function of a random variable $X$ is defined entirely by the knowledge of all its moments. A distribution is then completely defined by all its moments and two distinct distributions cannot have the same moments.

### 6.2.2 Soot Kinetics

The present kinetic soot model is based on the kinetic model developed by Kazakov and Frenklach [109]. The gas phase kinetics are modeled with the ABF model [67], featuring pyrolysis and oxidation of $C_2H_4$, and including PAH up to pyrene $A_4$ ($C_{16}H_{10}$).

The soot particles are assumed spherical, with their mass defined by the number of carbon atoms they contain. The diameter of a soot particle of class $k$ is given by:

$$d_k = \left( \frac{6 m_k}{\pi \rho_s} \right)^{\frac{1}{3}}, \tag{6.27}$$

with the soot density taken to be $\rho_s = 1800$ kg/m$^3$.

Nucleation of soot particles is modeled as coalescent coagulation of pyrene, $A_4$. Therefore, nascent soot particles contain 32 carbon atoms. The rate of nucleation

$R$ is given by [109]:

$$R = 2.2\sqrt{\frac{4\pi k_B T}{m_{\mathrm{C_{16}H_{10}}}}} d^2_{\mathrm{C_{16}H_{10}}} N^2_{av} [\mathrm{C_{16}H_{10}}]^2, \tag{6.28}$$

where $[\mathrm{C_{16}H_{10}}]$ is the concentration of pyrene. The factor of 2.2 is the Van der Waals enhancement factor [156]. Note that this expression assumes coagulation in the free regime for pyrene. The diameter of $\mathrm{C_{16}H_{10}}$ is obtained through the formula [109]:

$$d_{\mathrm{C_{16}H_{10}}} = d_A \frac{4\sqrt{6}}{3}, \tag{6.29}$$

with $d_A$ the size of a single aromatic ring, $d_A = 2.416$ Å.

Coagulation by coalescent collisions is assumed. The collision frequency $\beta_{i,j}$ between soot particles of $i^{th}$ and $j^{th}$ class depends on their Knudsen numbers, $K_n$, defined by:

$$K_n = \frac{2\lambda}{d_k}, \tag{6.30}$$

where $d_k$ is the diameter of particles of class $k$ and $\lambda$ is the gas mean free path. In the free molecular regime (*i.e.,* $K_n \gg 1$), the collision frequency $\beta^f_{i,j}$ is given by [147]:

$$\beta^f_{i,j} = 2.2\sqrt{\frac{6k_B T}{\rho_s}} \left(\frac{3}{4\pi\rho_s}\right)^{\frac{1}{6}} \sqrt{\frac{1}{m_i} + \frac{1}{m_j}} \left(m_i^{\frac{1}{3}} + m_j^{\frac{1}{3}}\right)^2. \tag{6.31}$$

In the continuum regime, $K_n \ll 1$, the collision frequency $\beta^c_{i,j}$ is expressed by [109]:

$$\beta^c_{i,j} = \frac{2k_B T}{3\eta} \left(\frac{C_i}{m_i^{\frac{1}{3}}} + \frac{C_j}{m_j^{\frac{1}{3}}}\right) \left(m_i^{\frac{1}{3}} + m_j^{\frac{1}{3}}\right), \tag{6.32}$$

with $\eta$ the viscosity of the mixture and $C$ the Cunningham slip correction factor, which is given by [109]:

$$C = 1 + 1.257 K_n. \tag{6.33}$$

The evaluation of the coagulation coefficient for the transition regime, $1 < K_n < 10$ is also treated, but at the moment level. Its expression is presented in the next section.

Growth and oxidation of soot particles by surface reactions is modeled considering the surface reactions of mass addition by $C_2H_2$ through HACA mechanism and by $A_4$ surface condensation, and oxidation by $O_2$, OH.

The surface growth and oxidation by $C_2H_2$ and $O_2$ is assumed to be analogous, on a per site basis, to the corresponding gaseous rate of PAH species. Table 6.1 reports the reactions and their associated constants, extracted from [67].

Table 6.1: Surface growth mechanism. From [67]

| No. | Reaction | A $(cm^3mol^{-1}s^{-1})$ | n | $E_a$ $(kcal/mol)$ |
|---|---|---|---|---|
| $S_1$ | $C_{soot}{-}H + H \longrightarrow C_{soot}\cdot + H_2$ | 4.14 x $10^{13}$ | | 13.0 |
| $S_{-1}$ | $C_{soot}\cdot + H_2 \longrightarrow C_{soot}{-}H + H$ | 3.9 x $10^{12}$ | | 11.0 |
| $S_2$ | $C_{soot}{-}H + OH \longrightarrow C_{soot}\cdot + H_2O$ | 1.0 x $10^{10}$ | 0.734 | 1.43 |
| $S_{-2}$ | $C_{soot}\cdot + H_2O \longrightarrow C_{soot}{-}H + OH$ | 3.68 x $10^{8}$ | 1.139 | 17.1 |
| $S_3$ | $C_{soot}\cdot + H \longrightarrow C_{soot}{-}H$ | 2.0 x $10^{13}$ | | |
| $S_4$ | $C_{soot}\cdot + C_2H_2 \longrightarrow C_{soot}{-}H + H$ | 8.0 x $10^{7}$ | 1.56 | 3.8 |
| $S_5$ | $C_{soot}\cdot + O_2 \longrightarrow 2\,CO + products$ | 2.2 x $10^{12}$ | | 7.5 |
| $S_6$ | $C_{soot}{-}H + OH \longrightarrow CO + products$ | 0.13 | | |

Note: $k_{Si} = AT^n exp(-E_a/RT)$

Unlike PAH reactions, Step S4 of the HACA mechanism (addition of acetylene) for soot surface growth is not reversible. Surface reaction rates for a soot particle of class $k$ due to $C_2H_2$ is expressed as [149]:

$$W_{k,C_2H_2} = k_{S4}[C_2H_2]\alpha\dot{\chi}_S\pi\left(\frac{6m_k}{\pi\rho_s}\right)^{\frac{2}{3}}, \tag{6.34}$$

and, for $O_2$ oxidation, as [149]:

$$W_{k,O_2} = k_{S5}[O_2]\alpha\dot{\chi}_S\pi\left(\frac{6m_k}{\pi\rho_s}\right)^{\frac{2}{3}}, \tag{6.35}$$

where $\dot{\chi}_S$ is the number density of surface site activated whose value is determined considering steady state equilibrium between $C_{soot}\cdot$ and $C_{soot}$. This is given by:

$$\dot{\chi}_S = \frac{k_{S5}\left[O_2\right]\left(k_{S1}\left[H\right] + k_{S2}\left[OH\right]\right)}{k_{S-1}\left[H_2\right] + k_{S-2}\left[H_2O\right] + k_{S3}\left[H\right] + k_{S4}\left[C_2H_2\right] + k_{S5}\left[O_2\right]}\chi_S, \tag{6.36}$$

where $\chi_S$ is taken to be $2.3 \times 10^{15}$ cm$^{-2}$.

The steric factor $\alpha$ defined in Section 5.2.5 accounts for the fraction of surface carbon available for growth by $C_2H_2$ and oxidation by $O_2$. Its expression is given by [67]:

$$\alpha = \tanh\left[\frac{(12.65 - 5.63 \times 10^{-4}K^{-1}T)}{\log\mu_1} - 1.38 + 6.80 \times 10^{-5}K^{-1}T\right], \tag{6.37}$$

where $\mu_1$ is the reduced moment of first order (see below).

The surface reaction rate of oxidation by OH is expressed by a collision efficiency of 0.13 [149]:

$$W_{k,OH} = 0.13[OH]N_{av}\pi\left(\frac{6m_k}{\pi\rho_s}\right)^{\frac{2}{3}}\beta^f_{OH,k}, \tag{6.38}$$

where $\beta^f_{OH,k}$ is the collision frequency in free regime between a OH radical and a soot particle of class $k$, neglecting the Van der Waals enhancement factor.

Soot particles gain two carbon atoms during each reactive collision with $C_2H_2$, moving from class $k$ to class $k+2$. Oxidation by $O_2$ removes two carbon atoms, moving from class $k$ to class $k-2$. Oxidation by OH removes one carbon atom, moving from class $k$ to class $k-1$.

Growth of soot particles by PAH condensation is modeled assuming coalescent collisions in free molecular regime. The rate of growth for a particle of class $k$ is given by:

$$W_{k,\mathrm{A}_4} = \beta^f_{\mathrm{A}_4,k}[\mathrm{A}_4]. \tag{6.39}$$

Through the condensation of $\mathrm{A}_4$, a soot particle of class $k$ moves to class $k+16$.

### 6.2.3 Moments and Interpolative Closure

The method of moment proposes solves the evolution of a soot population by studying the evolution of its distribution moments. In this section the moment equations are provided. For simplicity, the Smoluchowski master equation for the transient evolution of a discrete particle distribution $\{N_{s,k}\}_{k=1:\infty}$ is considered [107]:

$$\begin{aligned}
\frac{dN_{s,1}}{dt} &= -\sum_{j=1}^{\infty} \beta_{1,j} N_{s,1} N_{s,j}, \\
\frac{dN_{s,i}}{dt} &= \frac{1}{2}\sum_{j=1}^{i-1} \beta_{j,i-j} N_{s,j} N_{s,i-j} - \sum_{j=1}^{\infty} \beta_{i,j} N_{s,i} N_{s,j},\ i = 2, \ldots, \infty.
\end{aligned} \tag{6.40}$$

The summation of $N_{s,k}$ over all the classes gives:

$$\sum_{i=1}^{\infty} \frac{dN_{s,i}}{dt} = \frac{1}{2}\sum_{i=1}^{\infty}\sum_{j=1}^{i-1} \beta_{j,i-j} N_{s,j} N_{s,i-j} - \sum_{i=1}^{\infty}\sum_{j=1}^{\infty} \beta_{i,j} N_{s,i} N_{s,j}. \tag{6.41}$$

Recognizing that:

$$\sum_{i=1}^{\infty}\sum_{j=1}^{i-1} \beta_{j,i-j} N_{s,j} N_{s,i-j} = \sum_{i=1}^{\infty}\sum_{j=1}^{\infty} \beta_{i,j} N_{s,i} N_{s,j}, \tag{6.42}$$

Eq. (6.41) becomes:

$$\sum_{i=1}^{\infty} \frac{dN_{s,i}}{dt} = -\frac{1}{2}\sum_{i=1}^{\infty}\sum_{j=1}^{\infty} \beta_{i,j} N_{s,i} N_{s,j}. \tag{6.43}$$

For any real $r$, the $r^{th}$ moment $M_r$ of the distribution is defined by:

$$M_r = \sum_{i=1}^{\infty} m_i^r N_{s,i}. \tag{6.44}$$

The reduced moments $\mu_r$ are defined by:

$$\mu_r = \frac{M_r}{M_0}. \tag{6.45}$$

It can be easily seen that $\mu_0 = 1$.

The evolution of the $0^{th}$ order moment $M_0$ is then given by:

$$\frac{dM_0}{dt} = -\frac{1}{2}\sum_{i=1}^{\infty}\sum_{j=1}^{\infty}\beta_{i,j}N_{s,i}N_{s,j}. \tag{6.46}$$

Note that $M_0$ gives the number of particles present in the soot ensemble, $M_1$ gives the total mass of soot, and $\mu_1$ gives the average soot mass divided by 12 g/mole.

The rate of variation of the first order moment, $M_1$, is derived in a similar manner. Assuming that $m_i = im_1$, the summation of $m_k N_{s,k}$ gives:

$$\begin{aligned}\frac{dM_1}{dt} &= m_1\left[\frac{1}{2}\sum_{k=1}^{\infty}\sum_{i=1}^{k-1}k\beta_{i,k-i}N_{s,i}N_{s,k-i} - \sum_{k=1}^{\infty}kN_{s,k}\sum_{i=1}^{\infty}\beta_{i,k}N_{s,i}\right], \\ &= m_1\left[\frac{1}{2}\sum_{k=1}^{\infty}\sum_{i=1}^{\infty}(k+i)\beta_{i,k}N_{s,i}N_{s,k} - \sum_{k=1}^{\infty}kN_{s,k}\sum_{i=1}^{\infty}\beta_{i,k}N_{s,i}\right],\end{aligned} \tag{6.47}$$

which is simplified by:

$$\frac{dM_1}{dt} = 0. \tag{6.48}$$

This result represents the conservation of mass for an ensemble undergoing only coagulation.

Similar derivations give the expressions of the higher order moments rate for coagulation:

$$\frac{dM_r}{dt} = \frac{1}{2}\sum_{k=1}^{r-1}\binom{r}{k}\left(\sum_{i=1}^{\infty}\sum_{j=1}^{\infty}m_i^k m_j^{r-k}\beta_{i,j}N_{s,i}N_{s,j}\right). \tag{6.49}$$

The principal difficulty is the non-additive character of the collision coefficient $\beta$. Moreover, its expression depends on the Knudsen number of the particles involved. However, this difficulty can be addressed using interpolative closure as shown below.

The general moment equations with coagulation, nucleation, and surface growth, are expressed by:

$$\frac{dM_0}{dt} = R_0 - G_0, \tag{6.50}$$

$$\frac{dM_1}{dt} = R_1 + W_1, \tag{6.51}$$

$$\frac{dM_2}{dt} = R_2 + G_2 + W_2, \tag{6.52}$$

$$\vdots$$

$$\frac{dM_r}{dt} = R_r + G_r + W_r, \tag{6.53}$$

where $R$, $G$, and $W$ are the nucleation, coagulation, and surface growth terms, respectively. Their expressions are given below. The number of soot particles increases by nucleation and decreases only by coagulation. Burnout of soot particles is not taken into account in this model.

The summation term in Eq. (6.49) can be expressed as a function of the moments without any approximation in the continuum collision regime $K_n \ll 1$. Recall from Eq. (6.32) that $\beta^c_{i,j}$ is given by:

$$\beta^c_{i,j} = \frac{2k_BT}{3\eta}\left(\frac{C_i}{m_i^{\frac{1}{3}}} + \frac{C_j}{m_j^{\frac{1}{3}}}\right)\left(m_i^{\frac{1}{3}} + m_j^{\frac{1}{3}}\right). \tag{6.54}$$

The expression of $C_i$ is given by Eq. (6.33). Substituting Eq. (6.32) into Eq. (6.49) gives:

$$G_0^c = \frac{2k_BT}{3\eta}\left[1 + \mu_{\frac{1}{3}}\mu_{-\frac{1}{3}} + 2.514\lambda\left(\frac{\pi\rho_s}{6}\right)^{\frac{1}{3}}\left(\mu_{-\frac{1}{3}} + \mu_{\frac{1}{3}}\mu_{-\frac{2}{3}}\right)\right]M_0^2, \tag{6.55}$$

for the $0^{th}$ order moment. Similarly, the coagulation rates for the higher order moments (except the fisrt) are obtained:

$$G_r^c = \frac{k_B T}{3\eta} \sum_{k=1}^{r-1} \binom{r}{k} \left(2\mu_k \mu_{r-k} + \mu_{k+\frac{1}{3}} \mu_{r-k-\frac{1}{3}} + \mu_{k-\frac{1}{3}} \mu_{r-k+\frac{1}{3}}\right) M_0^2 + \\ 2.514\lambda \left(\frac{\pi \rho_s}{6}\right)^{\frac{1}{3}} \frac{k_B T}{3\eta} \\ \times \sum_{k=1}^{r-1} \binom{r}{k} \left(\left(\mu_{k-\frac{1}{3}} \mu_{r-k} + \mu_k \mu_{r-k-\frac{1}{3}} + \mu_{k+\frac{1}{3}} \mu_{r-k-\frac{2}{3}} + \mu_{k-\frac{2}{3}} \mu_{r-k+\frac{1}{3}}\right)\right) M_0^2. \tag{6.56}$$

Knowledge of the fractional order moments is required to close the system. Frenklach [148] proposed achieving system closure by interpolating the fractional order moments from the logarithm of the whole order moments, which are known, using Lagrangian polynomials. In this present work, the first 6 moments are solved. The positive-order fractional moments are computed by Lagrange interpolation:

$$\log \mu_p = L_p(\log \mu_0, \log \mu_1, \ldots, \log \mu_6), \tag{6.57}$$

where $L_p$ represents the Lagrangian interpolation operator with respect to $p$, the moment order. The negative-order fractional moments can be solved by extrapolation from the first three moments [149]:

$$\log \mu_p = L_p(\log \mu_0, \log \mu_1, \log \mu_2). \tag{6.58}$$

Equation (6.56) indicates that extrapolation is needed for the $r_{max}+\frac{1}{3}$ moment, with $r_{max}$ being the number of moments solved. The logarithm of the fractional moment is linear with the moment order $r$ for $r$ greater than 3, with good accuracy between the exact method from the master equation and the interpolation technique [147, 149].

The coagulation coefficient in the free molecular regime is treated in a similar manner but requires additional attention. Recall from Eq. (6.31) that the coagulation coefficient in the free molecular regime, $\beta_{i,j}^f$, is given by:

$$\beta_{i,j}^f = 2.2\sqrt{\frac{6k_BT}{\rho_s}}\left(\frac{3}{4\pi\rho_s}\right)^{\frac{1}{6}}\sqrt{\frac{1}{m_i}+\frac{1}{m_j}}\left(m_i^{\frac{1}{3}}+m_j^{\frac{1}{3}}\right)^2. \tag{6.59}$$

Substituting Eq. (6.31) into Eqs. (6.46) and (6.49) gives:

$$G_0^f = \frac{1}{2}K_f\sum_{i=1}^{\infty}\sum_{j=1}^{\infty}(m_i+m_j)^{\frac{1}{2}}(m_i^{\frac{1}{3}}+m_j^{\frac{1}{3}})^2 m_i^{-\frac{1}{2}}m_j^{-\frac{1}{2}}N_{s,i}N_{s,j}, \tag{6.60}$$

$$G_r^f = \frac{1}{2}K_f\sum_{k=1}^{r-1}\binom{r}{k}\sum_{i=1}^{\infty}\sum_{j=1}^{\infty}(m_i+m_j)^{\frac{1}{2}}(m_i^{\frac{1}{3}}+m_j^{\frac{1}{3}})^2 m_i^{k-\frac{1}{2}}m_j^{r-k-\frac{1}{2}}N_{s,i}N_{s,j}, \tag{6.61}$$

with:

$$K_f = 2.2\sqrt{\frac{6k_BT}{\rho_s}}\left(\frac{3m_{\mathrm{C}}}{4\pi\rho_s}\right)^{\frac{1}{6}}, \tag{6.62}$$

and with $m_{\mathrm{C}}$ the mass of a carbon atom.

Similarly to the expression of coagulation in the continuum regime, $G_r^f$ is expressed as a function of the distribution moments. However, because of the presence of $(m_i+m_j)^{\frac{1}{2}}$, a full expansion of the sums is not possible. To overcome this difficulty, this term is evaluated by Lagrangian interpolation. First, a grid function $f_l^{x,y}$ is defined:

$$f_l^{x,y} = \frac{1}{M_0^2}\sum_{i=1}^{\infty}\sum_{j=1}^{\infty}(m_i+m_j)^l(m_i^{\frac{1}{3}}+m_j^{\frac{1}{3}})^2 m_i^{x-\frac{1}{2}}m_j^{y-\frac{1}{2}}N_{s,i}N_{s,j}. \tag{6.63}$$

As a result of this definition, the rate of coagulation in the free molecular regime can be written as:

$$G_0^f = \frac{1}{2}K_f M_0^2 f_{\frac{1}{2}}^{0,0}, \tag{6.64}$$

$$G_r^f = \frac{1}{2}K_f M_0^2\sum_{k=1}^{r-1}\binom{r}{k}f_{\frac{1}{2}}^{r,r-k}. \tag{6.65}$$

For $l = 0, 1, 2, \ldots$, $f_l^{x,y}$ can be expressed in exact terms, using fractional-order moments. For example, $f_0^{x,y}$ is expressed:

$$f_0^{x,y} = 2\mu_{x-\frac{1}{6}}\mu_{y-\frac{1}{6}} + \mu_{x-\frac{1}{2}}\mu_{y+\frac{1}{6}} + \mu_{x+\frac{1}{6}}\mu_{y-\frac{1}{2}}, \tag{6.66}$$

and for any $l \in \mathbb{N}$, the grid function is expressed by:

$$f_l^{x,y} = \sum_{k=0}^{l} \binom{l}{k} \left( \mu_{l-k+x+\frac{1}{6}}\mu_{k+y-\frac{1}{2}} + \mu_{l-k+x-\frac{1}{2}}\mu_{k+y+\frac{1}{6}} + 2\mu_{l-k+x-\frac{1}{6}}\mu_{k+y-\frac{1}{6}} \right). \tag{6.67}$$

The fraction-order moments appearing in the expression of $f_l^{x,y}$ are evaluated through Lagrangian interpolation using whole-order moments, as described above. The logarithm values of the grid function at $l = 1/2$ are evaluated by Lagrangian interpolation. For example, $f_{\frac{1}{2}}^{0,0}$ is evaluated by:

$$f_{\frac{1}{2}}^{0,0} = \left(f_0^{0,0}\right)^{\frac{3}{8}} \left(f_1^{0,0}\right)^{\frac{3}{4}} \left(f_2^{0,0}\right)^{-\frac{1}{8}}. \tag{6.68}$$

This allows the computation of the coagulation terms in the free-coagulation regime $G_r^f$.

The final expression of the coagulation term $G_r$ is found from the harmonic mean between the continuum and free-molecular regimes:

$$G_r = \frac{G_r^f G_r^c}{G_r^f + G_r^c},\ r = 0, 2, 3, \ldots \tag{6.69}$$

This approximation was shown to reproduce the behavior of aerosols in the transition regime with an appreciable gain in computational time [109].

The integrated expression of nucleation rate, $R_r$, is given by:

$$R_0 = 2.2\sqrt{\frac{4\pi k_B T}{m_{\mathrm{A}_4}}} d_{\mathrm{A}_4}^2 N_{av}^2 [\mathrm{A}_4]^2, \tag{6.70}$$

$$R_r = 2.2\sqrt{\frac{4\pi k_B T}{m_{\mathrm{A}_4}}} d_{\mathrm{A}_4}^2 N_{av}^2 [\mathrm{A}_4]^2 m_1^r,\ r = 1, \ldots, 5, \tag{6.71}$$

where $m_1$ is the mass of nascent soot particle and is equal to 32 amu.

The rate of surface growth and oxidation, $W_r$, with $r \geq 1$ does not affect $M_0$ and it is the resultant of the contributions of surface growth by $C_2H_2$ addition and $A_4$ condensation, and oxidation by OH and $O_2$, as mentioned in Section 6.2.2. Therefore, $W_r$ is expressed by:

$$W_r = W_{r,C_2H_2} + W_{r,A_4} + W_{r,O_2} + W_{r,OH} \tag{6.72}$$

where $W_{r,C_2H_2}$, $W_{r,A_4}$, $W_{r,O_2}$, and $W_{r,OH}$ are the contributions of $C_2H_2$, $A_4$, $O_2$, and OH, respectively. The contribution of surface growth by $C_2H_2$ addition is expressed by:

$$W_{r,C_2H_2} = \pi \left(\frac{6m_C}{\pi\rho_s}\right)^{\frac{2}{3}} k_{S4}[C_2H_2]\alpha\dot{\chi}_S M_0 \sum_{k=0}^{r-1} \binom{r}{k} \mu_{k+\frac{2}{3}} (2)^{r-k}, \tag{6.73}$$

the contribution of $A_4$ condensation is given by:

$$\begin{aligned} W_{r,A_4} = 2.2\sqrt{\frac{\pi k_B T}{2m_C}} N_{av} [A_4] M_0 \sum_{k=0}^{r-1} \binom{r}{k} \Bigg( \frac{2}{3} d_{A_4}^2 n_{C,A_4}^{r-k+\frac{1}{2}} \mu_k \dots \\ +2 \left(\frac{6m_C}{\pi\rho_s}\right)^{\frac{1}{3}} d_{A_4} \sqrt{\frac{2}{3}} n_{C,A_4}^{r-k} \mu_{k+\frac{1}{3}} + \left(\frac{6m_C}{\pi\rho_s}\right)^{\frac{1}{3}} n_{C,A_4}^{r-k-\frac{1}{2}} \mu_{k+\frac{2}{3}} \Bigg), \end{aligned} \tag{6.74}$$

The contribution of oxidation by $O_2$ is given by:

$$W_{r,O_2} = k_{S5}[O_2]\alpha\dot{\chi}_S \pi \left(\frac{6m_C}{\pi\rho_s}\right)^{\frac{2}{3}} M_0 \sum_{k=0}^{r-1} \binom{r}{k} \mu_{k+\frac{2}{3}} (-2)^{r-k}, \tag{6.75}$$

and the contribution of oxidation by OH to the surface oxidation is given by:

$$W_{r,OH} = \pi \left(\frac{6m_C}{\pi\rho_s}\right)^{\frac{2}{3}} \sqrt{\frac{\pi k_B T}{2m_{OH}}} k_{S6} [OH] N_{av} M_0 \sum_{k=0}^{r-1} \binom{r}{k} \mu_{k+\frac{2}{3}} (-1)^{r-k}, \tag{6.76}$$

where $d_{A_4}$ is the diameter of the pyrene molecule, as expressed by Eq. (6.29) and $n_{C,A_4}$ represents the number of carbon atoms contained by $A_4$, i.e., 16.

## 6.3 Implementation

The method of moment with interpolative closure, MOMIC, described above was implemented in the code presented in Chapter 3. Rates of production of H, OH, $O_2$, $H_2$, $A_4$, $C_2H_2$, and CO were modified to account for the effects of creation/consumption due to soot. For each of these species, the production term $\dot{\omega}_k$ in Eqs. (3.3) and (3.2) was defined by $\dot{\omega}_k = \dot{\omega}_{k,CHEMKIN} + \dot{\omega}_{k,MOMIC}$ with $\dot{\omega}_{k,CHEMKIN}$ the $k^{th}$ species production rate due to gas phase reaction and predicted by CHEMKIN, and $\dot{\omega}_{k,MOMIC}$ the $k^{th}$ species production rate due to surface reactions or nucleation and predicted by MOMIC.

Six equations were added to the governing equations to account for the dynamic evolution of the first six moments $M_r$ of the PSDF. The momemt conservation equations are derived from the GDE, Eq. (6.12).

Assuming spherical symmetry, the expression of the GDE in spherical coordinates becomes:

$$\frac{\partial N_k}{\partial t} + \frac{1}{r^2}\frac{\partial}{\partial r}\left(r^2 U_r N_k\right) - \frac{1}{r^2}\frac{\partial}{\partial r}\left(r^2 D_k \frac{\partial N_k}{\partial r}\right) + \frac{1}{r^2}\frac{\partial}{\partial r}\left(r^2 U_T N_k\right) = \left[\frac{\partial N_k}{\partial t}\right]_{nucleation} + \left[\frac{\partial N_k}{\partial t}\right]_{coagulation} + \left[\frac{\partial N_k}{\partial t}\right]_{growth} + \left[\frac{\partial N_k}{\partial t}\right]_{oxidation}. \quad (6.77)$$

Multiplying Eq. (6.77) by $m_k^r$, with $r \in \mathbb{N}$ and summing for all the $k$ gives:

$$\frac{\partial}{\partial t}\left(\sum_{k=1}^{\infty} m_k^r N_k\right) + \frac{1}{r^2}\frac{\partial}{\partial r}\left(r^2 U_r \sum_{k=1}^{\infty} m_k^r N_k\right) - \frac{1}{r^2}\frac{\partial}{\partial r}\left(r^2 \sum_{k=1}^{\infty} m_k^r D_k \frac{\partial N_k}{\partial r}\right) + \frac{1}{r^2}\frac{\partial}{\partial r}\left(r^2 U_T \sum_{k=1}^{\infty} m_k^r N_k\right) = R_r + G_r + W_r. \quad (6.78)$$

This equation is simplyfied assuming that the free-molecular regime is applicable for the diffusivity coefficient. Therefore, one can write: $D_k = D_0 m_k^{-\frac{2}{3}}$. Recognizing

that:

$$M_r = \sum_{k=1}^{\infty} m_k^r N_k, \tag{6.79}$$

and after multiplication of Eq. (6.78) by $A(r) = 4\pi r^2$, the $r^{th}$ moment conservation equation is obtained:

$$A(r)\frac{\partial M_r}{\partial t} + \frac{\partial}{\partial r}\left(\frac{\dot{m}}{\rho}M_r\right) - \frac{\partial}{\partial r}\left(A(r)D_0\frac{\partial M_{r-\frac{2}{3}}}{\partial r}\right) + \frac{\partial}{\partial r}\left(A(r)U_T M_r\right) = A(r)\dot{M}_r, \tag{6.80}$$

with $\dot{M}_r = R_r + G_r + W_r$.

The moments of a distribution can be very large, which may result in an ill-conditioned Jacobian matrix leading to the non-convergence of the modified Newton algorithm. To overcome this difficulty, the logarithms of the moments are solved in lieu of the moments. Defining:

$$Y_r = \log(M_r + 1), \tag{6.81}$$

Eq. (6.80) becomes:

$$\begin{aligned} &A(r)\frac{\partial \exp Y_r}{\partial t} + \frac{\partial}{\partial r}\left(\frac{\dot{m}}{\rho}\exp Y_r\right) \\ &- \frac{\partial}{\partial r}\left(A(r)D_0\frac{\partial \exp Y_{r-\frac{2}{3}}}{\partial r}\right) + \frac{\partial}{\partial r}\left(A(r)U_T \exp Y_r\right) = A(r)\dot{M}_r. \end{aligned} \tag{6.82}$$

Expanding the derivative terms, this equation is then expressed by:

$$\begin{aligned} &A(r)\frac{\partial Y_r}{\partial t} + \left(\frac{\dot{m}}{\rho} + A(r)U_T\right)\frac{\partial Y_r}{\partial r} + \frac{\partial}{\partial r}\left(\frac{\dot{m}}{\rho} + A(r)U_T\right) \\ &- \frac{\mu_{r-\frac{2}{3}} - M_0^{-1}}{\mu_r - M_0^{-1}}\left[A(r)D_0\left(\frac{\partial Y_{r-\frac{2}{3}}}{\partial r}\right)^2 + \frac{\partial}{\partial r}\left(A(r)D_0\frac{\partial Y_{r-\frac{2}{3}}}{\partial r}\right)\right] \\ &- A(r)\dot{M}_r \exp\left(-Y_r\right) = 0. \end{aligned} \tag{6.83}$$

The diffusive transport of soot is neglected, yielding:

$$A(r)\frac{\partial Y_r}{\partial t}+\left(\frac{\dot{m}}{\rho}+A(r)U_T\right)\frac{\partial Y_r}{\partial r}+\frac{\partial}{\partial r}\left(\frac{\dot{m}}{\rho}+A(r)U_T\right)-A(r)\dot{M}_r\exp\left(-Y_r\right)=0. \quad (6.84)$$

The thermophoretic velocity $U_T$ is found assuming an accomodation coefficient of $\alpha = 0.925$. The expression of $U_T$ becomes (see Eq. (6.13)):

$$U_T = -0.55\nu\frac{\partial \log T}{\partial r}. \quad (6.85)$$

The equations of conservation of moments are discretized following the methods presented in Chapter 3. The convective term is discretized using a first order scheme. This scheme is preferred over a second order scheme because it adds artificial diffusion that makes the equations less sensitive to the initial conditions and therefore eases convergence of the Newton algorithm.

Effects of thermophoresis can be as important as convection, therefore no assumption can be made on the sign of:

$$a = \frac{\dot{m}}{\rho} - A(r)0.55\nu\frac{\partial \log T}{\partial r}. \quad (6.86)$$

An upwind scheme is used [61] to solve this issue. The convective term of Eq. (6.84) is discretized by:

$$\left(\frac{\dot{m}}{\rho}+A(r)U_T\right)\frac{\partial Y_r}{\partial r} \approx \frac{a_i+|a_i|}{2}\left(\frac{Y_{r,i}-Y_{r,i-1}}{x_i-x_{i-1}}\right)+\frac{a_i-|a_i|}{2}\left(\frac{Y_{r,i+1}-Y_{r,i}}{x_{i+1}-x_i}\right). \quad (6.87)$$

The transport velocity $a_i$ is evaluated in $x_i$. Its expression requires the evaluation of $\frac{\partial \log T}{\partial r}$. This term is discretized using the second order scheme described in Chapter 3.

The discretization of the term $\dfrac{\partial a}{\partial r}$ requires special attention to preserve the three-banded shape of the Jacobian. The velocity $a$ is evaluated at $x_{i-\frac{1}{2}}$ and $x_{i+\frac{1}{2}}$ with:

$$a_{i-\frac{1}{2}} = \frac{\dot{m}_{i-\frac{1}{2}}}{\rho_{i-\frac{1}{2}}} - 0.55 A_{i-\frac{1}{2}} \nu_i \left( \frac{\log T_i - \log T_{i-1}}{x_i - x_{i-1}} \right), \tag{6.88}$$

$$a_{i+\frac{1}{2}} = \frac{\dot{m}_{i+\frac{1}{2}}}{\rho_{i+\frac{1}{2}}} - 0.55 A_{i+\frac{1}{2}} \nu_i \left( \frac{\log T_{i+1} - \log T_i}{x_{i+1} - x_i} \right), \tag{6.89}$$

with $x_{i+\frac{1}{2}} = 0.5(x_i + x_{i+1})$.

The mass flow rate $\dot{m}$ at $x_{i-\frac{1}{2}}$ is evaluated by averaging its value between $x_{i-1}$ and $x_i$. The mixture density $\rho_{i-\frac{1}{2}}$ is computed through the knowledge of the thermodynamic state of the mixture at this location. This is averaged between $x_{i-1}$ and $x_i$. Note that the mixture kinetic viscosity $\nu$ is evaluated only at $x_i$. This is motivated by a reduction of the computational time; the evaluation of transport coefficients represents 21% of the CPU time (as shown in Table 3.2); and the variation of $\nu$ between $x_{i-\frac{1}{2}}$ and $x_{i+\frac{1}{2}}$ is not significant.

Thus the discretization of the term $\dfrac{\partial a}{\partial r}$ is expressed, in its fully developed form, by:

$$\begin{aligned} \left.\frac{\partial a}{\partial r}\right|_{r=x_i} = & \frac{\dfrac{m_{i+1}+m_i}{\rho_{i+\frac{1}{2}}} - \dfrac{m_i+m_{i-1}}{\rho_{i-\frac{1}{2}}}}{x_{i+1}-x_{i-1}} \\ & - 0.55\nu_i \times \frac{2}{x_{i+1}-x_{i-1}} \left[ A_{i+\frac{1}{2}} \left( \frac{\log T_{i+1} - \log T_i}{x_{i+1} - x_i} \right) - A_{i-\frac{1}{2}} \left( \frac{\log T_i - \log T_{i-1}}{x_i - x_{i-1}} \right) \right]. \end{aligned} \tag{6.90}$$

From Eqs. (6.87) and (6.90), a three band-shaped Jacobian structure is obtained. This is required for the Gauss-elimination algorithm.

The presence of soot inside the flame enhances radiative heat losses and absorption. The inclusion of soot in radiative heat transfer is modeled by the addition

of a new term in the expression of the spectral absorption coefficient $\kappa_\lambda$ present in the RTE, see Eq. (3.81).

The spectral absorption coefficient $\kappa_\lambda$ is then defined by:

$$\kappa_\lambda = \kappa_{\lambda,\mathrm{CO_2}} + \kappa_{\lambda,\mathrm{H_2O}} + \kappa_{\lambda,\mathrm{CO}} + \kappa_{\lambda,soot}, \tag{6.91}$$

where the contribution of soot $\kappa_{\lambda,soot}$ is assumed to be independent of the wavelength $\lambda$ and is defined such that [93]:

$$\int_\lambda \kappa_{\lambda,soot} d\lambda = 1600 T f_v, \tag{6.92}$$

with $f_v$ the soot volume fraction, expressed by:

$$f_v = \frac{m_\mathrm{C} \mu_1 M_0}{\rho_s}, \tag{6.93}$$

where $m_\mathrm{C}\mu_1$ represents the average mass of a soot particle.

### 6.3.1 Verification

The verification of the soot model implementation was performed by simulating soot formation inside premixed flame JW1.69 [67,140,150]. This choice was made because both experimental and numerical results for this flame are available [157].

The JW1.69 flame was experimentally studied by Jander, even though the experimental details were not directly published. However, this flame was used by Frenklach and by Kraft to calibrate their soot formation models. This flame is a burner-stabilized ethylene-air flame with an ambient pressure of 1 bar. The mixture is composed (in mole fraction) of 12.66% of $C_2H_4$, 18.34% of $O_2$, and 69% of $N_2$.

The flow velocity was 5.9 cm/s, the global C/O ratio was 0.69, and the measured flame temperature was 1711 K.

The numerical code was modified to model this flame. This involved a modification of the boundary conditions at the outer boundary were vanishing temperature and species gradients were imposed. The surface area $A(r)$ was kept constant to account for the Cartesian geometry of this problem.

The experimental temperature profile was obtained from [157] and was used as a constant profile through the flame. Therefore the energy equation was not computed, which is common for such simulations. First a steady state solution with gas-phase only was obtained. This solution and an initial guess for the soot moments were used as a starting point for the computation of soot with nucleation only. Once a converged solution was obtained, coagulation was added, then surface growth by $C_2H_2$ and PAH, and finally surface oxidation. This succession of computations was necessary because the code was extremely sensitive to the initial guess, especially for soot formation. Note that an initial soot profile must be prescribed for convergence; the code cannot achieve convergence starting from an initially null soot profile.

Predicted steady-state results were compared with experimental results (in terms of soot volume fraction) and computed results from [157]. Figure 6.2 plots the predicted and experimental soot volume fractions. Satisfactory agreement between experimental and predicted results are obtained, validating the implementation of the soot formation code.

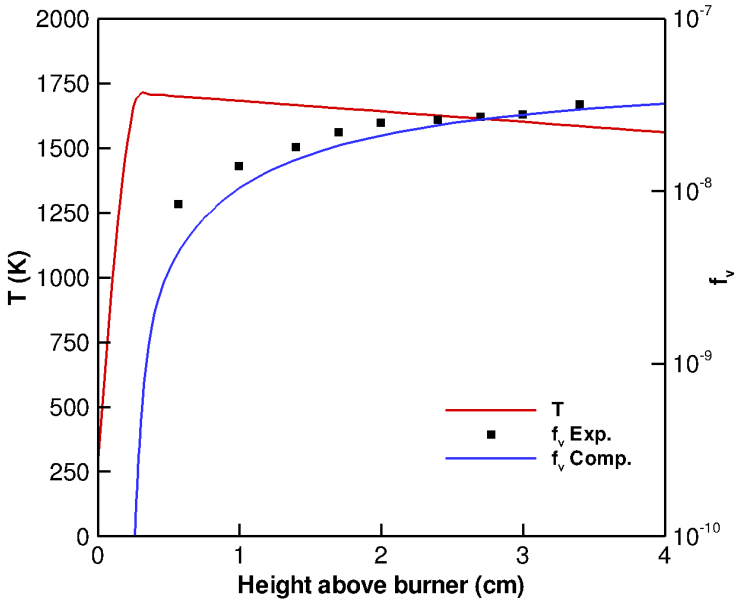


Figure 6.2: Flame JW1.69 experimental and predicted soot volume fractions.

### 6.3.2 Soot Radiation Test

To validate the implementation of the soot absorption coefficient and the interactions of soot radiation with the energy equation, the test presented below was performed. Starting from a reference solution, which includes only gas phase species reactions and radiation, a new solution was computed with the presence of a flat soot profile. This test aimed to quantify a decrease of temperatures due to the soot presence.

Flame 5 of Table 5.1 was the reference flame for this tests. This normal flame is defined by the following parameters:

(a) $X_{O2} = 0.28$ , $X_{C2H4} = 0.18$,

(b) $T_{ad} = 2306$ K,

(c) $\dot{m} = 8.38$ mg/s.

The computational domain boundary was set to $r_{start} = 0.3175$ cm (burner location) and $r_{end} = 1.2$ cm (outer boundary location). A peak temperature of $T_{flame} = 1883$ K located at a radius of $r_{flame} = 0.704$ cm was predicted for the reference case. The heat release rate was predicted to be $Q_c = 71.27$ W, with predicted radiative heat losses, due to gas radiation, of $Q_r = 3.64$ W.

The soot volume fraction was held constant across the flame and equal to $f_v = 10^{-4}$. Figure 6.3 plots the resulting steady-state temperature profiles.

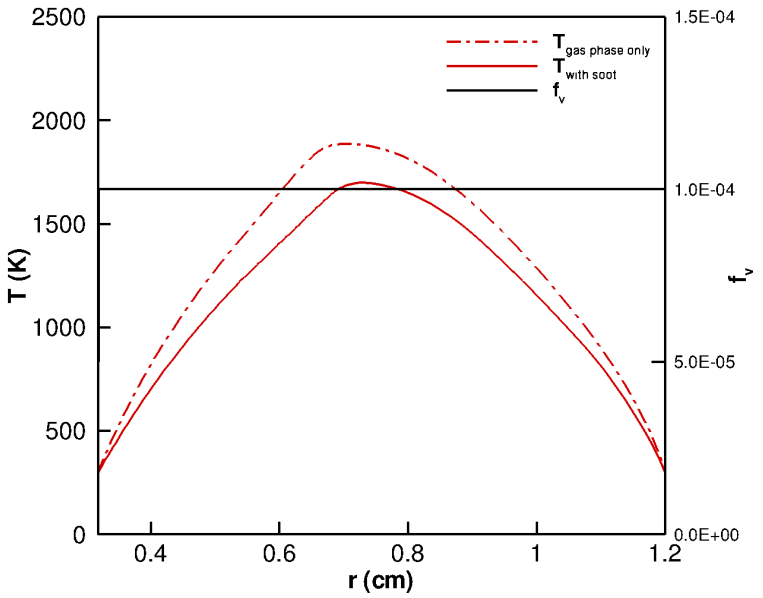


Figure 6.3: Flame 5 steady state temperature with flat soot profile, $f_v = 10^{-4}$. Comparison with the reference case is shown.

Results obtained for the case with the constant soot profile are:

(a) $r_{flame} = 0.7272$ cm,

(b) $T_{flame} = 1710$ K,

(c) $Q_r = 14.35$ W,

(d) $Q_c = 71.25$ W.

The results show a significant change in flame characteristics. The presence of the uniform soot profile decreases the peak temperature by more than 100 K. The radiative heat loss increases from 3.6 W to 14.35 W. Note that the flame radius increases as the flame looses more energy by radiation. This is predicted by Eq. (2.32). This test validates the implementation of the soot absorption coefficient and the coupling between soot radiation and the energy equation.

## 6.4 Soot Formation in Steady Spherical Diffusion Flames

In this section, results from steady state numerical simulations of soot formation in spherical diffusion flames using the soot code described above are presented. Predictions of soot formation are obtained through a four-step process:

(1) First, starting from the gas phase solution and a initial guess for the soot profile, a solution with only nucleation (from pyrene) is computed.

(2) Second, a new solution is computed with both nucleation and coagulation.

(3) Third, a new solution is obtained with the nucleation, coagulation, and surface growth (growth by $C_2H_2$ addition and $A_4$ condensation).

(4) Finally, the solution with the contribution of nucleation ,coagulation, surface growth, and oxidation is obtained.

Flame 5 is the flame of study. Radiative heat losses from gas-phase species and soot particles are modeled. Temperature boundaries are held constant at 300 K. Domain boundaries are considered as sinks for soot particles, which gives the following condition for the logarithms of the soot moments $Y_r$ at both boundaries:

$$Y_r = 0,\ r = 0, 1, 2, 3, 4, 5. \tag{6.94}$$

Computations with nucleation are initialized using a converged gas-phase solution with an initial soot profile. This initial soot profile is a flat profile with a soot volume fraction equals of $f_v = 10^{-11}$. The PSDF moments are adjusted considering a constant distribution of a mono-disperse aerosol with 32 carbon atoms per particle. Note that the initial soot profile influences considerably the convergence. By trial and error, an initial profile similar to the one described above was found to gives the fastest rate of convergence.

### 6.4.1 Nucleation

In this section, results obtained for Flame 5 with the sole contribution of nucleation are presented. Nucleation is an important process since it increases the number of soot particles present. In the present model, soot particles are created by

nucleation and their density number is reduced by coagulation. Surface reactions are assumed to influence only the mass present in the soot population. Figure 6.4 plots the temperature and the predicted soot volume fraction profiles across the computational domain.

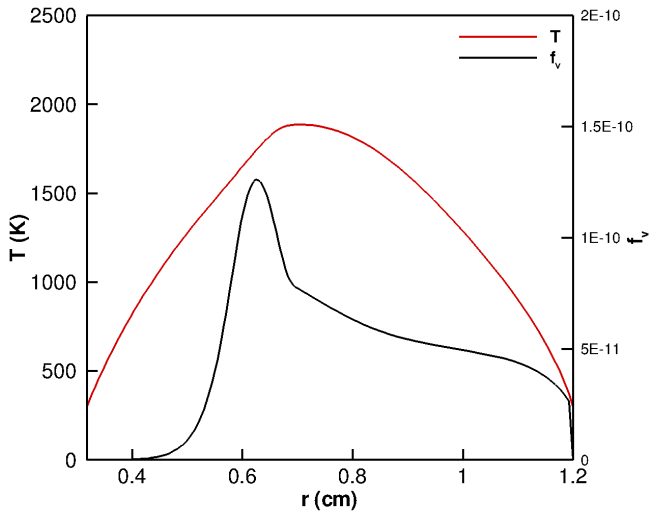


Figure 6.4: Flame 5 predicted temperature and soot volume profiles with nucleation only.

The soot volume fraction profile peaks at a value of $f_v = 1.26^{-10}$ at a radius $r$ =0.63 cm. The temperature at this location is about 1750 K, located slightly inside the peak temperature, $T_f = 1885$ K found at $r = 0.704$ cm. The flame characteristics are similar to the reference case. The radiative heat losses are predicted to be 3.64 W, which is similar to the reference case. The small load of soot produced by nucleation is not significant enough to modify the general characteristics of the flame. The peak of soot volume fraction is followed first by a pronounced decrease and then by a lesser and nearly constant decay on the oxidizer side of the flame.

The step decrease in soot volume fraction results from thermophoresis. Due to the presence of temperature gradients, soot particles migrate toward cooler parts of the flame. Since nucleation occurs on the fuel side of the flame, soot particles tend to migrate toward the burner but they face the effects of convection, which increases near the burner surface due to the spherical geometry. An equilibrium point is found at the location where convection and transport by thermophoresis are balanced.

### 6.4.2 Coagulation

In this section, results with the joint contribution of nucleation and coagulation are presented. Recall that the code models coagulation of soot particles as coalescent collisions. The following scheme is followed: when a particle of class $i$ collides with a particle of class $j$, they combine into a new spherical particle of class $i + j$. Coagulation does not participate in the variation of the overall mass of the soot ensemble, represented by $M_1$. But it decreases the soot particle density number. Also, nucleation modifies the shape of the PSDF, giving it a log-normal shape.

Figure 6.5 plots the steady-state solution with soot nucleation and coagulation obtained from the previous steady-state solution.

The flame temperature, flame location, and heat losses remain identical. Note that the soot volume fraction profile is similar to the one obtained with the sole contribution of nucleation, with a slighter higher peak soot volume fraction of $f_{v,max} = 1.9 \times 10^{-10}$.

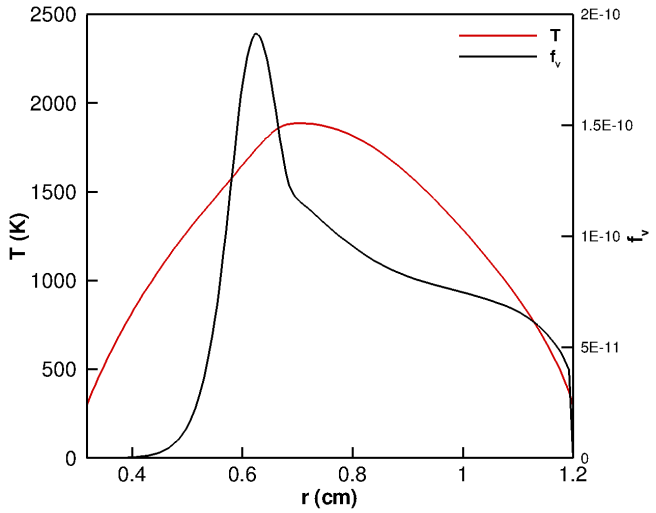


Figure 6.5: Flame 5 predicted temperature and soot volume profiles with nucleation and coagulation.

### 6.4.3 Surface Growth

The third step of the computation process is the inclusion of surface growth by $C_2H_2$ and $A_4$ condensation. Unlike soot coagulation, this does not modify the number of soot particles present but does increase the mass of soot. Figure 6.6 represents the predicted soot volume fraction after nucleation, coagulation, and surface growth by $C_2H_2$ and $A_4$ addition. The increase in mass is significant, increasing the peak soot volume fraction from $1.9 \times 10^{-10}$ to $6.93 \times 10^{-8}$. This increase is not sufficient to have a significant impact on the flame characteristics which remain the same, apart from a small increase in heat losses of 3.67 W. The peak location at $r = 0.66$ cm is, however, shifted closer to the location of peak temperature.

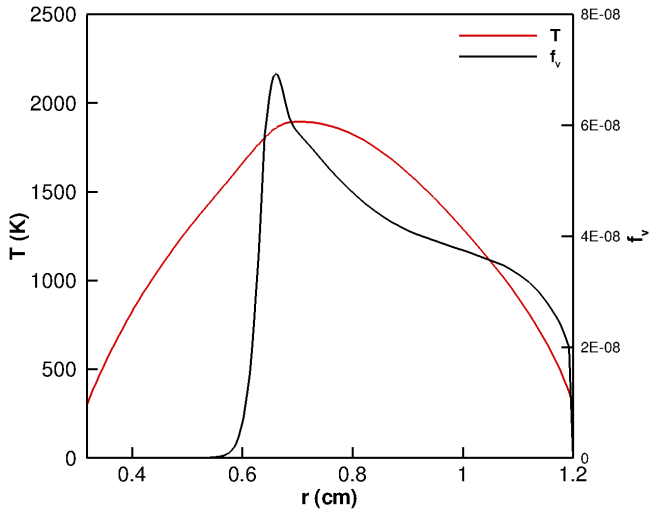


Figure 6.6: Flame 5 predicted temperature and soot volume profiles with nucleation, coagulation and surface growth.

### 6.4.4 Oxidation

The final steady state solution is obtained by enabling soot oxidation by $O_2$ and OH. Particle oxidation removes mass and hence decreases moments $M_1$ - $M_5$. In the current model, $M_0$ is not affected by oxidation.

However, in real flames oxidation can lead to the destruction of a soot particle. This decreases the soot particle density number, $M_0$, which may in turn decrease the rate of soot oxidation, since this rate is proportional to the average particle surface area given by $\mu_{\frac{2}{3}}$. If $M_0$ remains constant while $M_1$ decreases due to oxidation, Lagrangian interpolation may overestimate $\mu_{\frac{2}{3}}$. To overcome this issue, $\mu_{\frac{2}{3}}$ is extrapolated from $M_1$ to $M_5$ for the cases where surface oxidation dominates.

However, this is not sufficient to fully overcome the absence of soot burn-out model and oxidation may reduce $M_1$ below $M_0$, which has no physical basis and

hinders convergence. Since oxidation in diffusion flames occurs mostly in fuel lean areas where particle nucleation is unlikely, oxidation is modeled by controlling the average mass or number of carbon atoms per particle, $\mu_1$, and assuming absence of soot when $\mu_1$ falls below a threshold value, which is taken as four carbon atoms for this work. Note that this is less than the initial number of 32 carbon atoms present in nascent particles. When this occurs at a mesh point located on the oxidizer side, the value of all moments are set to zero between this point and the outer boundary flame.

The predicted soot volume fraction and temperature profilew are shown in Fig. 6.7. Oxidation decreases the peak of soot volume fraction to $2.1 \times 10^{-8}$. The

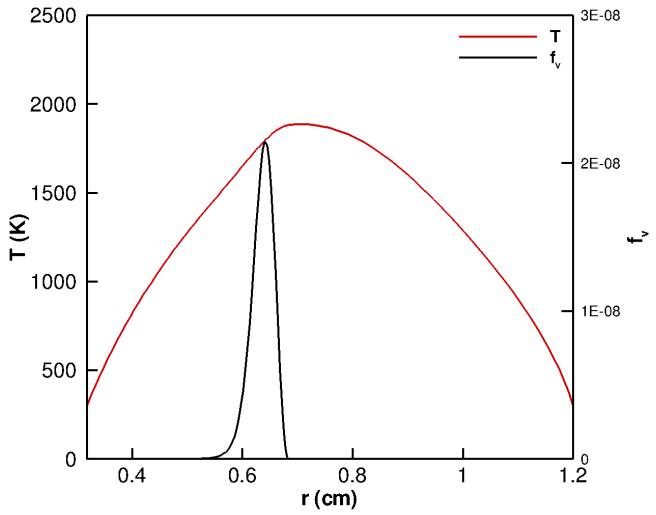


Figure 6.7: Predicted temperature and soot volume profiles for spherical diffusion Flame 5.

peak value is located at $r = 0.64$ cm, which is closer to the location of the peak soot volume fraction with only nucleation and coagulation. The temperature here

is $T = 1800$ K. Beyond $r = 0.6819$ cm, no soot is found.

Interesting insights are obtained by studying the structure of this flame in C/O space as illustrated in Fig. 6.8. The local C/O ratio associated with the peak of soot volume fraction is $C/O = 0.5$. Soot free conditions are observed for $C/O$ less than 0.43.

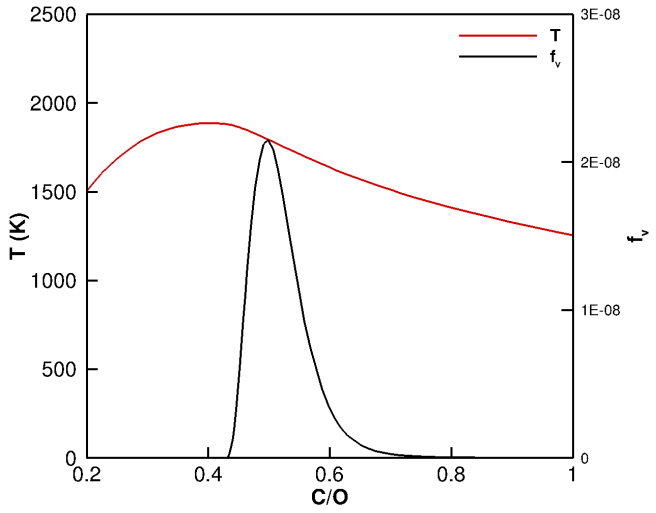


Figure 6.8: Predicted temperature and soot volume profiles in C/O space for spherical diffusion Flame 5.

The logarithms of the PSDF moments are plotted in Fig. 6.9. Near the burner, the 6 moments behave similarly and the space between each curve is constant. This corresponds to a mono-disperse soot distribution. Near the flame location, departure from the mono-disperse distribution is observed, as $M_1$ - $M_5$ increase (due to surface growth and coagulation) while $M_0$ decreases (due to coagulation).

Figure 6.10 shows the rate of nucleation and surface growth for $M_1$ in C/O space. Nucleation occurs earlier in the flame than surface growth does. Nucleation

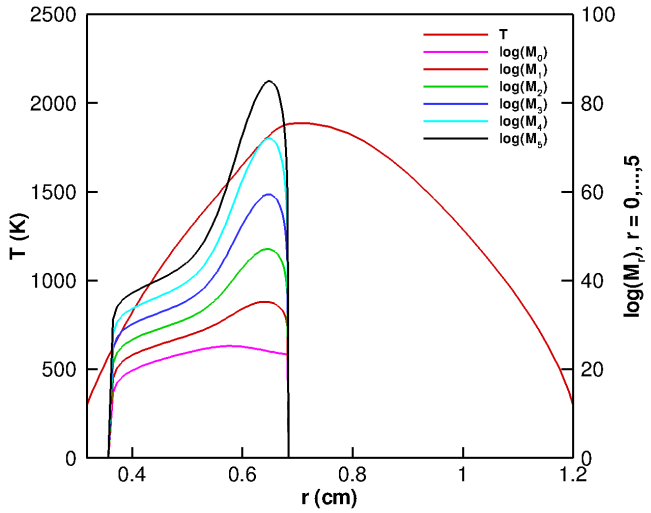


Figure 6.9: Predicted temperature and logarithm of the soot moments for spherical diffusion Flame 5.

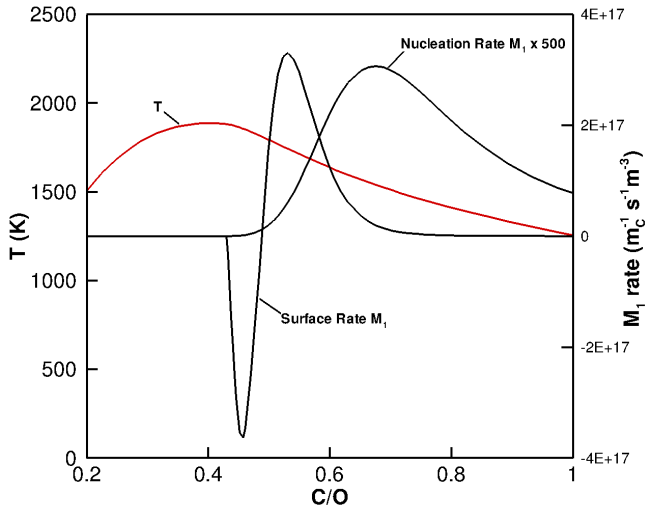


Figure 6.10: Predicted temperature and rates of surface growth and nucleation in C/O space for spherical diffusion Flame 5.

rate peaks at C/O = 0.67 and has a peak value about 1/500 times that of the peak value of surface growth, which is located where C/O = 0.53. The rate of surface growth becomes negative for C/O below 0.5, with a peak value greater than the maximum value of surface growth.

## 6.5 Discussion and Summary

The method of moments allows fast computations of the soot population dynamics by reducing the GDE to six equations. This method was successfully implemented and used to model soot formation inside a flame. The model includes most of the physical phenomena that contribute to soot formation. Radiative heat losses due to the presence of soot were predicted using a simple radiative model based on the soot volume fraction and temperature.

Soot formation in a steady state spherical diffusion flame was modeled for a reference flame (Flame 5) over a small domain that models the initial conditions of transient spherical diffusion flames.

Surface growth was observed to be the dominant process in mass addition to the soot population. Peak soot volume fraction was found at a local C/O ratio of 0.53. Oxidation was predicted to be the dominant process in locations with C/O ratio below 0.5. Radiative heat losses due to soot were small.

Further improvements are required, principally in the treatment of soot oxidation. The actual formulation of soot depletion due to oxidation needs to be modified to account for the burn-out of the smallest soot particle. Several approaches may

be considered to overcome this issue. A first solution would be to add a new governing equation modeling the evolution of the smallest soot particles population, $N_1$. The evaluation of $N_1$ would be used to account for the decrease in the total soot density number, $M_0$, due to the burn-out of the smallest soot particles. Another solution would be to assume the shape of the PSDF in oxidation regions and to extrapolate the value of $M_0$ based on the knowledge of the total mass of the soot population, $M_1$. However, this approach may introduce more uncertainties than the first solution proposed.

Another improvement could be made in the treatment of soot radiative losses. In the present work, the soot radiative absorption coefficient is found empirically. A more specific treatment of the soot radiation can be achieved by considering the effects of the PSDF shape in the radiative absorption coefficient. This would increase the accuracy of the radiative heat loss prediction.

# Chapter 7

# Conclusions and Future Directions

Spherical diffusion flames have several unique characteristics that make them attractive from experimental and mathematical perspectives. Due to spherical symmetry, their spatiality is reduced to one dimension, allowing their numerical investigation through the use of detailed chemistry and transport models with reasonable computational cost.

In this work, spherical diffusion flames were numerically investigated for various conditions. The general characteristics of spherical diffusion flames and their previous studies were reviewed in Chapter 2.

A comprehensive description of the numerical model used to predict spherical diffusion flames was presented in Chapter 3. The numerical code features a detailed chemistry model for the pyrolysis and oxidation of fuel, involving up to 101 species and 544 reactions. Governing equations were discretized using first and second order spatial schemes and transient problems were solved using implicit time marching combined with a modified Newton method. Radiation from $CO_2$, $O_2$, and $H_2O$ were described by solving the radiative transfer equation using the discrete ordinates method.

In Chapter 4, the behavior of micro-diffusion hydrogen flames was numerically investigated. Experimentally observed weak hydrogen flames near kinetic extinction were modeled. Predicted mass flow rates near extinction agree with those observed experimentally. Effects of the burner size and mass flow rate on the flame structure, and kinetics, were predicted. It was found that the burner may truncate the flame structure and force a partially burning combustion regime with extensive $O_2$ leakage, accelerating kinetic extinction. The lowest mass flow rates sustaining an adiabatic flame were predicted.

A brief description of soot phenomenology was provided in Chapter 5. A detailed study of spherical $C_2H_4$ diffusion flames exhibiting sooting limits were presented. Sooting limits were expressed in terms of critical C/O ratio, temperature, and characteristic transport time scale. A critical local C/O ratio at sooting limits was identified and effects of time and temperature were reported.

Chapter 6 reported the incorporation of soot modeling capabilities in the numerical code. Dynamics of the soot population with the effects of nucleation, coagulation, surface growth by HACA mechanism and PAH condensation, and soot particle oxidation by OH and $O_2$, were modeled using the method of moments using the first six moments. Radiative heat losses by soot particles were modeled. These new capabilities were used to model soot formation inside a steady state spherical diffusion flame resembling initial conditions for transient modeling. This new feature offers new capabilities to study the spherical flame sooting limits in Chapter 5 and would validate the present observations performed with the consideration of only gas-phase species.

As mentioned in Chapter 6, the treatment of soot oxidation needs additional improvements to fully model soot burn-out. In addition, soot radiative heat losses can be improved by the use of a more detailed model, with the full consideration of the soot particle size density function and offering a more fundamental description of soot radiation.

# Appendix A

# GRI-Mech 3.0

GRI-Mech 3.0 is an optimized mechanism designed to model natural gas combustion, including NO formation and reburn chemistry. Developped by Gas Research Institute, this mechanism contains 325 reactions and 53 species [64]. The reactions are given below. The atomic elements considered are O,H,C,N, and AR. The 53 species involved are listed in the table below. The mechanism is expressed below using the CHEMKIN format [58].

Table A.1: Species considered in GRI-Mech 3.0.

| | | | | | | | |
|---|---|---|---|---|---|---|---|
| $H_2$ | H | O | $O_2$ | OH | $H_2O$ | $HO_2$ | $H_2O_2$ |
| C | CH | $CH_2$ | $CH_2$(S) | $CH_3$ | $CH_4$ | CO | $CO_2$ |
| HCO | $CH_2O$ | $CH_2OH$ | $CH_3O$ | $CH_3OH$ | $C_2H$ | $C_2H_2$ | $C_2H_3$ |
| $C_2H_4$ | $C_2H_5$ | $C_2H_6$ | HCCO | $CH_2CO$ | HCCOH | N | NH |
| $NH_2$ | $NH_3$ | NNH | NO | $NO_2$ | $N_2O$ | HNO | CN |
| HCN | $H_2CN$ | HCNN | HCNO | HOCN | HNCO | NCO | $N_2$ |
| AR | $C_3H_7$ | $C_3H_8$ | $CH_2CHO$ | $CH_3CHO$ | | | |

```
REACTIONS
2O+M<=>O2+M                                 1.200E+17   -1.000        .00
H2/ 2.40/ H2O/15.40/ CH4/ 2.00/ CO/ 1.75/ CO2/ 3.60/ C2H6/ 3.00/ AR/  .83/
O+H+M<=>OH+M                                5.000E+17   -1.000        .00
H2/2.00/ H2O/6.00/ CH4/2.00/ CO/1.50/ CO2/2.00/ C2H6/3.00/ AR/ .70/
O+H2<=>H+OH                                 3.870E+04    2.700    6260.00
O+HO2<=>OH+O2                               2.000E+13     .000        .00
O+H2O2<=>OH+HO2                             9.630E+06    2.000    4000.00
O+CH<=>H+CO                                 5.700E+13     .000        .00
```

```
O+CH2<=>H+HCO                                 8.000E+13     .000        .00
O+CH2(S)<=>H2+CO                              1.500E+13     .000        .00
O+CH2(S)<=>H+HCO                              1.500E+13     .000        .00
O+CH3<=>H+CH2O                                5.060E+13     .000        .00
O+CH4<=>OH+CH3                                1.020E+09    1.500    8600.00
O+CO(+M)<=>CO2(+M)                            1.800E+10     .000    2385.00
   LOW/ 6.020E+14     .000    3000.00/
H2/2.00/ O2/6.00/ H2O/6.00/ CH4/2.00/ CO/1.50/ CO2/3.50/ C2H6/3.00/ AR/ .50/
O+HCO<=>OH+CO                                 3.000E+13     .000        .00
O+HCO<=>H+CO2                                 3.000E+13     .000        .00
O+CH2O<=>OH+HCO                               3.900E+13     .000    3540.00
O+CH2OH<=>OH+CH2O                             1.000E+13     .000        .00
O+CH3O<=>OH+CH2O                              1.000E+13     .000        .00
O+CH3OH<=>OH+CH2OH                            3.880E+05    2.500    3100.00
O+CH3OH<=>OH+CH3O                             1.300E+05    2.500    5000.00
O+C2H<=>CH+CO                                 5.000E+13     .000        .00
O+C2H2<=>H+HCCO                               1.350E+07    2.000    1900.00
O+C2H2<=>OH+C2H                               4.600E+19   -1.410   28950.00
O+C2H2<=>CO+CH2                               6.940E+06    2.000    1900.00
O+C2H3<=>H+CH2CO                              3.000E+13     .000        .00
O+C2H4<=>CH3+HCO                              1.250E+07    1.830     220.00
O+C2H5<=>CH3+CH2O                             2.240E+13     .000        .00
O+C2H6<=>OH+C2H5                              8.980E+07    1.920    5690.00
O+HCCO<=>H+2CO                                1.000E+14     .000        .00
O+CH2CO<=>OH+HCCO                             1.000E+13     .000    8000.00
O+CH2CO<=>CH2+CO2                             1.750E+12     .000    1350.00
O2+CO<=>O+CO2                                 2.500E+12     .000   47800.00
O2+CH2O<=>HO2+HCO                             1.000E+14     .000   40000.00
H+O2+M<=>HO2+M                                2.800E+18    -.860        .00
O2/ .00/ H2O/ .00/ CO/ .75/ CO2/1.50/ C2H6/1.50/ N2/ .00/ AR/ .00/
H+2O2<=>HO2+O2                                2.080E+19   -1.240        .00
H+O2+H2O<=>HO2+H2O                            11.26E+18    -.760        .00
H+O2+N2<=>HO2+N2                              2.600E+19   -1.240        .00
H+O2+AR<=>HO2+AR                              7.000E+17    -.800        .00
H+O2<=>O+OH                                   2.650E+16    -.6707  17041.00
2H+M<=>H2+M                                   1.000E+18   -1.000        .00
H2/ .00/ H2O/ .00/ CH4/2.00/ CO2/ .00/ C2H6/3.00/ AR/ .63/
2H+H2<=>2H2                                   9.000E+16    -.600        .00
2H+H2O<=>H2+H2O                               6.000E+19   -1.250        .00
2H+CO2<=>H2+CO2                               5.500E+20   -2.000        .00
H+OH+M<=>H2O+M                                2.200E+22   -2.000        .00
H2/ .73/ H2O/3.65/ CH4/2.00/ C2H6/3.00/ AR/ .38/
H+HO2<=>O+H2O                                 3.970E+12     .000     671.00
H+HO2<=>O2+H2                                 4.480E+13     .000    1068.00
H+HO2<=>2OH                                   0.840E+14     .000     635.00
```

```
H+H2O2<=>HO2+H2                          1.210E+07    2.000    5200.00
H+H2O2<=>OH+H2O                          1.000E+13     .000    3600.00
H+CH<=>C+H2                              1.650E+14     .000        .00
H+CH2(+M)<=>CH3(+M)                      6.000E+14     .000        .00
     LOW  /  1.040E+26   -2.760   1600.00/
     TROE/   .5620  91.00  5836.00  8552.00/
H2/2.00/ H2O/6.00/ CH4/2.00/ CO/1.50/ CO2/2.00/ C2H6/3.00/ AR/ .70/
H+CH2(S)<=>CH+H2                         3.000E+13     .000        .00
H+CH3(+M)<=>CH4(+M)                      13.90E+15    -.534     536.00
     LOW  /  2.620E+33   -4.760   2440.00/
     TROE/   .7830   74.00  2941.00  6964.00 /
H2/2.00/ H2O/6.00/ CH4/3.00/ CO/1.50/ CO2/2.00/ C2H6/3.00/ AR/ .70/
H+CH4<=>CH3+H2                           6.600E+08    1.620   10840.00
H+HCO(+M)<=>CH2O(+M)                     1.090E+12     .480    -260.00
     LOW  /  2.470E+24   -2.570    425.00/
     TROE/   .7824  271.00  2755.00  6570.00 /
H2/2.00/ H2O/6.00/ CH4/2.00/ CO/1.50/ CO2/2.00/ C2H6/3.00/ AR/ .70/
H+HCO<=>H2+CO                            7.340E+13     .000        .00
H+CH2O(+M)<=>CH2OH(+M)                   5.400E+11     .454    3600.00
     LOW  /  1.270E+32   -4.820   6530.00/
     TROE/   .7187  103.00  1291.00  4160.00 /
H2/2.00/ H2O/6.00/ CH4/2.00/ CO/1.50/ CO2/2.00/ C2H6/3.00/
H+CH2O(+M)<=>CH3O(+M)                    5.400E+11     .454    2600.00
     LOW  /  2.200E+30   -4.800   5560.00/
     TROE/   .7580   94.00  1555.00  4200.00 /
H2/2.00/ H2O/6.00/ CH4/2.00/ CO/1.50/ CO2/2.00/ C2H6/3.00/
H+CH2O<=>HCO+H2                          5.740E+07    1.900    2742.00
H+CH2OH(+M)<=>CH3OH(+M)                  1.055E+12     .500      86.00
     LOW  /  4.360E+31   -4.650   5080.00/
     TROE/   .600  100.00  90000.0  10000.0 /
H2/2.00/ H2O/6.00/ CH4/2.00/ CO/1.50/ CO2/2.00/ C2H6/3.00/
H+CH2OH<=>H2+CH2O                        2.000E+13     .000        .00
H+CH2OH<=>OH+CH3                         1.650E+11     .650    -284.00
H+CH2OH<=>CH2(S)+H2O                     3.280E+13    -.090     610.00
H+CH3O(+M)<=>CH3OH(+M)                   2.430E+12     .515      50.00
     LOW  /  4.660E+41   -7.440   14080.0/
     TROE/   .700  100.00  90000.0 10000.00 /
H2/2.00/ H2O/6.00/ CH4/2.00/ CO/1.50/ CO2/2.00/ C2H6/3.00/
H+CH3O<=>H+CH2OH                         4.150E+07    1.630    1924.00
H+CH3O<=>H2+CH2O                         2.000E+13     .000        .00
H+CH3O<=>OH+CH3                          1.500E+12     .500    -110.00
H+CH3O<=>CH2(S)+H2O                      2.620E+14    -.230    1070.00
H+CH3OH<=>CH2OH+H2                       1.700E+07    2.100    4870.00
H+CH3OH<=>CH3O+H2                        4.200E+06    2.100    4870.00
H+C2H(+M)<=>C2H2(+M)                     1.000E+17   -1.000        .00
```

```
     LOW  /  3.750E+33   -4.800   1900.00/
     TROE/   .6464  132.00  1315.00  5566.00 /
H2/2.00/ H2O/6.00/ CH4/2.00/ CO/1.50/ CO2/2.00/ C2H6/3.00/ AR/ .70/
H+C2H2(+M)<=>C2H3(+M)                     5.600E+12     .000    2400.00
     LOW  /  3.800E+40   -7.270   7220.00/
     TROE/   .7507   98.50  1302.00  4167.00 /
H2/2.00/ H2O/6.00/ CH4/2.00/ CO/1.50/ CO2/2.00/ C2H6/3.00/ AR/ .70/
H+C2H3(+M)<=>C2H4(+M)                     6.080E+12     .270     280.00
     LOW  /  1.400E+30   -3.860   3320.00/
     TROE/   .7820  207.50  2663.00  6095.00 /
H2/2.00/ H2O/6.00/ CH4/2.00/ CO/1.50/ CO2/2.00/ C2H6/3.00/ AR/ .70/
H+C2H3<=>H2+C2H2                          3.000E+13     .000        .00
H+C2H4(+M)<=>C2H5(+M)                     0.540E+12     .454    1820.00
     LOW  /  0.600E+42   -7.620   6970.00/
     TROE/   .9753  210.00   984.00  4374.00 /
H2/2.00/ H2O/6.00/ CH4/2.00/ CO/1.50/ CO2/2.00/ C2H6/3.00/ AR/ .70/
H+C2H4<=>C2H3+H2                          1.325E+06    2.530   12240.00
H+C2H5(+M)<=>C2H6(+M)                     5.210E+17    -.990    1580.00
     LOW  /  1.990E+41   -7.080   6685.00/
     TROE/   .8422  125.00  2219.00  6882.00 /
H2/2.00/ H2O/6.00/ CH4/2.00/ CO/1.50/ CO2/2.00/ C2H6/3.00/ AR/ .70/
H+C2H5<=>H2+C2H4                          2.000E+12     .000        .00
H+C2H6<=>C2H5+H2                          1.150E+08    1.900    7530.00
H+HCCO<=>CH2(S)+CO                        1.000E+14     .000        .00
H+CH2CO<=>HCCO+H2                         5.000E+13     .000    8000.00
H+CH2CO<=>CH3+CO                          1.130E+13     .000    3428.00
H+HCCOH<=>H+CH2CO                         1.000E+13     .000        .00
H2+CO(+M)<=>CH2O(+M)                      4.300E+07    1.500   79600.00
     LOW  /  5.070E+27   -3.420  84350.00/
     TROE/   .9320  197.00  1540.00 10300.00 /
H2/2.00/ H2O/6.00/ CH4/2.00/ CO/1.50/ CO2/2.00/ C2H6/3.00/ AR/ .70/
OH+H2<=>H+H2O                             2.160E+08    1.510    3430.00
2OH(+M)<=>H2O2(+M)                        7.400E+13    -.370        .00
     LOW  /  2.300E+18    -.900  -1700.00/
     TROE/   .7346   94.00  1756.00  5182.00 /
H2/2.00/ H2O/6.00/ CH4/2.00/ CO/1.50/ CO2/2.00/ C2H6/3.00/ AR/ .70/
2OH<=>O+H2O                               3.570E+04    2.400   -2110.00
OH+HO2<=>O2+H2O                           1.450E+13     .000    -500.00
 DUPLICATE
OH+H2O2<=>HO2+H2O                         2.000E+12     .000     427.00
 DUPLICATE
OH+H2O2<=>HO2+H2O                         1.700E+18     .000   29410.00
 DUPLICATE
OH+C<=>H+CO                               5.000E+13     .000        .00
OH+CH<=>H+HCO                             3.000E+13     .000        .00
```

```
OH+CH2<=>H+CH2O                           2.000E+13     .000        .00
OH+CH2<=>CH+H2O                           1.130E+07    2.000    3000.00
OH+CH2(S)<=>H+CH2O                        3.000E+13     .000        .00
OH+CH3(+M)<=>CH3OH(+M)                    2.790E+18   -1.430    1330.00
     LOW  /  4.000E+36   -5.920   3140.00/
     TROE/   .4120  195.0  5900.00  6394.00/
H2/2.00/ H2O/6.00/ CH4/2.00/ CO/1.50/ CO2/2.00/ C2H6/3.00/
OH+CH3<=>CH2+H2O                          5.600E+07    1.600    5420.00
OH+CH3<=>CH2(S)+H2O                       6.440E+17   -1.340    1417.00
OH+CH4<=>CH3+H2O                          1.000E+08    1.600    3120.00
OH+CO<=>H+CO2                             4.760E+07    1.228      70.00
OH+HCO<=>H2O+CO                           5.000E+13     .000        .00
OH+CH2O<=>HCO+H2O                         3.430E+09    1.180    -447.00
OH+CH2OH<=>H2O+CH2O                       5.000E+12     .000        .00
OH+CH3O<=>H2O+CH2O                        5.000E+12     .000        .00
OH+CH3OH<=>CH2OH+H2O                      1.440E+06    2.000    -840.00
OH+CH3OH<=>CH3O+H2O                       6.300E+06    2.000    1500.00
OH+C2H<=>H+HCCO                           2.000E+13     .000        .00
OH+C2H2<=>H+CH2CO                         2.180E-04    4.500   -1000.00
OH+C2H2<=>H+HCCOH                         5.040E+05    2.300   13500.00
OH+C2H2<=>C2H+H2O                         3.370E+07    2.000   14000.00
OH+C2H2<=>CH3+CO                          4.830E-04    4.000   -2000.00
OH+C2H3<=>H2O+C2H2                        5.000E+12     .000        .00
OH+C2H4<=>C2H3+H2O                        3.600E+06    2.000    2500.00
OH+C2H6<=>C2H5+H2O                        3.540E+06    2.120     870.00
OH+CH2CO<=>HCCO+H2O                       7.500E+12     .000    2000.00
2HO2<=>O2+H2O2                            1.300E+11     .000   -1630.00
 DUPLICATE
2HO2<=>O2+H2O2                            4.200E+14     .000   12000.00
 DUPLICATE
HO2+CH2<=>OH+CH2O                         2.000E+13     .000        .00
HO2+CH3<=>O2+CH4                          1.000E+12     .000        .00
HO2+CH3<=>OH+CH3O                         3.780E+13     .000        .00
HO2+CO<=>OH+CO2                           1.500E+14     .000   23600.00
HO2+CH2O<=>HCO+H2O2                       5.600E+06    2.000   12000.00
C+O2<=>O+CO                               5.800E+13     .000     576.00
C+CH2<=>H+C2H                             5.000E+13     .000        .00
C+CH3<=>H+C2H2                            5.000E+13     .000        .00
CH+O2<=>O+HCO                             6.710E+13     .000        .00
CH+H2<=>H+CH2                             1.080E+14     .000    3110.00
CH+H2O<=>H+CH2O                           5.710E+12     .000    -755.00
CH+CH2<=>H+C2H2                           4.000E+13     .000        .00
CH+CH3<=>H+C2H3                           3.000E+13     .000        .00
CH+CH4<=>H+C2H4                           6.000E+13     .000        .00
CH+CO(+M)<=>HCCO(+M)                      5.000E+13     .000        .00
```

```
     LOW  /  2.690E+28   -3.740   1936.00/
     TROE/   .5757  237.00  1652.00  5069.00 /
H2/2.00/ H2O/6.00/ CH4/2.00/ CO/1.50/ CO2/2.00/ C2H6/3.00/ AR/ .70/
CH+CO2<=>HCO+CO                          1.900E+14     .000   15792.00
CH+CH2O<=>H+CH2CO                        9.460E+13     .000    -515.00
CH+HCCO<=>CO+C2H2                        5.000E+13     .000        .00
CH2+O2=>OH+H+CO                          5.000E+12     .000    1500.00
CH2+H2<=>H+CH3                           5.000E+05    2.000    7230.00
2CH2<=>H2+C2H2                           1.600E+15     .000   11944.00
CH2+CH3<=>H+C2H4                         4.000E+13     .000        .00
CH2+CH4<=>2CH3                           2.460E+06    2.000    8270.00
CH2+CO(+M)<=>CH2CO(+M)                   8.100E+11     .500    4510.00
     LOW  /  2.690E+33   -5.110   7095.00/
     TROE/   .5907  275.00  1226.00  5185.00 /
H2/2.00/ H2O/6.00/ CH4/2.00/ CO/1.50/ CO2/2.00/ C2H6/3.00/ AR/ .70/
CH2+HCCO<=>C2H3+CO                       3.000E+13     .000        .00
CH2(S)+N2<=>CH2+N2                       1.500E+13     .000     600.00
CH2(S)+AR<=>CH2+AR                       9.000E+12     .000     600.00
CH2(S)+O2<=>H+OH+CO                      2.800E+13     .000        .00
CH2(S)+O2<=>CO+H2O                       1.200E+13     .000        .00
CH2(S)+H2<=>CH3+H                        7.000E+13     .000        .00
CH2(S)+H2O(+M)<=>CH3OH(+M)               4.820E+17   -1.160    1145.00
     LOW  /  1.880E+38   -6.360   5040.00/
     TROE/   .6027  208.00  3922.00  10180.0 /
H2/2.00/ H2O/6.00/ CH4/2.00/ CO/1.50/ CO2/2.00/ C2H6/3.00/
CH2(S)+H2O<=>CH2+H2O                     3.000E+13     .000        .00
CH2(S)+CH3<=>H+C2H4                      1.200E+13     .000    -570.00
CH2(S)+CH4<=>2CH3                        1.600E+13     .000    -570.00
CH2(S)+CO<=>CH2+CO                       9.000E+12     .000        .00
CH2(S)+CO2<=>CH2+CO2                     7.000E+12     .000        .00
CH2(S)+CO2<=>CO+CH2O                     1.400E+13     .000        .00
CH2(S)+C2H6<=>CH3+C2H5                   4.000E+13     .000    -550.00
CH3+O2<=>O+CH3O                          3.560E+13     .000   30480.00
CH3+O2<=>OH+CH2O                         2.310E+12     .000   20315.00
CH3+H2O2<=>HO2+CH4                       2.450E+04    2.470    5180.00
2CH3(+M)<=>C2H6(+M)                      6.770E+16   -1.180     654.00
     LOW  /  3.400E+41   -7.030   2762.00/
     TROE/   .6190  73.20  1180.00  9999.00 /
H2/2.00/ H2O/6.00/ CH4/2.00/ CO/1.50/ CO2/2.00/ C2H6/3.00/ AR/ .70/
2CH3<=>H+C2H5                            6.840E+12     .100   10600.00
CH3+HCO<=>CH4+CO                         2.648E+13     .000        .00
CH3+CH2O<=>HCO+CH4                       3.320E+03    2.810    5860.00
CH3+CH3OH<=>CH2OH+CH4                    3.000E+07    1.500    9940.00
CH3+CH3OH<=>CH3O+CH4                     1.000E+07    1.500    9940.00
CH3+C2H4<=>C2H3+CH4                      2.270E+05    2.000    9200.00
```

```
CH3+C2H6<=>C2H5+CH4                          6.140E+06    1.740   10450.00
HCO+H2O<=>H+CO+H2O                           1.500E+18   -1.000   17000.00
HCO+M<=>H+CO+M                               1.870E+17   -1.000   17000.00
H2/2.00/ H2O/ .00/ CH4/2.00/ CO/1.50/ CO2/2.00/ C2H6/3.00/
HCO+O2<=>HO2+CO                              13.45E+12     .000     400.00
CH2OH+O2<=>HO2+CH2O                          1.800E+13     .000     900.00
CH3O+O2<=>HO2+CH2O                           4.280E-13    7.600   -3530.00
C2H+O2<=>HCO+CO                              1.000E+13     .000    -755.00
C2H+H2<=>H+C2H2                              5.680E+10    0.900    1993.00
C2H3+O2<=>HCO+CH2O                           4.580E+16   -1.390    1015.00
C2H4(+M)<=>H2+C2H2(+M)                       8.000E+12     .440   86770.00
     LOW  /  1.580E+51   -9.300  97800.00/
     TROE/   .7345  180.00  1035.00  5417.00 /
H2/2.00/ H2O/6.00/ CH4/2.00/ CO/1.50/ CO2/2.00/ C2H6/3.00/ AR/ .70/
C2H5+O2<=>HO2+C2H4                           8.400E+11     .000    3875.00
HCCO+O2<=>OH+2CO                             3.200E+12     .000     854.00
2HCCO<=>2CO+C2H2                             1.000E+13     .000        .00
N+NO<=>N2+O                                  2.700E+13     .000     355.00
N+O2<=>NO+O                                  9.000E+09    1.000    6500.00
N+OH<=>NO+H                                  3.360E+13     .000     385.00
N2O+O<=>N2+O2                                1.400E+12     .000   10810.00
N2O+O<=>2NO                                  2.900E+13     .000   23150.00
N2O+H<=>N2+OH                                3.870E+14     .000   18880.00
N2O+OH<=>N2+HO2                              2.000E+12     .000   21060.00
N2O(+M)<=>N2+O(+M)                           7.910E+10     .000   56020.00
     LOW  /  6.370E+14     .000  56640.00/
H2/2.00/ H2O/6.00/ CH4/2.00/ CO/1.50/ CO2/2.00/ C2H6/3.00/ AR/ .625/
HO2+NO<=>NO2+OH                              2.110E+12     .000    -480.00
NO+O+M<=>NO2+M                               1.060E+20   -1.410        .00
H2/2.00/ H2O/6.00/ CH4/2.00/ CO/1.50/ CO2/2.00/ C2H6/3.00/ AR/ .70/
NO2+O<=>NO+O2                                3.900E+12     .000    -240.00
NO2+H<=>NO+OH                                1.320E+14     .000     360.00
NH+O<=>NO+H                                  4.000E+13     .000        .00
NH+H<=>N+H2                                  3.200E+13     .000     330.00
NH+OH<=>HNO+H                                2.000E+13     .000        .00
NH+OH<=>N+H2O                                2.000E+09    1.200        .00
NH+O2<=>HNO+O                                4.610E+05    2.000    6500.00
NH+O2<=>NO+OH                                1.280E+06    1.500     100.00
NH+N<=>N2+H                                  1.500E+13     .000        .00
NH+H2O<=>HNO+H2                              2.000E+13     .000   13850.00
NH+NO<=>N2+OH                                2.160E+13    -.230        .00
NH+NO<=>N2O+H                                3.650E+14    -.450        .00
NH2+O<=>OH+NH                                3.000E+12     .000        .00
NH2+O<=>H+HNO                                3.900E+13     .000        .00
NH2+H<=>NH+H2                                4.000E+13     .000    3650.00
```

```
NH2+OH<=>NH+H2O                          9.000E+07    1.500    -460.00
NNH<=>N2+H                               3.300E+08     .000        .00
NNH+M<=>N2+H+M                           1.300E+14    -.110    4980.00
H2/2.00/ H2O/6.00/ CH4/2.00/ CO/1.50/ CO2/2.00/ C2H6/3.00/ AR/ .70/
NNH+O2<=>HO2+N2                          5.000E+12     .000        .00
NNH+O<=>OH+N2                            2.500E+13     .000        .00
NNH+O<=>NH+NO                            7.000E+13     .000        .00
NNH+H<=>H2+N2                            5.000E+13     .000        .00
NNH+OH<=>H2O+N2                          2.000E+13     .000        .00
NNH+CH3<=>CH4+N2                         2.500E+13     .000        .00
H+NO+M<=>HNO+M                           4.480E+19   -1.320     740.00
H2/2.00/ H2O/6.00/ CH4/2.00/ CO/1.50/ CO2/2.00/ C2H6/3.00/ AR/ .70/
HNO+O<=>NO+OH                            2.500E+13     .000        .00
HNO+H<=>H2+NO                            9.000E+11     .720     660.00
HNO+OH<=>NO+H2O                          1.300E+07    1.900    -950.00
HNO+O2<=>HO2+NO                          1.000E+13     .000   13000.00
CN+O<=>CO+N                              7.700E+13     .000        .00
CN+OH<=>NCO+H                            4.000E+13     .000        .00
CN+H2O<=>HCN+OH                          8.000E+12     .000    7460.00
CN+O2<=>NCO+O                            6.140E+12     .000    -440.00
CN+H2<=>HCN+H                            2.950E+05    2.450    2240.00
NCO+O<=>NO+CO                            2.350E+13     .000        .00
NCO+H<=>NH+CO                            5.400E+13     .000        .00
NCO+OH<=>NO+H+CO                         0.250E+13     .000        .00
NCO+N<=>N2+CO                            2.000E+13     .000        .00
NCO+O2<=>NO+CO2                          2.000E+12     .000   20000.00
NCO+M<=>N+CO+M                           3.100E+14     .000   54050.00
H2/2.00/ H2O/6.00/ CH4/2.00/ CO/1.50/ CO2/2.00/ C2H6/3.00/ AR/ .70/
NCO+NO<=>N2O+CO                          1.900E+17   -1.520     740.00
NCO+NO<=>N2+CO2                          3.800E+18   -2.000     800.00
HCN+M<=>H+CN+M                           1.040E+29   -3.300  126600.00
H2/2.00/ H2O/6.00/ CH4/2.00/ CO/1.50/ CO2/2.00/ C2H6/3.00/ AR/ .70/
HCN+O<=>NCO+H                            2.030E+04    2.640    4980.00
HCN+O<=>NH+CO                            5.070E+03    2.640    4980.00
HCN+O<=>CN+OH                            3.910E+09    1.580   26600.00
HCN+OH<=>HOCN+H                          1.100E+06    2.030   13370.00
HCN+OH<=>HNCO+H                          4.400E+03    2.260    6400.00
HCN+OH<=>NH2+CO                          1.600E+02    2.560    9000.00
H+HCN(+M)<=>H2CN(+M)                     3.300E+13     .000        .00
      LOW /  1.400E+26   -3.400    1900.00/
H2/2.00/ H2O/6.00/ CH4/2.00/ CO/1.50/ CO2/2.00/ C2H6/3.00/ AR/ .70/
H2CN+N<=>N2+CH2                          6.000E+13     .000     400.00
C+N2<=>CN+N                              6.300E+13     .000   46020.00
CH+N2<=>HCN+N                            3.120E+09    0.880   20130.00
CH+N2(+M)<=>HCNN(+M)                     3.100E+12     .150        .00
```

```
     LOW  /  1.300E+25   -3.160    740.00/
     TROE/   .6670  235.00  2117.00  4536.00 /
H2/2.00/ H2O/6.00/ CH4/2.00/ CO/1.50/ CO2/2.00/ C2H6/3.00/ AR/ 1.0/
CH2+N2<=>HCN+NH                          1.000E+13     .000   74000.00
CH2(S)+N2<=>NH+HCN                       1.000E+11     .000   65000.00
C+NO<=>CN+O                              1.900E+13     .000        .00
C+NO<=>CO+N                              2.900E+13     .000        .00
CH+NO<=>HCN+O                            4.100E+13     .000        .00
CH+NO<=>H+NCO                            1.620E+13     .000        .00
CH+NO<=>N+HCO                            2.460E+13     .000        .00
CH2+NO<=>H+HNCO                          3.100E+17   -1.380    1270.00
CH2+NO<=>OH+HCN                          2.900E+14    -.690     760.00
CH2+NO<=>H+HCNO                          3.800E+13    -.360     580.00
CH2(S)+NO<=>H+HNCO                       3.100E+17   -1.380    1270.00
CH2(S)+NO<=>OH+HCN                       2.900E+14    -.690     760.00
CH2(S)+NO<=>H+HCNO                       3.800E+13    -.360     580.00
CH3+NO<=>HCN+H2O                         9.600E+13     .000   28800.00
CH3+NO<=>H2CN+OH                         1.000E+12     .000   21750.00
HCNN+O<=>CO+H+N2                         2.200E+13     .000        .00
HCNN+O<=>HCN+NO                          2.000E+12     .000        .00
HCNN+O2<=>O+HCO+N2                       1.200E+13     .000        .00
HCNN+OH<=>H+HCO+N2                       1.200E+13     .000        .00
HCNN+H<=>CH2+N2                          1.000E+14     .000        .00
HNCO+O<=>NH+CO2                          9.800E+07    1.410    8500.00
HNCO+O<=>HNO+CO                          1.500E+08    1.570   44000.00
HNCO+O<=>NCO+OH                          2.200E+06    2.110   11400.00
HNCO+H<=>NH2+CO                          2.250E+07    1.700    3800.00
HNCO+H<=>H2+NCO                          1.050E+05    2.500   13300.00
HNCO+OH<=>NCO+H2O                        3.300E+07    1.500    3600.00
HNCO+OH<=>NH2+CO2                        3.300E+06    1.500    3600.00
HNCO+M<=>NH+CO+M                         1.180E+16     .000   84720.00
H2/2.00/ H2O/6.00/ CH4/2.00/ CO/1.50/ CO2/2.00/ C2H6/3.00/ AR/ .70/
HCNO+H<=>H+HNCO                          2.100E+15    -.690    2850.00
HCNO+H<=>OH+HCN                          2.700E+11     .180    2120.00
HCNO+H<=>NH2+CO                          1.700E+14    -.750    2890.00
HOCN+H<=>H+HNCO                          2.000E+07    2.000    2000.00
HCCO+NO<=>HCNO+CO                        0.900E+13     .000        .00
CH3+N<=>H2CN+H                           6.100E+14    -.310     290.00
CH3+N<=>HCN+H2                           3.700E+12     .150     -90.00
NH3+H<=>NH2+H2                           5.400E+05    2.400    9915.00
NH3+OH<=>NH2+H2O                         5.000E+07    1.600     955.00
NH3+O<=>NH2+OH                           9.400E+06    1.940    6460.00
NH+CO2<=>HNO+CO                          1.000E+13     .000   14350.00
CN+NO2<=>NCO+NO                          6.160E+15   -0.752     345.00
NCO+NO2<=>N2O+CO2                        3.250E+12     .000    -705.00
```

```
N+CO2<=>NO+CO                             3.000E+12     .000   11300.00
O+CH3=>H+H2+CO                            3.370E+13     .000        .00
O+C2H4<=>H+CH2CHO                         6.700E+06    1.830     220.00
O+C2H5<=>H+CH3CHO                         1.096E+14     .000        .00
OH+HO2<=>O2+H2O                           0.500E+16     .000   17330.00
  DUPLICATE
OH+CH3=>H2+CH2O                           8.000E+09     .500   -1755.00
CH+H2(+M)<=>CH3(+M)                       1.970E+12     .430    -370.00
   LOW/ 4.820E+25  -2.80  590.0 /
   TROE/ .578  122.0  2535.0  9365.0 /
H2/2.00/ H2O/6.00/ CH4/2.00/ CO/1.50/ CO2/2.00/ C2H6/3.00/ AR/ .70/
CH2+O2=>2H+CO2                            5.800E+12     .000    1500.00
CH2+O2<=>O+CH2O                           2.400E+12     .000    1500.00
CH2+CH2=>2H+C2H2                          2.000E+14     .000   10989.00
CH2(S)+H2O=>H2+CH2O                       6.820E+10     .250    -935.00
C2H3+O2<=>O+CH2CHO                        3.030E+11     .290      11.00
C2H3+O2<=>HO2+C2H2                        1.337E+06    1.610    -384.00
O+CH3CHO<=>OH+CH2CHO                      2.920E+12     .000    1808.00
O+CH3CHO=>OH+CH3+CO                       2.920E+12     .000    1808.00
O2+CH3CHO=>HO2+CH3+CO                     3.010E+13     .000   39150.00
H+CH3CHO<=>CH2CHO+H2                      2.050E+09    1.160    2405.00
H+CH3CHO=>CH3+H2+CO                       2.050E+09    1.160    2405.00
OH+CH3CHO=>CH3+H2O+CO                     2.343E+10    0.730   -1113.00
HO2+CH3CHO=>CH3+H2O2+CO                   3.010E+12     .000   11923.00
CH3+CH3CHO=>CH3+CH4+CO                    2.720E+06    1.770    5920.00
H+CH2CO(+M)<=>CH2CHO(+M)                  4.865E+11    0.422   -1755.00
    LOW/ 1.012E+42  -7.63  3854.0/
    TROE/ 0.465  201.0  1773.0  5333.0 /
H2/2.00/ H2O/6.00/ CH4/2.00/ CO/1.50/ CO2/2.00/ C2H6/3.00/ AR/ .70/
O+CH2CHO=>H+CH2+CO2                       1.500E+14     .000       .00
O2+CH2CHO=>OH+CO+CH2O                     1.810E+10     .000       .00
O2+CH2CHO=>OH+2HCO                        2.350E+10     .000       .00
H+CH2CHO<=>CH3+HCO                        2.200E+13     .000       .00
H+CH2CHO<=>CH2CO+H2                       1.100E+13     .000       .00
OH+CH2CHO<=>H2O+CH2CO                     1.200E+13     .000       .00
OH+CH2CHO<=>HCO+CH2OH                     3.010E+13     .000       .00
CH3+C2H5(+M)<=>C3H8(+M)                    .9430E+13    .000       .00
     LOW/ 2.710E+74  -16.82  13065.0 /
     TROE/ .1527  291.0  2742.0  7748.0 /
H2/2.00/ H2O/6.00/ CH4/2.00/ CO/1.50/ CO2/2.00/ C2H6/3.00/ AR/ .70/
O+C3H8<=>OH+C3H7                          1.930E+05    2.680   3716.00
H+C3H8<=>C3H7+H2                          1.320E+06    2.540   6756.00
OH+C3H8<=>C3H7+H2O                        3.160E+07    1.800    934.00
C3H7+H2O2<=>HO2+C3H8                      3.780E+02    2.720   1500.00
CH3+C3H8<=>C3H7+CH4                       0.903E+00    3.650   7154.00
```

```
CH3+C2H4(+M)<=>C3H7(+M)                    2.550E+06    1.600   5700.00
      LOW/ 3.00E+63  -14.6  18170./
      TROE/ .1894  277.0  8748.0  7891.0 /
H2/2.00/ H2O/6.00/ CH4/2.00/ CO/1.50/ CO2/2.00/ C2H6/3.00/ AR/ .70/
O+C3H7<=>C2H5+CH2O                         9.640E+13     .000       .00
H+C3H7(+M)<=>C3H8(+M)                      3.613E+13     .000       .00
      LOW/ 4.420E+61  -13.545  11357.0/
      TROE/ .315  369.0  3285.0  6667.0 /
H2/2.00/ H2O/6.00/ CH4/2.00/ CO/1.50/ CO2/2.00/ C2H6/3.00/ AR/ .70/
H+C3H7<=>CH3+C2H5                          4.060E+06    2.190    890.00
OH+C3H7<=>C2H5+CH2OH                       2.410E+13     .000       .00
HO2+C3H7<=>O2+C3H8                         2.550E+10    0.255   -943.00
HO2+C3H7=>OH+C2H5+CH2O                     2.410E+13     .000       .00
CH3+C3H7<=>2C2H5                           1.927E+13   -0.320       .00
END
```

# Appendix B

# Temporal Evolution of Sooting Limit Flames

In this appendix, predicted characteristics of the sooting limit flames from [55] are presented. All the numerical simulations were performed using the ABF model [67].

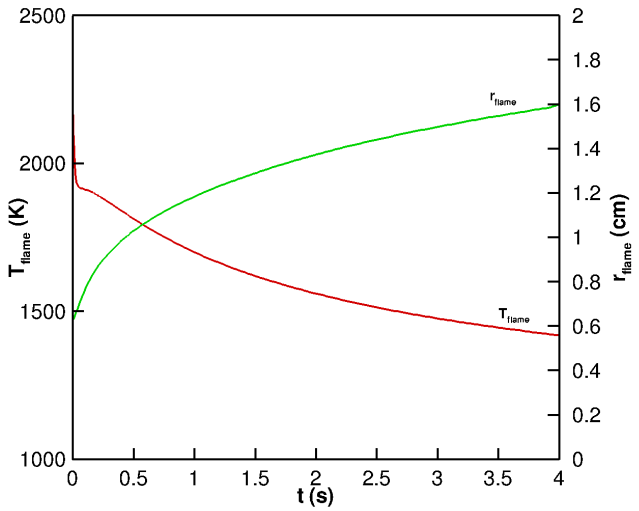


Figure B.1: Predicted flame radius and peak temperature of Flame 1, from ignition ($t = 0$ s) to 4 s.

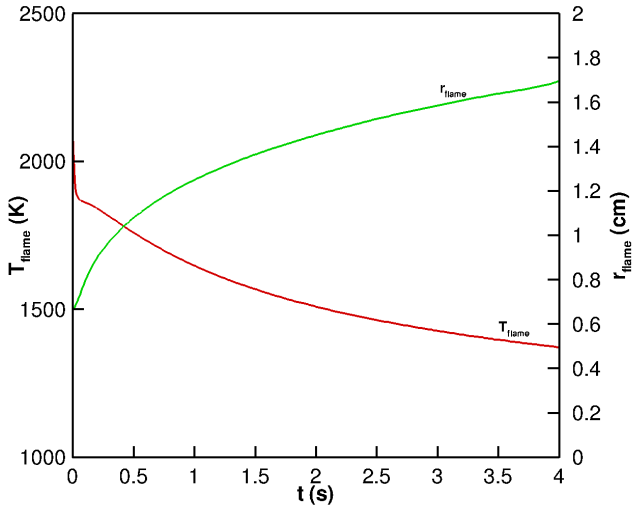


Figure B.2: Predicted flame radius and peak temperature of Flame 2, from ignition ($t = 0$ s) to 4 s.

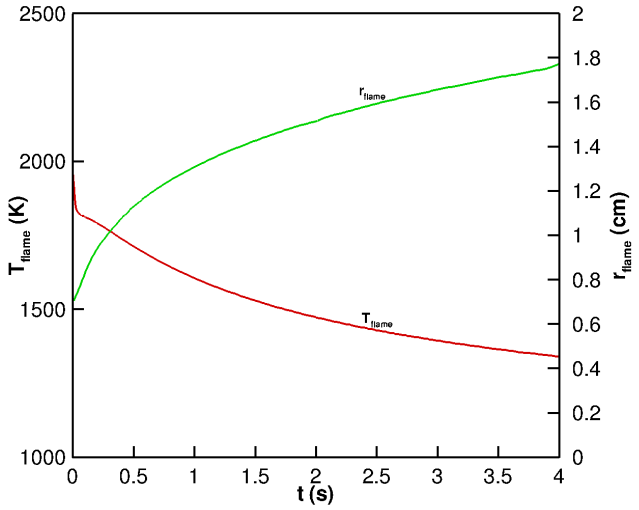


Figure B.3: Predicted flame radius and peak temperature of Flame 3, from ignition ($t = 0$ s) to 4 s.

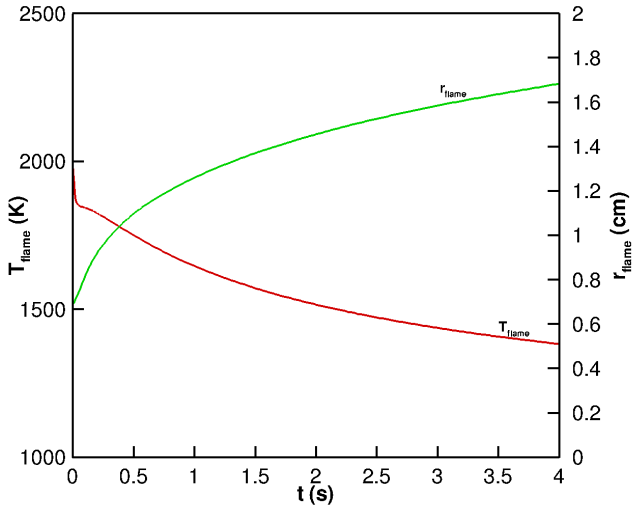


Figure B.4: Predicted flame radius and peak temperature of Flame 4, from ignition ($t = 0$ s) to 4 s.

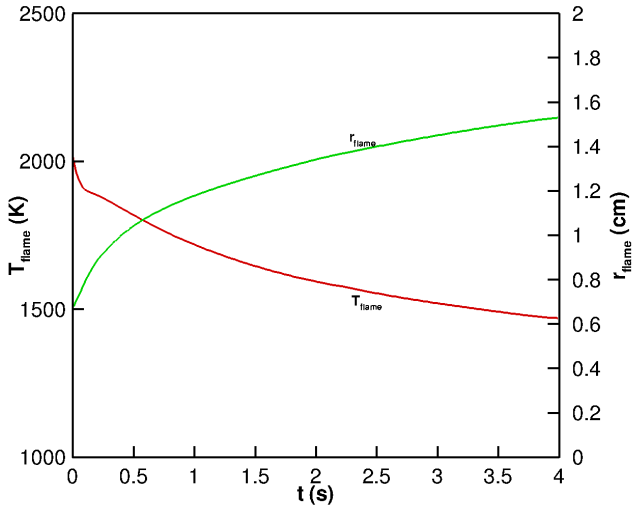


Figure B.5: Predicted flame radius and peak temperature of Flame 5, from ignition ($t = 0$ s) to 4 s.

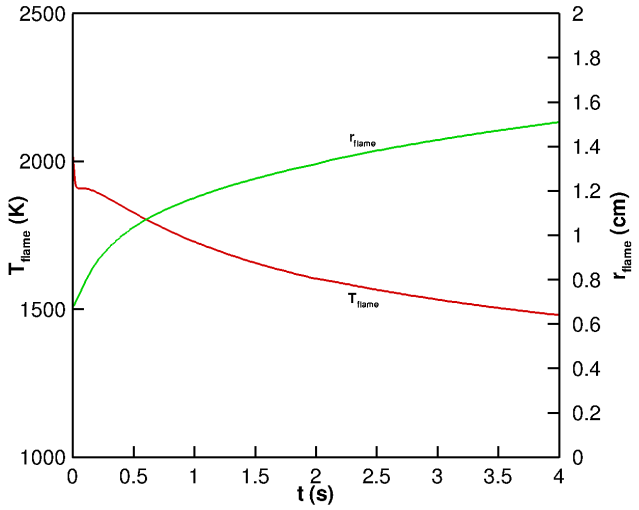


Figure B.6: Predicted flame radius and peak temperature of Flame 6, from ignition ($t = 0$ s) to 4 s.

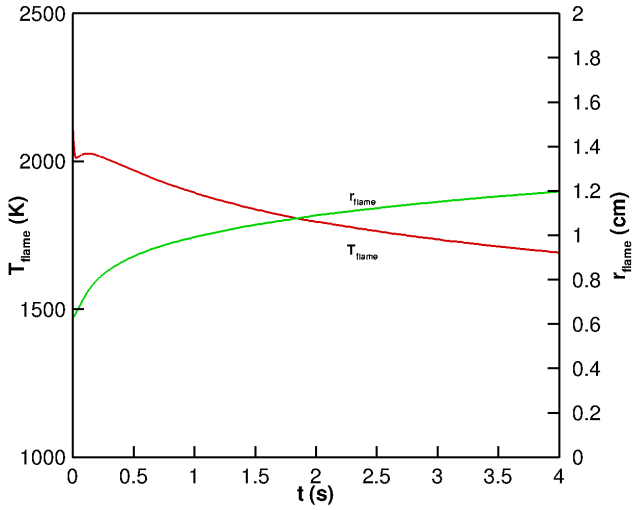


Figure B.7: Predicted flame radius and peak temperature of Flame 7, from ignition ($t = 0$ s) to 4 s.

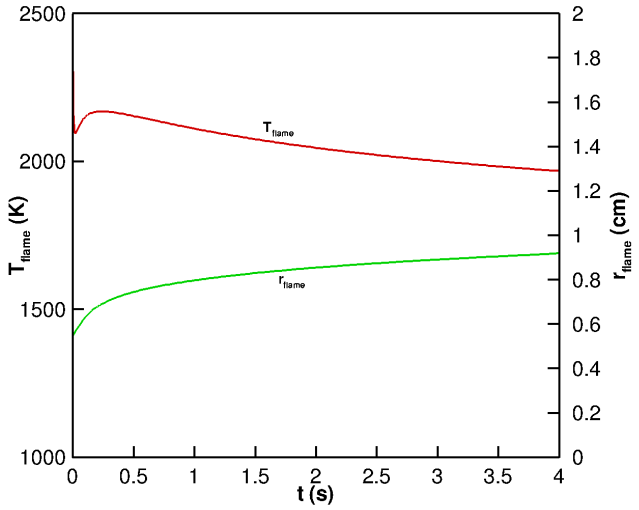


Figure B.8: Predicted flame radius and peak temperature of Flame 8, from ignition ($t = 0$ s) to 4 s.

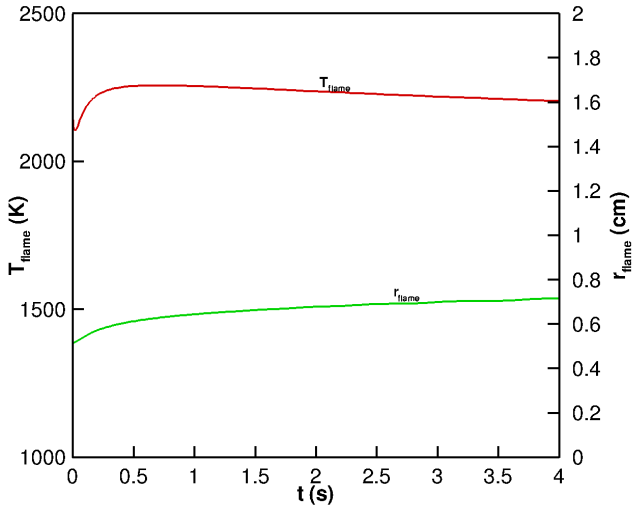


Figure B.9: Predicted flame radius and peak temperature of Flame 9, from ignition ($t = 0$ s) to 4 s.

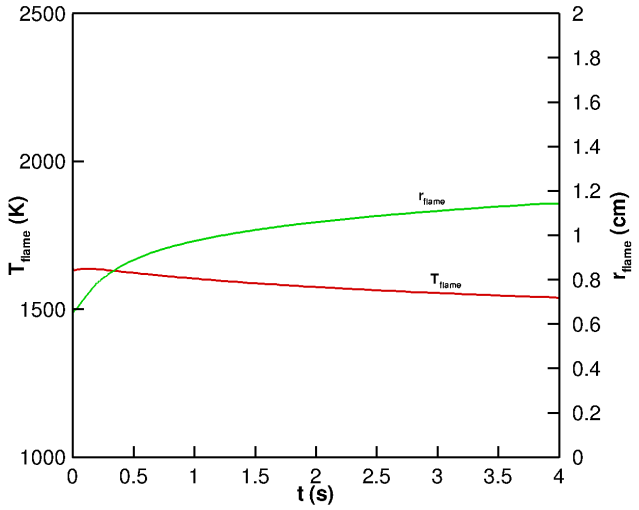


Figure B.10: Predicted flame radius and peak temperature of Flame 10, from ignition ($t = 0$ s) to 4 s.

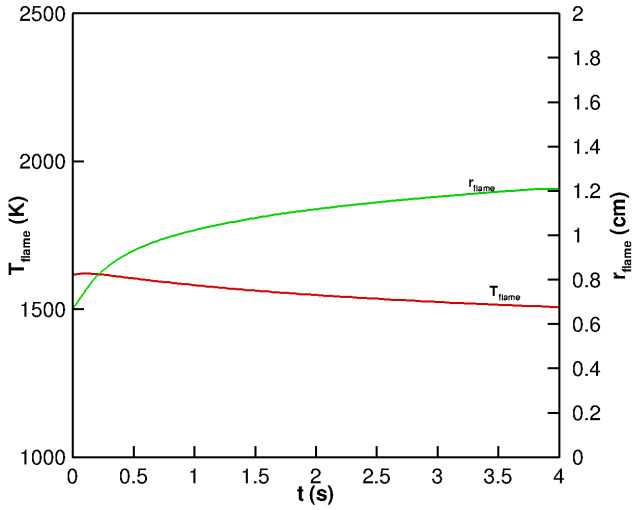


Figure B.11: Predicted flame radius and peak temperature of Flame 11, from ignition ($t = 0$ s) to 4 s.

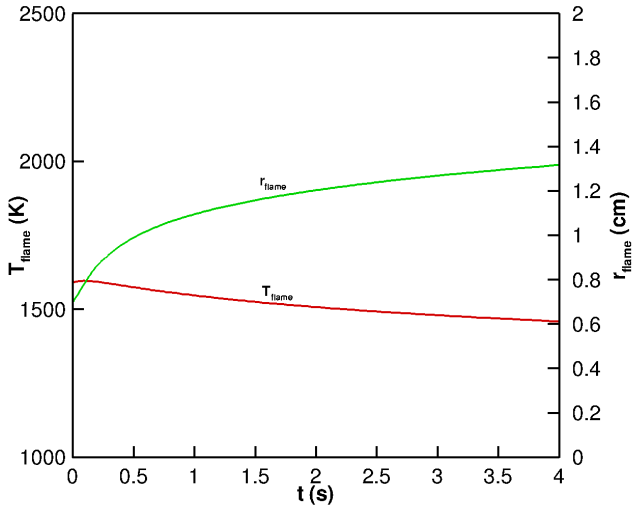


Figure B.12: Predicted flame radius and peak temperature of Flame 12, from ignition ($t = 0$ s) to 4 s.

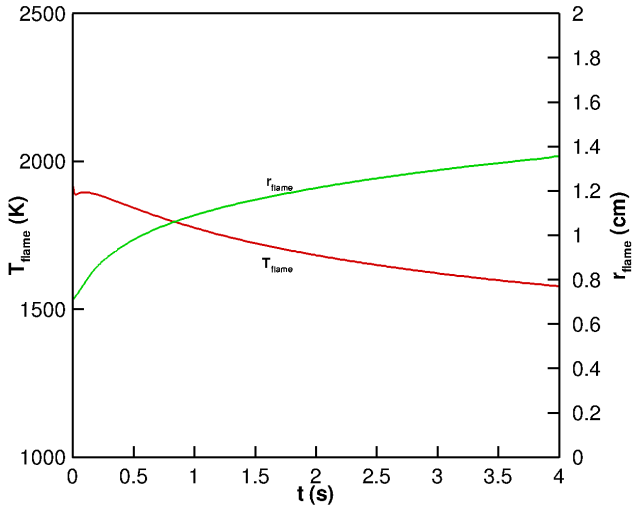


Figure B.13: Predicted flame radius and peak temperature of Flame 13, from ignition ($t = 0$ s) to 4 s.

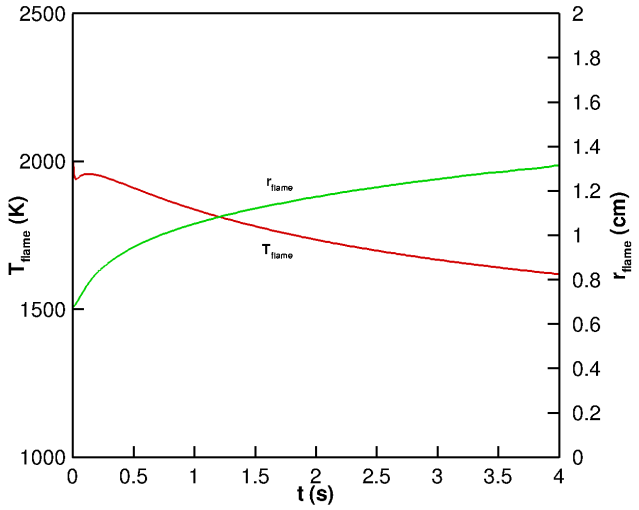


Figure B.14: Predicted flame radius and peak temperature of Flame 14, from ignition ($t = 0$ s) to 4 s.

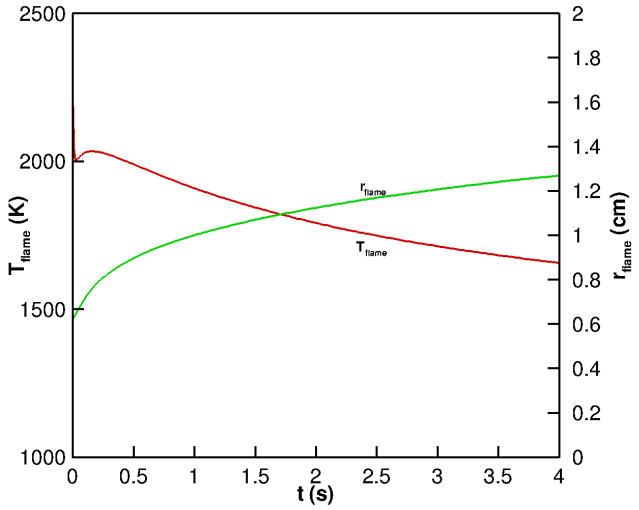


Figure B.15: Predicted flame radius and peak temperature of Flame 15, from ignition ($t = 0$ s) to 4 s.

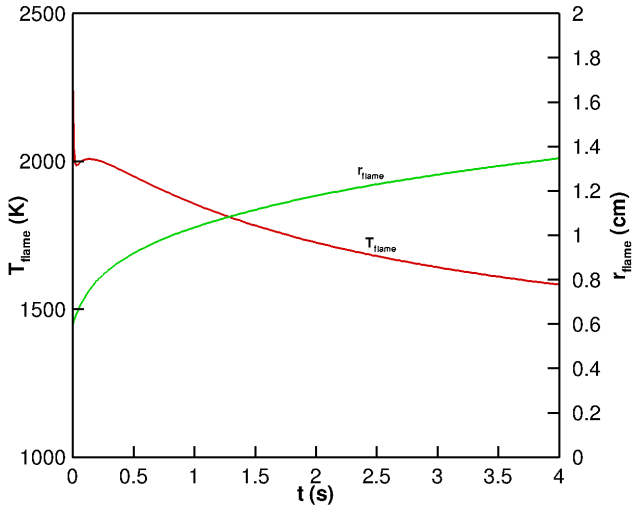


Figure B.16: Predicted flame radius and peak temperature of Flame 16, from ignition ($t = 0$ s) to 4 s.

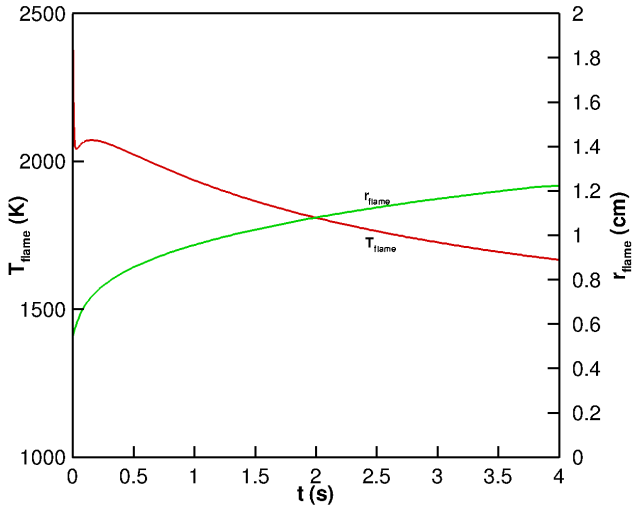


Figure B.17: Predicted flame radius and peak temperature of Flame 17, from ignition ($t = 0$ s) to 4 s.

# Appendix C

# Structure of Sooting Limit Flames

This appendix presents the predicted profiles of temperature $T$, mixture fraction $Z$, local scalar dissipation rate $\chi$, and local C/O ratio for the 17 flames at their sooting limits.The chemistry model used for the predictions is ABF model [67]. Similar results are obtained when using GRI-Mech 3.0 [64].

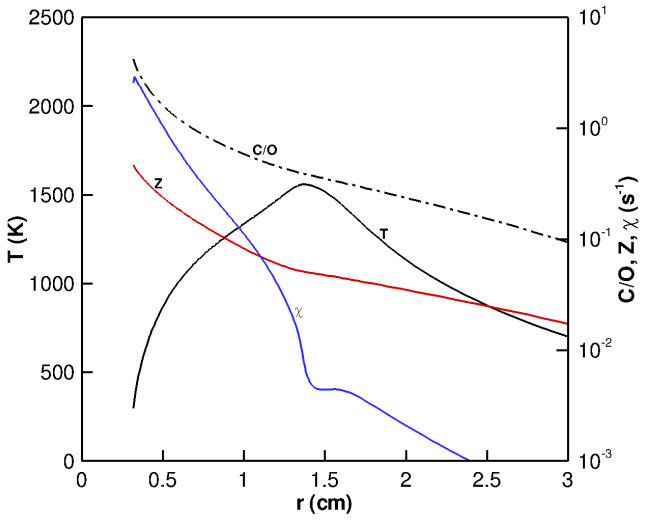


Figure C.1: Predicted $T$, C/O, $Z$, and $\chi$ profiles from Flame 1 at its sooting limits, 2 s after ignition.

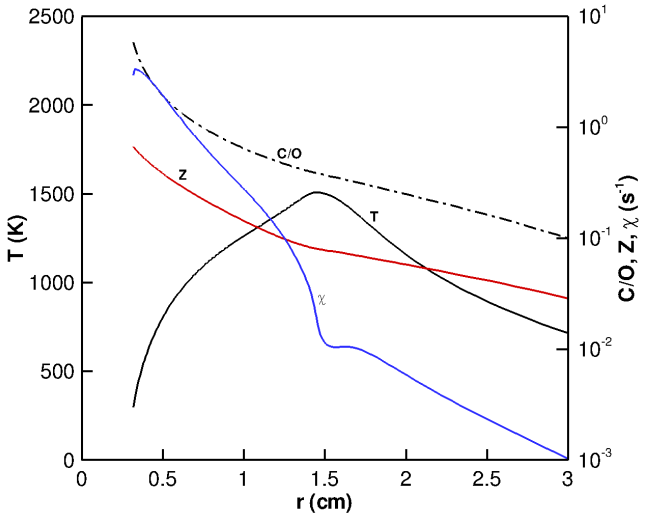


Figure C.2: Predicted $T$, C/O, $Z$, and $\chi$ profiles from Flame 2 at its sooting limits, 2 s after ignition.

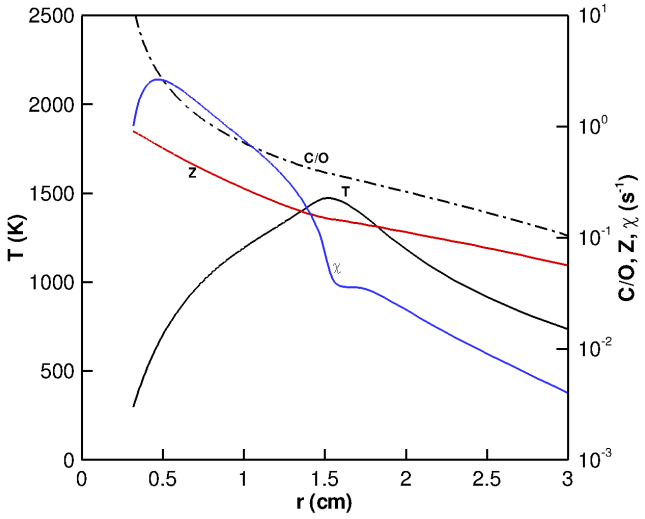


Figure C.3: Predicted $T$, C/O, $Z$, and $\chi$ profiles from Flame 3 at its sooting limits, 2 s after ignition.

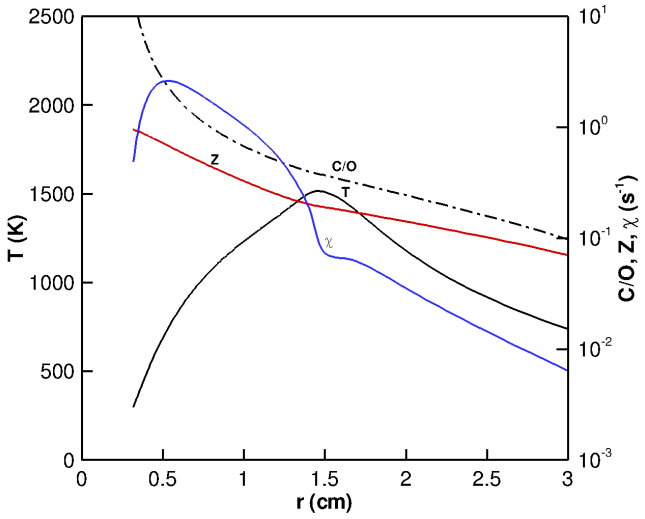


Figure C.4: Predicted $T$, C/O, $Z$, and $\chi$ profiles from Flame 4 at its sooting limits, 2 s after ignition.

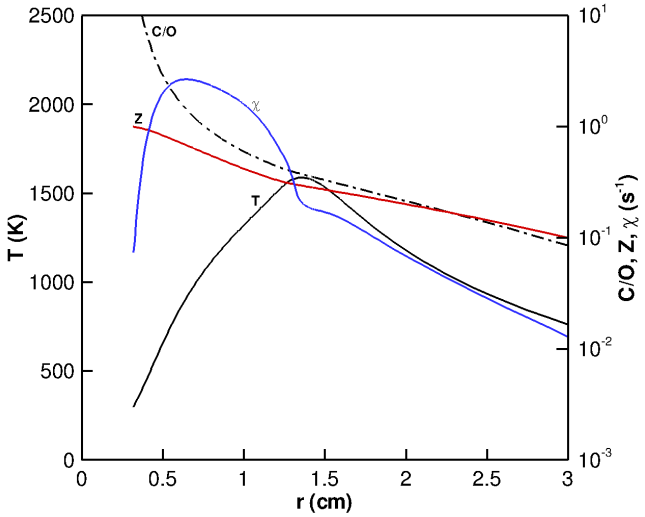


Figure C.5: Predicted $T$, C/O, $Z$, and $\chi$ profiles from Flame 5 at its sooting limits, 2 s after ignition.

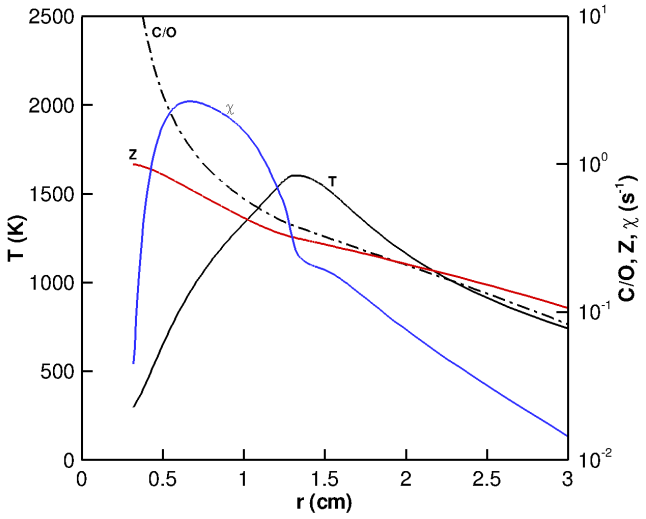


Figure C.6: Predicted $T$, C/O, $Z$, and $\chi$ profiles from Flame 6 at its sooting limits, 2 s after ignition.

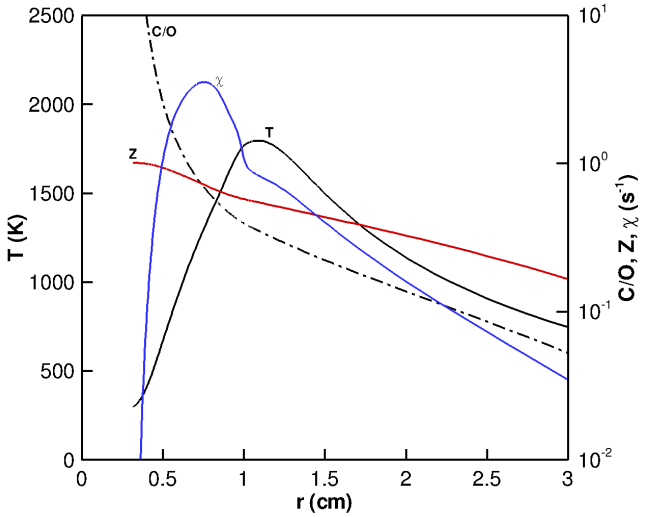


Figure C.7: Predicted $T$, C/O, $Z$, and $\chi$ profiles from Flame 7 at its sooting limits, 2 s after ignition.

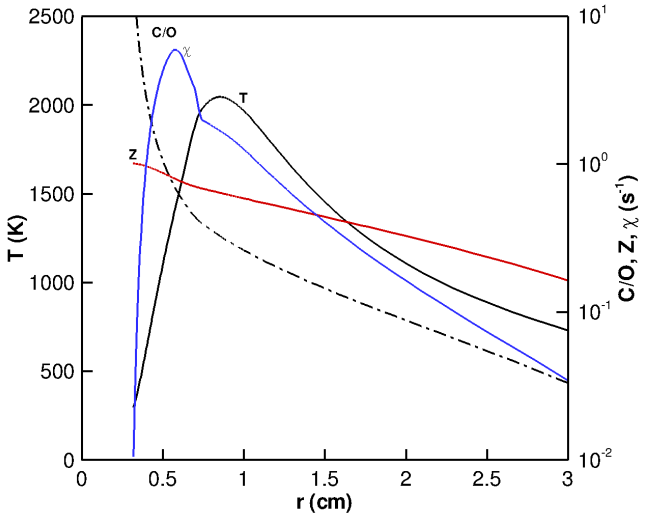


Figure C.8: Predicted $T$, C/O, $Z$, and $\chi$ profiles from Flame 8 at its sooting limits, 2 s after ignition.

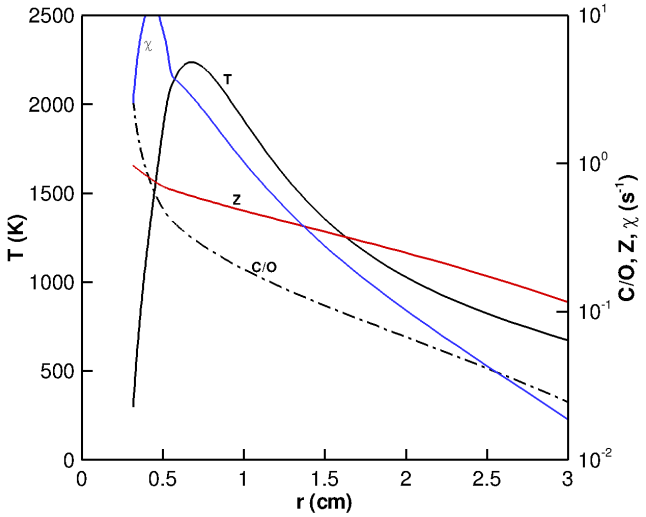


Figure C.9: Predicted $T$, C/O, $Z$, and $\chi$ profiles from Flame 9 at its sooting limits, 2 s after ignition.

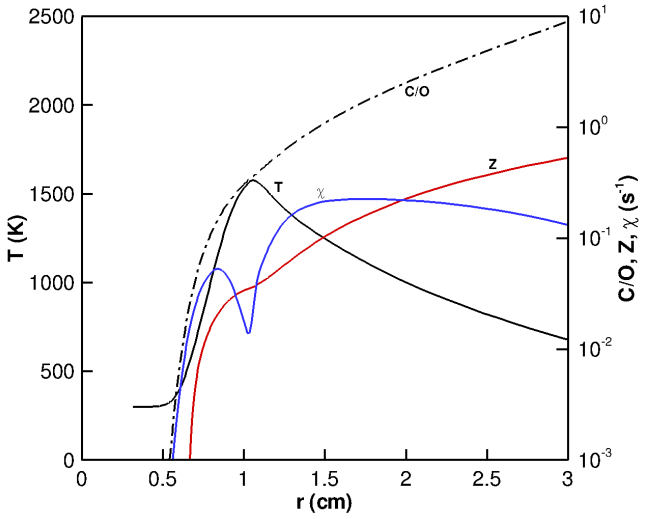


Figure C.10: Predicted $T$, C/O, $Z$, and $\chi$ profiles from Flame 10 at its sooting limits, 2 s after ignition.

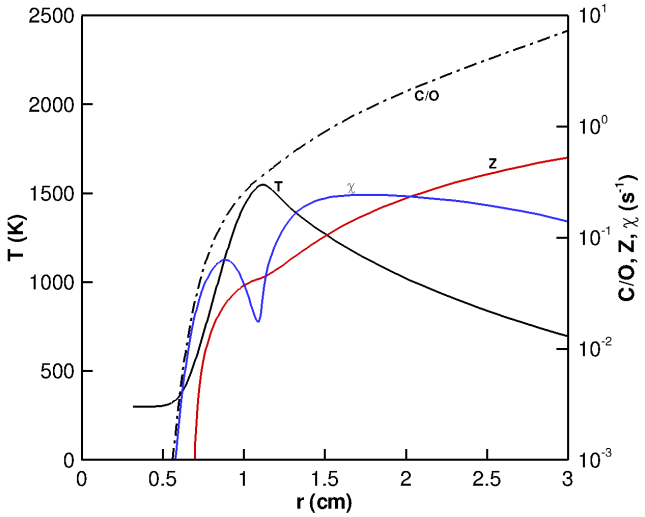


Figure C.11: Predicted $T$, C/O, $Z$, and $\chi$ profiles from Flame 11 at its sooting limits, 2 s after ignition.

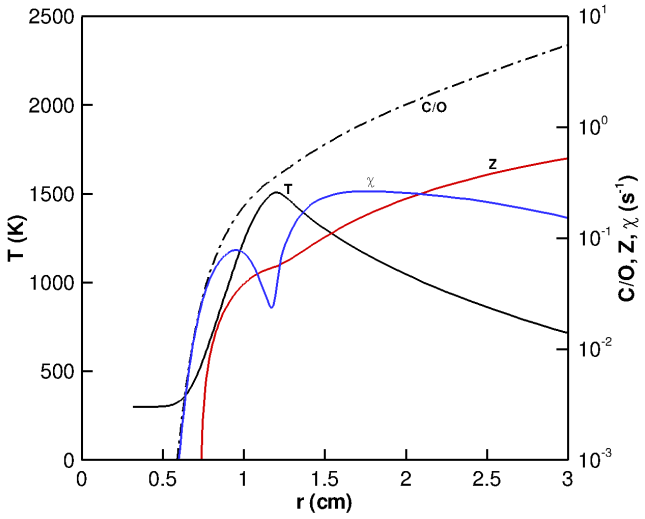


Figure C.12: Predicted $T$, C/O, $Z$, and $\chi$ profiles from Flame 12 at its sooting limits, 2 s after ignition.

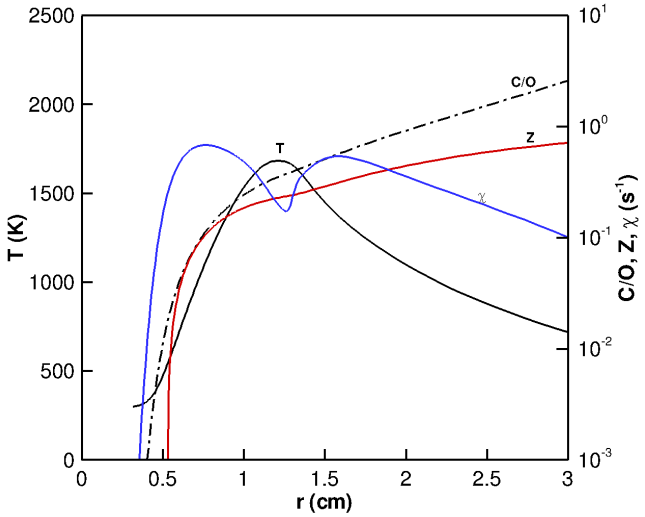


Figure C.13: Predicted $T$, C/O, $Z$, and $\chi$ profiles from Flame 13 at its sooting limits, 2 s after ignition.

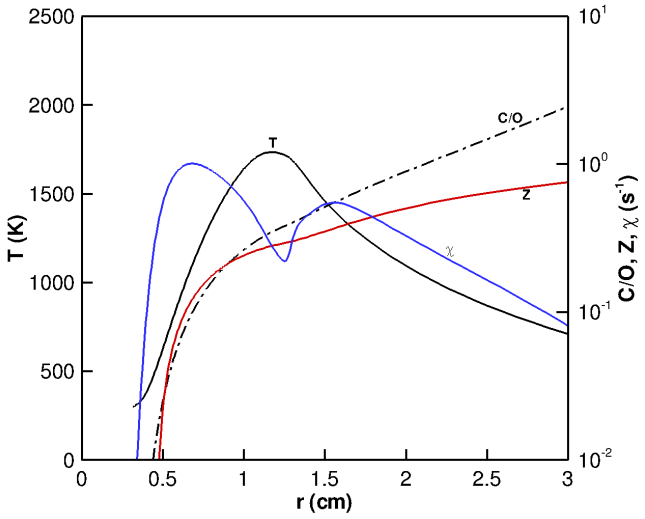


Figure C.14: Predicted $T$, C/O, $Z$, and $\chi$ profiles from Flame 14 at its sooting limits, 2 s after ignition.

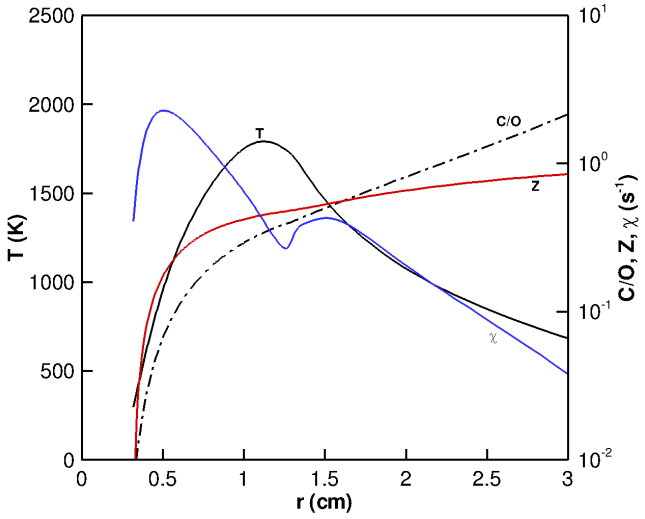


Figure C.15: Predicted $T$, C/O, $Z$, and $\chi$ profiles from Flame 15 at its sooting limits, 2 s after ignition.

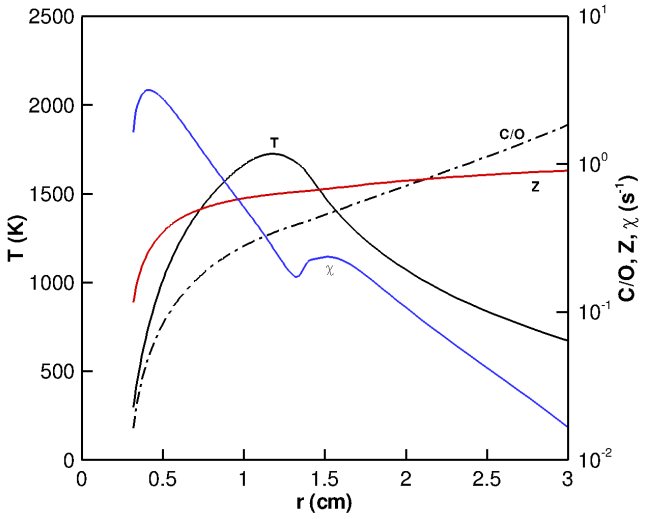


Figure C.16: Predicted $T$, C/O, $Z$, and $\chi$ profiles from Flame 16 at its sooting limits, 2 s after ignition.

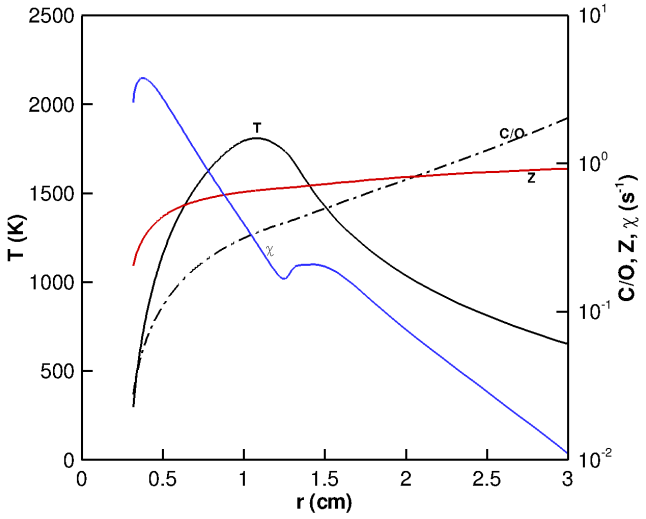


Figure C.17: Predicted $T$, C/O, $Z$, and $\chi$ profiles from Flame 17 at its sooting limits, 2 s after ignition.

# Appendix D

# Temporal Evolution of Total Production of $C_2H_2$ and $A_4$

In this appendix, the total molar production of acetylene ($C_2H_2$) and pyrene assimilates, denoted $\omega_{A4}$ and which comprises the formation of $A_4$, $A_4^-$, $A_3C_2H$, and $A_3C_2H_2$ is calculated. The temporal evolution of total production of $A_4$ and assimilates is magnified by a factor $10^5$ and is plotted with the temporal evolution of total production of $C_2H_2$ and temperature.

The total productioni is computed by integrating the molar production of the species of study over the whole domain:

$$\omega_k = \iiint_{\mathscr{X}} \dot{\omega}_k dV. \tag{D.1}$$

All the simulations were performed with the ABF model [67].

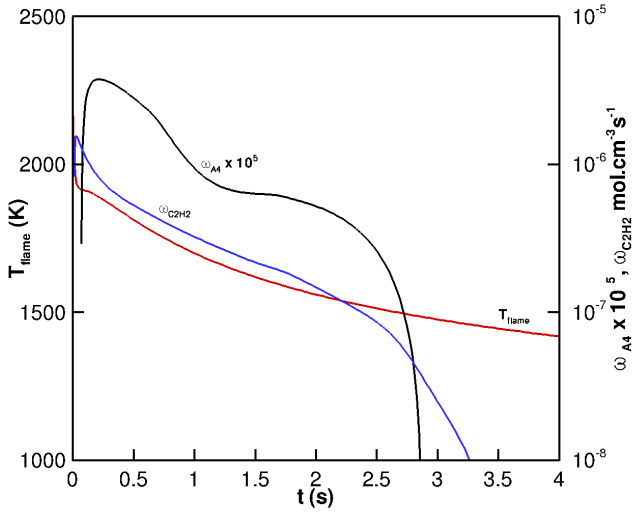


Figure D.1: Temporal evolution of $T$ and total molar production of $C_2H_2$ and A4 assimilates for Flame 1. Note that $\omega_{A4}$ is magnified by a factor $10^5$.

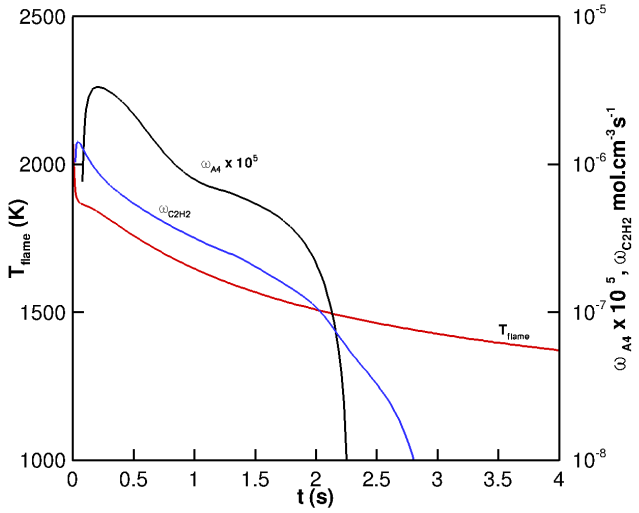


Figure D.2: Temporal evolution of $T$ and total molar production of $C_2H_2$ and A4 assimilates for Flame 2. Note that $\omega_{A4}$ is magnified by a factor $10^5$.

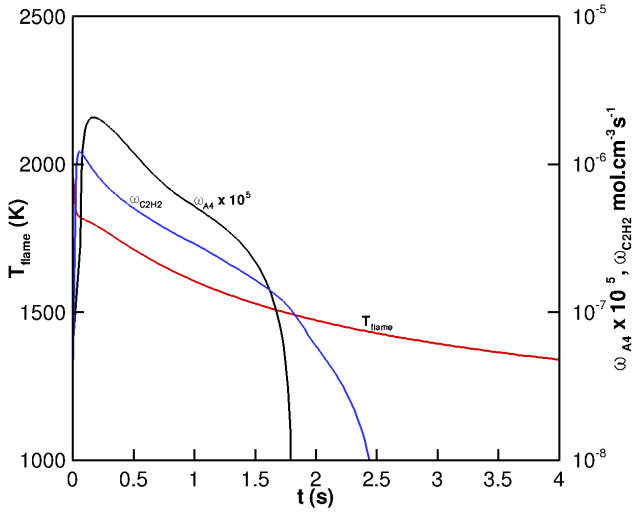


Figure D.3: Temporal evolution of $T$ and total molar production of $C_2H_2$ and A4 assimilates for Flame 3. Note that $\omega_{A4}$ is magnified by a factor $10^5$.

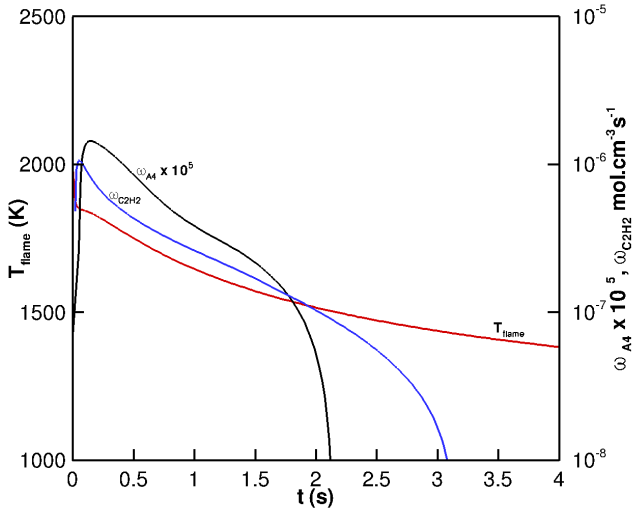


Figure D.4: Temporal evolution of $T$ and total molar production of $C_2H_2$ and A4 assimilates for Flame 4. Note that $\omega_{A4}$ is magnified by a factor $10^5$.

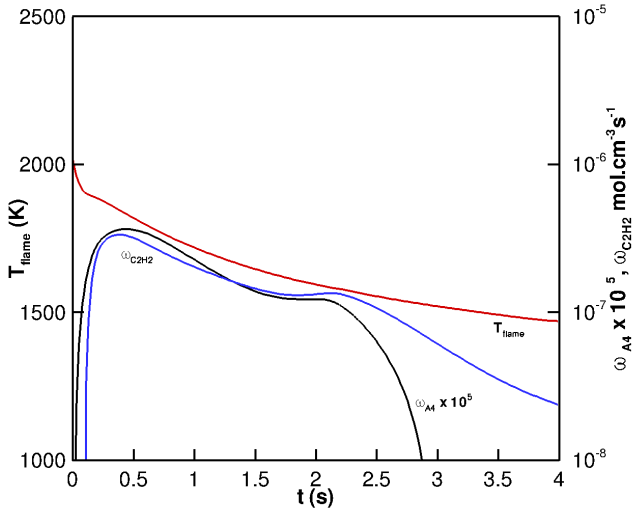


Figure D.5: Temporal evolution of $T$ and total molar production of $C_2H_2$ and A4 assimilates for Flame 5. Note that $\omega_{A4}$ is magnified by a factor $10^5$.

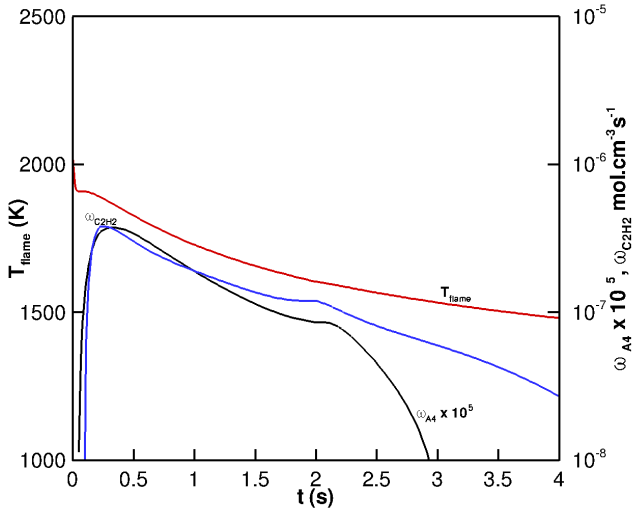


Figure D.6: Temporal evolution of $T$ and total molar production of $C_2H_2$ and A4 assimilates for Flame 6. Note that $\omega_{A4}$ is magnified by a factor $10^5$.

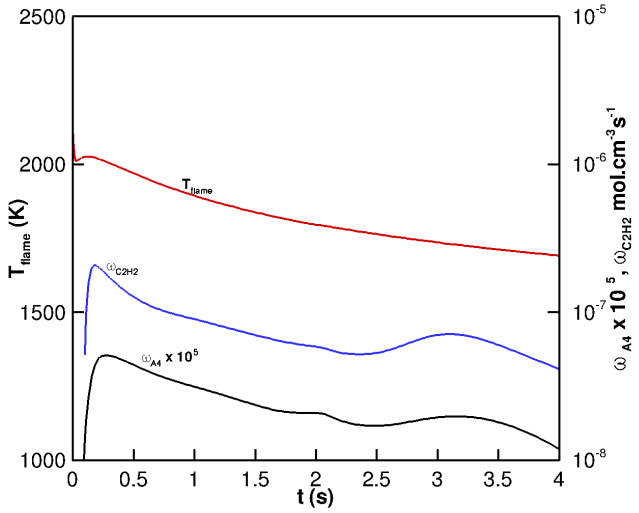


Figure D.7: Temporal evolution of $T$ and total molar production of $C_2H_2$ and A4 assimilates for Flame 7. Note that $\omega_{A4}$ is magnified by a factor $10^5$.

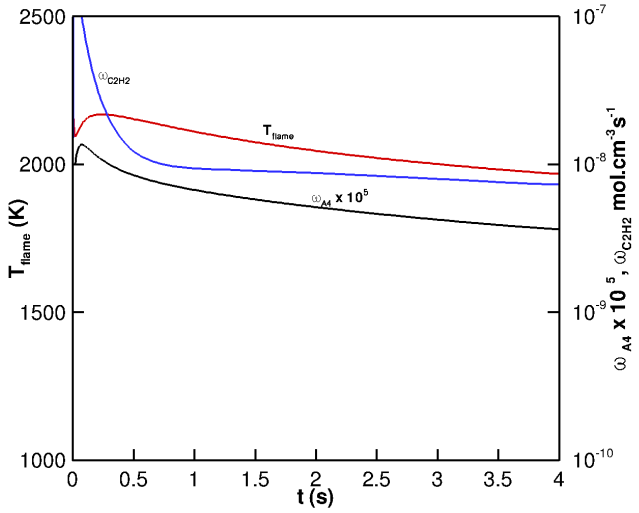


Figure D.8: Temporal evolution of $T$ and total molar production of $C_2H_2$ and A4 assimilates for Flame 8. Note that $\omega_{A4}$ is magnified by a factor $10^5$.

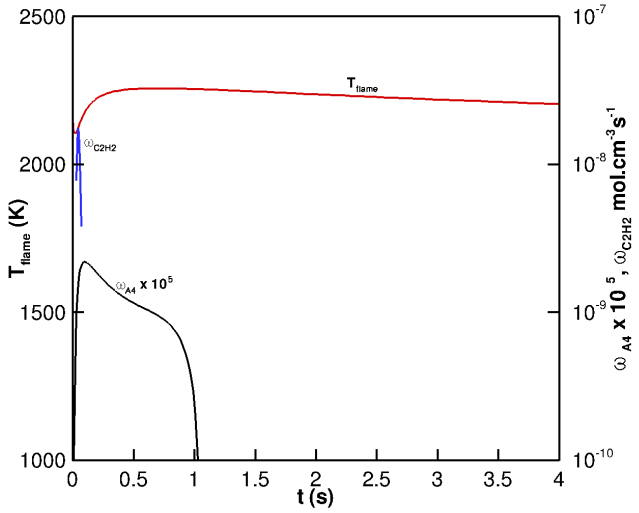


Figure D.9: Temporal evolution of $T$ and total molar production of $C_2H_2$ and A4 assimilates for Flame 9. Note that $\omega_{A4}$ is magnified by a factor $10^5$.

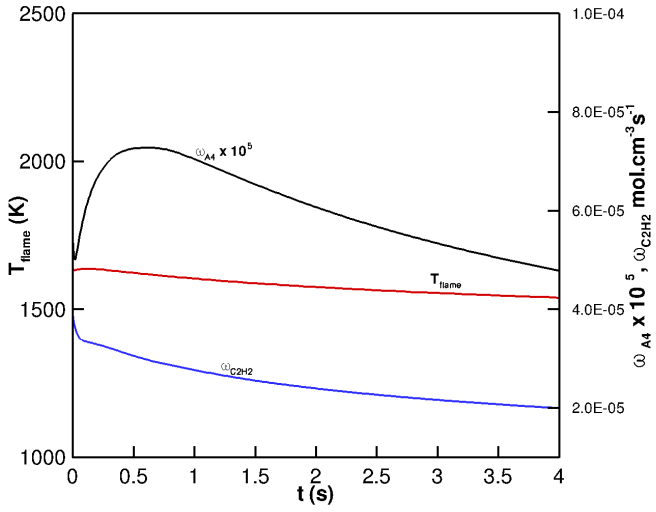


Figure D.10: Temporal evolution of $T$ and total molar production of $C_2H_2$ and A4 assimilates for Flame 10. Note that $\omega_{A4}$ is magnified by a factor $10^5$.

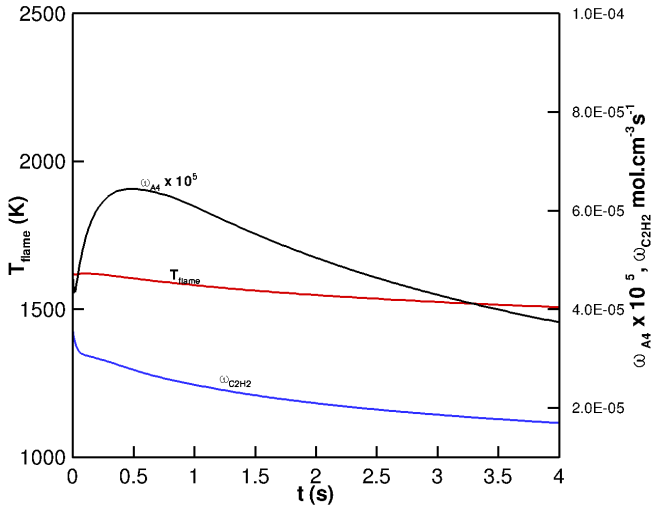


Figure D.11: Temporal evolution of $T$ and total molar production of $C_2H_2$ and A4 assimilates for Flame 11. Note that $\omega_{A4}$ is magnified by a factor $10^5$.

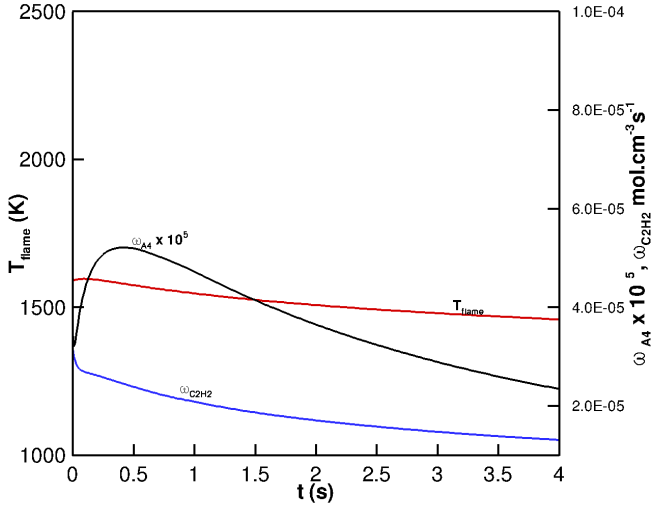


Figure D.12: Temporal evolution of $T$ and total molar production of $C_2H_2$ and A4 assimilates for Flame 12. Note that $\omega_{A4}$ is magnified by a factor $10^5$.

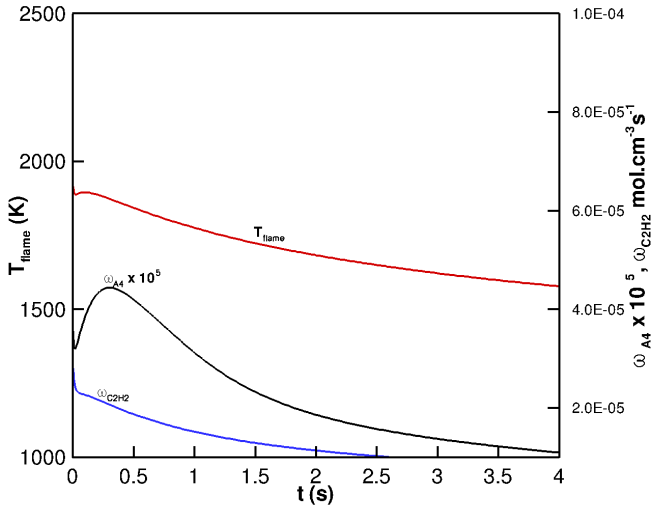


Figure D.13: Temporal evolution of $T$ and total molar production of $C_2H_2$ and A4 assimilates for Flame 13. Note that $\omega_{A4}$ is magnified by a factor $10^5$.

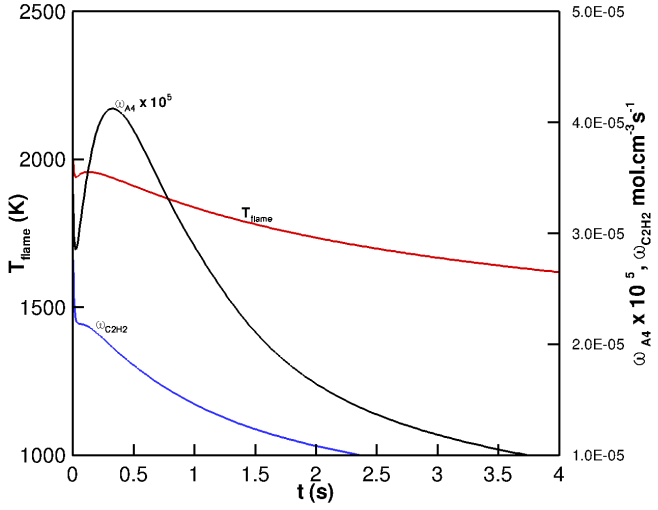


Figure D.14: Temporal evolution of $T$ and total molar production of $C_2H_2$ and A4 assimilates for Flame 14. Note that $\omega_{A4}$ is magnified by a factor $10^5$.

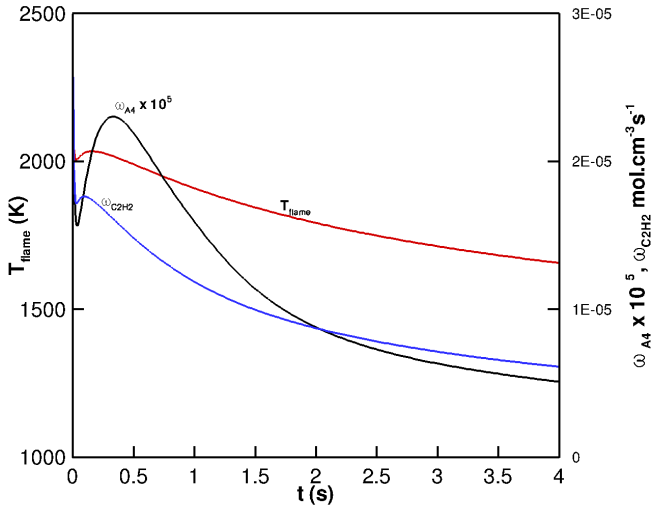


Figure D.15: Temporal evolution of $T$ and total molar production of $C_2H_2$ and A4 assimilates for Flame 15. Note that $\omega_{A4}$ is magnified by a factor $10^5$.

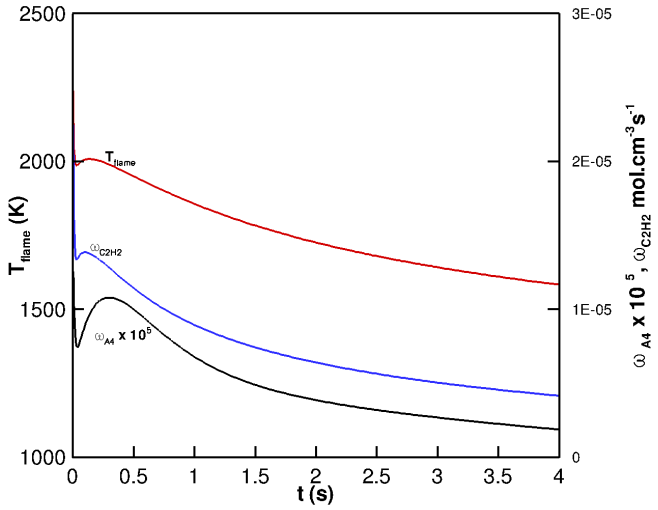


Figure D.16: Temporal evolution of $T$ and total molar production of $C_2H_2$ and A4 assimilates for Flame 16. Note that $\omega_{A4}$ is magnified by a factor $10^5$.

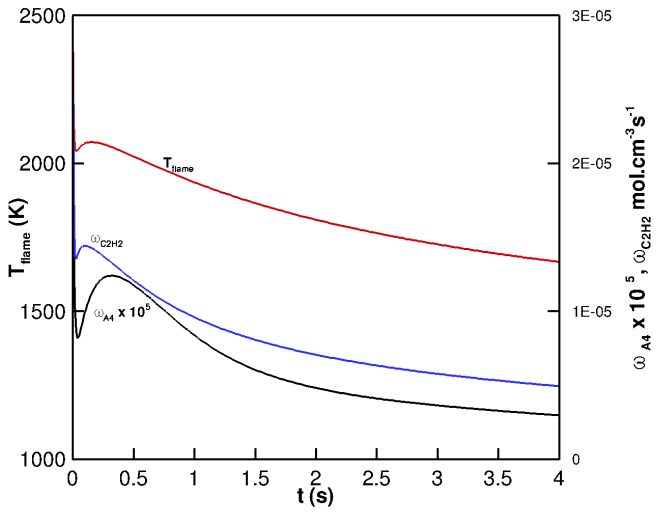


Figure D.17: Temporal evolution of $T$ and total molar production of $C_2H_2$ and A4 assimilates for Flame 17. Note that $\omega_{A4}$ is magnified by a factor $10^5$.

# Bibliography


[1] J. Goudsblom, *Fire and civilization*. Allen Lane London, 1992.

[2] A.L. Lavoisier, *Mémoire sur la combustion en général*. Académie des sciences, 1780.

[3] S. Carnot, *Réflexions sur la puissance motrice du feu et sur les machines propres à développer cette puissance*. Bachelier Paris, 1824.

[4] Energy Information Administration, "Annual energy review 2007," Energy Information Administration, Tech. Rep., 2007.

[5] B. Brunekreef and S.T. Holgate, "Air pollution and health," *The Lancet*, vol. 360, no. 9341, pp. 1233–1242, 2002.

[6] R.K. Pachauri and A. Reisinger, *Climate Change 2007: Synthesis Report*. IPCC, 2008.

[7] Energy Information Administration, "International energy annual 2006," Energy Information Administration, Tech. Rep., 2006.

[8] M.J. Karter, *Fire loss in the United States during 2006*. National Fire Protection Association, 2007.

[9] C.K. Law, *Combustion physics*. Cambridge University Press, 2006.

[10] S.P. Burke and T.E.W. Schumann, "Diffusion flames," *Industrial & Engineering Chemistry*, vol. 20, no. 10, pp. 998–1004, 1928.

[11] E.R. Hawkes, R. Sankaran, J.C. Sutherland, and J.H. Chen, "Direct numerical simulation of turbulent combustion: fundamental insights towards predictive models," in *Journal of Physics: Conference Series*, vol. 16, no. 1. Institute of Physics Publishing, 2005, pp. 65–79.

[12] D.O. Lignell, J.H. Chen, P.J. Smith, T. Lu, and C.K. Law, "The effect of flame structure on soot formation and transport in turbulent nonpremixed flames using direct numerical simulation," *Combustion and Flame*, vol. 151, no. 1-2, pp. 2–28, 2007.

[13] R.W. Bilger, "The structure of diffusion flames," *Combustion Science and Technology*, vol. 13, no. 1, pp. 155–170, 1976.

[14] R.W. Bilger, "Turbulent jet diffusion flames," *Progress in Energy and Combustion Science*, vol. 1, no. 2-3, pp. 87–109, 1976.

[15] N. Peters, "Laminar flamelet concepts in turbulent combustion," in *Symposium(International) on Combustion, 21 st, Munich, Federal Republic of Germany*, 1988, pp. 1231–1250.

[16] H. Pitsch and N. Peters, "A consistent flamelet formulation for non-premixed combustion considering differential diffusion effects," *Combustion and Flame*, vol. 114, no. 1, pp. 26–40, 1998.

[17] N. Peters, "Local quenching due to flame stretch and non-premixed turbulent combustion," *Combustion Science and Technology*, vol. 30, no. 1, pp. 1–17, 1983.

[18] F.A. Williams, "Progress in knowledge of flamelet structure and extinction," *Progress in Energy and Combustion Science*, vol. 26, no. 4-6, pp. 657–682, 2000.

[19] H. Pitsch, M. Chen, and N. Peters, "Unsteady flamelet modeling of turbulent hydrogen-air diffusion flames," in *Symposium(International) on Combustion*, vol. 1. Combustion Institute, 1998, pp. 1057–1064.

[20] D. Carbonell, A. Oliva, and C.D. Perez-Segarra, "Implementation of two-equation soot flamelet models for laminar diffusion flames," *Combustion and Flame*, vol. 156, no. 3, pp. 621–632, 2009.

[21] M. Matalon, "On flame stretch," *Combustion Science and Technology*, vol. 31, no. 3, pp. 169–181, 1983.

[22] Y.M. Kim and H.J. Kim, "Multidimensional effects on structure and extinction process of counterflow nonpremixed hydrogen-air flames," *Combustion Science and Technology*, vol. 137, no. 1, pp. 51–80, 1998.

[23] J.D. Buckmaster and G.S.S. Ludford, *Theory of laminar flames*. Cambridge, New York, 1982.

[24] K. Mills and M. Matalon, "Burner-generated spherical diffusion flames," *Combustion Science and Technology*, vol. 129, no. 1, pp. 295–319, 1997.

[25] A. Linan, "The asymptotic structure of counterflow diffusion flames for large activation energies," *Acta Astronautica*, vol. 1, pp. 1007–1039, 1974.

[26] J.Y. Hwang and S.H. Chung, "Growth of soot particles in counterflow diffusion flames of ethylene," *Combustion and Flame*, vol. 125, no. 1-2, pp. 752–762, 2001.

[27] D.X. Du, R.L. Axelbaum, and C.K. Law, "Experiments on the sooting limits of aerodynamically-strained diffusion flames," in *Symposium(International) on Combustion, 22 nd, Seattle, WA*, 1988, pp. 387–394.

[28] H.Y. Wang, W.H. Chen, and C.K. Law, "Extinction of counterflow diffusion flames with radiative heat loss and nonunity Lewis numbers," *Combustion and Flame*, vol. 148, no. 3, pp. 100–116, 2007.

[29] B.H. Chao, S. Liu, and R.L. Axelbaum, "On soot inception in nonpremixed flames and the effects of flame structure," *Combustion Science and Technology*, vol. 138, no. 1, pp. 105–135, 1998.

[30] D.X. Du, R.L. Axelbaum, and C.K. Law, "Soot formation in strained diffusion flames with gaseous additives," *Combustion and Flame*, vol. 102, no. 1-2, pp. 11–20, 1995.

[31] G.A.E. Godsave, "Studies of the combustion of drops in a fuel spraythe burning of single drops of fuel," in *Fourth Symposium (International) on Combustion*, 1953, pp. 818–830.

[32] D.B. Spalding, "The combustion of liquid fuels," *Symposium (International) on Combustion*, vol. 4, no. 1, pp. 847–864, 1953, fourth Symposium (International) on Combustion.

[33] F.A. Williams, *Combustion theory the fundamental theory of chemically reacting flow systems*. Perseus Books, 1985.

[34] S. Ulzama and E. Specht, "An analytical study of droplet combustion under microgravity: Quasi-steady transient approach," *Proceedings of the Combustion Institute*, vol. 31, no. 2, pp. 2301–2308, 2007.

[35] Merrill K. King, "An unsteady-state analysis of porous sphere and droplet fuel combustion under microgravity conditions," *Symposium (International) on Combustion*, vol. 26, no. 1, pp. 1227–1234, 1996.

[36] S.R. Turns, *An introduction to combustion: concepts and applications*. McGraw-Hill New York, 2002.

[37] K. Mills and M. Matalon, "Extinction of spherical diffusion flames in the presence of radiant loss," in *Symposium(International) on Combustion, 27 th*, vol. 2, 1998, pp. 2535–2542.

[38] B.H. Chao, C.K. Law, and J.S. Tien, "Structure and extinction of diffusion flames with flame radiation," in *Symposium(International) on Combustion, 23 rd, Orleans, France*, 1991, pp. 523–531.

[39] C.J. Sung, D.L. Zhu, and C.K. Law, "On Micro-Buoyancy Spherical Diffusion Flames and a Double Luminous Zone Structure of the Hydrogen/Methane Flame," in *Symposium(International) on Combustion*, vol. 2. Combustion Institute, 1998, pp. 2559–2566.

[40] R.J. Kee, J.F. Grcar, M.D. Smooke, J.A. Miller, and E. Meeks, "Premix: A FORTRAN Program for Modeling Steady Laminar One-Dimensional Premixed Flames," Sandia National Laboratories Report No. SAND85-8240, Tech. Rep., 1987.

[41] S.D. Tse, D. Zhu, C.J. Sung, Y. Ju, and C.K. Law, "Microgravity burner-generated spherical diffusion flames: experiment and computation," *Combustion and Flame*, vol. 125, no. 4, pp. 1265–1278, 2001.

[42] K.J. Santa, B.H. Chao, P.B. Sunderland, D.L. Urban, D.P. Stocker, and R.L. Axelbaum, "Radiative extinction of gaseous spherical diffusion flames in microgravity," *Combustion and Flame*, vol. 151, no. 4, pp. 665–675, 2007.

[43] A. Atreya, S. Agrawal, K. R. Sacksteder, , and H. R. Baum, "Observations of methane and ethylene diffusion flames stabilized around a blowing porous sphere under microgravity conditions," in *32nd Aerospace Sciences Meeting and Exhibit*, 1994.

[44] S. Berhan, M.K. Chernovsky, S. Filatyev, A. Atreya, and K.R. Sacksteder, "The effects of chemical kinetics and radiation on flame radius and temperature prediction of unsteady spherical diffusion flames in microgravitya comparison with experiments," in *41 st Aerospace Sciences Meeting and Exhibit*, 2003.

[45] M.K. Chernovsky, A. Atreya, and K.R. Sacksteder, "Transient measurements of temperature and radiation intensity in spherical microgravity diffusion flame," in *44 nd Aerospace Sciences Meeting and Exhibit*, 2006.

[46] M.K. Chernovsky, A. Atreya, and H.G. Im, "Effect of co2 diluent on fuel versus oxidizer side of spherical diffusion flames in microgravity," *Proceedings of the Combustion Institute*, vol. 31, no. 1, pp. 1005 – 1013, 2007.

[47] S.W. Yoo, E.W. Christiansen, and C.K. Law, "Oscillatory extinction of spherical diffusion flames: Micro-buoyancy experiment and computation," *Proceedings of the Combustion Institute*, vol. 29, no. 1, pp. 29–36, 2002.

[48] E.W. Christiansen, S.D. Tse, and C.K. Law, "A computational study of oscillatory extinction of spherical diffusion flames," *Combustion and Flame*, vol. 134, no. 4, pp. 327–337, 2003.

[49] S. Cheatham and M. Matalon, "Near-limit oscillations of spherical diffusion flames," *AIAA journal*, vol. 34, no. 7, pp. 1403–1409, 1996.

[50] D.L. Dietrich, H.D. Ross, Y. Shu, P. Chang, and J.S. TÍen, "Candle flames in non-buoyant atmospheres," *Combustion Science and Technology*, vol. 156, no. 1, pp. 1–24, 2000.

[51] S. Liu, B.H. Chao, and R.L. Axelbaum, "A theoretical study on soot inception in spherical burner-stabilized diffusion flames," *Combustion and Flame*, vol. 140, no. 1-2, pp. 1–23, 2005.

[52] O.A. Ezekoye and Z. Zhang, "Soot oxidation and agglomeration modeling in a microgravity diffusion flame," *Combustion and Flame*, vol. 110, no. 1-2, pp. 127–139, 1997.

[53] M. Fairweather, W. P. Jones, and R. P. Lindstedt, "Predictions of radiative transfer from a turbulent reacting jet in a cross-wind," *Combustion and Flame*, vol. 89, no. 1, pp. 45 – 63, 1992.

[54] P.B. Sunderland, R.L. Axelbaum, D.L. Urban, B.H. Chao, and S. Liu, "Effects of structure and hydrodynamics on the sooting behavior of spherical microgravity diffusion flames," *Combustion and Flame*, vol. 132, no. 1-2, pp. 25–33, 2003.

[55] P.B. Sunderland, D.L. Urban, D.P. Stocker, B.H. Chao, and R.L. Axelbaum, "Sooting limits of microgravity spherical diffusion flames in oxygen-enriched air and diluted fuel," *Combustion Science and Technology*, vol. 176, no. 12, pp. 2143–2164, 2004.

[56] K.J. Santa, Z. Sun, B.H. Chao, P.B. Sunderland, R.L. Axelbaum, D.L. Urban, and D.P. Stocker, "Numerical and experimental observations of spherical diffusion flames," *Combustion Theory and Modelling*, vol. 11, no. 4, pp. 639–652, 2007.

[57] E.W. Christiansen, S.D. Tse, and C.K. Law, "A computational study of oscillatory extinction of spherical diffusion flames," *Combustion and Flame*, vol. 134, no. 4, pp. 327–337, 2003.

[58] R.J. Kee, F.M. Rupley, E. Meeks, and J.A. Miller, "Chemkin-III: a Fortran chemical kinetics package for the analysis of gas-phase chemical and plasma kinetics," Sandia National Laboratories Report No. SAND96-8216, Tech. Rep., 1996.

[59] R.J. Kee, G. Dixon-Lewis, J. Warnatz, M.E. Coltrin, J.A. Miller, and H.K. Moffat, "A Fortran Computer Code Package for the Evaluation of Gas-Phase Multicomponent Transport Properties," Sandia National Laboratories Report No. SAND86-8246, Tech. Rep., 1988.

[60] J.F. Grcar, "The Twopnt program for boundary value problems," Sandia National Laboratories Report No. SAND91-8230, Tech. Rep., 1991.

[61] H. Lomax, T.H. Pulliam, D.W. Zingg, T.H. Pulliam, and D.W. Zingg, *Fundamentals of computational fluid dynamics*. Springer Berlin, 2001.

[62] R.J. Kee, M.E. Coltrin, and P. Glarborg, *Chemically reacting flow: theory and practice*. Wiley-Interscience, 2005.

[63] I.K. Argyros, *Convergence and applications of Newton-type iterations*. Springer Verlag, 2008.

[64] G.P. Smith, D.M. Golden, M. Frenklach, N.W. Moriarty, B. Eiteneer, M. Goldenberg, C.T. Bowman, R.K. Hanson, S. Song, W.C. Gardiner *et al.*, "GRI-Mech version 3.0," 1999.

[65] R. Chen and R.L. Axelbaum, "Scalar dissipation rate at extinction and the effects of oxygen-enriched combustion," *Combustion and Flame*, vol. 142, no. 1-2, pp. 62–71, 2005.

[66] H. Wang and M. Frenklach, "A detailed kinetic modeling study of aromatics formation in laminar premixed acetylene and ethylene flames," *Combustion and Flame*, vol. 110, no. 1-2, pp. 173–221, 1997.

[67] J. Appel, H. Bockhorn, and M. Frenklach, "Kinetic modeling of soot formation with detailed chemistry and physics: laminar premixed flames of C2 hydrocarbons," *Combustion and Flame*, vol. 121, no. 1-2, pp. 122–136, 2000.

[68] T.P. Coffee and J.M. Heimerl, "Transport algorithms for premixed, laminar steady-state flames," *Combustion and Flame*, vol. 43, pp. 273 – 289, 1981.

[69] C.R. Wilke, "A viscosity equation for gas mixtures," *The Journal of Chemical Physics*, vol. 18, p. 517, 1950.

[70] P. Riviere, D. Scutaru, A. Soufiani, and J. Taine, "A new CK data base suitable from 300 K to 2500 K for spectrally correlated radiative transfer in CO2-H2O-transparent gas mixtures," in *Proceedings of the 10th International Heat Transfer Conference, Taylor & Francis*, 1994.

[71] L.S. Rothman, A. Barbe, D. Chris Benner, L.R. Brown, C. Camy-Peyret, M.R. Carleer, K. Chance, C. Clerbaux, V. Dana, V.M. Devi *et al.*, "The HITRAN molecular spectroscopic database: edition of 2000 including updates through 2001," *Journal of Quantitative Spectroscopy and Radiative Transfer*, vol. 82, no. 1-4, pp. 5–44, 2003.

[72] W. Malkmus, "Random Lorentz Band Model with Exponential-Tailed Sˆ-1 Line-Intensity Distribution Function," *Journal of the Optical Society of America*, vol. 57, no. 3, pp. 323–329, 1967.

[73] B.G. Carlson and K.D. Lathrop, "Transport theory-the method of discrete ordinates," *Computing methods in reactor physics*, pp. 165–266, 1968.

[74] J.R. Tsai, M.N. Ozisik, and F. Santarelli, "Radiation in spherical symmetry with anisotropic scattering and variable properties," *Journal of Quantitative Spectroscopy and Radiative Transfer*, vol. 42, no. 3, pp. 187–199, 1989.

[75] T. Sghaier, M. S. Sifaoui, and A. Soufiani, "Study of radiation in spherical media using discrete ordinates method associated with the finite legendre transform," *Journal of Quantitative Spectroscopy and Radiative Transfer*, vol. 64, no. 4, pp. 339 – 351, 2000.

[76] T. Songtao, "A computational study of spherical diffusion flames in microgravity with gas radiation," Ph.D. dissertation, The University of Michigan, 2008.

[77] R.W. Bilger, "The structure of turbulent nonpremixed flames," in *Symposium(International) on Combustion, 22 nd, Seattle, WA*, 1989, pp. 475–488.

[78] P.D. Ronney. [Online]. Available: http://carambola.usc.edu/Research/MicroFIRE/

[79] A.C. Fernandez-Pello, "Micropower generation using combustion: issues and approaches," *Proceedings of the Combustion Institute*, vol. 29, no. 1, pp. 883–899, 2002.

[80] S.A. Jacobson and A.H. Epstein, "An informal survey of power MEMS," in *Proceedings of the International Symposium on Micro-Mechanical Engineering*, 2003, pp. 513–20.

[81] F.G. Roper, "The prediction of laminar jet diffusion flame sizes: Part I. Theoretical model," *Combustion and Flame*, vol. 29, pp. 219–226, 1977.

[82] H. Ban, S. Venkatesh, and K. Saito, "Convection-diffusion controlled laminar micro flames," *ASME, Transactions, Journal of Heat Transfer*, vol. 116, no. 4, pp. 954–959, 1994.

[83] L.M. Matta, Y. Neumeier, B. Lemon, and B.T. Zinn, "Characteristics of microscale diffusion flames," in *Symposium(International) on Combustion, 29 th*, 2002, pp. 933–939.

[84] T.S. Cheng, C.P. Chen, C.S. Chen, Y.H. Li, C.Y. Wu, and Y.C. Chao, "Characteristics of microjet methane diffusion flames," *Combustion Theory and Modelling*, vol. 10, no. 5, pp. 861–881, 2006.

[85] T.S. Cheng, Y.C. Chao, C.Y. Wu, Y.H. Li, Y. Nakamura, K.Y. Lee, T. Yuan, and T.S. Leu, "Experimental and numerical investigation of microscale hydrogen diffusion flames," in *Symposium (International) on Combustion, 30 th*, no. 2. Elsevier, 2005, pp. 2489–2497.

[86] Y. Nakamura, H. Yamashita, and K. Saito, "A numerical study on extinction behaviour of laminar micro-diffusion flames," *Combustion Theory and Modelling*, vol. 10, no. 6, pp. 927–938, 2006.

[87] Kazunori Kuwana, Nami Tagami, Satoru Mizuno, and Tamio Ida, "Extinction of laminar jet diffusion microflames," *Proceedings of the Combustion Institute*, vol. 32, no. 2, pp. 3115–3121, 2009.

[88] P.D. Ronney, M.S. Wu, H.G. Pearlman, and K.J. Weiland, "Experimental study of flame balls in space: Preliminary results from STS-83," *AIAA journal*, vol. 36, no. 8, pp. 1361–1368, 1998.

[89] M.S. Butler, R.L. Axelbaum, C.W. Moran, and P.B. Sunderland, "2008-01-0726 Flame Quenching Limits of Hydrogen Leaks," *SAE SP*, vol. 2166, p. 119, 2008.

[90] M.S. Butler, C.W. Moran, P.B. Sunderland, and R.L. Axelbaum, "Limits for hydrogen leaks that can support stable flames," *International Journal of Hydrogen Energy*, 2009.

[91] B.J. Lee and S.H. Chung, "Stabilization of lifted tribrachial flames in a laminar nonpremixed jet," *Combustion and Flame*, vol. 109, no. 1-2, pp. 163–172, 1997.

[92] T.S. Cheng, C.Y. Wu, C.P. Chen, Y.H. Li, Y.C. Chao, T. Yuan, and T.S. Leu, "Detailed measurement and assessment of laminar hydrogen jet diffusion flames," *Combustion and Flame*, vol. 146, no. 1-2, pp. 268–282, 2006.

[93] H. Bockhorn, *Soot formation in combustion: mechanisms and models*. Springer, Berlin, 1994.

[94] I. Glassman, F.L. Dryer, and R.F. Sawyer, *Physical and Chemical Aspects of Combustion: A Tribute to Irvin Glassman*. Taylor & Francis, 1997.

[95] B.S. Haynes and H.G. Wagner, "Soot formation," *Progress in Energy and Combustion Science*, vol. 7, no. 4, pp. 229–273, 1981.

[96] I. Glassman, "Soot formation in combustion processes," in *Symposium(International) on Combustion, 22 nd, Seattle, WA*, 1989, pp. 295–311.

[97] I. Glassman, "Sooting laminar diffusion flames: Effect of dilution, additives, pressure, and microgravity," in *Symposium (International) on Combustion, 27 th*, vol. 1, 1998, pp. 1589–1596.

[98] M. Frenklach, "Reaction mechanism of soot formation in flames," *Physical Chemistry Chemical Physics*, vol. 4, no. 11, pp. 2028–2037, 2002.

[99] Z.A. Mansurov, "Soot Formation in Combustion Processes (Review)," *Combustion, Explosion, and Shock Waves*, vol. 41, no. 6, pp. 727–744, 2005.

[100] D.L. Urban and G.M. Faeth, "Soot research in combustion science: Introduction and review of current work," in *AIAA, Aerospace Sciences Meeting and Exhibit, 39 th, Reno, NV*, 2001.

[101] G.M. Faeth and Ü.Ö. Köylü, "Soot morphology and optical properties in non-premixed turbulent flame environments," *Combustion science and technology*, vol. 108, no. 4, pp. 207–229, 1995.

[102] H. Richter and J.B. Howard, "Formation of polycyclic aromatic hydrocarbons and their growth to soota review of chemical reaction pathways," *Progress in Energy and Combustion Science*, vol. 26, no. 4-6, pp. 565–608, 2000.

[103] I. Glassman, *Combustion*. Academic Press, 1996.

[104] C.J. Sun, C.J. Sung, H. Wang, and C.K. Law, "On the structure of nonsooting counterflow ethylene and acetylene diffusion flames," *Combustion and Flame*, vol. 107, no. 4, pp. 321–335, 1996.

[105] M. Frenklach, D.W. Clary, W.C. Gardiner, and S.E. Stein, "Effect of fuel structure on pathways to soot," *Symposium (International) on Combustion*, vol. 21, no. 1, pp. 1067 – 1076, 1988, twenty-First Symposium(International) on Combustion.

[106] C.A. Schuetz and M. Frenklach, "Nucleation of soot: Molecular dynamics simulations of pyrene dimerization," *Proceedings of the Combustion Institute*, vol. 29, no. 2, pp. 2307–2314, 2002.

[107] M. Smoluchowski, "Versuch einer mathematischen Theorie der Koagulationskinetik kolloider Losungen," *Z. phys. Chem*, vol. 92, pp. 129–168, 1917.

[108] S.K. Friedlander, *Smoke, dust, and haze*. Wiley New York, 1977.

[109] A. Kazakov and M. Frenklach, "Dynamic modeling of soot particle coagulation and aggregation: Implementation with the method of moments and application to high-pressure laminar premixed flames," *Combustion and Flame*, vol. 114, no. 3-4, pp. 484–501, 1998.

[110] A. Kazakov and M. Frenklach, "On the relative contribution of acetylene and aromatics to soot particle surface growth," *Combustion and Flame*, vol. 112, no. 1-2, pp. 270–274, 1998.

[111] M. Frenklach, "On surface growth mechanism of soot particles," *Symposium (International) on Combustion*, vol. 26, no. 2, pp. 2285 – 2293, 1996.

[112] K.G. Neoh, J.B. Howard, and A.F. Sarofim, *Particulate carbon: Formation during combustion*. Plenum New York, 1981.

[113] M.M. Harris, G.B. King, and N.M. Laurendeau, "Influence of temperature and hydroxyl concentration on incipient soot formation in premixed flames," *Combustion and Flame*, vol. 64, no. 1, pp. 99–112, 1986.

[114] P. Markatou, H. Wang, and M. Frenklach, "A computational study of sooting limits in laminar premixed flames of ethane, ethylene, and acetylene," *Combustion and Flame*, vol. 93, no. 4, pp. 467–482, 1993.

[115] F. Takahashi and I. Glassman, "Sooting correlations for premixed flames," *Combustion Science and Technology*, vol. 37, no. 1, pp. 1–19, 1984.

[116] D.X. Du, R.L. Axelbaum, and C.K. Law, "The influence of carbon dioxide and oxygen as additives on soot formation in diffusion flames," in *Symposium(International) on Combustion, 23 nd*, vol. 23, 1990, pp. 1501–1507.

[117] J. Du and R.L. Axelbaum, "The effect of flame structure on soot-particle inception in diffusion flames," *Combustion and Flame*, vol. 100, no. 3, pp. 367–375, 1995.

[118] R.A. Dobbins, "Soot inception temperature and the carbonization rate of precursor particles," *Combustion and Flame*, vol. 130, no. 3, pp. 204–214, 2002.

[119] R.J. Santoro, T.T. Yeh, J.J. Horvath, and H.G. Semerjian, "The transport and growth of soot particles in laminar diffusion flames," *Combustion Science and Technology*, vol. 53, no. 2, pp. 89–115, 1987.

[120] P.B. Sunderland and G.M. Faeth, "Soot formation in hydrocarbon/air laminar jet diffusion flames," *Combustion and Flame*, vol. 105, no. 1-2, pp. 132–146, 1996.

[121] R.A. Tesner and S.V. Shurupov, "Soot formation from acetylene-benzene mixture," *Combustion Science and Technology*, vol. 92, no. 1, pp. 61–67, 1993.

[122] K.C. Lin and G.M. Faeth, "Effects of hydrodynamics on soot formation in laminar opposed-jet diffusion flames," *Journal of Propulsion and Power*, vol. 12, no. 4, pp. 691–698, 1996.

[123] M.E. Decroix and W.L. Roberts, "Transient flow field effects on soot volume fraction in diffusion flames," *Combustion Science and Technology*, vol. 160, no. 1, pp. 165–189, 2000.

[124] S. Gordon and B.J. McBride, *Computer program for calculation of complex chemical equilibrium compositions and applications*. National Aeronautics and Space Administration, Office of Management, Scientific and Technical Information Program, 1996.

[125] B.M. Kumfer, S.A. Skeen, and R.L. Axelbaum, "Soot inception limits in laminar diffusion flames with application to oxy-fuel combustion," *Combustion and Flame*, vol. 154, no. 3, pp. 546 – 556, 2008.

[126] X. Zhou and S. Mahalingam, "A suitable mixture fraction for diffusion flames of wood pyrolysis gas," *Combustion and Flame*, vol. 133, no. 1-2, pp. 197–199, 2003.

[127] B.M. Kumfer, S.A. Skeen, R. Chen, and R.L. Axelbaum, "Measurement and analysis of soot inception limits of oxygen-enriched coflow flames," *Combustion and Flame*, vol. 147, no. 3, pp. 233–242, 2006.

[128] I.M. Kennedy, "Models of soot formation and oxidation," *Progress in Energy and Combustion Science*, vol. 23, no. 2, pp. 95–132, 1997.

[129] H.F. Calcote and D.M. Manos, "Effect of molecular structure on incipient soot formation," *Combustion and Flame*, vol. 49, pp. 289–304, 1983.

[130] S. Yan, E.G. Eddings, A.B. Palotas, R.J. Pugmire, and A.F. Sarofim, "Prediction of sooting tendency for hydrocarbon liquids in diffusion flames," *Energy Fuels*, vol. 19, no. 6, pp. 2408–2415, 2005.

[131] I.M. Khan, G. Greeves, and D.M. Probert, "Air Pollution Control in Transport Engines," *Institution of Mechanical Engineers*, p. 205, 1971.

[132] P.A. Tesner, T.D. Snegiriova, and V.G. Knorre, "Kinetics of dispersed carbon formation (Particle formation rates in thermal decomposition of acetylene in diffusion flame, noting activation energy)," *Combustion and Flame*, vol. 17, pp. 253–260, 1971.

[133] J.B. Moss, C.D. Stewart, and K.J. Syed, "Flowfield modelling of soot formation at elevated pressure," in *Twenty-Second Symposium (International) on Combustion*, 1988, pp. 413–423.

[134] J.B. Moss, C.D. Stewart, and K.J. Young, "Modeling soot formation and burnout in a high temperature laminar diffusion flame burning under oxygen-enriched conditions," *Combustion and Flame*, vol. 101, no. 4, pp. 491–500, 1995.

[135] K.M. Leung, R.P. Lindstedt, and W.P Jones, "A simplified reaction mechanism for soot formation in nonpremixed flames," *Combustion and Flame*, vol. 87, no. 3-4, pp. 289 – 305, 1991.

[136] C.R. Kaplan, C.R. Shaddix, and K.C. Smyth, "Computations of enhanced soot production in time-varying CH4/air diffusion flames," *Combustion and Flame*, vol. 106, no. 4, pp. 392–405, 1996.

[137] C.W. Lautenberger, J.L. de Ris, N.A. Dembsey, J.R. Barnett, and H.R. Baum, "A simplified model for soot formation and oxidation in CFD simulation of non-premixed hydrocarbon flames," *Fire Safety Journal*, vol. 40, no. 2, pp. 141–176, 2005.

[138] J. Boulanger, F. Liu, W.S. Neill, and G.J. Smallwood, "An improved soot formation model for 3D diesel engine simulations," *Journal of Engineering for Gas Turbines and Power*, vol. 129, p. 877, 2007.

[139] M. Balthasar and M. Kraft, "A stochastic approach to calculate the particle size distribution function of soot particles in laminar premixed flames," *Combustion and Flame*, vol. 133, no. 3, pp. 289–298, 2003.

[140] J. Singh, M. Balthasar, M. Kraft, and W. Wagner, "Stochastic modeling of soot particle size and age distributions in laminar premixed flames," *Proceedings of the Combustion Institute*, vol. 30, no. 1, pp. 1457–1465, 2005.

[141] R.I.A. Patterson and M. Kraft, "Models for the aggregate structure of soot particles," *Combustion and Flame*, vol. 151, no. 1-2, pp. 160–172, 2007.

[142] R.I.A Patterson, "Numerical Modelling of Soot Formation," Ph.D. dissertation, University of Cambridge, 2007.

[143] F. Gelbard and J.H. Seinfeld, "The general dynamic equation for aerosols-theory and application to aerosol formation and growth," *Journal of Colloid Interface Science*, vol. 68, pp. 363–382, 1979.

[144] M.D. Smooke, C.S. McEnally, L.D. Pfefferle, R.J. Hall, and M.B. Colket, "Computational and experimental study of soot formation in a coflow, laminar diffusion flame," *Combustion and Flame*, vol. 117, no. 1-2, pp. 117–139, 1999.

[145] M.D. Smooke, M.B. Long, B.C. Connelly, M.B. Colket, and R.J. Hall, "Soot formation in laminar diffusion flames," *Combustion and Flame*, vol. 143, no. 4, pp. 613–628, 2005.

[146] Q. Zhang, H. Guo, F. Liu, G.J. Smallwood, and M.J. Thomson, "Modeling of soot aggregate formation and size distribution in a laminar ethylene/air coflow diffusion flame with detailed PAH chemistry and an advanced sectional aerosol dynamics model," *Proceedings of the Combustion Institute*, vol. 32, no. 1, pp. 761–768, 2009.

[147] M. Frenklach and S.J. Harris, "Aerosol dynamics modeling using the method of moments," *Journal of colloid and interface science*, vol. 118, no. 1, pp. 252–261, 1987.

[148] M. Frenklach, "Dynamics of discrete distribution for Smoluchowski coagulation model," *Journal of colloid and interface science*, vol. 108, no. 1, pp. 237–242, 1985.

[149] M. Frenklach, "Method of moments with interpolative closure," *Chemical Engineering Science*, vol. 57, no. 12, pp. 2229–2239, 2002.

[150] A. Kazakov, H. Wang, and M. Frenklach, "Detailed modeling of soot formation in laminar premixed ethylene flames at a pressure of 10 bar," *Combustion and Flame*, vol. 100, no. 1-2, pp. 111–120, 1995.

[151] H. Wang, D.X. Du, D.X. Sung, and C.K. Law, "Experiments and numerical simulation on soot formation in opposed-jet ethylene diffusion flames," in *Symposium (International) on Combustion, 26 th*, vol. 26. Combustion Institute, 1996, pp. 2359–2368.

[152] Y. Yoshihara, A. Kazakov, H. Wang, and M. Frenklach, "Reduced mechanism of soot formation-application to natural gas fueled Diesel combustion," in *Symposium (International) on Combustion, 25 th.* Combustion Institute, 1994, pp. 941–941.

[153] H.A.E.R. El-Asrag, "Large Eddy Simulation Subgrid Model for Soot Prediction," Ph.D. dissertation, Georgia Institute of Technology, 2006.

[154] H.A.E.R. El-Asrag and S. Menon, "Large eddy simulation of soot formation in a turbulent non-premixed jet flame," *Combustion and Flame*, vol. 156, no. 2, pp. 385–395, 2009.

[155] N.L. Johnson and F.C. Leone, *Statistics and Experimental Design.* John Wiley & Sons, New-York, 1964.

[156] S.J. Harris and I.M. Kennedy, "The coagulation of soot particles with van der waals forces," *Combustion Science and Technology*, vol. 59, no. 4, pp. 443–454, 1988.

[157] Computational Modelling Group, "Cambridge soot database." [Online]. Available: http://como.cheng.cam.ac.uk/